Czech Technical University in Prague
Faculty of Nuclear Sciences and Physical Engineering
Department of Physical Electronics

Development of High-Repetition-Rate Picosecond Thin-Disk Lasers

Doctoral Thesis

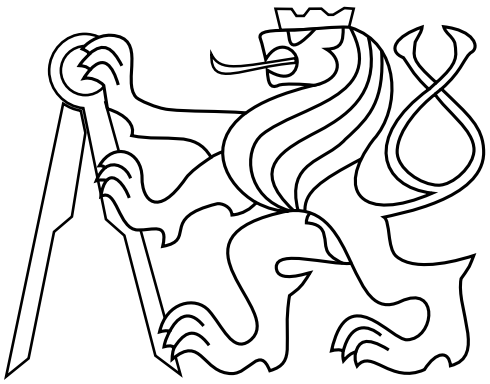

Author: **Ing. Jiří Mužík**
Supervisor: **Prof. Ing. Václav Kubeček, DrSc.**
Supervisor Specialist: **Ing. Martin Smrž, Ph.D.**

Bibliographic entry

AUTHOR	**Ing. Jiří Mužík** Czech Technical University in Prague Faculty of Nuclear Sciences and Physical Engineering Department of Physical Electronics
TITLE OF DISSERTATION	Development of High-Repetition-Rate Picosecond Thin-Disk Lasers
DEGREE PROGRAMME	Application of Natural Sciences
FIELD OF STUDY	Physical Engineering
SUPERVISOR	Prof. Ing. Václav Kubeček, DrSc. Department of Physical Electronics, FNSPE CTU
SUPERVISOR SPECIALIST	Ing. Martin Smrž, Ph.D. HiLASE Centre, Institute of Physics CAS
ACADEMIC YEAR	2020/2021
NUMBER OF PAGES	142
KEYWORDS	Thin-disk lasers, Regenerative amplifier, Yb:YAG, Cryogenic picosecond laser, Yb:YGAG ceramics, Erbium lasers

Bibliografický záznam

AUTOR	**Ing. Jiří Mužík** České vysoké učení technické v Praze Fakulta jaderná a fyzikálně inženýrská Katedra fyzikální elektroniky
NÁZEV DIZERTAČNÍ PRÁCE	Vývoj vysokorepetičních pikosekundových tenkodiskových laserů
STUDIJNÍ PROGRAM	Aplikace přírodních věd
STUDIJNÍ OBOR	Fyzikální inženýrství
ŠKOLITEL	Prof. Ing. Václav Kubeček, DrSc. Katedra fyzikální elektroniky FJFI ČVUT
ŠKOLITEL-SPECIALISTA	Ing. Martin Smrž, Ph.D. Centrum HiLASE, Fyzikální ústav AV ČR
AKADEMICKÝ ROK	2020/2021
POČET STRAN	142
KLÍČOVÁ SLOVA	Tenkodiskové lasery, Regenerativní zesilovač, Yb:YAG, Kryogenní pikosekundový laser, Yb:YGAG keramika, Erbiové lasery

Abstract

This doctoral thesis pursues the research and development of solid-state lasers with high average output power, ultrashort pulse duration, high repetition rate, and output beam quality close to the diffraction limit. Laser systems with these attributes find numerous applications not only in industry, but also in science, medicine, and other fields. In order to obtain these – to some extent contradicting – parameters from a single laser device, the thin-disk laser concept was selected as the most suitable one and it is also the central topic of this work.

In the introductory chapter, known solid-state laser materials are summarized with focus on those suitable for high-power laser generation. Methods most frequently used in high-power lasers are discussed and current state-of-the-art ultrafast ytterbium thin-disk lasers are overviewed.

The first part of the experimental section covers investigation of novel ceramic gain media that have potential for use in thin-disk lasers. An ytterbium-doped transparent ceramic from mixed garnet YGAG ($Y_3Ga_2Al_3O_{12}$) was tested and confirmed as a promising alternative to the widely-used Yb:YAG crystal, especially for ultrashort pulse generation at low temperature, which are conditions generally highly advantageous for solid-state laser performance. The developed picosecond, liquid-nitrogen-cooled laser oscillator utilized mode locking with a semiconductor absorber mirror (SESAM) and generated laser pulses with duration of 2.4 ps, a four times shorter value than what has been reported with a cryogenic Yb:YAG laser. Another investigated material was erbium-doped ceramic sesquioxide Y_2O_3, offering emission wavelength in an attractive spectral range around 2.7 μm, i.e. near the boundary of the mid-IR region – this makes it an interesting option for extension of thin-disk laser technology. The main advantage of this laser material is its suitability for diode pumping with well-accessible 1-μm semiconductor lasers. After several developmental stages, a compact watt-level continuous-wave laser with optical-to-optical efficiency of 14.3% and nearly diffraction-limited beam quality was constructed.

The main part of this work describes the development of a picosecond thin-disk laser system PERLA C based on Yb:YAG gain medium. Its architecture and individual modules and sub-systems are presented in detail. A system of fiber and solid-state laser amplifiers was developed and chirped pulse amplification (CPA) technique was implemented in this laser system. The main thin-disk regenerative amplifier with ring cavity reached its target parameters, i.e. average output power over 500 W at repetition rate of 100 kHz with extraction efficiency over 43% and beam quality parameter M^2 around 1.4. At 50-kHz repetition rate then the maximum pulse energy was 9 mJ. During the development, particular attention was paid to the design of the optical resonator, implementation of an electro-optic switch (Pockels cell) including suppression of piezoelectric resonances in its nonlinear crystals, and preventing pulse distortions by nonlinear optical effects. For pulse compression, application of chirped volume Bragg grating (CVBG) was tested, but due to poor beam quality, a highly efficient Treacy-type grating

compressor with dielectric diffraction gratings was used instead. Measured duration of output pulses was 1.03 ps and compression was, due to operational reasons, demonstrated at power up to 350 W. The most important application results achieved with this laser system are mentioned as well. The PERLA C laser system belongs among the most powerful picosecond laser amplifiers of today and it is the most powerful single-thin-disk regenerative amplifier reported to this day.

Abstrakt

Předkládaná dizertační práce je věnována výzkumu a vývoji pevnolátkových laserů s vysokým středním výstupním výkonem, velmi krátkou délkou pulzu, vysokou opakovací frekvencí a s kvalitou svazku blízkou difrakční mezi. Laserové systémy takovýchto parametrů nacházejí bohaté uplatnění zejména v průmyslových aplikacích, ale také ve vědě a výzkumu, v lékařství a dalších odvětvích lidské činnosti. Pro dosažení těchto do jisté míry protichůdných požadavků byla jako nejvhodnější využita tenkodisková koncepce laserového prostředí, která je zároveň průvodním tématem této práce.

V úvodní části jsou stručně shrnuty známé pevnolátkové laserové materiály se zaměřením na ty s vlastnosmi vhodnými pro výkonové lasery. Probrány jsou nejpoužívanější techniky používané ve výkonových laserových systémech a současný stav vývoje ytterbiových tenkodiskových laserů s krátkými pulzy.

V první části experimentu byly studovány atraktivní keramické aktivní materiály, které by v blízké době mohly najít uplatnění právě v tenkodiskových laserech. Testována byla transparentní keramika z ytterbiem dopovaného smíšeného granátu YGAG ($Y_3Ga_2Al_3O_{12}$), která se ukázala jako slibná alternativa k široce používanému krystalu Yb:YAG, a to zejména pro generaci ultrakrátkých pulzů za nízkých teplot, jež jsou obecně pro pevnolátkové lasery příznivé. Sestavený pikosekundový laserový oscilátor chlazený tekutým dusíkem využíval synchronizaci módů polovodičovým saturovatelným absorbérem (SESAM) a dokázal generovat laserové pulzy délky 2,4 ps, což je hodnota čtyřikrát nižší než bylo dosaženo s kryogenním Yb:YAG laserem. Dalším zkoumaným materiálem byl keramický, erbiem dopovaný seskvioxid Y_2O_3, který umožňuje laserovou generaci v aplikačně velmi žádané oblasti 2,7 μm, tedy na prahu střední infračervené oblasti – jednalo by se tak o zajímavé rozšíření možností tenkodiskových laserů. Hlavní výhodou tohoto materiálu je, že k poměrně účinnému fungování laseru postačuje buzení dobře dostupnými polovodičovými lasery na vlnové délce kolem 1 μm. Po několika fázích vývoje byl vyvinut kompaktní wattový kontinuální laser s optickou účinností 14,3 % a kvalitou svazku blízkou difrakčnímu limitu.

Hlavní část práce se pak zabývá vývojem pikosekundového tenkodiskového laserového systému PERLA C využívajícího aktivního prostředí Yb:YAG. Podrobně popsána je jeho architektura a jednotlivé moduly a podsystémy. Vyvinuta byla soustava vláknových a pevnolátkových předzesilovačů a implementována byla metoda zesilování čerpovaných pulzů (CPA). Hlavní tenkodiskový regenerativní zesilovač s kruhovým rezonátorem dosáhl plánovaných parametrů, tzn. středního výkonu přes 500 W na opakovací frekvenci 100 kHz s extrakční účinností přes 43 % a s kvalitou svazku danou parametrem M^2 blízkým 1,4. Na opakovací frekvenci 50 kHz pak byla dosažena energie v pulzu přes 9 mJ. Zvláštní pozornost při vývoji zesilovače byla věnována návrhu optického rezonátoru, realizaci elektrooptické závěrky (Pockelsovy cely), včetně eliminace piezoelektrických vibrací v jejích krystalech, a udržení nežádoucích optických nelineárních jevů v systému na přijatelné úrovni. Pro kompresi výstupních pulzů

byla testována možnost použití čerpovaných objemových Braggovských mřížek (CVBG), ale kvůli neuspokojivé kvalitě svazku byla dána přednost kompresoru Treacyho typu s dielektrickými difrakčními mřížkami s difrakční účinností kolem 99 %. Změřená délka výstupních pulzů pak byla 1.03 ps a komprese byla z provozních důvodů demonstrována s výkonem do 350 W. V rámci práce jsou též shrnuty nejvýznamnější experimentální výsledky dosažené s laserovým systémem PERLA C. Tento vysoce účinný tenkodiskový laser patří mezi nejvýkonnější pikosekundové zesilovače současnosti a v rámci regenerativních zesilovačů s jedním tenkým diskem se jedná o vůbec nejvýkonnější laserový zesilovač.

Table of Contents

List of used abbreviations and symbols

AC, ACF	Autocorrelation (function)
ANDi	All-normal-dispersion (fiber oscillator)
AoD	Angle of diffraction
AoI	Angle of incidence
AOM	Acousto-optic modulator
AR	Anti-reflection
a.u.	Arbitrary units
ASE	Amplified spontaneous emission
BBO	Beta barium borate [β-Ba$(BO_2)_4$]
BME	Bergmann Messgeräte Entwicklung KG
BW	Bandwidth
CaF_2	Calcium fluoride
CAS	Czech Academy of Science
CC	Concave
CE	Conversion efficiency
CFBG	Chirped fiber Bragg grating
CO_2	Carbon dioxide
CPA	Chirped-pulse amplification
CS	Cross section
CuW	Copper-tungsten (mixture)
CVBG	Chirped volume Bragg grating
CVD	Chemical vapor deposited (diamond)
CW	Continuous-wave
CX	Convex
d.c.	Duty cycle
DPA	Divided pulse amplification
DC	Direct current
DCF	Double-clad fiber
DG	Delay generator
DOE	Diffractive optical element
DL	Diode laser
DPSSL	Diode-pumped solid-state laser
DUV	Deep ultraviolet (range from 280 to 200 nm)
EDFA	Erbium-doped fiber amplifier
EO, EOM	Electro-optic (modulator)
ESA	Excited-state absorption

ETH	Swiss Federal Institute of Technology in Zürich
FE	Front end
FNSPE CTU	Faculty of Nuclear Sciences and Physical Engineering of the Czech Technical University in Prague
FR	Faraday rotator
FWHM	Full width at half maximum
GaAs	Gallium arsenide
GDD	Group delay dispersion
GVD	Group velocity dispersion
He-Ne	Helium-neon (gas mixture)
HHG	High harmonics generation
HR	High-reflection
HWP	Half-wave plate
IFSW	Institut für Strahlwerkzeuge (Institute for Laser Tools of the University of Stuttgart)
KGW	$KGd(WO_4)_2$ (potassium gadolinium tungstate)
KYW	$KY(WO_4)_2$ (potassium yttrium tungstate)
LD	Laser diode
LMA	Large mode area (fiber)
MIR	Mid-infrared (spectral region of $\approx$ 3-8 μm)
MIT	Massachusetts Institute of Technology
ML	Mode locking
MOPA	Master oscillator – power amplifier
MPA	Multipass amplifier
MPQ	Max-Planck Institut für Quantenoptik (Garching, Germany)
NA	Numerical aperture
NIFS	National Institute for Fusion Science (Toki, Japan)
NIR	Near-infrared (spectral region of $\approx$ 0.75-1.4 μm)
PBS	Polarization beam splitter
PC, PCell	Pockels cell
PD	Photodiode
PM	Polarization-maintaining (fiber)
PMMA	Poly(methyl methacrylate)
O-O	Optical-to-optical (efficiency)
OPCPA	Optical parametric chirped-pulse amplification
RE	Rare-earth (element), lanthanide
RoC	Radius of curvature
QCW	Quasi-continuous-wave

QML	Q-switched mode-locking
QWP	Quarter-wave plate
RA	Regenerative amplifier
RBW	Resolution bandwidth
RF	Radio-frequency
RMS	Root-mean-square
SCF	Single-crystal-fiber (amplifier)
SEM	Scanning electrone microscope
SESAM	Semiconductor saturable absorber mirror
SF	Self-focusing
SM	Single-mode (fiber)
SPM	Self-phase modulation
SRS	Stimulated Raman scattering
SSL	Solid-state lasers
SW	Standing-wave (linear cavity)
TD	Thin-disk
TDM	Thin-disk module (TD laser head)
TFP	Thin-film polarizer
TiO_2	Titanium dioxide
TOD	Third-order dispersion
UC	Upconversion
UV	Ultraviolet (spectral region of 10-400 nm)
VBG	Volume Bragg grating
YAG	Yttrium aluminum garnet ($Y_3Al_5O_{12}$)
YAP	Yttrium aluminum perovskite ($YAlO_3$)
YDFA	Ytterbium-doped fiber amplifier
YGAG	Yttrium gallium aluminum garnet ($Y_3Ga_2Al_3O_{12}$)
YGG	Yttrium gallium garnet ($Y_3Ga_5O_{12}$)
YLF	Yttrium lithium fluoride ($LiYF_4$)
Y_2O_3	Yttria (yttrium(III) oxide)
ZPL	Zero-phonon-line
η	Slope efficiency
λ, Λ	Wavelength, grating period
ν	Frequency
σ	Cross section
τ	Temporal duration
ϕ, φ	Phase (time domain), spectral phase
ω	Angular velocity

A	Area
B	B-integral (accumulated nonlinear phase shift)
c	Speed of light in vacuum
d	Distance
e	Euler's number
E	Energy
F	Fluence
f	Focal distance
G, g	Gain, gain coefficient
$h\nu$	Photon energy
L	Length
n, n_0	Refractive index
n_2	Nonlinear refractive index
P	Power
t	Time
V	Voltage
w	Beam radius (at $1/e^2$ level)

Chapter 1

Introduction

Ultrafast high-repetition-rate high-average-power lasers are a key tool for further progress in many industrial and scientific application. They help to increase processing speed in many advanced manufacturing processes, requiring high precision and the unique properties of ultrafast optical pulses, or improve the signal-to-noise ratio in various scientific applications.

The HiLASE Centre [1], based in Dolní Břežany, Czechia, focuses on development of such laser sources. Its main research activities are research and development of advanced laser systems and their applications in industry and science. The work presented in this thesis represents a part of its extensive research activities in the field of thin-disk lasers [A3,A4]. The author's responsibility was the development of a thin-disk beamline with the highest repetition rate within the project (variable in range from 50 to 200 kHz). Introduced are also important results of investigation of more rare laser materials, which were deemed as promising for further development of the group's research activities.

In this chapter, a brief historical overview of evolution of solid-state lasers is given in Sec. 1.1 and the most important of their many applications are mentioned in Sec. 1.2. The main goals of this thesis are then introduced in Sec. 1.3.

The second chapter approaches solid-state laser media in Sec. 2.1, with focus on ytterbium- and erbium-doped materials. Some important technical aspects of high-power lasers are described in Sec. 2.2, together with an introduction of the thin-disk laser concept and an overview of the current state-of-the-art in this field. The Chap. 3 then covers the measuring methods and instruments used in the experimental part of this work.

The Chapter 4 presents the experimental results obtained with small-scale laser oscillators. A picosecond cryogenic oscillator based on novel ceramic laser material Yb:YGAG is introduced in Sec. 4.1. Development of an efficient diode-pumped $\approx$ 3-μm laser source using Er:Y_2O_3 ceramics as the gain medium is described in Sec. 4.2. The main part of the experimental work is included in the Chapter 5, covering in detail the development of a high-repetition-rate picosecond thin-disk laser system PERLA C, including a half-kilowatt thin-disk regenerative amplifier.

Finally, a summary of results that have emerged from this work, and their impact to the progress of laser science, are presented in Chap. 6.

1.1 Laser: The invention and historical perspective

The theoretical foundations of laser operation were laid in 1917 by A. Einstein [2], who described, based on the work of M. Planck on black-body radiation [3], the three fundamental processes of interaction between electromagnetic radiation and matter: absorption, spontaneous

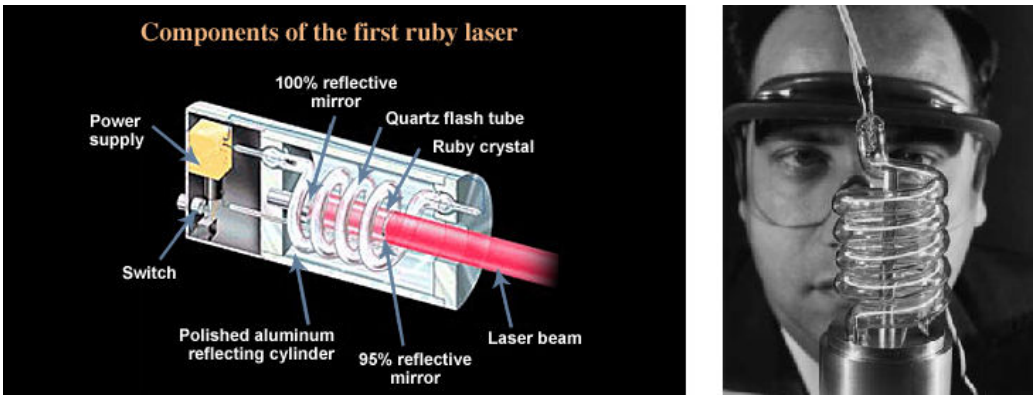

Fig. 1.1: The first ruby laser of Theodor H. Maiman. Left – its technical design (the interior of the laser was cooled by forced air flow, which is not apparent here); right – some newer unit being inspected by the inventor (the crystal and flash lamp used in the original laser were shorter). Adopted from [6].

emission, and stimulated emission. Although all these three processes take place in a running laser, utilizing the stimulated emission for light generation or amplification is the defining and distinguishing feature of a laser[1] device.

It took several decades before the necessary theoretical background was built up and first operating device based on this principle was demonstrated. Predecessor of the laser, emitting in the microwave region – so called *maser* – was invented in 1953 by Townes, Gordon, and Zeigler [4]. The "optical maser" was next, as several research groups in the USA and the Soviet Union investigated the cornerstones of laser technology: suitable active materials with multi-level energy structure, possibility of optical pumping, and introduction of optical feedback by means of open resonators. The main struggle was to store enough energy in the active medium to obtain population inversion and thus optical gain. Finally, in May 1960, T. Maiman developed a flash-lamp-pumped ruby laser (chromium-doped corundum, Cr^{3+}:Al_2O_3) emitting red light at wavelength of 694 nm [5]. This laser is shown in Fig. 1.1.

It seems fitting for such a high-tech field of science that although most of the essential ideas and techniques were coined only months or few years after this initial invention, they are still being honed and elaborated until these days. In the same year with the ruby oscillator, a second laser, cryogenic uranium-doped CaF_2 (a four-level system, unlike the three-level ruby) was constructed [7], as well as the first gas laser, employing a He-Ne mixture [8]. The first fiber laser using the waveguide effect in glass was introduced only a year later [9]. Laser action in semiconductor (GaAs laser diode) was reported in 1962 [10] and two years later, first diode-pumped solid-state laser (GaAs-pumped U:CaF_2) was reported [11]. Also the main methods for short laser pulse generation were devised – the Q-switching of a ruby laser in 1962 [12] and mode-locking in a He-Ne laser one year later [13].

Many different types of lasers emerged and, when classified according to the type of their gain medium, the most important classes have been the solid-state lasers (doped insulator lasers such as the ruby laser, but also fiber lasers and semiconductor lasers), gas lasers (including excimer, metal-vapor and chemical lasers), and liquid dye lasers. Within this work, the term *solid-state lasers* is used specifically for the doped insulator lasers.

The output power of first lasers was very limited and major effort was put in increasing the laser power and intensity. Two most promising laser materials for power scaling were at the time the solid-state neodymium-doped YAG ($Y_3Al_5O_{12}$, main emission wavelength of 1.064 μm)

[1] LASER – acronym for Light Amplification by Stimulated Emission of Radiation

and gaseous CO_2 (10.6 μm wavelength), both introduced in 1964 [14, 15]. For generation with high intensity and high-average-power laser pulses, which is the main scope of this thesis, the solid-state lasers have been more promising, with the flash-lamp pumped Nd:YAG crystal being the usual material of choice.

After increasing the average power of the solid-state lasers by several orders of magnitude, the largest potential for further increase in the peak power and intensity of their output lay in shortening the pulse duration. Using the mode-locking technique, generation of sub-picosecond pulses was possible as early as in the 1970s, while other methods, such as Q-switching, were limited to pulse widths by three or more orders of magnitude longer and to much lower pulse repetition rate (limiting the average power), although they could directly offer an incomparably higher pulse energy. Amplification of pulses from a mode-locked laser oscillator was a favorable way for obtaining intense light, soon so intense that the damage threshold of optical materials in the laser amplifiers became a limit that could not be bypassed just by enlarging the laser beam. A remedy was found in 1985, when the chirped-pulse amplification technique (CPA) was introduced [16], which consisted in stretching the broadband oscillator pulses in time to decrease the intensity in the amplifiers and compressing the pulses afterwards close to their initial duration. As the stretching factor could be as high as 1000 or even more, this method significantly moved the frontiers of high-intensity laser technology.

Significant drawback of neodymium lasers to short pulse generation (and to their use in CPA laser systems) is their relatively narrow gain bandwidth. One exception were the Nd:glass lasers with broad emission spectrum well-suited for femtosecond operation. The glass could be easily fabricated in large dimensions compared to crystalline materials – allowing storage of large amount of energy – and enabled pulse amplification with kJ-level energy. However, very low thermal conductivity of glass materials made these lasers unsuitable for high-repetition-rate and high-average-power operation. About the same time as the CPA technique, a titanium-doped sapphire [17] emerged as a perfect material for short pulse generation and almost entirely substituted dye lasers in the field of ultrafast optics (Ti:Sa gradually reached 5 fs pulse duration [18]). Typically pumped with green lasers, Ti:sapphire has an extremely broad gain spectrum and wavelength tunability from ca. 0.65 to 1.1 μm, favorable thermo-mechanical properties and it has allowed construction of laser systems reaching unprecedently high peak power (current record holder is the 10-petawatt system in ELI-NP, Romania [19]), although these extreme systems are very limited in terms of repetition rate and average power.

In mid-1980s, several-watt diode lasers became commercially available and turned into an interesting source for pumping solid-state lasers. While many neodymium-doped materials including Nd:YAG had absorption spectra well-suited for pumping with krypton-filled flash lamps, diode pumping offered increased efficiency and reliability and also allowed use of new configurations in the laser design. Moreover, there were well-known laser materials that, although deemed as unpromising with flash-lamp pumping, seemed to be tailored for diode pumping. A good example are the ytterbium-doped materials (discussed further in Sec. 2.1.2) with only two energy level manifolds and a single absorption band that is too narrow for flash-lamp pumping. With narrowband diode pump, its simple energy-level structure was turned into an advantage and in early 1990's, first diode-pumped Yb:YAG laser was demonstrated [20].

The following decades were marked by power-scaling and maturing of the laser technology. Some of the new approaches are described in Sec. 2.2. One of them was invention of the thin-disk geometry by A. Giesen et al. in 1992 [21] that perfectly utilized then recently rediscovered Yb:YAG gain medium and allowed for principally unlimited power scaling of high-beam-quality, ultrafast solid-state lasers and it also made possible the results presented within this thesis.

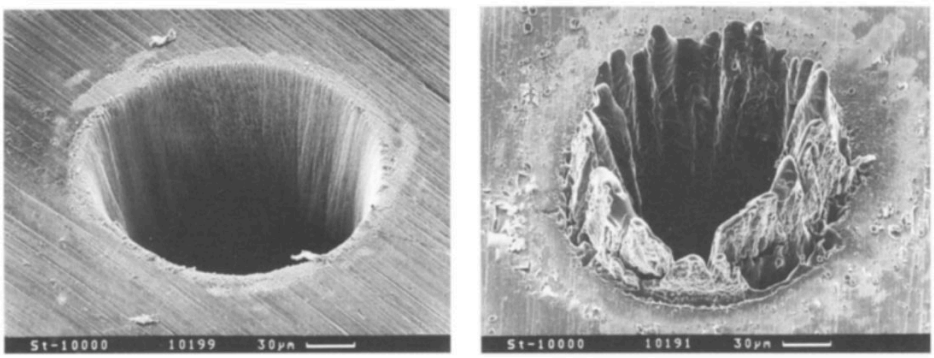

(a) (b)

Fig. 1.2: Comparison of SEM photographs of a hole drilled in 100 μm thick steel foil with Ti:sapphire laser (wavelength of 780 nm) and (a) 200-fs, 120-μJ pulses, (b) 3.3-ns, 1-mJ pulses [25].

1.2 Laser applications

At the time of its invention, the laser was described as a "solution looking for a problem" [22] – there was no obvious application prepared for a device producing intense, monochromatic and directed beam of highly monochromatic light. However, very soon after developing the first ruby prototype, ruby lasers were used in eye surgery and skin treatment in 1961. For the military, early lasers seemed too weak for direct use, yet Q-switched ruby laser was adopted for range finding as soon as in 1964 [23]. With improving parameters of lasers and with general technological progress, a great variety of applications has emerged; the following paragraphs capture only a selection of their most important uses.

Use of lasers in material processing brought new possibilities, improved precision and economy to processes such as engraving and marking, soldering and welding, or cutting, drilling and surface structuring. For many of these industrial applications, use of ultrafast lasers (producing picosecond or femtosecond pulses) is highly beneficial, since they allow to easily exceed the ablation threshold of material. In case of sufficient energy in a short pulse, material can be efficiently removed from the workpiece without significant heating of the surroundings of the processed spot. This leads to e.g. cleaner holes without excessive melting and defects in their surroundings. A comparison of drilling with nanosecond and sub-picosecond pulses is shown in Fig. 1.2. High-energy laser pulses can be also used for material hardening by so-called laser shock peening, inducing internal mechanical stress in the surface and thus increasing the lifetime of heavy-duty components, especially those under high cyclic load [24].

Lasers have been applied in abundance also in medicine. As already mentioned, first medical use of laser was in ophthalmology – to destroy a retinal tumor. Lasers are now a standard tool for e.g. treating the retinal detachment and cataracts, or in refractive surgery for vision correction, improving quality of life (as the author can testify) of millions of people every year. In surgical operations, lasers operating in the spectral region around 3 μm, such as erbium lasers, are the most suitable, since the absorption of water (and so in tissue) is maximal around 2.8 μm (see Fig. 1.3). With use of optical fibers, less invasive endoscopic operations are also feasible (urology, cardiology, etc.). Lasers were successfully used in many ways also in dermatology and cosmetic surgery, dentistry, for cancer treatment and others.

Lasers can provide means for precise measurements of different physical quantities. The first applications were range finding and bar code scanning. Nowadays, laser scanning can precisely map 3D objects, while lidars and atmospheric remote sensing based on laser spec-

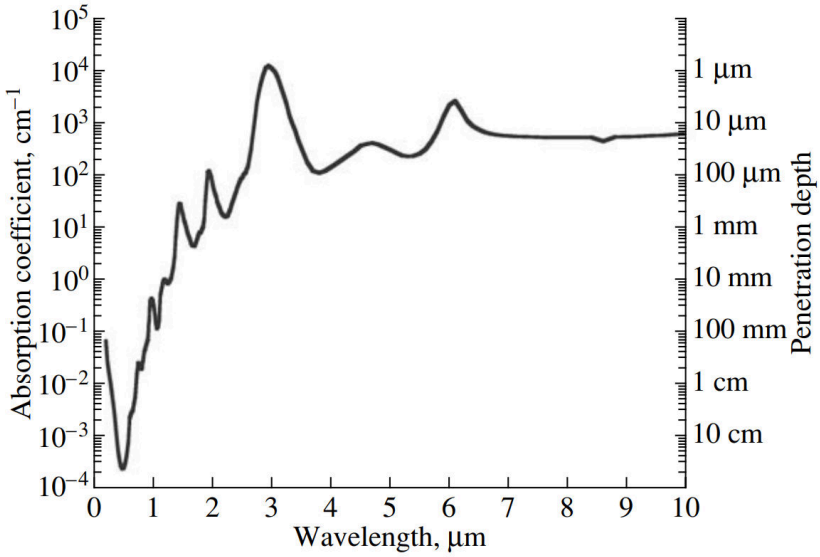

Fig. 1.3: Spectral dependence of water absorption coefficient and penetration depth [26].

troscopy greatly facilitate aerial navigation and land surveying. Ultrafast mode-locked lasers working as optical clocks can be used for extremely precise time and frequency measurements, while Doppler velocimeters can measure velocity of almost arbitrarily fast moving objects. Various fiber sensors can also monitor stress for instance in the frame of airplanes or in buildings and structures; a comprehensive list of laser uses in metrology would make for an entire chapter.

Lasers have been always attractive for military applications. Although high-power lasers have been tested for shooting down small aircraft and missiles, more frequent use is for target designation or infrared countermeasures blinding detectors of e.g. enemy missiles. There are also other uses, such as secure optical communication and lidar, that are not exclusive for military purposes.

Another field lasers have revolutionized are communications. Optical fibers enabled high-capacity, long-distance data transmission and installing a new optical internet connection is becoming more cost-efficient for homes than standard, slower wired connection. Lasers allow for high-capacity free-space communications, such as the data transfer between satellites orbiting the Earth. In data storing, lasers have been used for reading and recording CDs and other optical disks, and have more potential for holographic data storage.

Beside these general applications, high-power, high-repetition-rate ultrafast 1-μm solid-state lasers, which are the main subject of this thesis, have additional attractive industrial applications. They can be used to produce large functional surfaces by means of laser-induced periodic surface structures (LIPSS) by multi-beam nanostructuring, making surfaces with anti-corrosion, anti-icing, anti-bacteria, self-cleaning, hydrophilic or superhydrophobic properties. Thanks to the multi-beam approach with thousands of beams, high average power of these lasers can be utilized without overexposing the workpiece and increase the manufacturing speed by orders of magnitude.

Another field is EUV litography, where laser-produced plasma, generated by powerful CO_2 lasers from tin droplets, is used to produce 13.5 nm radiation further utilized for the litography process. In order to increase the conversion efficiency of EUV generation, it is beneficial to pre-heat the droplets with a 1-μm picosecond laser (conversion efficiency higher by 60% compared to nanosecond pre-pulses [A5]). The typical repetition rate of the irradiation process is 100 kHz and few-mJ lasers operating at this frequency are ideal for the pre-pulse source. Similarly,

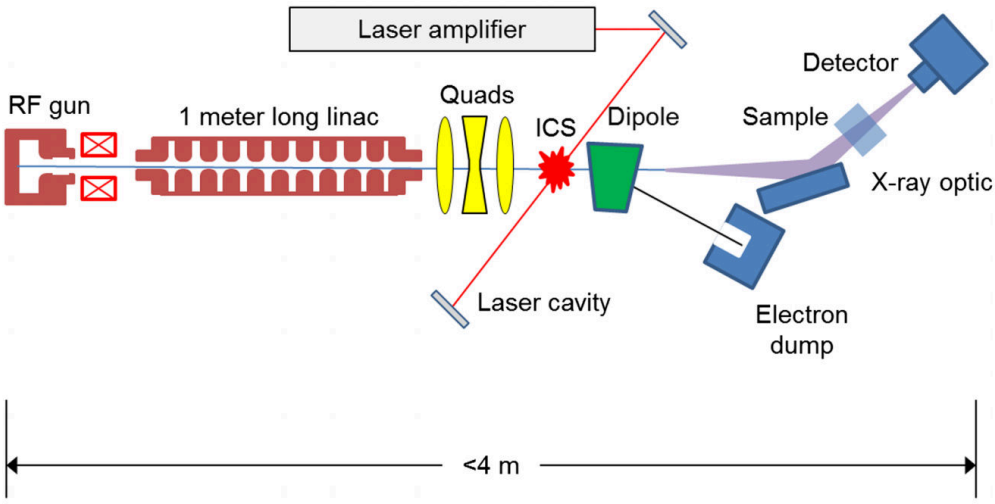

Fig. 1.4: Schematic of a compact linear-accelerator-based X-ray source utilizing a high-energy, 1-kHz thin-disk laser for inverse Compton scattering (ICS) [27].

EUV generation via plasma produced this way may be used also for inspection of litographic masks. High-repetition-rate, high-power ultrafast lasers are thus essential for development of new generations of microchips.

Lasers of similar parameters can be also used together with a linear electron accelerator as an X-ray source via inverse Compton scattering (Fig. 1.4) [27], although sources with longer wavelength than 1-μm would be more efficient (if the technology advances sufficiently), since they can produce hotter plasma. Other interesting applications of such sources would be an initiator of electron emission from photocathodes in free-electron lasers for their improved reliability and lifetime [28], or development of a "laser lightning rod", creating a conductive channel in the atmosphere from ground to clouds [29].

1.3 Objectives of this thesis

The main goal of this dissertation thesis is research and development of high-power, ultrafast thin-disk lasers. As listed below, the task of advancing the solid-state laser technology in this field was approached in two ways – by developing an advanced thin-disk laser system based on already available materials and techniques, and by investigating new laser materials. This way, the presented work can be divided in two main areas:

1. Investigation of laser materials with potential of further expanding the capabilities of thin-disk laser technology over those achievable with Yb:YAG disks:
   - Research on Yb:YGAG ceramics, verifying that its capability of ultrashort pulse generation and amplification at low temperature is superior to Yb:YAG (Sec. 4.1)
   - Examination of Er:Y_2O_3 ceramics as an attractive material for direct diode-pumped laser generation in the 3-μm spectral region (Sec. 4.2)
2. Design, development, and commissioning of a kW-class Yb:YAG thin-disk laser system PERLA C with following parameters:
   - High average output power – ideally over 500 W

- High repetition rate – 100 kHz with possibility of switching to 50 and 200 kHz
- Duration of the output pulses below 2 ps
- Good beam quality with M^2 parameter < 1.5
- Compact and robust laser system – using a setup with a single thin disk

At the beginning of this work, such laser source has not been reported in the literature nor it was available commercially. Still today, it is a state-ot-the-art laser system with large application potential. The laser system is thoroughly described in Chapter 5.

The outcomes of this research effort are summarized in Chapter 6.

Chapter 2

Solid-state laser materials and contemporary state of development

2.1 Solid-state laser materials

The term solid-state lasers (SSL) is usually referring to the class of doped insulator lasers with the gain material consisting of a transparent host in crystalline, ceramic, or glass form that is enriched with a precise stechiometric amount of active ions ("dopants" or "activators") with electronic structure supporting lasing transitions (semiconductor lasers operate on different principles and are usually treated separately). While the activator determines most of the spectroscopic properties of the laser material, the host is responsible particularly for its thermo-mechanical qualities.

First part of this section covers the known active ions in SSL with focus on the most commonly used activators. The second and third part focuses on ytterbium and erbium laser materials that are further investigated in Chapter 4 and 5. The last section then points out the specifics of low-temperature operated SSL materials.

2.1.1 Active ions in solid-state laser materials

Laser action has been achieved with ions from three groups of chemical elements – from transition metals (Ti, V, Cr, Mn, Fe, Co, and Ni), rare-earth metals (lanthanides – Ce, Pr, Nd, Sm, Eu, Tb, Dy, Ho, Er, Tm, and Yb), and from one actinoid (uranium). All ions, including emission wavelengths of their known laser transitions, are listed in Tab. 2.1. Furthermore, optical gain was reported in crystals with following ions: Ti^{4+}, Cu^{+}, Rh^{2+}, Ag^{+}, In^{+}, Tl^{+}, and $(UO_2)^{2+}$ [30].

Solid-state lasers are optically pumped. The classical approach has been to employ a gas discharge lamp pump, such as a xenon- or krypton-filled flash lamp or an arc lamp, or less frequently an incandescent tungsten lamp. Such flash lamps can generate very high peak power and have very broad emission spectrum (see Fig. 2.1) that can easily cover the pump region of the gain medium, making one type of flash lamp applicable for many different laser materials. On the other hand, only a small portion of the pump radiation happens to coincide with the optimum pump region of the gain medium, the rest is either unabsorbed (escaping or heating the pump chamber), absorbed by the host crystal and heating it, or absorbed and exciting the active ions into different (higher) excited state, further increasing the heat load on the active medium. Flash lamps are also not directional, necessitating use of side-pump geometry with reflectors or a pump chamber with transparent cooling medium.

Tab. 2.1: Spectral ranges of laser emission for known active ions (ordered by atomic number). UV wavelengths are shown in purple, visible wavelengths in its respective color, and IR is represented in black (MIR transitions are underlined). The data are compiled from [30–33].

Active ion	Emission wavelength [μm]
Ti^{3+}	0.611, 0.66-1.18
V^{2+}	1.05-1.33
Cr^{2+}	1.88-3.50
Cr^{3+}	0.680-0.704, 0.740-0.890, 0.86-1.48
Cr^{4+}	1.167-1.950
Mn^{5+}	1.168-1.181
Fe^{2+}	3.53-5.05
Co^{2+}	1.62-2.5
Ni^{2+}	1.314-1.939
Ce^{3+}	0.286-0.326
Pr^{3+}	0.479-0.489, 0.522-0.578, 0.598-0.622, 0.632-0.662, 0.670, 0.699, 0.709, 0.717-0.754, 0.901-0.940, 0.996-1.022, 1.047-1.070, 1.334-1.347, 1.523, 1.611-1.644, 2.31-2.59, 3.605, 5.117-5.242, 7.24
Nd^{3+}	0.172, 0.380, 0.413, 0.730, 0.879-0.947, 0.97, 1.037-1.120, 1.18, 1.306-1.486, 1.833, 5.15
Sm^{2+}	0.679-0.745
Sm^{3+}	0.593-0.605
Eu^{2+}	0.556-0.576
Eu^{3+}	0.611-0.619
Tb^{3+}	0.544, 4.9-5.5
Dy^{2+}	2.359-2.366
Dy^{3+}	0.572-0.574, 0.663, 0.751, 1.4, 2.432, 2.972-3.040, 4.31-4.38
Ho^{3+}	0.551, 0.750-0.761, 0.979-1.018, 1.014-1.031, 1.190-1.216 1.391-1.408, 1.486-1.491, 1.673, 1.933-2.171, 2.35-2.377, 2.83-3.05, 3.369, 3.893-3.914
Er^{3+}	0.470, 0.544-0.562, 0.618, 0.670, 0.694-0.722, 0.843-0.863, 1.166, 1.22-1.26, 1.529-1.664, 1.645-1.777, 1.68, 1.965-2.003, 2.66-3.01, 3.41, 4.75
Tm^{2+}	1.116
Tm^{3+}	0.348, 0.453-0.458, 0.482-0.486, 0.511, 0.650, 0.792-0.799, 0.810, 1.462-1.505, 1.568-1.580, 1.85-2.18, 2.274-2.46
Yb^{3+}	0.980-1.108
U^{3+}	2.234-2.827

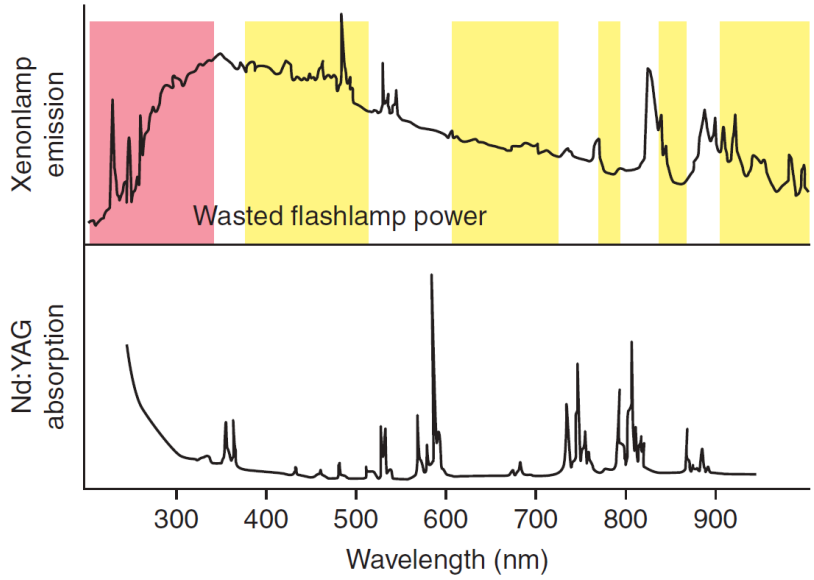

Fig. 2.1: The source of ineffectiveness of flash-lamp-pumped SSL (Nd:YAG in this case). The yellow-shaded areas of Xe-filled lamp emission spectrum are not absorbed by Nd ions and are wasted, while the red area is absorbed by the host YAG, heating it. In addition, most of the light absorbed by neodymium overexcites it, further decreasing laser efficiency. Adopted from [34].

The diode lasers have much narrower emission spectrum, which can precisely match the pump band of the gain medium, so virtually every pump photon can excite one active ion, maximizing the laser efficiency. Apart from higher monochromaticity, diode-laser output is also much brighter, which facilitates distribution of the pump light and allows for improved pump layout (end-pumping) for brighter solid-state lasers. Also diode lasers operate at much lower voltage, improving the laser safery; however, they are much more sensitive to electric shocks and optical feedback. Diode pumping brings fundamental advantages mainly for high-average-power and high-beam-quality applications. With the price difference between lamp- and diode-pumped solutions gradually decreasing, diode-pumped SSL currently dominate the solid-state laser technology and for applications with low requirements on beam quality and peak power (short pulse duration), semiconductor lasers are direct competitors to SSL.

The laser transitions listed in Tab. 2.1 show that SSL can almost fully cover wavelength range from 172 nm (vacuum UV) to 7.24 μm (far end of MIR). However, only some lasing schemes have the potential for efficient and high-power operation.

Second part of this section lists activators and their laser transitions that have shown some significant application potential, primarily in line with the objectives of this thesis. Co-doped laser materials, i.e. media with more than one activator, are not considered here. Such schemes were used mostly with lamp pumping to boost pump efficiency of a gain medium by adding an active ion with more favorable absorption spectrum. With coinciding energy levels of the activators, the absorbed energy could be transferred to the lasing ion. One example of such material is Cr,Tm,Ho:YAG crystal [35], where Cr^{3+} is convenient for flash-lamp pumping, Ho^{3+} is the working ion with attractive 2.1 μm emission wavelength, and Tm^{3+} mediates the energy transfer between Cr and Ho ions. However, co-doping generally deteriorates properties of laser material (such as thermal conductivity), and for high-power lasers it is therefore preferable to look for a different pump scheme or laser material.

Titanium lasers The transition metals with optical transitions in electrons of the 3d shell generally possess very broad absorption and gain bandwidths with high cross section values, but short fluorescence lifetimes usually in order of microseconds. Broad gain bandwidth allows wide wavelength tuning and femtosecond pulse generation.

The only widely used host for Ti^{3+} ion is sapphire. Its absorption spectrum covers approximately 0.45-0.6 μm (typically pumped with green argon or frequency-doubled Nd:YAG lasers) and emission spectrum spans over range of 0.65-1.1 μm with peak at 800 nm. As mentioned in the introductory chapter, Ti:sapphire lasers made possible generation of unprecedentedly short and intense laser pulses (few-cycle, few-fs pulses and 10-PW-level peak power, respectively [18, 19]). However, high-average-power capabilities are somehow limited, mainly due to relatively high quantum defect. A thin-disk titanium sapphire laser has been under development at IFSW Stuttgart [36], but its performance (reaching 10-W-level in CW) has remained behind expectations so far.

Chromium lasers Chalcogenides activated by divalent chromium are of great interest for ultrashort pulse generation in spectral range from 1.9 to 3.5 μm with emission peak around 2.5 μm and pumping wavelength range of 1.5-2.0 μm (region of erbium and thulium lasers). The main Cr^{2+} host materials are ZnSe and ZnS, with ZnS having slightly superior thermo-optic properties. Thanks to their exceptionally wide gain bandwidth, they support generation of few-cycle pulses as short as 30 fs [37].

Output power of 140 W was demonstrated with Cr^{2+}:ZnSe in continuous-wave operation with a rotating-disk configuration [38]. The main obstacle in power scaling of these lasers is the very high thermo-optic coefficient of chalcogenides leading to strong thermal lensing in the gain medium. In a laser system employing the chirped-pulse amplification technique (CPA), peak power of almost 10 GW was reached with repetition rate of 1 kHz at wavelength of 2.4 μm [39].

Lasers based on trivalent chromium cover mainly the boundary between red and NIR spectral region (0.68-0.89 μm). Besides the original ruby (Cr^{3+}:Al_2O_3) laser, alexandrite (Cr^{3+}-doped chrysoberyl, $BeAl_2O_4$) lasers came into prominence as sources suitable for both high-power and ultrafast operation between 700 and 800 nm [40]. Alexandrite has been also proposed as a promising material for thin-disk lasers [41].

Iron lasers From the known laser materials operating in the mid infrared region (3-8 μm), the most efficient ones are iron-doped chalcogenides, namely the Fe:ZnSe, which shares many favorable attributes with the aforementioned Cr:ZnSe. The pump region is 2.8-4.4 μm with peak around 3 μm, which can be covered using e.g. erbium and chromium lasers or hydrogen fluoride chemical laser, and the emission range stretches from 3.4 μm to 5 μm with highest gain at 4.4 μm. Main disadvantage of this material is its very short upper-state lifetime at room temperature (370 ns), which can be evaded by either cooling the medium to cryogenic temperature (increasing the lifetime by two orders of magnitude) or by employing short-pulsed pump.

In pulsed regime, average output power as high as 35 W was demonstrated at 4.1 μm [42]. Ultrashort pulse generation is possible using these mid-IR lasers. A CPA laser system producing 150-fs pulses with energy of 3.5 mJ was reported in 2019 [43], achieving peak power of more than 20 GW. This system was operating only at very low repetition rate of 10 Hz, but significantly improved pulse repetition should be achievable with upgraded pump lasers.

Neodymium lasers Trivalent rare-earth (RE) metal ions (i.e. lanthanides) feature some of the most useful solid-state laser materials (energy-level structure of RE ions in this section is shown

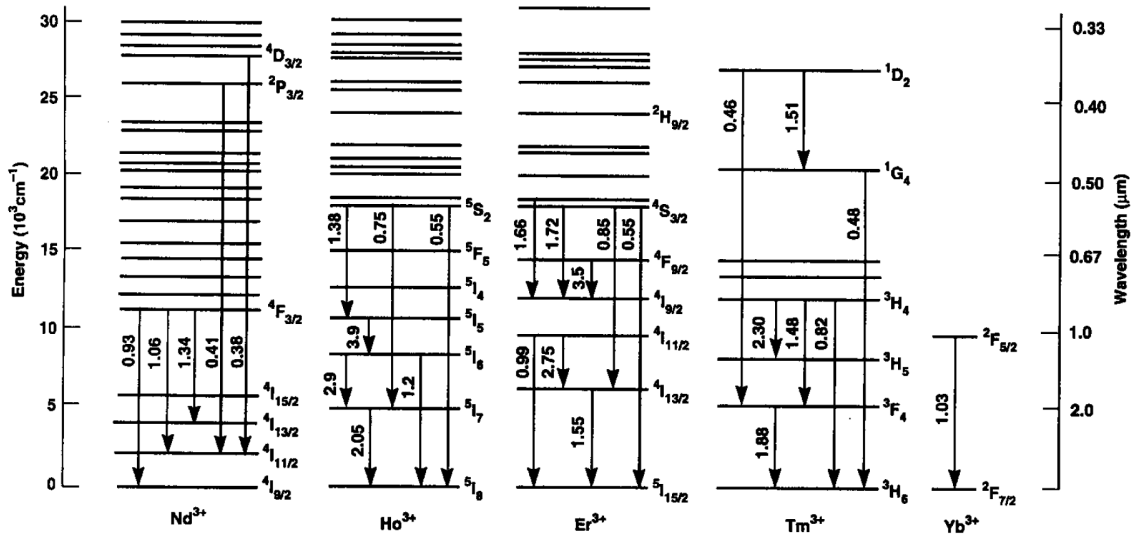

Fig. 2.2: Energy structure of trivalent lanthanides most widely used in SSL – trivalent neodymium, holmium, erbium, thulium, and ytterbium ions [30].

in Fig. 2.2). Their electronic transitions take place within the 4f shell and in comparison with transition metals, they provide longer upper-state lifetimes at a cost of lower gain bandwidth.

The first commonly used RE laser activator (and the third overall after Cr^{3+} and U^{3+}) was the Nd^{3+} ion. It provided laser generation with more than 240 crystalline hosts (most notable are YAG, YVO_4, YAP, or YLF) [32]. Its complex electron structure supports many different laser transitions and is suitable for flash-lamp pumping. The most typically utilized emission wavelengths in the NIR region are around 0.94, 1.06, and 1.34 μm and in case of diode pumping, usual pump wavelength is between 0.8 and 0.9 μm.

The strongest laser transition $^4F_{3/2} \rightarrow {}^4I_{11/2}$ at 1.06 μm allows an efficient operation thanks to high emission cross section and purely four-level behavior. In many regards, Nd:YAG is the ideal laser material for high-power laser operation, offering continuous-wave output power up to 100-kW level [44]. In the field of single-shot/low-repetition-rate high-energy pulses, the current generation of Nd:glass laser systems has potential to reach energies as high as 25 kJ in ultrashort pulses [45]. Nevertheless, in the last two decades, Nd materials have faced strong competition from ytterbium-doped media that offer improved thermal management and dispositions for ultrashort pulse amplification.

Ytterbium lasers Thanks to their unique energy structure with only two energy level manifolds ($^2F_{7/2}$ and $^2F_{5/2}$), ytterbium materials are currently the workhorse for high-power laser operation with minimum collateral heat deposition. Ideally suited for diode pumping, Yb^{3+} lasers superseded the neodymium-doped materials in many applications, particularly in high-average-power ultrafast pulse generation. Sec. 2.1.2 pursues these gain media.

Erbium lasers The lasing action with Er^{3+} was first demonstrated at wavelength of 2.94 μm with highly-doped YAG crystal in 1975 [46]. It used the $^4H_{11/2} \rightarrow {}^4H_{13/2}$ transition that covers spectral range of 2.7-3.0 μm. This transition is usually self-terminating ($^4H_{11/2}$ has shorter lifetime than $^4H_{13/2}$), but this can be overcome thanks to higher rate of upconversion processes occurring with higher Er^{3+}-doping concentration, although it still leads to a quasi-three-level behavior of these media. The laser performance of erbium materials is not very extraordinary in terms of their power output and efficiency, but unlike other MIR SSL materials, they are

perfectly suited for pumping with 1-μm diode lasers and represent the easiest way of direct laser generation in the 3-μm region, while their potential for short pulse generation has not yet been thoroughly examined. With the 3-μm wavelength they are also very attractive for medical applications. Sec. 2.1.3 concerns these materials in more detail.

However, the most extensively used laser channel in Er^{3+} nowadays is ${}^4H_{13/2} \rightarrow {}^4H_{15/2}$ with emission wavelength around 1.55 μm. It is mainly a domain of erbium fiber lasers, which play an important role in today's optical fiber communications.

Thulium lasers The only widely used laser transition of thulium laser materials is the ${}^3F_4 \rightarrow {}^3H_6$ with emission wavelength of 1.85-2.18 μm. These lasers are conveniently pumped around 0.8 μm (${}^3H_6 \rightarrow {}^3H_4$) with good availability of laser diode pump sources. This laser scheme is attractive thanks to a cross-relaxation process ${}^3H_4 + {}^3H_6 \rightarrow 2 \times {}^3F_4$ that increases the quantum efficiency of the pumping process close to 2. This allows for efficient operation in the 2-μm spectral region, although the heat deposition is still large compared to Yb and Ho materials. Another advantage is their long upper-state lifetime, typically around 10 ms. However, this is counter-balanced by low emission cross section on the order of 10^{-21} cm^2.

2-μm thulium lasers are used mainly for medical applications and plastic welding, and are suitable for pumping holmium and Cr^{2+} lasers. The Tm^{3+} ion is used mostly with crystalline YAG, YLF, or YAP hosts or in fiber lasers. Compared to the Ho^{3+} lasers operating at slightly longer wavelengths, their emission is strongly affected by absorption of atmospheric water vapor.

Thulium-doped materials were not investigated so thoroughly for high-peak power generation, since holmium-doped laser materials, emitting in the same spectral region, show greater potential for short-pulse and high-power generation. A notable example of a gigawatt thulium laser is a small-scale sub-picosecond Tm:YAP regenerative amplifier reported in [47].

Holmium lasers Ho^{3+}-doped materials lasers are of great interest thanks to their 2.1-μm ${}^5I_7 \rightarrow {}^5I_8$ transition. Similarly to ytterbium, only two energy manifolds are involved, leading to a very low quantum defect. Therefore, holmium materials have potential to become an equivalent to ytterbium media in the short-wave IR region. The pump wavelength region spans from 1.6 to 2.0 μm, where available diode lasers are expansive and with limited power (although 40 W of output power was demonstrated with 1.9-μm-diode-pumped Ho:YAG [48]). Usual pump source for these lasers are thulium fiber and solid-state lasers.

Typical holmium host materials are YAG and YLF crystals. Ho:YLF was reported to amplify picosecond laser pulses up to 39 mJ [49], yet there seems to occur a limitation in pulse duration (shortest pulse duration over 4 ps [50]). Thin-disk Ho:YAG lasers are promising for achieving high peak power at 2 μm. In continuous-wave operation, output power of 50 W was demonstrated [51] and pulses as short as 220 fs were generated from a 25-W mode-locked thin-disk oscillator [52].

Holmium lasers can also operate at 2.8-2.9 μm with energy transfer scheme very similar to Er^{3+} media. Corresponding pump wavelength around 1.1 μm is less convenient than in case of Er^{3+} and their laser performance is somewhat inferior to erbium materials [53], making those a more attractive choice.

Within this work, I performed experiments with ytterbium- and erbium-doped laser materials; these are the subjects of following sections. However, our research group investigates also thulium, holmium, neodymium, and chromium laser media. It has been a great opportunity to

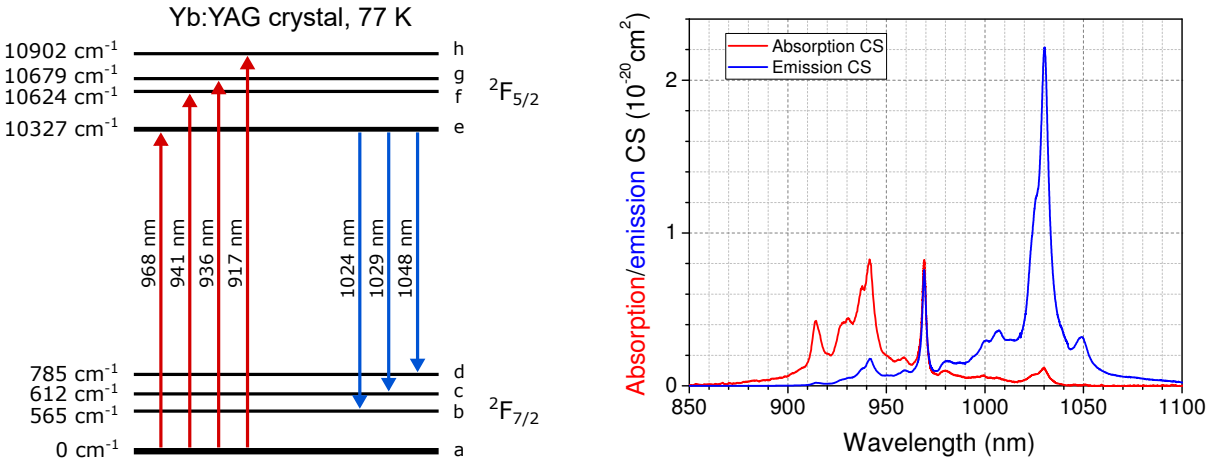

Fig. 2.3: Energy level structure of trivalent ytterbium ion in Yb^{3+}:YAG crystal (energy values from [31]). Right – Absorption and emission cross sections of Yb:YAG at room temperature (data taken by V. Jambunathan).

realize some differences in practical aspects that occur when working with different SSL materials operating in various spectral regions, although the fundamental principles are universal.

2.1.2 Ytterbium-doped laser materials

The trivalent ytterbium ion has only two optically accessible electronic states, the ground state $^2F_{7/2}$ and excited state $^2F_{5/2}$ (Fig. 2.2). This means that no excited-state absorption or upconversion losses can occur in these media (although quenching processes can take place for high Yb concentrations above 15%) and also the quantum defect (difference in pump and signal photon energies) is low. However, the levels in both manifolds are not much separated and thermal population of the higher levels is not negligible. In the case of Yb:YAG [Fig. 2.3(a)], the lower laser level of the major 1030-nm laser transition (c-sublevel of $^2F_{7/2}$) has in the thermal equilibrium at room temperature thermal population of about 5%. This determines the quasi-three-level behavior of Yb-doped media, leading to higher lasing threshold and lower laser efficiency at low pump intensity compared to four-level media[2] such as neodymium lasers (with well-separated ground-state and lower-laser level). Efficient mitigation of the quasi-three-level nature of these materials can be achieved through cryogenic cooling (Sec. 2.1.4).

During the search for the ideal SSL materials, it emerged that the most distinguished host materials belong in the Y_2O_3–Al_2O_3 system [31], with the most significant representatives being the yttrium aluminum garnet (YAG, $Y_3Al_5O_{12}$) and yttrium aluminum perovskite (YAP, $YAlO_3$). They combine broadband transparency, good mechanical and thermo-optic properties, and reasonable spectroscopic attributes. Thanks to its properties and well-developed production process, the Yb:YAG crystal became the material of choice for 1-μm high-power lasers. Material properties of Yb:YAG and some other prominent ytterbium-doped media are listed in Tab. 2.2.

The main advantages of Yb:YAG are e.g. its hardness, high thermal conductivity, and relatively high emission cross section. An interesting alternative for some applications (such as thin-disk lasers) is Yb:LuAG ($Lu_3Al_5O_{12}$) that offers higher thermal conductivity at high doping concentrations (Lu ions are closer in size to Yb than yttrium) [54], although the situation

[2]Three-level laser media, on the other hand, have common ground-state and lower energy level – more than one half of the active ions must be excited in order to achieve population inversion and laser gain. The ruby laser is a three-level system.

Tab. 2.2: Room-temperature properties of various Yb-doped laser crystals: YAG – $Y_3Al_5O_{12}$, LuAG – $Lu_3Al_5O_{12}$, YAP – $YAlO_3$, YLF – $LiYF_4$, CaF_2, and KYW – $KY(WO_4)_2$. Values of thermal conductivity κ, thermo-optic coefficient dn/dT (for anisotropic materials, the highest value is listed), and thermal shock resistance parameter R_T apply for undoped crystals. λ_e – central emission wavelength, σ_e – peak emission cross section, $\Delta\lambda$ – emission bandwidth, $\lambda_p^{(ZPL)}$ – zero-phonon-line pump wavelength, τ_L – upper-state lifetime. Data adopted from [53, 56–61].

Host crystal	YAG	LuAG	YAP	YLF	CaF_2	KYW
Symmetry	cubic	cubic	orthorombic	tetragonal	cubic	monoclinic
λ_e [nm]	1031	1030	1039	1020	1045	1025
σ_e [10^{-20} cm^2]	2.1	3	0.6	0.81	0.25	3
$\Delta\lambda$ [nm]	9	6.5	5	14	70	24
$\lambda_p^{(ZPL)}$ [nm]	968	970	978	972	979	981
τ_L [ms]	0.95	0.95	0.48	2.2	2.4	0.3
κ [W/(m·K)]	11.2	8.3	10	5.3	9.7	2.7
dn/dT [10^{-6} K^{-1}]	7.8	8.3	11.7	-6.6	-10.6	-14.6
R_T [W/cm]	7.9	/	5.5	1.3	1.2	/

for undoped crystals is the opposite one. Ytterbium-doped garnets have also comparatively narrow emission bandwidth allowing pulse generation with duration of several hundreds fs at best (although extreme cases as 49 fs Yb:YAG thin-disk oscillator have emerged [55]). For femtosecond oscillators, laser media such with broad bandwidth such as CaF_2, KYW [$KY(WO_4)_2$], KGW [$KGd(WO_4)_2$], or CALGO ($CaGdAlO_4$) are more suitable. The fluorides and tungstates are much softer and and more brittle than garnets, limiting their use in high-power applications.

The ytterbium materials feature broad pumping band around 0.94 μm [Fig. 2.3(b)], which is conventionally used for pumping. However, there is also an option of pump scheme with significantly (by $\approx 35\%$) lower quantum defect – the zero-phonon-line (ZPL) pumping directly to the upper laser level, at wavelength around 0.97-0.98 μm. The absorption line is fairly narrow with few nm bandwidth – requiring wavelength-stabilized diodes– but it helps to significantly reduce heat deposition in the active medium [62]. For low-repetition-rate lasers requiring high energy storage in the gain medium, ZPL pumping is not suitable, since no more than 50% of the active ions can be excited due to similar values of absorption and emission cross sections at this wavelength.

Thanks to their characteristic attributes, ytterbium-doped materials and especially Yb:YAG are frequently used in high-average-power lasers. These are the subject of Sec. 2.2.

2.1.3 Erbium-doped laser materials for the 3-μm spectral region

The laser transition of erbium-doped materials around 2.7-3 μm is attractive due to extremely high absorption of water and water vapor in this region (e.g. for medical applications, remote sensing) or for driving wavelength conversion both to high harmonics (down to extreme UV or even X-ray region) and mid and far infrared. The pump transition $^4I_{15/2} \rightarrow ^4 I_{11/2}$ at approximately 980 nm terminates directly at the upper laser level and can be easily covered with well-accessible InGaAs diode lasers.

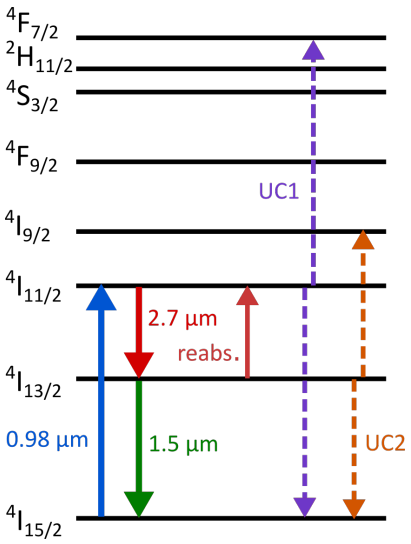

Fig. 2.4: Energy level structure and transitions in erbium-doped media. UC – upconversion (process UC1 is detrimental for 2.8-µm lasing action, while UC2 is beneficial).

The energy diagram of Er^{3+} ion with transitions relevant for the 3-µm operation is shown in Fig. 2.4. The lasing scheme for the ${}^4I_{11/2} \rightarrow {}^4 I_{13/2}$ channel seems as a typical four-level scheme, but since the lifetime of the lower laser level is significantly higher than for the upper-state level, these lasers exhibit a quasi-three-level behavior due to population accumulation on the lower laser level and consequent re-absorption [53]. Therefore, this laser transition is normally self-terminating, impeding efficient continuous-wave operation. This can be ameliorated by optimizing doping concentration of erbium ions and maximizing the rate of upconversion process ${}^4I_{13/2} + {}^4 I_{13/2} \rightarrow {}^4 I_{9/2} + {}^4 I_{15/2}$ (denoted as UC2 in Fig. 2.4) depopulating the lower laser level or employ simultaneous laser action at 1.5 µm. This optimum doping concentration is host-dependent [63].

Tab. 2.3 shows selected parameters of some of the most used erbium laser materials. The Er:YAG was the first erbium crystal used for ≈ 3-µm lasing operation and its optimum doping concentration is around 50%. It is widely used in practice, e.g. in medical lasers, but due to high phonon energies, it has very short upper-state lifetime and at high doping concentration, also its thermal conductivity decreases.

In general, hosts with low phonon energy such as fluorides or sesquioxides are more suitable for laser operation at these longer wavelengths. When comparing the fluoride (such as YLF and CaF_2) and sesquioxide hosts (most prominent are Y_2O_3 and Lu_2O_3), the sesquioxides evince significantly better mechanical properties and thermal conductivity. Due to the very high quantum defect of this lasing scheme and consequent intense heat load on the gain medium, the thermal conductivity is essential. On the other hand, sesquioxides have very high melting point (over 2400 °C), making production of their monocrystals difficult and expensive. Therefore, they are usually used in polycrystalline (ceramic) form. For these reasons, we chose Er:Y_2O_3 ceramics for 2.7-µm laser generation in Sec. 4.2.

2.1.4 Effects of cryogenic cooling on gain medium

Many of the first laser devices, including the second laser (U:CaF_2 [7]), were operated at low temperatures, since this way it was easier to achieve the optical gain. Typical operational temperature of cryogenic lasers is that of liquid nitrogen – 77 K – although cooling with liquid

Tab. 2.3: Room-temperature properties of various erbium-doped laser crystals: YAG – $Y_3Al_5O_{12}$, YAP – $YAlO_3$, Y_2O_3, Lu_2O_3, and YLF – $LiYF_4$. Values of thermal conductivity κ, thermo-optic coefficient dn/dT (for anisotropic materials, the highest value is listed), and melting point T_m stand for undoped crystals. λ_l – typical $\approx$ 3-µm emission wavelength, τ_L – fluorescence decay times for lower and upper laser level, E_p^{max} – maximum phonon energy. Data were taken from [53, 64] and Tab. 2.2.

Host crystal	YAG	YAP	Y_2O_3	Lu_2O_3	YLF
λ_l [µm]	2.94	2.92	2.71	2.71	2.8
τ at $^4I_{13/2}$ [ms]	2.9	4.1	15.9	-	10.9
τ at $^4I_{11/2}$ [ms]	0.294	0.83	2.4	-	4.1
E_p^{max} [cm$^-$1]	700	550	383	-	400
κ [W/(m·K)]	11.2	10	13.4	12.8	5.3
dn/dT [10^{-6} K^{-1}]	7.8	11.7	8.3	9.1	-6.6
T_m [K]	2200	2140	2703	2723	1092

helium to temperature as low as 4 K is also occasionally used. Operating the laser medium at cryogenic temperature substantially enhances its spectroscopic and material properties. In RE earth ions (i.e. lanthanides), cross section of both absorption and stimulated emission are at lower temperature increased several times due to reduced spectral broadening (case of Yb:YAG is shown in Fig. 4.1 and 4.2 on p. 34). Quasi-three-level media, such as ytterbium, thulium, or holmium materials with the lower laser level in the same manifold as the ground state, operate as four-level systems at low temperature thanks to reduced thermal population of the lower laser level (given by Boltzmann distribution). This leads to reduced lasing threshold and higher efficiency. For many materials, longer upper-state lifetime and lower rate of quenching and collective energy-transfer processes can be observed.

Also properties of the host material improve at low temperature. Thanks to longer mean free path of phonons due to reduced thermal vibrations in the crystal lattice, thermal conductivity of the material raises significantly, reducing temperature gradients in the medium. Furthermore, thermal lensing is reduced also thanks to decrease in thermo-optic and thermal expansion coefficients. Change in these parameters for Yb:YAG is recorded in Tab. 2.4. Collectively, improvement in these three parameters leads to radical reduction of thermal lensing and possibly to improved beam quality. Reduced thermal expansion also reduces mechanical stress in the material and helps to prevent fracture of the material.

Cryogenic cooling brings also two major disadvantages. Beside the need for cooling mechanism (a reservoir with the cryogen or a Stirling engine), the gain medium also has to be placed in vacuum chamber in order to prevent water vapor condensation on the optical interface. This adds significant complexity to the laser system. The other drawback, emerging in case of rare-earth-doped materials, is strong gain bandwidth reduction at low temperature (for Yb:YAG the bandwidth is reduced more than six times, as shown in Tab. 4.1 on p. 35). This is an issue mainly for generation and amplification of ultrashort laser pulses with cryogenic RE-doped lasers. Significant limitation of the Yb:YAG material in this regard led us to investigation of an alternative material (Yb:YGAG, Yb-doped mixed garnet $Y_3Ga_2Al_3O_{12}$) in Sec. 4.1.

Regarding the 3-µm erbium materials discussed in the previous section, cryogenic cooling is highly advantageous for high-power operation. Beside improving the material properties of

Tab. 2.4: Thermo-optic properties of YAG at room temperature (300 K) and cryogenic temperature (100 K) [57]. Values of thermal conductivity with asterisk hold for highly-doped (15 at.%) Yb:YAG. LLL – lower laser level.

Temperature	300 K	100 K
Thermal conductivity [W/(m·K)]	11.2 (6.7*)	46.1 (16.4*)
Thermo-optic coefficient [10^{-6} K^{-1}]	7.8	0.9
Thermal expansion coeff. [10^{-6} K^{-1}]	6.14	1.95
Thermal population of LLL	4.65%	0.015%

the host, it can also significantly increase their upper-laser-level lifetime, improve the ratio of upper- and lower-laser-level lifetimes, and increase lasing efficiency. For instance, while the maximum CW power obtained from Er:Y_2O_3 ceramics at room temperature is 2.05 W [63], at liquid-nitrogen temperature as much as 14 W has been demonstrated in CW [65].

In conclusion, operation of the laser medium at cryogenic temperature is a classical and powerful technique for scaling lasers to high-average power and improving their beam quality. Increased complexity of the laser associated with low-temperature operation is often worth considering given its significant benefits. However, its use is limited when working with ultrashort laser pulses.

2.2 High-average-power laser systems

2.2.1 Intensity-reducing techniques for laser amplification

Chirped-pulse amplification (CPA)

In 1980s, researchers in field of high-power pulsed lasers were dealing with amplification limits due to high intensity of short pulses and onset of nonlinear self-focusing. Strickland and Mourou came with an idea[3] to use a technique already established in radar technology and to stretch the pulses reversibly in time before reaching the amplifier and recompress them at the output of the laser system [16]. The proposed laser system with master oscillator – regenerative amplifier (MOPA) scheme with Yb:YAG and Yb:glass gain medium, respectively, is shown in Fig. 2.5. This method was named chirped-pulse amplification (CPA).

At that time, all the necessary ingredients were known – for linear stretching of pulses they used material dispersion in 1.4 km long single-mode silica fiber (also an alternative, a Martinez-type grating stretcher with normal dispersion, was invented a year before [66]) and for pulse compression they employed a dual-grating compressor scheme introduced by Treacy [67]. With this setup, it was possible to obtain pulses with 1 mJ pulse energy and 2 ps pulse duration.

Although the idea of this method is quite straightforward, various obstacles may be encountered during its actual implementation. For amplification of long pulses with narrower spectrum, e.g. with duration of several ps or more, one has to use impractically large amount of dispersion and possibly different approach should be considered (such as coherent beam combining [68] or the DPA method mentioned below). In the frame of this work, the CPA technique was im-

[3] In 2018, this invention earned them one half of the Nobel Prize in Physics.

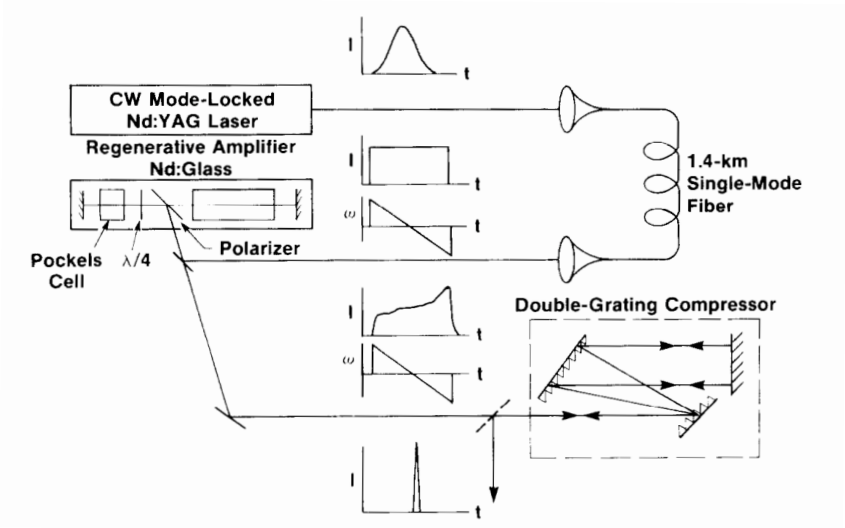

Fig. 2.5: Nd-based laser system used for the first demonstration of the CPA technique [16].

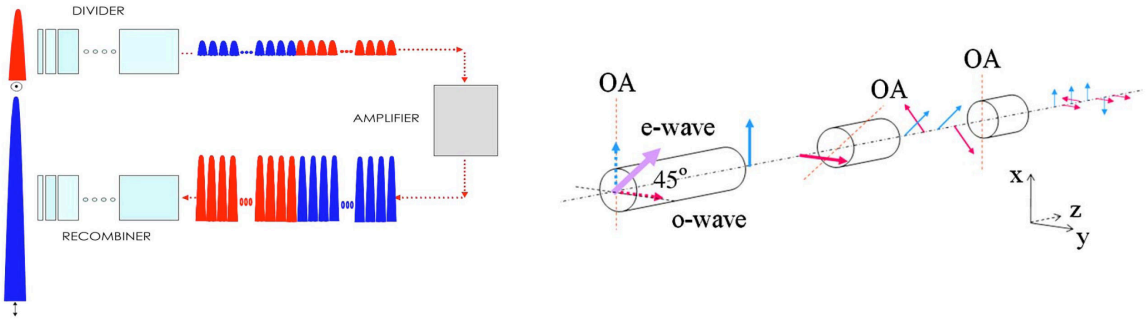

Fig. 2.6: Left: the principle of DPA (red pulses are horizontally polarized, blue ones are vertically polarized) [71]; right: possible arrangement of divider/recombiner using a series of birefringent crystals with changing length [72]. OA – optical axis.

plemented and optimized in the thin-disk laser system described in Chap. 5, as it is described in Sec. 5.4.

So-called optical parametric chirped-pulse amplification (OPCPA) is a special case of this method, applied on nonlinear optical parametric amplifiers seeded with chirped pulses in synchronization with short pump pulses [69]. The main difference from the classical laser amplifiers is that parametric amplification does not intrinsically generate heat. At large scale, multistage OPCPA with Ti:sapphire pumping lasers has allowed reaching extreme peak powers of 10-PW level [19, 70].

Divided-pulse amplification (DPA)

An alternative method to CPA is the divided-pulse amplification [71]. Here, the peak pulse power is reduced by dividing the seed pulse into a series of weaker pulses and after amplification these are recombined back into a single pulse. The division could be performed using a sequence of beam splitters, but the typical divider/recombiner arrangement is a sequence of birefringent crystals with optical axes mutually tilted by 45° and with various lengths (long enough so the relative delay between differently polarized pulses is larger than pulse duration), as shown in Fig. 2.6.

Series of N crystals allows for up to 2^N pulse copies and in case each crystal is twice longer than the previous one, the pulses are equidistant. The pulses can be recombined in a separate combiner with an opposite sequence of the same crystals as in the divider or, by sending the pulses in reverse direction and utilizing a Faraday rotator, the divider can act also as the recombiner.

DPA is an interesting option to CPA and for picosecond pulses it may lead to simpler and cheaper setups. However, it limits polarization management within the amplifier (in this form it is not compatible with regenerative amplification) and also its use in high-energy and high-power laser systems is limited [73].

2.2.2 Advanced geometries of solid-state active media

The typical geometry of solid-state media is a rod shape, with the gain medium side-cooled (transversely to the direction of beam propagation). For both end- and side-pumped configurations, the transverse temperature profile has approximately parabolic shape. The typical diameter of laser rods is in the order of several millimeters – with limited thermal conductivity of laser materials, a strong temperature gradient arises in the laser rod under intense pumping, possibly leading to its fracture and promoting stress-induced birefringence. Furthermore, as a result of thermally-induced change of refractive index and thermal expansion, the parabolic temperature profile makes such gain medium act as a (thermal) lens, affecting the propagation of the laser beam.

These adverse effects cannot be mitigated simultaneously by increasing the diameter or length of the laser rod [23]. The stress fracture limit does not depend on the diameter of the rod and more heat can be dissipated from a rod crystal before breaking it only by making it longer (and possibly reducing its doping concentration). However, this does not suppress other adverse thermo-optic effects; e.g. the optical path difference forming the thermal lens – at given pump power – sums up over a longer and colder rod similarly as over a shorter rod with higher peak temperature. Excessively long active medium also brings other constraints on design of the optical resonator and is generally unsuitable for end-pumped configurations with low-brightness pump source. Nevertheless, this principle is advantageously utilized in fiber lasers and, to some extent, in single-crystal fiber lasers and amplifiers.

Since there are clear limitations in power scaling of rod lasers, several different approaches were introduced. These consist in different shape and way of heat management of the gain medium and their aim is to offer a true power scalability, i.e. a systematic way of increasing output power of the laser without deterioration of other output parameters or encountering some other fundamental frontier.

Slab lasers

In order to decrease the light intensity and increase the amount of stored energy in the laser medium, it is clearly beneficial to increase its volume. The most straightforward approach to improve the heat removal and avoid limitations discussed above is to increase the surface-area-to-volume ratio of the gain medium by reducing its size in one dimension, giving it form of a thin slab. This slab is then cooled obviously through both its large faces. Especially when using flash lamps and transparent cooling medium, the gain element may be face pumped with good pump homogeneity. With a high-brightness pump source (diode lasers), edge pumping is possible, bringing more flexible cooling options. Virtually every conceivable arrangement of the pump and laser beam path within the slab was tested and there are many working solutions for different laser conditions.

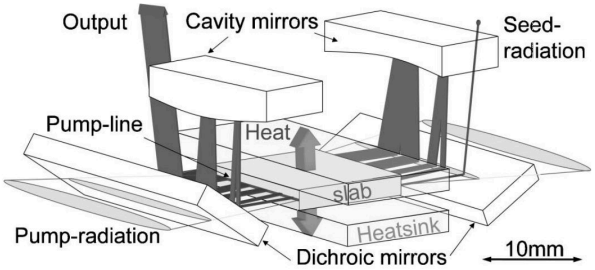

Fig. 2.7: Optical setup of an Innoslab amplifier [74].

In the basic configuration, where the slab gain medium is only replacing the laser rod, several new issues arise. The geometrical asymmetry suggests use of a cavity with strongly elliptic eigenmode in order to efficiently extract energy form the slab. Due to the dominant one-dimensional heat transfer, the emerged temperature gradient is one-dimensional as well, inducing a strong cylindrical lens. Therefore, it is more difficult to extract the energy from slab medium in a good-quality beam.

A possible remedy is to use a *zig-zag* path of the laser beam through the slab with total internal reflection on the slab side faces or with reflection on external mirrors parallel to faces of the slab – instead of a straight-propagating beam. This way, the cylindrical thermal lensing is mostly averaged out. However, due to bulging of its faces, the beam quality is still deteriorated, the output beam usually requires conversion to a circular beam, and generally fabrication cost is high, wider application of zig-zag slab lasers has been limited [23].

For high-average-power, ultrashort pulse operation, the most suitable is the Innoslab geometry (Fig. 2.7) with side pumping and diverging zig-zag propagation of the signal beam through the slab, which helps to keep intensity along the beam fairly constant. For a single-pass amplifier with confocal cavity, up to 9 passes with amplification factor around 10^3 may be achieved and with the single pass scheme the nonlinear effects are minimized [75]. Average power as high as 1.1 kW was produced in a good-quality beam with 615 fs pulse duration using two stage Yb:YAG Innoslab amplifiers [74] and due to high repetition rate of 20 MHz (pulse energy 55 μJ) it was not necessary to use the CPA technique. More recently, 54-mJ, 1.5-ps pulses at 10-kHz repetition rate were reported with a CPA-based two-stage Innoslab system [76]; despite the half-kilowatt average power, the measured M^2 was 1.1. These parameters make the Innoslab lasers a direct competitor to thin-disk lasers, although due to their nature they are limited in maximum pulse energy, similarly to high-power ultrafast fiber lasers.

Laser systems with extremely high pulse energies above the kJ level are also based on the slab geometry, although in this case the laser radiation propagates through the large faces. For example, the largest laser system at National Ignition Facility consists of 192 beamlines of ≈ 6-kJ frequency-tripled, flash-lamp-pumped Nd:glass lasers [77] and its nanosecond pulses can be shot with period of 8 hours. The recovery time of such single-shot systems is generally in the order of minutes or hours and the cooling process takes place between the shots.

A possible modification of this high-energy slab technology for high-repetition-rate operation (over 1 Hz in this context), is to use a gain medium with higher thermal conductivity, diode pumping, and to cool the laser slabs with gas. The most powerful laser of this kind is BIVOJ system based on DiPOLE 100 [78] installed at HiLASE Centre. In this case, six 10×10 mm^2 Yb:YAG ceramic slabs of its main 100-J multipass amplifier are cooled with laminar flow of 150-K helium gas (Fig. 2.8). Efficient thermal management allows operation at repetition rate up to 10 Hz. Recently, this laser with 10-ns pulse duration was upgraded to energy of 146 J (1.46 kW average power), which is a record for this class of lasers [79]. Future development

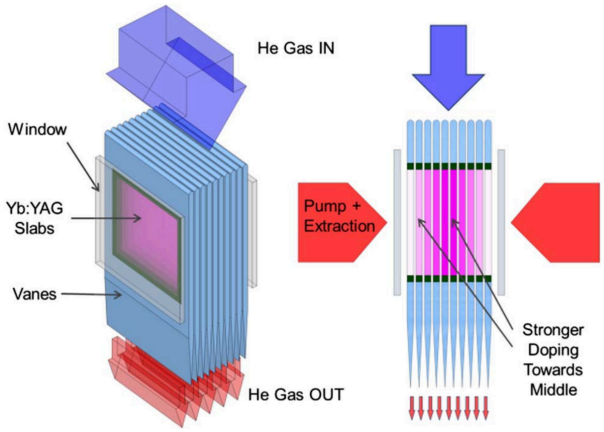

Fig. 2.8: A possible layout of a gas-cooled multislab amplifier [78].

of this platform will be aimed to picosecond pulse generation and to higher repetition rates (100 Hz).

Thin-disk lasers

In 1991, the group of T. Y. Fan from MIT Lincoln Laboratory demonstrated the first diode-pumped Yb:YAG laser [20] and pointed out its potential for high-power laser generation. After seeing their presentation, Adolf Giesen from Institut für Strahlwerkzeuge (IFSW) of the University of Stuttgart came with an idea for a new type of laser combining low heat generation in Yb:YAG with a new geometry of gain medium with improved cooling capabilities – using an active medium in shape of a very thin sheet with a reflective back side (for both pump and laser wavelength) contacted to a heatsink, thus acting as an active mirror.

Typical thickness of such disk is in the order of few hundreds of μm, leading to effective heat removal, since it is generated very close to the heatsink. The key difference with thin-disk laser concept is the dominant direction of heat extraction – unlike in rod or slab geometry, the disk is cooled in the longitudinal direction and with flat-top distribution of pump radiation, almost uniform temperature distribution over the active area can be attained. This greatly reduces the thermal lensing and wavefront aberrations resulting from beam reflection off the disk, allowing for output beam quality superior to other types of solid-state lasers.

Another advantage of this approach is the power scalability of such lasers. By increasing the pump power while enlarging the pump area proportionally (i.e. keeping the same pump intensity), the temperature of the disk remains almost constant and the extracted output power may be increased correspondingly, also with the laser light intensity maintained at similar level. This means that disk-geometry lasers can be power-scaled straightforwardly just by increasing the size of thin disks, although some complications may arise, such as need for large mode sizes for single-mode operation (complicating the resonator design) or increased amplified spontaneous emission (ASE) in the transverse direction. For pulsed lasers with high peak powers, large mode area on the disk and low thickness also greatly suppress the nonlinear effects occurring in the disk.

On the other hand, thinness of the disk leads to low absorption and gain per double-pass through the disk (single reflection). To some extent, the absorption is increased by using highly-doped laser material (in case of Yb:YAG, concentrations as high as $\approx 10\%$ or even higher are used). The original design of Giesen et al. [21] shown in Fig. 2.9 used an 8-pass layout with four spherical mirrors imaging pump light from the fiber bundle of the pump diodes on the disk

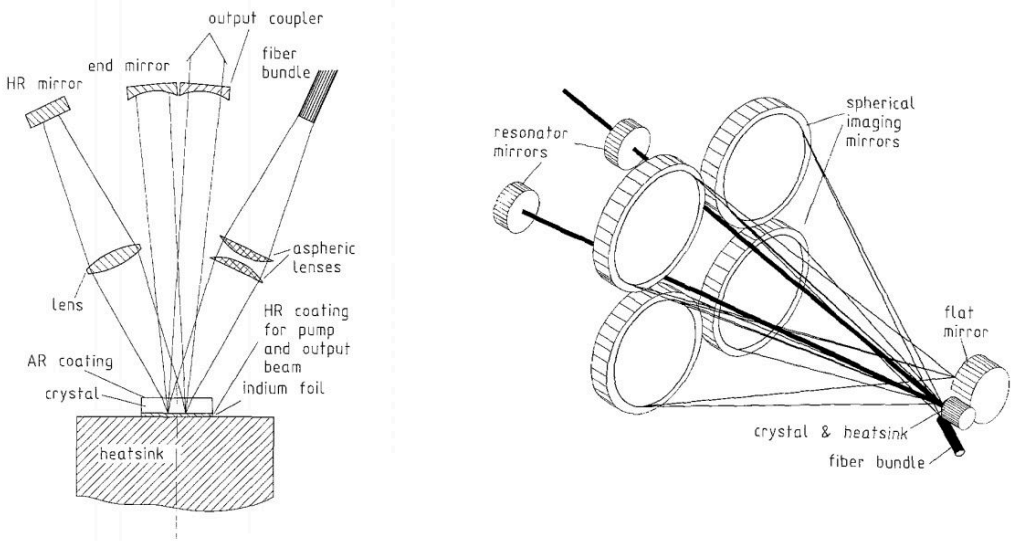

Fig. 2.9: The original layout of a thin-disk laser with an 8-pass pumping scheme as proposed by Giesen et al. [21].

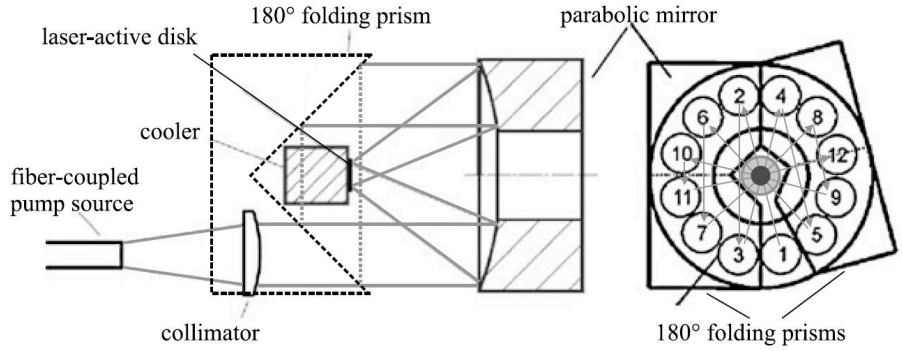

Fig. 2.10: Pump chamber of a thin-disk module with 24 passes of the pump beam through the disk [80]. This setup was used in Chap. 5.

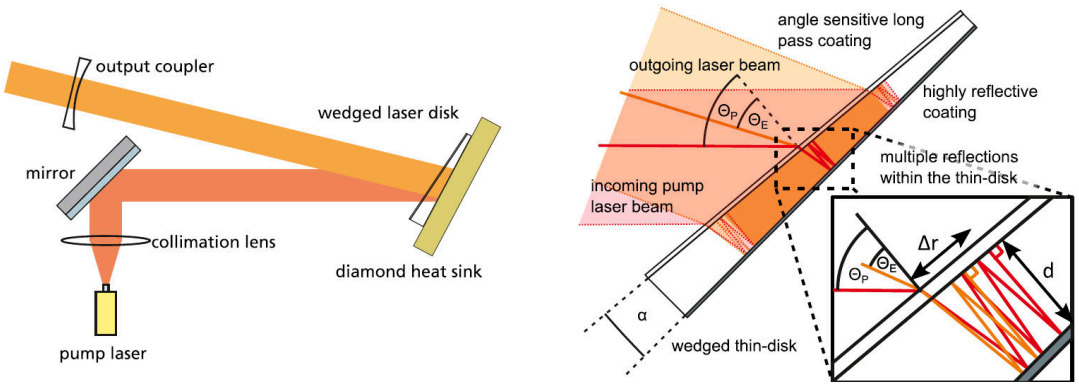

Fig. 2.11: Concept of a monolithic thin-disk laser as presented in [81].

four times. However, for thinner disks and high pump intensity leading to pump saturation, and especially for zero-phonon-line pumped lasers, eight passes of pump light are insufficient and large portion of the pump light would be directed back towards the pump laser. An improved setup, illustrated in Fig. 2.10, was later invented [82]. It uses 4-f imaging with a collimation lens and parabolic mirror for the first double pass, while additional reflections are accomplished using the parabolic mirror and two folding prism pairs. With a back-reflecting mirror after the twelfth reflection off the parabolic mirror, such thin-disk module can provide 24 passes through the disk (the case in Fig. 2.10). With modified back-reflector or larger module with smaller angle between the prism pairs, more than 40 passes of pump light through the disk can be achieved, effectively dealing with the low double-pass reflection in thin disk.

Due to low double-pass gain of thin disks, they require high number of passes through the disk for significant amplification as well, leading to complex multipass amplifiers or regenerative amplifiers with high number of roundtrips. On the other hand, unlike with fiber or slab lasers, thin disks are typically operated with a highly saturated gain at low output-coupling rates. For this reason, thin-disk amplifiers are much less sensitive to back reflections (e.g. from an experimental setup) and therefore they can be often operated without an optical isolator in the output beam [75].

An interesting variation of the thin-disk concept, introduced in 2019 [83], eliminates the need for complicated pump chamber by using a wedged disk with a special dielectric coating on its front face. This thin 7 at.% Yb:LuAG wedge with 1° angle and 100-310 μm thickness has the back side HR-coated for both pump 969 nm and laser 1030 nm wavelengths and wide range of angles. The front face is then transmitting the pump light for angle of incidence (AoI) higher than 45.5° and the laser light over 27.5°, for lower AoI the coating is highly reflective. Both beams are launched (Fig. 2.11) at the disk under an angle slightly greater than the limit angle, so the reflected beams get trapped in the wedged disk. This way, around 22 reflections for pump and 14 for laser beam were accomplished [81]. The potential of this concept for further development was proven in continuous-wave operation by achieving 890 W of output power with 50% optical-to-optical efficiency and gain factor over 10 (*cf.* the value of ≈ 1.1 for standard thin disk, estimated in Sec. 5.3.4, Fig. 5.28).

Over the years, thin-disk lasers made it possible to obtain output parameters unprecedented in laser technology, especially in the field of diffraction-limited, high-average-power pulsed lasers. The next section covers the most powerful thin-disk laser systems presented up to date.

2.2.3 State-of-the-art high-average-power ultrafast ytterbium thin-disk lasers

High-average-power laser system with picosecond or femtosecond pulse duration and good beam quality close to the diffraction limit are attractive for many advanced laser applications. Especially the 1-μm ytterbium lasers are the most versatile laser tools thanks to their high efficiency and well-practicable wavelength conversion possibilities, extending their spectral range from deep ultraviolet to mid-infrared.

For kW-level operation with excellent beam quality and some substantial pulse energy (mJ-level and higher), thin-disks lasers are the most suitable technology, with possible alternatives in ytterbium Innoslab and fiber lasers, although these are much more limited in the maximum pulse energy (currently to some 50 mJ [76] and 10 mJ [84], respectively). For each topology of thin-disk laser systems discussed here, the highest average power was reported exclusively with Yb:YAG and all laser systems mentioned in this section were based on this material – if not stated otherwise.

Performance of *continuous-wave thin-disk lasers* can provide some projection of what are the limits in power-scaling of this technology. The most powerful thin-disk system comprising 10 disks in a single laser resonator was developed by the Boeing company [85] and provided 28 kW in multi-mode operation (M^2 of 2.7) with 43% O-O (optical-to-optical) efficiency. In multi-mode operation, the maximum power from single disk of more than 10 kW was extracted by Trumpf Laser GmbH [86] with 63% O-O efficiency and highly multi-mode beam (M^2 of 10.7). In single-mode operation, 10 kW were obtained this year by Trumpf [87] from a laser system with two polarization-combined oscillators and a multipass amplifier (i.e. 3 disk in total) with M^2 of 1.76 and O-O efficiency of 51%. With single disk oscillator, 500 W of average power in truly diffraction-limited beam ($M^2 < 1.05$) was presented also with 51% O-O efficiency [88]. 1.1-kilowatt power was later achieved by a Singaporean research group with somewhat lower beam quality (M^2 of 1.4) and O-O efficiency of 40% [89]. These last two results are the most relevant for the ultrafast lasers addressed in the rest of this section and in Chap. 5.

It is possible to generate ultrashort pulses with high-average-power from thin-disk lasers in two ways – either with a single-stage system, i.e. with a mode-locked thin-disk oscillator, or using a MOPA scheme with low-power front end and regenerative or multipass thin-disk amplifier. In general, laser oscillators are much less complex than multi-stage systems, but they offer less parameter flexibility and lower pulse energy, since their repetition rate is given by the length of their optical resonator. The rest of this section covers these two approaches and Tab. 2.5 lists the most powerful systems reported in literature, showing the tremendous progress that the thin-disk technology has made over the last decade.

The first **thin-disk oscillator** was developed at ETH Zürich in 2000 [90] and employed the passive mode locking technique with semiconductor saturable absorber mirror (SESAM, this method was used also in Sec. 4.1). Its 16.2 W of output power and 730 fs pulse duration made it at the time the most powerful femtosecond laser oscillator and the pulse energy was 0.5 μJ (due to high repetition rate of 35 MHz). Improvements in thin-disk and SESAM manufacturing allowed power scaling over 200 W level – 242 W with 80-μJ, 1.1-ps pulses [91], weaker 17-μJ pulses with only 580 fs pulse duration at 275 W [91], and currently record-holding 350 W oscillator produced 40 μJ, 940-fs pulses in 2019 [92]; further increase in output power to 500 W is planned for the near future. In order to obtain such high pulse energy and short pulse duration, the laser requires operation in low-pressure (30 mbar) nitrogen atmosphere. Also other ytterbium-doped materials were tested with SESAM mode-locking, and from the power point-of-view, the most notable was 141-W, 740-fs Yb:Lu_2O_3 oscillator [93] (this material has higher thermal conductivity and emission bandwidth than Yb:YAG). It should be noted that output beam quality of thin-disk oscillator is typically excellent ($M^2 < 1.1$).

The alternative technique extensively used in Ti:sapphire lasers, Kerr-lens mode locking, was successfully used with thin-disk laser in 2011 [94] with 45-W, 270-fs pulses. In short time, the research group at MPQ Garching scaled the KLM oscillators to performance level comparable to SESAM lasers. The maximum power demonstrated output power was 270 W with 14-μJ, 330 fs pulses [95], all in standard atmosphere. The KLM mode locking does not require demanding development of the SESAM element and can provide shorter pulses (even down to 49 fs from Yb:YAG [55], although at cost of drastically decreased efficiency), but it seems less versatile than SESAM mode locking, especially in terms of output energy. Finally, for some applications it is possible to enhance oscillator's parameters by using the intracavity beam – this way Eilanlou et al. generated XUV light via HHG from a 48-W, 15-MHz KLM thin-disk oscillator [96]; the intracavity pulses with 436 fs duration had 57 μJ energy and 860 W average power.

Tab. 2.5: Parameters of selected high-average-power (≥100 W), high-repetition-rate (≥1 kHz) femtosecond and picosecond Yb:YAG thin-disk lasers. P_{av} – average output power, E_p – pulse energy, f_{rep} – repetition rate, τ_p – pulse duration, M^2 – beam quality parameter.

P_{av}	E_p	f_{rep}	τ_p	M^2	Year	Ref.
MODE-LOCKED OSCILLATORS						
155 W[a]	10 μJ	15.6 MHz	140 fs	1.1	2016	[97]
242 W[b]	80 μJ	3 MHz	1.07 ps	1.05	2014	[91]
270 W[a]	14.4 μJ	18.8 MHz	330 fs	<1.1	2014	[95]
275 W[b]	17 μJ	16.3 MHz	583 fs	<1.05	2012	[98]
350 W[b]	40 μJ	8.9 MHz	940 fs	-	2019	[92]
REGENERATIVE AMPLIFIERS						
100 W	1 mJ	100 kHz	1.6 ps	<1.3	2015	This work
220 W	220 mJ	1 kHz	1.9 ps	<1.4	2015	[99]
300 W	30 mJ	10 kHz	1.6 ps	-	2013	[100]
554 W[c]	5.5 mJ	100 kHz	1.03 ps	1.4	2019	This work
1.05 kW	200 mJ	5 kHz	1.05 ps	1.09	2017	[101]
MULTIPASS AMPLIFIERS						
528 W	413 μJ	1.28 MHz	294 fs	1.28	2020	[102]
720 W	720 mJ	1 kHz	920 fs	2.1	2020	[29]
1.03 kW	206 mJ	5 kHz	<500 fs	1.15	2020	[103]
1.4 kW	4.7 mJ	300 kHz	6.5 ps	<1.4	2015	[104]
1.6 kW	3.9 mJ	400 kHz	1.3 ps	1.5	2020	[105]

[a] KLM mode locking (MPQ Garching group) [b] SESAM mode locking (ETH Zürich group)
[c] 554 W is uncompressed power, compression to 1 ps was demonstrated up to 350 W

For pulse amplification with thin-disk gain medium, **regenerative amplifier** is a natural choice of architecture, since it overcomes the drawback low single-pass gain of a thin disk by allowing high number of passes of the seed pulse through the disk, making possible values of amplification factor as high as 10^6. The principle of operation of a regenerative amplifier (RA) is in detail described in Chap. 5. In short, RA is in fact a laser oscillator (i.e. a gain medium in optical cavity) equipped with an electro-optic modulator (EOM) serving as a polarization switch for locking a seed pulse in the cavity and after a sufficient number of cavity roundtrips it ejects the amplified pulse from the resonator. Its major advantages are its flexibility and good beam quality thanks to the use of a stable optical resonator. Its weak point is the EOM implemented as a Pockels cell with quite bulky nonlinear crystals (length in order of several cm), which limit the achievable peak power due to emerging nonlinear effects (self-phase modulation and self-focusing caused by Kerr effect).

The first thin-disk RA was developed in 1997 at ETH Zürich [106] and it generated 180-μJ, 2.3-ps pulses at 750 Hz repetition rate (1.35 W of average power). Further increase in

average power required improvements in thin-disk technology and high-voltage switches for Pockels cells, allowing higher operating voltage at increased repetition rate. First 100-W-level RA was reported in 2009 with 25-mJ, 1.6-ps pulses at 3 kHz repetition rate (75 W of average power) [107]. Two high-energy, 1-kHz picosecond RAs worth mentioning were developed at the Institute of Physics CAS, a 45-mJ single-disk system at HiLASE by Michal Chyla [108] and a 100-mJ dual-disk system by Jakub Novák et al. at ELI Beamlines [109]. The highest energy from a room-temperature thin-disk regenerative amplifier is currently 0.5 J at 100 Hz with 2.2-ps pulse duration obtained from two large Yb:YAG disks (diameter 25 mm) [110]. At the time our work on 500-W single-disk RA started, the most powerful amplifier was the 300-W, 10-kHz system from Trumpf Scientific Lasers [100]. The current state-of-the-art regenerative amplifier with two disks was presented by Nubbemeyer et al. in 2017 [101], reaching kilowatt average power level in 200-mJ, 5-kHz picosecond pulses in diffraction-limited beam and at 10-kHz repetition rate, it was possible to achieve output power of 1.4 kW for several minutes.

Even higher output power and pulse energy may be obtained using a **multipass amplifier** (MPA) after a smaller-scale regenerative amplifier. To overcome the low gain of a thin disk, setups with large number (usually between 10 and 50) of passes through the disk are used, requiring exceptional mechanical stability of its components. Furthermore, the absence of an optical resonator makes it more difficult to maintain good quality of the amplified beam. On the other hand, since there is no need for an electro-optic switch or other bulk optical element, kilowatt, high-repetition-rate amplifiers can produce pulses with multi-mJ energy without using the CPA technique.

The first, 48-pass TD amplifier was constructed at IFSW Stuttgart in 2003 with 12-mJ pulse energy at kilohertz repetition rate [111]. The current frontiers in output parameters of thin-disk lasers are represented by MPAs from Trumpf, with the highest pulse energy of 720 mJ (1 kHz, 920 fs, M^2 of 2.1) obtained from a 4-disk, two-stage MPA using CPA technique [29] and the highest average power of 1.6 kW in single-mode beam (M^2 of 1.5) was produced by a CPA-free, two-stage MPA operating at 400-kHz frequency with 1.3-ps pulse duration [105].

Chapter 3

Used methods and measuring instruments

This chapter lists measuring instruments used in experiments described in Chapters 4 and 5.

3.1 Measurement of laser power

Measurement of average laser power was the most frequent one during the experiments. While the output power of pump diode lasers was measured only before assembling the laser or while replacing the pump, laser output power was measured almost continuously.

Used power meters are listed in Tab. 3.1. Most of them were thermals sensors based on thermopile principle (series of bimetallic junction around the measuring area, producing voltage proportionate to absorbed power). They are relatively slow (response time of several seconds), but cover a wide power range and have almost flat spectral response over a broad spectral range.

The only exception was Ophir PD300-3W, which was based on a silicon photodiode. Therefore, it had about 10 times shorter response time (0.2 s) and much higher sensitivity, but narrower spectral range with typical Si-photodiode spectral response. It was used to measure low power output of fiber amplifiers and low power beams in general. It could be used for measuring power up to 100 mW with removed filter and up to 3 W with the filter clipped on.

3.2 Measurement of optical spectra

Optical spectra presented in this work were obtained using devices listed in Tab. 3.2. For measuring spectra in the vicinity of 1-μm wavelength, spectrometers based on Czerny–Turner design with a linear CCD-array detector a light delivery using optical fiber were used for their high precision and simple and quick use. Czerny–Turner scheme includes an entrance slit (in this case the fiber-core tip), a concave collimating mirror directing the light onto a diffraction grating, and focusing concave mirror imaging the different diffracted spectral components onto their respective places on the sensor (or on an output slit in case of a monochromator). The spectrometers for 1-μm range had high spectral resolution around 0.2 nm and were utilized with a 50-μm-core multi-mode fiber. For measurements of beams with power above $\approx$ 20 mW and below 1 W (or where the beam could be attenuated), the fiber was connected to an integration sphere Thorlabs IS200-4 in order to provide more accurate measurement. In case of the pump diode lasers, where the beam could not be attenuated, the measurement was performed on a diffuse reflection off a power meter.

In the 3-μm spectral region, spectra were acquired with an Oriel MS 257 monochromator and Hamamatsu C12492-210 InAs photodiode (spectral range 1-3.5 μm, 50 kHz bandwidth).

Tab. 3.1: List of power meters used in the experiments. RA – main regenerative amplifier of PERLA C, FE – front end of PERLA C.

Manufacturer & model	Spectral range	Max. power	Min. power	Typical application
Coherent PM5K	0.19-11 μm	5 kW	100 W	Pump diode lasers
Ophir 1000W-BB-34-QUAD	0.19-20 μm	1 kW	5 W	RA output
Ophir FL500A	0.19-20 μm	500 W	500 mW	Compressed RA output
Ophir 12A-P	0.15-8 μm	12 W	2 mW	PERLA C in general
Ophir 3A-P	0.15-8 μm	3 W	15 μW	Preamplifier, Er:Y_2O_3
Ophir PD300-3W	0.35-1.1 μm	3 W	5 nW	Fiber FE
Molectron PM3	0.3-11 μm	2 W	50 μW	Yb:YGAG
Thorlabs S310C	0.19-25 μm	10 W	10 mW	Yb:YGAG
Laser Precision RT-150CHD	–	150 W	–	Yb:YGAG

Tab. 3.2: List of spectrometers used in the experiments. CT – Czerny–Turner arrangement with a linear detector, FC – fiber-coupled.

Manufacturer & model	Spectral range	Resolution	Type	Typical application
Ocean Optics HR4000	909-1075 nm	0.17 nm	CT, FC	PERLA C, Yb:YGAG
Narran BR8	968-1075 nm	≈ 0.2 nm	CT, FC	PERLA C
Oriel MS257	2.5-3.25 μm	≈ 2 nm	Monochromator	Er:Y_2O_3

This setup could provide also temporarily-resolved measurements. The monochromator was also of Czerny–Turner type and was used with 50-μm slits and with Oriel 77774 grating, giving spectral resolution around 2 nm.

3.3 Temporal characterization of ultrafast laser pulses

Temporal measurements of the laser output were usually done with a photodiode and oscilloscope. In Er:Y_2O_3 experiment, the already mentioned InAs photodiode Hamamatsu C12492-210 (50 kHz bandwidth) was employed and all measurements were performed on millisecond-scale. For 1-μm measurements on nanosecond scale and longer, all of the many used silicon and InGaAs photodiodes and oscilloscopes were fast enough for accurate measurements.

The rise time τ_{RT} (defined on levels from 10% to 90%) of a photodiode or an oscilloscope can be estimated from its bandwidth f_{3dB} as [112, 113]

$$\tau_{RT} \approx \frac{0.35}{f_{3dB}}.$$

The response of the whole measuring system with rise time of the photodiode τ_{PD} and oscilloscope τ_{osc} to a short pulse with duration τ_{real} may be assessed approximately as [113]

$$\tau_{meas} \approx \sqrt{\tau_{real}^2 + \tau_{PD}^2 + \tau_{osc}^2}.$$

For sub-nanosecond-scale characterization, InGaAs photodiode EOT ET-3500 with 15-GHz bandwidth was used. On PERLA C, it was connected to a 16-GHz, 80-GS/s oscilloscope Agilent DSOX91604A, yielding theoretical system response time of 32 ps, although the real response time to $\approx$ 1-ps pulses was near 45 ps. The measurements with Yb:YGAG oscillator were performed with the same photodiode and with oscilloscope LeCroy SDA 9000 with 9-GHz bandwidth and 40-GS/s sampling rate. This system's response time theoretically is 45 ps, but experience from the other laser systems showed value around 70 ps. For pulse train observation and for measurement of stretched pulses in the CPA laser system, this measurement technique was sufficient.

Electronic methods are too slow for measuring duration of ultrafast pulses and optical methods have to be used instead (I studied these in detail in [B3]). For picosecond pulses, the typical technique is autocorrelation measurement, in this work it was the intensity autocorrelation with second harmonics generation. PERLA C was characterized with a commercial autocorrelator APE PulseCheck (maximum scanning range 50 ps), while Yb:YGAG oscillator was measured with a laboratory-made autocorrelator with even longer scanning range of more than 200 ps. Autocorrelation may give only an estimation of pulse duration for some assumed pulse shape.

More precise methods are FROG (frequency-resolved optical gating [114]) and SPIDER (spectral phase interferometry for direct electric-field reconstruction [115]), both allowing complete temporal characterization (intensity and phase), mainly for femtosecond pulses. From these two, for longer, picosecond pulses FROG is more suitable, since SPIDER requires higher spectrograph resolution and large amount of dispersion for longer pulse widths. Compressed pulses from PERLA C were characterized also using a FROG option for the APE PulseCheck autocorrelator, consisting of a thicker nonlinear crystal (with more wavelength-selective phase matching) and modified optics.

Mode-locked output of the Yb:YGAG oscillator was also characterized using a 3-GHz RF spectrum analyzer Rohde & Schwarz FSL3.

3.4 Other measurements

Beam profiles were measured using CCD and CMOS laser beam profilers. The output of PERLA C main amplifier was monitored using CINOGY CMOS-1.001-Nano with resolution of 2048×2048, CMOS chip active area of 11.3×11.3 mm^2 and 60-dB dynamic range (10-bit depth). The rest of the measurements on PERLA C was performed with Spiricon SP620U CCD profiler with resolution of 1600×1200 pixels, chip active area of 6.5×4.8 mm^2 and dynamic range of 62 dB (12-bit depth).

For Yb:YGAG experiment, CCD profiler DataRay WincamD-UCD23 was utilized with resolution of 1360×1024, 8.8×6.6 mm^2 sensor size and dynamic range of 60 dB (14-bit depth). For the 3-μm measurement, no profiler was available. The beam was visualized only with temperature-sensitive liquid-crystal sheets (produced by Edmund Optics) and measured using the knife-edge technique, which was used also for the beam quality measurement.

Beam quality of the PERLA C laser system was characterized using an M^2-measurement device developed by Laser-Laboratorium Göttingen, Germany, and measured according to the ISO 11146-1 standard. For the Yb:YGAG laser, the WincamD profiler was manually translated.

Temperature measurements were performed using thermal images cameras from FLIR. The temperature measurement of the thin-disk and Er:Y_2O_3 was done with camera A35 having 320×256 px microbolometric sensor and temperature range of -40 to 550 °C. Other measurements were performed with handheld camera E50 with 240×180 px sensor and temperature measurement range of -20 to 650 °C.

3.5 Design of optical systems using approximation of geometrical optics

In approximation of geometric optics, the laser beam propagating along axis z can be described with a light ray with position x_1 and propagating angle α_1 (for 2D case). Propagation of this ray through a linear system may be described using a matrix $\mathbb{M}$ with elements A, B, C, D [116]

$$\begin{pmatrix} x_2 \\ \alpha_2 \end{pmatrix} = \mathbb{M} \begin{pmatrix} x_1 \\ \alpha_1 \end{pmatrix} = \begin{pmatrix} A & B \\ C & D \end{pmatrix} \begin{pmatrix} x_1 \\ \alpha_1 \end{pmatrix},$$

where x_2, α_2 are parameters of the output beam. This method is called the ABCD formalism. For most optical elements encountered in laser physics, this 2D approach can be used separately for saggital and tangential planes, however, if necessary, it can be generalized to a 3D case by adding two more coordinates (e.g. y and β) and expanding the matrix $\mathbb{M}$ to dimension of 4×4.

Linear elements can be concatenated simply by multiplying their matrices,

$$\mathbb{M} = \mathbb{M}_i \, \mathbb{M}_{i-1} \ldots \mathbb{M}_2 \, \mathbb{M}_1.$$

In case of an optical resonator, which is a set of optical elements, one cay obtain this way easily its ABCD matrix (for linear cavity, one has to take into consideration also the back-propagation of the beam).

ABCD formalism can be used also for Gaussian beams of wavelength λ, which can be described with a q-parameter, corresponding with the beam parameters w (beam radius) and R (wavefront radius of curvature) as

$$\frac{1}{q} = \frac{1}{R(z)} - \frac{i\lambda}{\pi w^2(z)}.$$

The input beam with q-parameter of q_{in} is then transformed by the system as

$$q_{out} = \frac{Aq_{in} + B}{Cq_{in} + D}.$$

Eigenmode of an optical resonator with ABCD matrix $\mathbb{M}$ maintains its q-parameter for each roundtrip, hence $q_{out} = q_{in}$. It can be shown [116] that the eigenmode exists and may be calculated from $\mathbb{M}$, if the resonator satisfies condition

$$-1 < \frac{A + D}{2} < 1. \tag{3.1}$$

This is the stability condition for an optical resonator.

The ABCD formalism was used throughout this work for designing optical resonators, since the conditions of geometric optics were met. For the calculations, I used programs ReZonator [117] and WinLase [118]. I have also implemented an equivalent calculation in the Python programming language, with a module for resonator optimization being still under preparation. Since this module has been not yet finished, there was no reason why not to use the aforementioned user-friendly programs for cavity design.

Chapter 4

Laser oscillators based on novel laser materials

This and the following chapter summarize the experimental results of this work. While the Chapter 5 deals solely with development of one larger-scale Yb:YAG thin-disk laser system, this chapter describes development of smaller laser oscillators. The main goal of these research activities was to test novel laser materials that have potential for use in thin-disk lasers, especially short-pulsed oscillators.

In this chapter, Section 4.1 presents investigation of the Yb:YGAG laser material, which is shown to be a superior alternative to Yb:YAG for ultrafast pulse generation at low temperature. The second section is then dedicated to 3-μm laser based on erbium-doped Y_2O_3 ceramic.

4.1 Development towards Yb:YGAG cryogenic oscillator

The ytterbium-doped YAG is an almost ideal gain material for high-power, short-pulse laser operation, as explained in Section 2.1.2. It possesses excellent material properties and its only major drawback is somewhat lower emission bandwidth, limiting the minimum achievable pulse duration at room temperature to the order of hundreds of femtoseconds. However, this fact is pronounced when operating at lower temperatures, in a regime attractive for high-power amplification due to enhanced thermo-optic and spectroscopic characteristics of the gain medium (see Section 2.1.4). When cooling down Yb:YAG from room temperature to the temperature of liquid nitrogen, its emission bandwidth is reduced more than six times. This makes generation and amplification of even several picoseconds long pulses much more difficult.

An effective way to minimize this effect and preserve as much of Yb:YAG's favorable material properties as possible is to tune its chemical composition. The alternative are the mixed garnets that derive from YAG ($Y_3Al_5O_{12}$) by substituting part of the aluminum ions with other metals like scandium or gallium. This results in inhomogeneous broadening of the lattice structure and variation of the crystal field strength, leading to the desired broadening of absorption and emission spectra of the material and possibly also to a shift in peak absorption and emission wavelengths. Studies on several of these materials, with neodymium or ytterbium doping and in both monocrystalline and ceramic form, were reported in the literature, including Nd:$Y_3Sc_2Al_3O_{12}$ ceramic [119], Nd:$Y_3ScAl_4O_{12}$ ceramic [120], Yb:$Y_3ScAl_4O_{12}$ ceramic [121], Nd:$Y_3Ga_xAl_{(5-x)}O_{12}$ single crystal [122], and Yb:$Gd_3Al_xGa_{(5-x)}O_{12}$ single crystal [123]. Our research group had access to another mixed-garnet ceramic material, Yb-doped $Y_3Ga_2Al_3O_{12}$ (Yb:YGAG) fabricated by Konoshima Chemical Co. Ltd. in Japan, a company renowned for production of high-quality transparent ceramics, especially garnets and sesquiox-

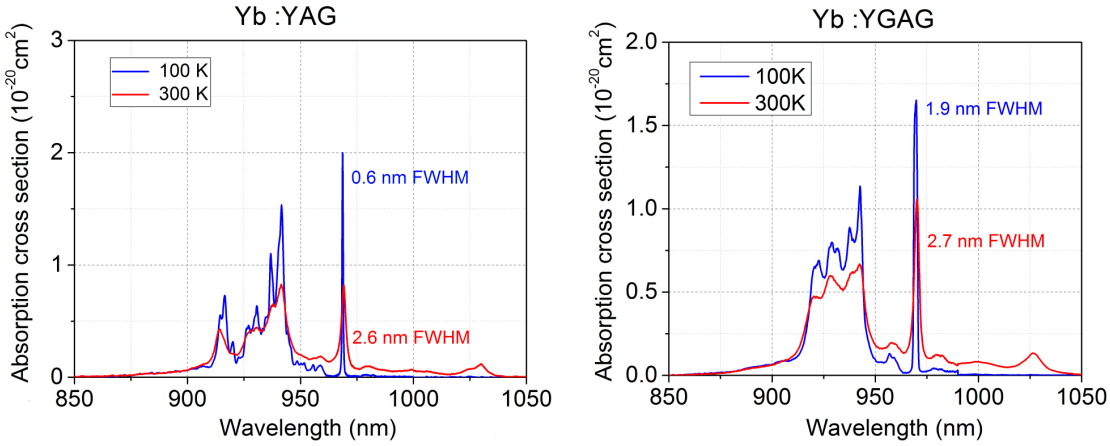

Fig. 4.1: Absorption cross sections of Yb:YAG and Yb:YGAG at room temperature and at 100 K (data measured by V. Jambunathan).

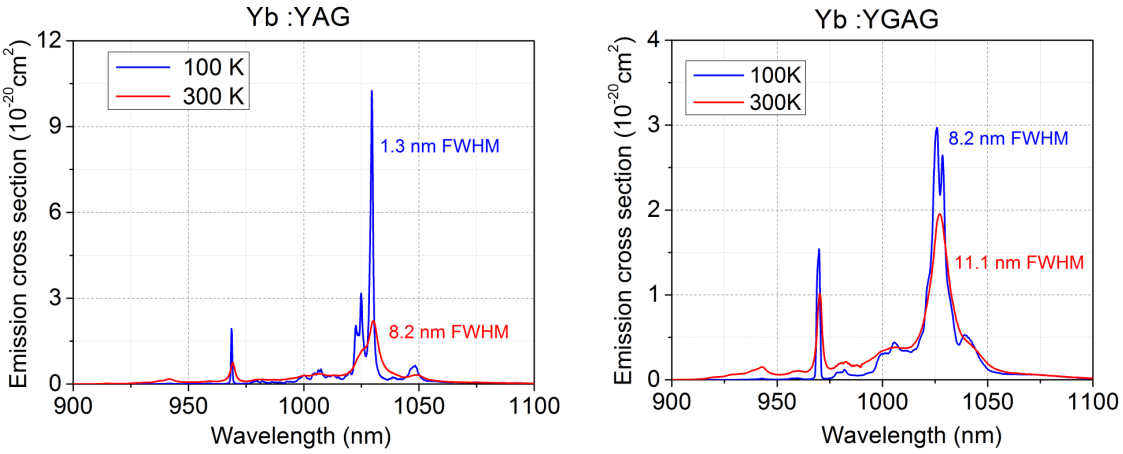

Fig. 4.2: Emission cross sections of Yb:YAG and Yb:YGAG at temperature of 300 K and at 100 K (data measured by V. Jambunathan).

ides [124]. This ceramic was previously examined with neodymium doping [125] and its promising spectroscopic properties at low temperature were demonstrated by V. Jambunathan et al. in [126].

The most important differences can be grasped by comparing its absorption and emission spectrum with Yb:YAG. As the Fig. 4.1 illustrates, absorption of Yb:YAG at room temperature ($\approx$ 300 K) peaks at 969 nm with cross section (CS) of $8 \cdot 10^{-21}$ cm^2 and bandwidth (BW) of 2.6 nm. At temperature of liquid nitrogen ($\approx$ 80 K), this absorption peak becomes more prominent with CS of $2 \cdot 10^{-20}$ cm^2 and BW of only 0.6 nm. This means that it is challenging to pump cryogenic Yb:YAG efficiently at the zero-phonon line even with wavelength-stabilized diode lasers and using the broad absorption band around 940 nm. The peak absorption wavelength of Yb:YGAG is shifted to 970 nm and its maximum room-temperature CS of $1.1 \cdot 10^{-20}$ cm^2 and 2.7 nm BW changes at 80 K only to $1.7 \cdot 10^{-20}$ cm^2 and 1.9 nm, respectively. This means that Yb:YGAG is much less demanding when it comes to zero-phonon-line pumping at low temperature.

Even more pronounced difference emerges for cross sections of stimulated emission (see Fig. 4.2). The maximum emission CS of Yb:YAG at 1030 nm increases five times when temperature is lowered from 300 K to 80 K, significantly increasing the achievable laser gain.

Tab. 4.1: Peak values of stimulated emission cross section and emission bandwidths of Yb:YAG (peak wavelength 1030 nm) and Yb:YGAG (peak at 1026 nm) at room temperature and at 80 K [126].

	Yb:YAG		Yb:YGAG	
Temperature [K]	300	80	300	80
Peak emission CS [10^{-20} cm^2]	2.21	11.01	1.96	3.07
Emission bandwidth [nm]	8.13	1.26	9.68	7.12

However, this is accompanied with more than six-fold reduction of its gain BW to 1.3 nm. With Yb:YGAG, both effects are mitigated, with the peak emission CS increased only by 56% and the emission BW reduced just by 26% to 7.12 nm, which should still allow sub-picosecond pulse generation. The corresponding values of emission CS and gain BW can be found in Table 4.1. It should be noted that the peak CS of Yb:YGAG is shifted to 1026 nm and at low temperatures, a subpeak at 1028 nm appears.

Beside these convenient spectroscopic properties of Yb:YGAG, there are several indisputable shortcomings of Yb:YAG. As can be expected from the more complex chemical composition, this mixed garnet possesses lower thermal conductivity. With 10 at.% concentration, the thermal conductivity of this ceramic was determined as 5.5 W/(m·K) [127], which is about 15% less than that of a single-crystal Yb:YAG of the same doping concentration [128], but still higher than with many other frequently used ytterbium laser materials with high doping. Another drawback is a poor market availability of this ceramic, since to our knowledge, this material is not ordinarily produced and has not yet been thoroughly researched, which brings even more motivation to investigate its laser performance.

The following sections summarize the research of Yb:YGAG ceramic at room and cryogenic temperature, comparison of its performance with Yb:YAG, and development of a SESAM-mode-locked picosecond cryogenic laser oscillator. The experiments were carried out in the laboratory of Professor Kubeček at the Department of Physical Engineering of FNSPE CTU. The results were presented at several conferences [A14,A16[4],A17] and published in *Optics Express* [A1].

4.1.1 Free-running operation and comparison with Yb:YAG

The sample of Yb:YGAG ceramic used in our experiment had doping concentration of 10 at.%, clear aperture of 3.6×3.6 mm^2 and thickness of 1.5 mm. Also samples with thickness of 0.5 mm and 1.0 mm were available (all cut from an original disk with 18 mm diameter), but the largest thickness was identified as the most suitable for laser experiments. Faces of the samples were anti-reflection (AR) coated for spectral range from 900 nm to 1100 nm by Crytur Turnov. To benchmark it against a well-known gain medium, we found a single-crystal Yb:YAG manufactured by the Union Carbide Corp. It had very similar parameters – 10 at.%, dimensions of $3 \times 3 \times 1.5$ mm^3, and AR-coated faces for 940 and 1030 nm wavelengths, making it an ideal match for the comparison.

The experimental setup for low-temperature operation is shown in Fig. 4.3. The gain medium was pumped with a fiber-coupled 40-W diode laser (Dilas M1F2S22-940.3-30C-SS2.1) at the wavelength of 940 nm with bandwidth of 2.6 nm. The pump light from the fiber (core

[4]Awarded by the 2015 ASSL Conference Outstanding Poster Presentation Award

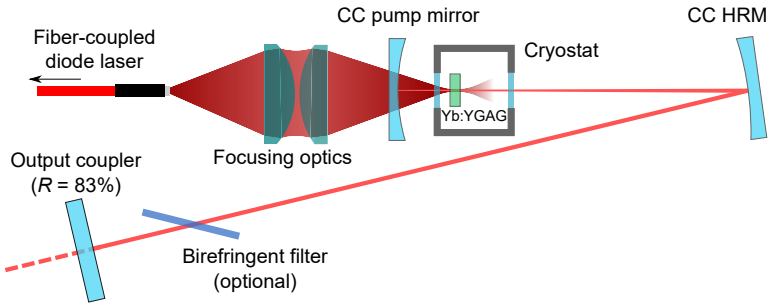

Fig. 4.3: Experimental setup for CW operation of Yb:YGAG laser at cryogenic temperature. For experiment with Yb:YAG, only the laser medium and its holder were changed. Similar setup was used for room-temperature operation. CC – concave, HRM – high-reflection mirror, R – reflectivity.

diameter of 200 μm and NA 0.22) was imaged by two 75-mm lenses onto the laser medium with a spot diameter of approximately 200 μm. The Yb:YGAG/Yb:YAG was mounted in a copper holder inside of a small cryostat with 5 mm thick BK7 windows, AR-coated for both 940 and 1030 nm, and cooled with liquid nitrogen to temperature of approximately 80 K. A 560 mm long optical resonator encompassed a concave pumping mirror (AR for 940 nm and HR for 1030 nm) with 100 mm radius of curvature (RoC), a concave folding mirror with 300 mm RoC, and a flat output coupler with reflectivity of 83% at 1030 nm; the resulting mode diameter in the laser ceramic was approximately 190 μm.

For room-temperature operation, we used similar layout with several differences. The pump source was a 5-W diode laser at 969-nm (for Yb:YGAG tuned to 970-nm via temperature adjustment) with output coupled into a fiber with 100 μm core diameter and NA of 0.22 and delivered to the laser using a pair of 50-mm lenses. The laser medium was left without active cooling outside the cryostat, allowing use of more compact cavity (also V-shaped, length of 380 mm) with a flat pump mirror and concave folding mirror with 100 mm RoC. The mode sizes of the pump beam and resonator and cavity eigenmode were the same as with the cryogenic setup.

The room-temperature experiment was performed in quasi-continuous-wave (QCW) regime with pump pulses with 2 ms pulse duration and 50 Hz repetition rate (duty cycle of 10%) to avoid overheating of the active medium. The Yb:YGAG laser was emitting at central wavelength of 1028.7 nm and the Yb:YAG laser at 1030.7 nm. Although effort was made to adjust the pump wavelength to the optimum for both media, the pump absorption[5] for both cases varied significantly – 76% with Yb:YGAG and only 65% with Yb:YAG – due to the different shapes of the zero-phonon-line absorption peak.

The maximum obtained output power with Yb:YGAG was 103 mW at 424 mW of pump power incident on the ceramic (slope efficiency of 30.2%), while with Yb:YAG it was only 81 mW at 424 mW of incident pump power (slope eff. 24.3%). When taking into account the estimated absorbed power [Fig. 4.4(a)], the difference in performance is smaller, with slope efficiency of 41.6% for Yb:YGAG and 37.3% for Yb:YAG and the optical-to-optical efficiency (the output to absorbed pump power ratio) was 32.4% and 29.3%, respectively.

As mentioned before, for cryogenic operation we used a more powerful 940 nm pump laser. Pumping in the broad conventional absorption band equalized the absorption rate to 81% for

[5]Measured at non-lasing condition near the threshold pump power, since it cannot be measured during laser operation. Considering the absorption rate as constant from this value brings realistic estimate of the real absorbed pump power. Pump absorption at non-lasing condition decreases with increasing pump intensity (power), while under lasing operation, the pump absorption is increased. Thus, applying the absorption rate measured for corresponding pump levels would lead to an unrealistically high calculated values of optical efficiency.

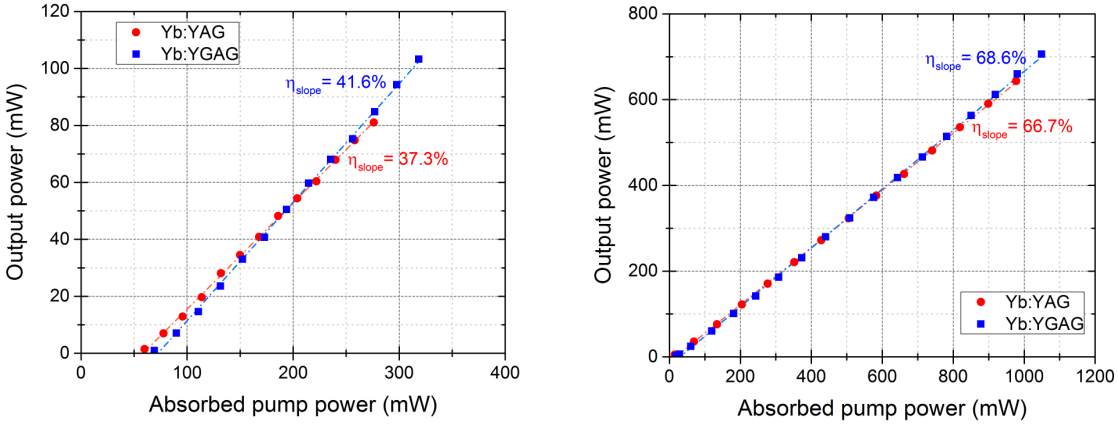

(a) (b)

Fig. 4.4: Comparison of room-temperature, QCW performance of Yb:YAG and Yb:YGAG at (a) room temperature with 969/970 nm pumping, (b) cryogenic temperature with 940 nm pumping.

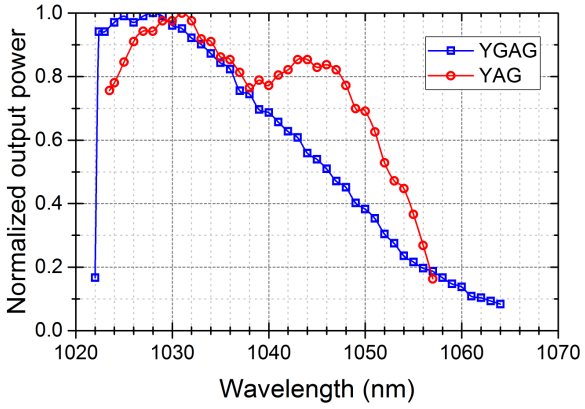

Fig. 4.5: Wavelength tunability achieved with Yb:YAG and Yb:YGAG at room temperature.

Yb:YGAG and 80% for Yb:YAG. Again, the comparison was performed in QCW regime, this time with 4 ms pulse duration and 10 Hz repetition rate (4% d.c.), which allowed to use full pump intensity of the diode laser without risking damage of the active medium.

At low temperature, the central lasing wavelength shifted to 1025.7 nm with Yb:YGAG and 1029.3 nm with Yb:YAG, the lasing performance improved significantly in both cases [Fig. 4.4(b)], and the differences in performance from the room-teperature case diminished, probably mainly due to change in the pump source. With Yb:YGAG the maximum output power was 706 mW (17.7 W power amplitude) at incident pump power of 1.29 W (slope efficiency 55.6%) and the optical-to-optical efficiency related to absorbed power was 67.3%. In case of Yb:YAG, the highest output power was 673 mW at 1.28 W incident pump power (slope efficiency 53.3%) and the optical-to-optical power was 65.8%. Also quality of the output beam of Yb:YGAG at full pump power was evaluated and the measured M^2 parameter was 1.2 for the horizontal plane and 1.4 for the vertical plane.

Room-temperature wavelength tuning range of both laser media was examined with a birefringent filter (2.8-mm thick quartz plate) inserted in the room-temperature setup next to the output coupler, which was this time replaced with an HR mirror in order to minimize losses in the cavity. With Yb:YGAG ceramic, we recorded a continuous tuning range from 1022.4 mm to 1064 nm with maximum output power obtained at 1028 and 1025 nm. The range achieved

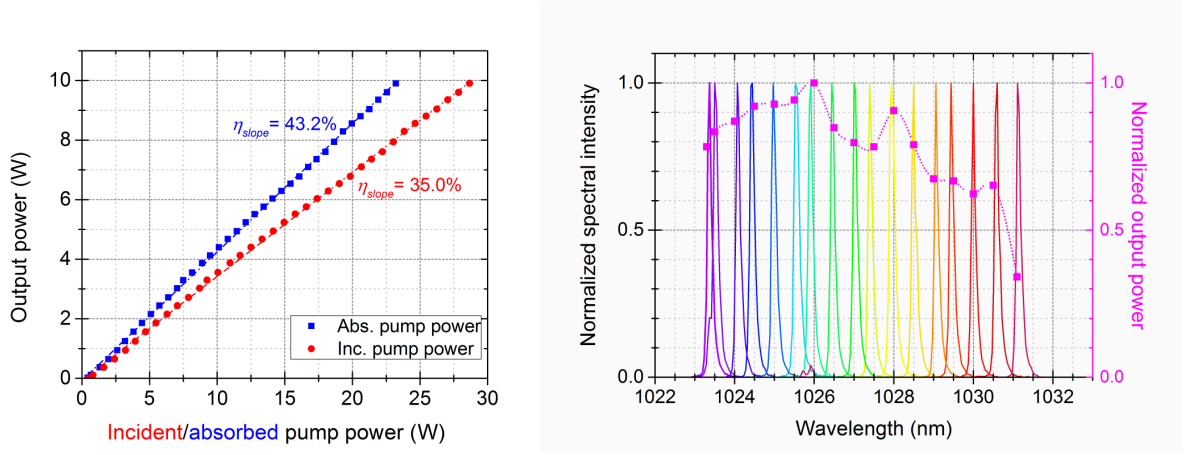

(a) (b)

Fig. 4.6: (a) Output power characteristics of the cryogenic Yb:YGAG laser in CW operation, (b) wavelength tunability of the Yb:YGAG laser at 80 K – normalized output spectra obtained with a birefringent filter and corresponding normalized output power.

with Yb:YAG was narrower, from 1023.5 nm to 1057 nm with peak power emitted at 1031 nm and a local maximum in output power emerged around 1044 nm. The measured data are plotted in Fig. 4.5.

From this direct comparison of both samples it can be concluded that the Yb:YGAG ceramic manufactured by Konoshima Chemical Co. is of high optical quality and good laser performance, on par with Yb:YAG single crystal at least for low-power operation. It was also confirmed that the inhomogeneous broadening of lattice structure occurring in the mixed garnet leads to broader absorption and emission spectra and also to a shift in emission wavelength, as indicated by the spectroscopic data.

Further work focused on CW operation of Yb:YGAG at cryogenic temperature. The thermal load on the laser medium under continuous pumping was much higher, which led to an increase in temperature of the ceramic and occurrence of thermal lensing, both causing deterioration of lasing efficiency and beam quality. The pump power was raised as high as 28.7 W, yielding maximum output power of 9.9 W with slope efficiency of 35.0% [Fig. 4.6(a)]. Estimating the same rate of pump absorption of 81% like for the QCW regime, the optical-to-optical efficiency related to the absorbed power was 42.7%, i.e. by 25% lower than in the QCW regime. The beam quality degraded significantly with pump power from an excellent value of 1.04 at 5 W of pumping to 1.5 in horizontal plane and 2.5 in vertical plane at full pump power. This was caused mainly by mode-mismatching at higher power due to the thermal lensing and the asymmetry in the beam quality is linked to the construction of the copper holder, where the heat removal from the bottom part was less efficient than from the upper half that was in direct contact with the cooling medium. Adapting the cavity design to the thermal lens and improving the copper holder should efficiently address these issues.

In continuous-wave operation the laser was emitting at 1025.6 nm. Wavelength tunability at 80 K was examined using the same birefringent filter like in the room-temperature setup and with a HR mirror instead of the output coupler. It was found that the output spectrum of Yb:YGAG pumped at 5.2 W can be tuned continuously from 1023.3 nm to 1031.1 nm with maximum output at 1026 nm, as shown in Fig. 4.6(b). This concluded the free-running experiment and we moved to short-pulse generation.

4.1.2 Mode-locking with cryogenic Yb:YGAG

For generation of ultrashort laser pulses we used the passive mode locking technique, which is actually the only method capable of delivering pulses with duration of several picoseconds or shorter. The mode-locked (ML) operation was formed using a semiconductor saturable absorber mirror (SESAM), which is a well-established technique [129] and we found it more suitable and robust than the alternative, Kerr-lens mode locking, based on nonlinear self-focusing altering the cavity eigenmode [130].

In order to obtain stable mode locking with a saturable absorber, the laser should operate above the *Q-switched mode locking threshold*

$$E_p^2 > E_L^{(sat)} E_{SA}^{(sat)} \Delta R \tag{4.1}$$

given by dynamics (described via rate equations) of a mode-locked laser [131]. Here, E_p is the intracavity pulse energy, $E_L^{(sat)}$, $E_{SA}^{(sat)}$ are saturation energies of the gain medium and saturable absorber, and ΔR is the modulation depth of the absorber. In the opposite case, it is likely that the laser would operate in a regime of Q-switched mode locking (QML) with large fluctuation in pulse energy. Such mode of operation is essentially inapplicable and for the saturable absorber it poses a significant risk of damage.

The equation (4.1) can be rewritten in a more approachable way as

$$(P_{cav}\tau_R)^2 > F_L^{(sat)} A_L F_{SA}^{(sat)} A_{SA} \Delta R, \tag{4.2}$$

where P_{cav} is the intracavity power (traceable from the output power and output coupling), τ_R is the cavity roundtrip time, $F_L^{(sat)}$, $F_{SA}^{(sat)}$ stand for the saturation fluence of the gain medium and saturable absorber, and A_L, A_{SA} are cavity eigenmode areas thereon. The saturation fluence of laser material is than determined by the photon energy $h\nu$, emission and absorption cross sections $\sigma_{em}, \sigma_{abs}$, and the number of passes through the gain medium per roundtrip m, i.e. by relation

$$F_L^{(sat)} = \frac{h\nu}{m(\sigma_{em} + \sigma_{abs})}. \tag{4.3}$$

Ytterbium-doped media have rather high saturation energy, which makes them prone to Q-switching instabilities when employed in SESAM mode locking. The saturation energy is approximately inversely proportional to the emission cross section. This means that in case of Yb:YAG it is five time reduced when cooled down to 80 K, while the saturation energy of Yb:YGAG decreases just by 36% – this is a trade-off for the broader emission bandwidth. Therefore, achieving stable mode locking regime with Yb:YGAG is more difficult and this makes the cavity design and SESAM choice more important. The cavity layout was based on the setup used for the CW operation, adding an extension with the saturable absorber. The modified, 1.2 m long resonator is shown in Fig. 4.7.

Compared to the original cavity, the flat output coupler was replaced with a flat HR mirror and a SESAM with a concave output coupler with 98.5% reflectivity and 200-mm RoC were added (so there are two output beams out of the cavity). As the absorber we used a commercially available SESAM from Batop GmbH (SAM-1064-2-10ps) with modulation depth, relaxation time, and saturation fluence of 1.2%, 10 ps, and 90 μJ/cm^2, respectively. We used a rather tight focusing on the absorber in order to meet the condition (4.2). The calculated eigenmode diameters (Fig. 4.8) in the gain medium and on the SESAM were approximately 190 μm and 104 μm.

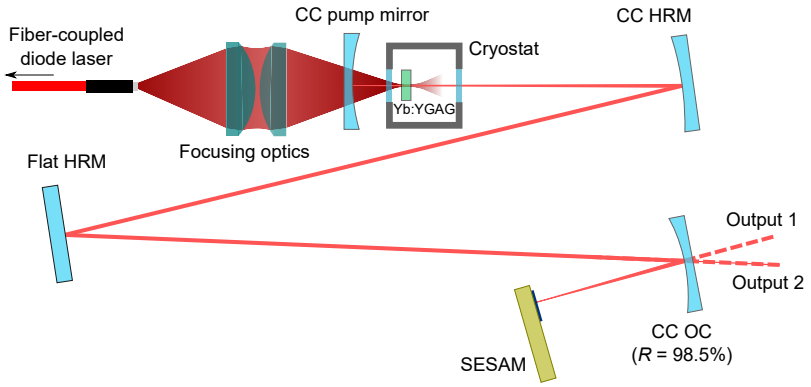

Fig. 4.7: Experimental layout for mode-locked operation of Yb:YGAG laser at cryogenic temperature. CC – concave, HRM – high-reflection mirror, OC – output coupler, R – reflectivity, SESAM – semiconductor saturable absorber mirror.

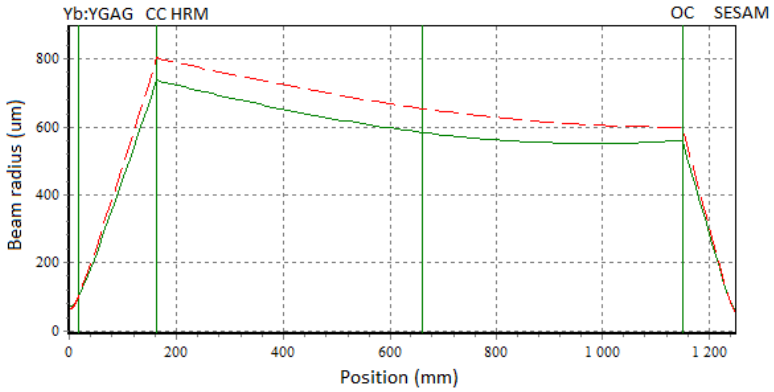

Fig. 4.8: Eigenmode radius along the cavity of the SESAM-mode-locked laser oscillator from Fig. 4.7 for the sagittal (red dashed line) and tangential plane (green line). Green vertical lines designate positions of optical elements; CC HRM – concave HR mirror, OC – output coupler.

With this setup and the gain medium cooled down to 80 K, we obtained stable and self-starting mode locking with output power of 194 mW (sum of power in both beams) at incident pump power of 3.9 W. The ML operation remained stable and without QML instabilities even with pulsed pumping (4 ms pump pulses). The output power was significantly lower than what was expected from the previous experiments. When analyzing the conditions in the cavity against the stability condition (4.2) as in Fig. 4.9, it turns out that such configuration should not even allow stable ML operation – higher intracavity power was assumed in the design process. This discrepancy is probably caused by inaccurate input parameters, but since this case it was a favorable one, no further investigation was performed. The fluence on the SESAM was estimated as 640 μJ/cm^2, which is 7 times its saturation fluence.

The laser oscillator operated at central wavelength of 1025.4 nm with spectral bandwidth of 0.64 nm (FWHM) and spectral shape corresponding to a transform-limited pulse with duration of 1.8 ps [Fig. 4.10(a)]. The spectrum showed a partial modulation with period of 0.2 nm, which could suggest presence of etalon effect in the 1.5-mm thick ceramic plate.

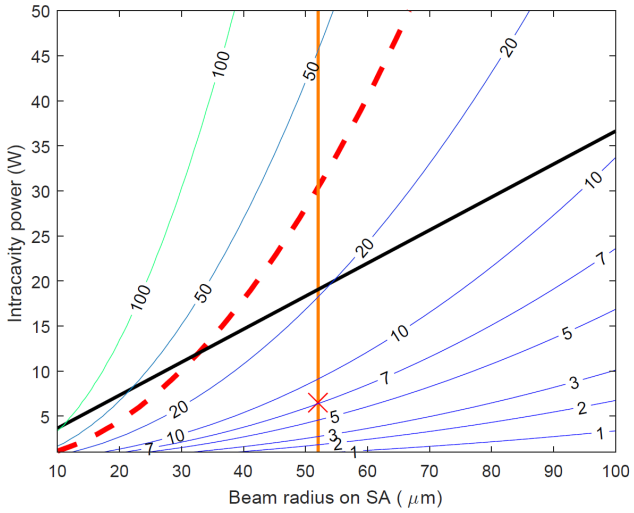

Fig. 4.9: Contour plot of SESAM saturation parameter ($F_{SA}/F_{SA}^{(sat)}$) dependance on average intracavity power (proportional to the pulse energy E_p) and mode radius on the saturable absorber. Black line represents the equation in (4.1), dashed red curve coincides with SESAM's damage threshold, orange line represents the chosen cavity configuration from Fig. 4.8, and red cross is the actual working point at which we obtained stable mode locking reported here.

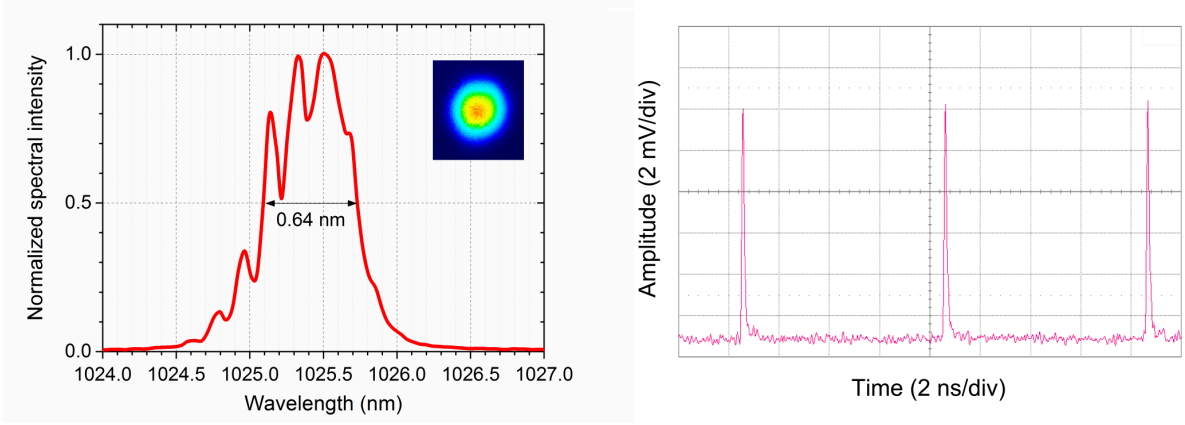

(a) (b)

Fig. 4.10: (a) optical spectrum of the cryogenic oscillator and beam profile (inset) measured behind the CC HRM from Fig. 4.7, (b) waveform of the output pulse train, acquired with a fast photodiode and oscilloscope.

Temporal characterization of the output laser pulses was first carried out using a photodiode with 35-ps rise time (EOT ET-3500), a 9-GHz digital oscilloscope (LeCroy SDA9000) and an RF spectrum analyzer. The pulse train with repetition rate of 119 MHz is shown in Fig. 4.10(b). The measured microwave spectrum (Fig. 4.11) confirmed stable CW mode-locked operation. To determine the pulse duration, we used a laboratory-made intensity autocorrelator with long delay stage. The acquired autocorrelation trace is shown in Fig. 4.12.

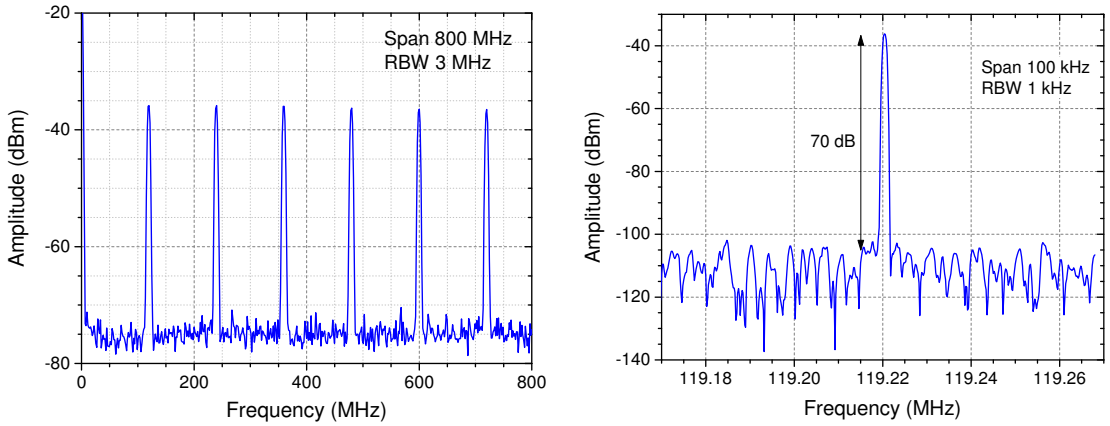

Fig. 4.11: Microwave spectrum of the 119 kHz output from the laser oscillator for two different frequancy spans. The signal-to-noise ratio of 70 dB indicates clean mode-locked operation. RBW – resolution bandwidth.

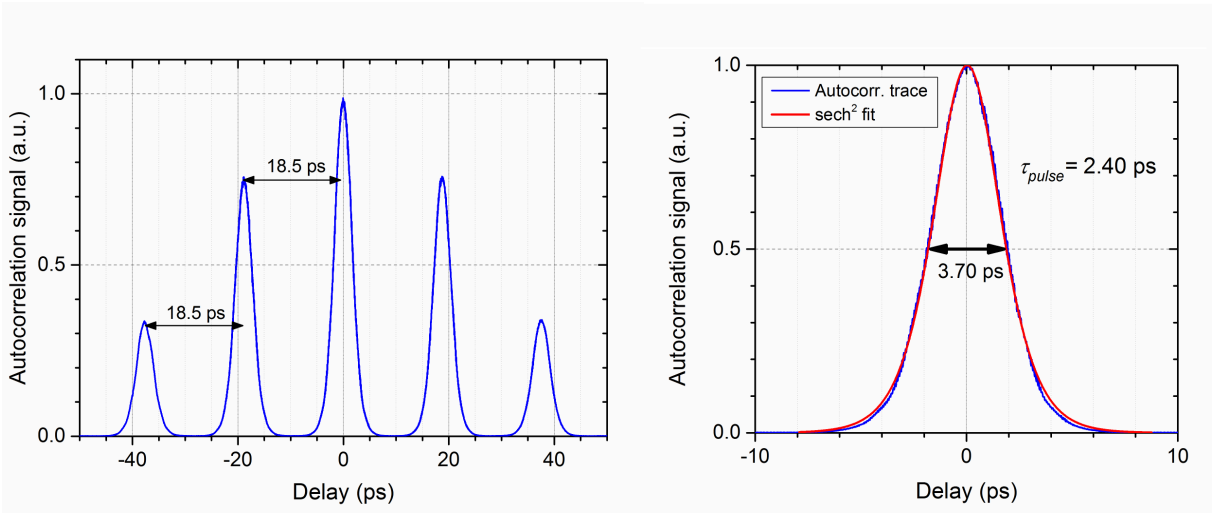

Fig. 4.12: Intensity autocorrelation trace of the output pulses (left) and a detail of the main peak fitted with a sech^2 function (right).

In the autocorrelation trace with large delay range, there are clearly evident multiple peaks separated equidistantly by 18.5 ps. The width of the main autocorrelation peak, as well as of the side peaks, was 3.70 ps, while their shape was very close to sech^2. Therefore we estimate a pulse duration of 2.40 ps, i.e. four times shorter than the minimum value ever reported with a cryogenic Yb:YAG (10 ps [132]).

The delay between pulses was 18.5 ps, corresponding to optical path of a double internal reflection in a 1.5-mm thick plate with refractive index of 1.85. The refractive index of YAG and YGG ($Y_3Ga_5O_{12}$) at 1.06 μm is 1.822 and 1.912, respectively [133]; therefore, this value is very plausible for their mixed garnet – Yb:YGAG (refraction index data for this material were not available). We slightly tilted the ceramic plate in order to mitigate the etalon effect, but as can be seen from both the output spectrum and autocorrelation, the internal reflection on the ceramic surface was still considerable. This might be caused by reduced effectiveness of its anti-reflection coating at low temperature. Possibly we could generate even shorter pulses with the same setup after suppressing these reflections, since a smoother output spectrum should be obtainable.

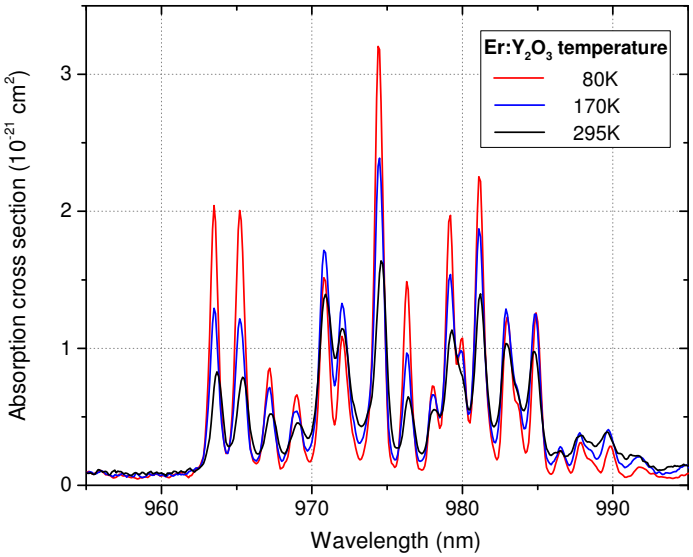

Fig. 4.13: absorption spectra of Er:Y_2O_3 near 1 μm measured at various temperatures.

In conclusion, this experiment with Yb:YGAG ceramics showed that its laser performance is comparable with Yb:YAG and it also confirmed its significant advantage for ultrashort pulse generation and amplification at cryogenic temperature. The work on Yb:YGAG was continued by Jaroslav Huynh by developing a regenerative amplifier delivering 405 fs long pulses at room temperature [127], and thin disks made of this material are under preparation for future experiments.

4.2 Erbium 2.7-μm laser

The erbium-doped materials exhibit favorable spectroscopic properties for direct mid-IR laser generation, as explained in detail in Section 2.1.3. The experiments with erbium-doped yttria ceramics (Er:Y_2O_3) were carried out in the laboratory of Professor Ryo Yasuhara at the National Institute for Fusion Science (NIFS, [134]). The ceramics were produced by the Konoshima Chemical Co. Ltd., by the same manufacturer like the Yb:YGAG ceramics that was examined within Section 4.1.

For 2.7 μm operation, the most efficient pump source is a ≈ 1-μm semiconductor laser. We investigated the absorption spectra of 2.3 at.% Er:Y_2O_3 using a spectrophotometer Shimadzu UV-3600 at the Department of Physical Engineering of FNSPE CTU. Although we planned to operate the laser only at room temperature, we used an opportunity to characterize the material in a liquid-nitrogen-cooled cryostat. The measured absorption spectrum for temperature from 80 to 295 K is in Fig. 4.13. It shows a strongly modulated absorption band from 963 to 985 nm with peak cross section at 974 nm and other strong absorption bands around 971 and 981 nm. At temperature of liquid nitrogen, the absorption cross section at peak wavelengths increases roughly by a factor of 2.

Due to the complex energy level structure of the Er^{3+} ion, (ground-state) absorption spectrum is not the only factor for choosing the optimum pump wavelength. The excited-state absorption (ESA) between levels $^4I_{11/2}$ and $^4F_{7/2}$ plays also an important role, since it occurs unfortunately in the very same spectral region. Some notion about the effect of ESA on the laser efficiency can be acquired from measurements with similar Er:Lu_2O_3 crystal by Li et

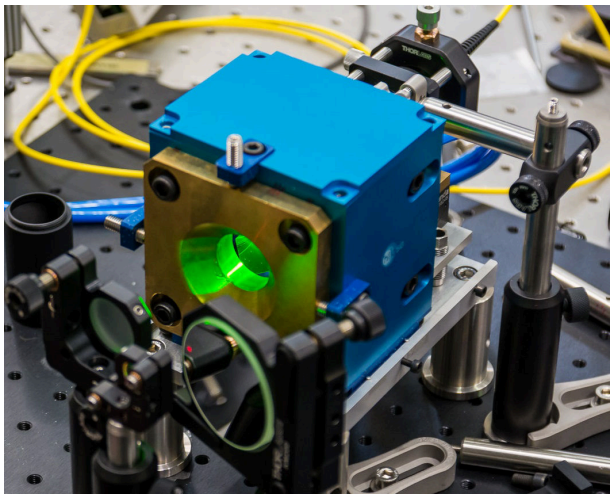

Fig. 4.14: The disk/active-mirror Er:Y_2O_3 laser in operation.

al. [135], showing that the most effective pump wavelegths are around 971, 974, and 980 nm. For Er:Y_2O_3, corresponding data are not available and we did not perform the pump-probe measurement ourselves; instead, we experimentally optimized the pump wavelength by controlling temperature of the 976-nm pump diode laser.

The next two sections cover the two phases of experiments performed with Er:Y_2O_3 ceramics at NIFS. In the first part (Section 4.2.1), we examined Er:Y_2O_3 samples with different parameters and established the methods of characterization for $\approx$ 3 μm lasers. We obtained laser oscillation from what possibly was the first 2.7-μm erbium active-mirror laser as well as from a rod-type laser, which was reported in [A19]. For the second stage of experiments (Section 4.2.2), we used a sample of Er:Y_2O_3 ceramic of refined parameters to obtain $\approx$ 1 W of continuous-wave laser output in a nearly diffraction-limited beam. This result was later published in *Laser Physics Letters* [A2].

4.2.1 Initial laser experiments with Er:Y_2O_3 ceramics

We started the experiments rather ambitiously by employing a disk (active-mirror) configuration. The available samples came in form of plates of various thickness (from 0.5 to 1.5 mm) and Er^{3+} concentration of 2.3 and 15 at.% with HR coating for 0.97 and 2.7 μm on the back side of ceramics. The most promising samples were bonded to heatsinks using a thermally conductive glue. We used a prototype thin-disk pump module developed at HiLASE for ytterbium thin-disk lasers (Fig. 4.14), in this case with pump spot diameter of 0.7 mm. A 55-W, 976-nm diode laser initially used was swapped for a 200 W, 981 nm to increase the pump intensity in QCW regime at the cost of lowering the duty cycle and lower pump absorption. The sample with most suitable parameters for lasing was the 1.5-mm thick plate with 2.3% concentration (the 15% samples were too thick for efficient heat removal). Such medium cannot be considered to be a thin disk, but the active-mirror configuration with a pump chamber using a ring elliptic mirror was the same like what is used in thin-disk lasers.

The initial 2.7 μm laser oscillation was detected when using the pump laser at highest current (peak power of 250 W) with d.c. of just 0.9%. With a 50 mm long cavity and a 98% output-coupling mirror, 5 mW of average output power was obtained with only 0.25% slope efficiency. It was not possible to use a shorter optical resonator due to dimensions of the pump chamber. Due to poor performance of the disk Er:Y_2O_3, we decided to continue with the common end-pumped rod geometry with a larger ceramic sample.

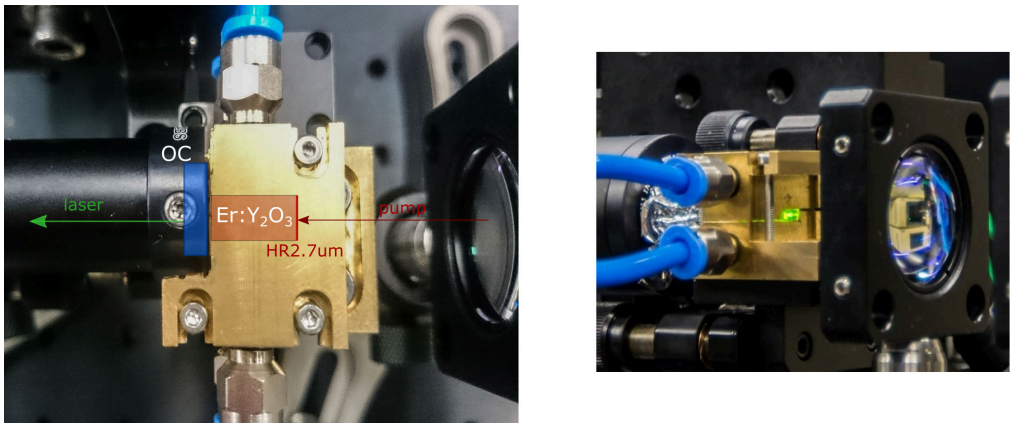

Fig. 4.15: First version of the rod Er:Y_2O_3 ceramic laser. Left: optical scheme with the output coupler mirror (OC) and high-reflection (HR) marked coating on one side of the crystal. Right – the laser with visible green-yellowish light formed by detrimental energy transfer processes in the laser medium.

The ceramic, we were able to obtain within a short time including coating, had clear aperture of 2×5 mm^2, length of 10 mm and high erbium concentration of 15%. One face was AR-coated for the 2.7 μm radiation, the other was high-reflective with high transmission for pump light. For pumping we utilized the 55-W, 976-nm diode laser. The absorption of pump light in the long sample with high concentration was very high, over 98% at non-lasing conditions. High quantum defect and occurring upconversion processes led to significant heat deposition in the pumped region and formation of a strong thermal lens. With this strong lens and a long ceramic sample, we needed to use as short cavity as possible (Fig 4.15). This effort was aided by the dichroic coating of the pumped face, but still a modification of the brass holder was necessary to fit the output coupler just about 0.5 mm from the ceramic.

The high heat generation prevented us from reaching threshold of CW operation. The laser was run instead in QCW regime with low duty cycle around 1%. The highest efficiency was achieved with an output mirror with reflectivity of 95.5%, which was lower than expected and led us to a presumption that the dichroic coatings from Sigma Koki (used also on the active-mirror disks) had lower reflection at 2.7 μm than specified. The threshold pump power with 20-Hz pulses and 1% d.c. was 260 mW and at pump power of 690 mW, output of 10.2 mW was obtained (i.e. peak output power of 1.02 W) with slope efficiency of 3%. Maximum output power of 25.4 mW was generated at repetition rate of 70 Hz with d.c. of 3.5%.

At this stage, the performance of the Er:Y_2O_3 ceramics was still far from expectations, although it was a significant improvement over the first experiment with the disk samples and it helped to mark the direction for more efficient mid-IR generation with erbium-doped yttria.

4.2.2 Efficient, high-brightness ceramic Er:Y_2O_3 laser

After the previous experiments, new ceramic sample was ordered with its parameters adjusted in order to obtain better laser performance. The Y_2O_3 ceramic still had 15 at.% Er^{3+} doping concentration, but for the sake of improved cooling, its clear aperture was reduced to 1×2 mm^2 and length of the sample was 5 mm (former 10-mm sample was clearly too long to obtain gain along the entire sample). Both its faces were polished but uncoated to rule out the possibility of defective coating layers, and thus the optical cavity had to be formed using two separate mirrors and made as short as possible to mitigate the effect of Fresnel reflections. The ceramic was

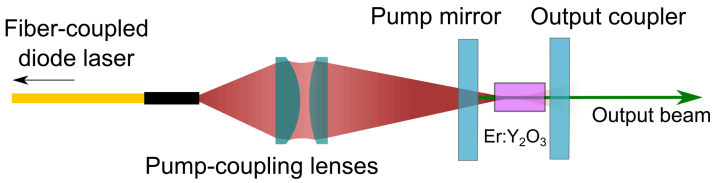

Fig. 4.16: Experimental setup of the high-brightness Er:Y_2O_3 ceramic laser.

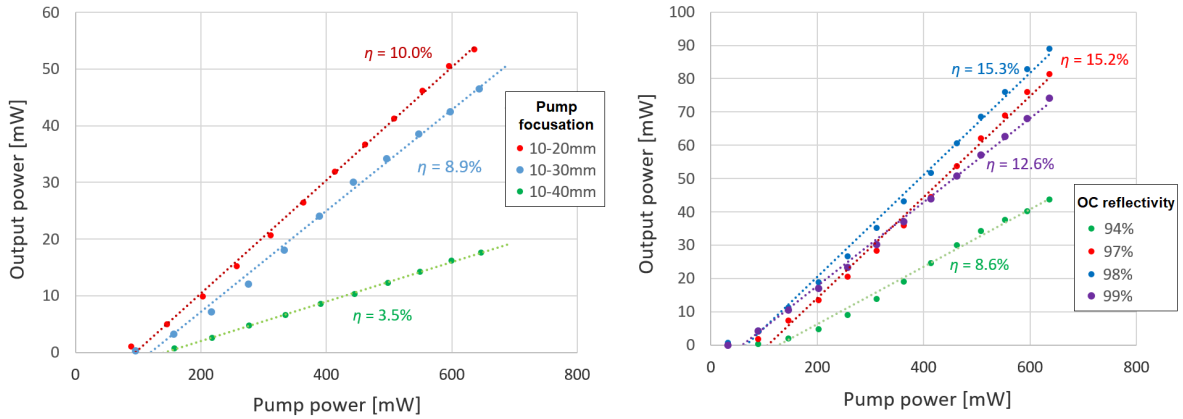

Fig. 4.17: Power characteristics of the Er:Y_2O_3 laser (a) for different configurations of the pump-delivery optics and (b) for various reflectivity of the output coupler. The laser was operated in QCW regime with 10% duty cycle. The indicated slope efficiencies are related to the incident pump power.

mounted in a brass water-cooled holder with thermal conductive paste and cooled with 16 °C water.

For pumping the laser ceramic, there were available two different diode lasers, a 55-W, broadband laser with central operating wavelength of 976 nm and spectral width (FWHM) of 5 nm (nLight e06.0550976105, same as in the previous setup) and a 9-W, narrowband VBG-stabilized laser emitting also at 976 nm with 0.4 nm bandwidth (BWT K976A02RN). Output of both pump lasers was coupled into fibers with a 105-μm core diameter and numerical aperture of 0.22.

The laser setup is shown in Fig. 4.16. Pump light was imaged on the ceramic using two plano-convex lenses with focal lengths of 10 mm and 20 mm, yielding a waist diameter of the pump beam equal to 210 μm. Also lens configurations with larger magnification factors were examined [Fig. 4.17(a)], but these resulted in lower laser efficiency. In resemblance of a microchip laser, the compact optical resonator consisted of two plane mirrors spaced by 7 mm, which was the minimum distance allowed by length of the gain medium and mounts of cavity mirrors. The pump mirror was HR-coated for 2.7 μm wavelength and had 97.9% transmittance for pump radiation. The optimum laser performance was obtained with an output-coupling mirror with 98.1% reflectivity, while other tested output couplers had reflectivity of 93.6%, 97.1%, and 98.7% [see Fig. 4.17(b)]. Stability of the cavity and diameter of its eigenmode were given by the thermal lens induced in the ceramic. The focal length of the emerged thermal lens f_{th} can be estimated as [136]

$$f_{th} = \frac{2\pi K_c\, w_p^2}{\xi P_{abs}} \left[\frac{dn}{dT} + (n-1)(1+\nu)\,\alpha_T + n^3\,\alpha_T\, C_r \right]^{-1}, \tag{4.4}$$

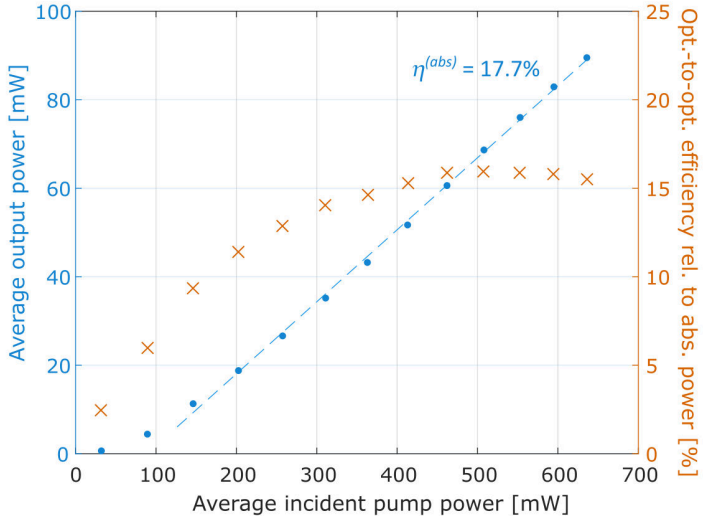

Fig. 4.18: Output power and efficiency (related to absorbed pump power) of the Er:Y_2O_3 laser in quasi-CW regime (10-Hz, 10-ms pump pulses).

where K_c is the thermal conductivity (4.6 W/(K·m) for Y_2O_3 as extrapolated from [137]), w_p is the average pump beam radius in the medium, ξ is the fractional thermal loading, which can be estimated as $1 - P_{out}/P_{abs}$ (ratio of output power P_{out} and absorbed pump power P_{abs}) [138], dn/dT stands for the thermo-optic coefficient ($\approx 8.5 \cdot 10^{-6}$ K^{-1} for Y_2O_3 [139]), $n = 1.879$ is the refractive index of Er:Y_2O_3 at 2.7 µm [140], ν is the Poisson's ratio (0.298 [141]), α_T is the thermal expansion coefficient ($\approx 6.5 \cdot 10^{-6}$ K^{-1} for Y_2O_3 [139]), and C_r indicates the photoelastic coefficient (estimate from the YAG crystal: 0.017 [23]). Focal lengths calculated for Er:Y_2O_3 using these parameters are on the order of 10 mm or even shorter.

The output power was measured with a thermopile power meter behind a Thorlabs FB2750-500 band-pass filter (center wavelength 2.75 µm and FWHM 0.5 µm). Spectral measurements in the 2.7-µm region were performed using an Oriel MS257 grating monochromator, Hamamatsu C12492-210 photodiode, and a digital oscilloscope. To facilitate the characterization in CW operation, the output beam was modulated with an optical chopper. For spectrum and beam quality measurements, the divergent output beam was collimated using a 50-mm lens. Temperature of the gain medium was monitored with a thermal camera (FLIR A35).

The laser was first operated with pulsed pumping (1-ms pulses at 10 Hz repetition rate, 1% duty cycle) to reduce heating of the gain medium and to allow higher peak pump power. Therefore, the pump source used here was the 55-W broadband diode laser, cooled down to 15 °C, shifting its central wavelength to 974 nm in order to achieve the best laser performance. The pump light absorption at low pumping level was 82% (more optimum than 98% obtained with the longer ceramic sample), but it increased to 90% at full pump power (measured at non-lasing conditions). This was caused partially by increased ESA and other detrimental energy-transfer processes in Er:Y_2O_3 during intense pumping and in part by the temperature-dependent drift of the pump laser wavelength at higher current.

The maximum average output power of 90 mW was obtained at 636 mW of incident pump power with slope efficiency of 17.7% with respect to the absorbed power (shown in Fig. 4.18). Under these conditions, the peak temperature in the ceramic rose to 37 °C. The corresponding peak power was roughly 9 W, and during relaxation oscillations at the start of each pulse it reached even several times higher intensities. With a beam of very small diameter, this led on several occasions to formation of damage spots on the pumped face of the gain medium.

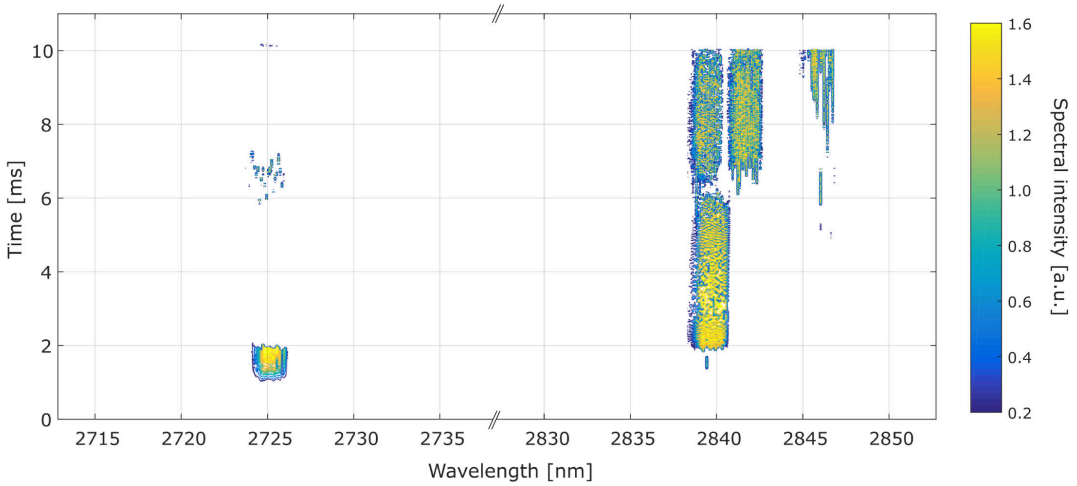

Fig. 4.19: Temporal evolution of output spectrum of the Er:Y_2O_3 laser in quasi-CW operation (10-ms pump pulses with 2-Hz repetition rate starting at time of 0 ms with power of 310 mW, i.e. peak pump power of 62 W). N.B. The horizontal axis is discontinued between 2735 and 2830 nm.

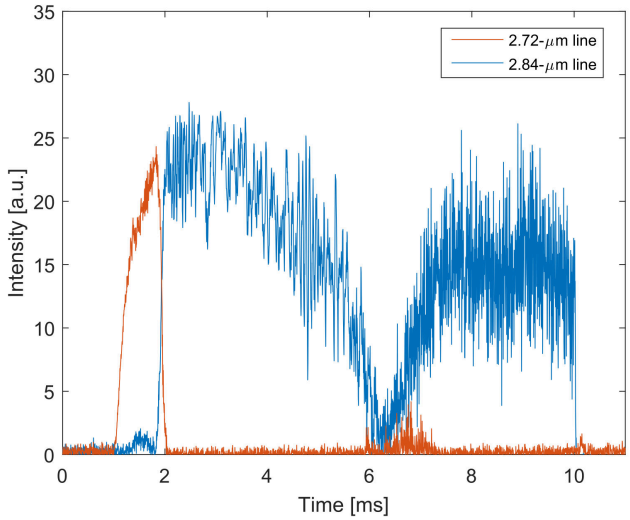

Fig. 4.20: Waveforms of the two spectral lines of the Er:Y_2O_3 laser in quasi-CW operation with 10-ms pump pulses (same data as in Fig. 4.19).

The output spectrum with 1-ms pump pulse duration was centered at wavelength of 2725 nm. However, when operating with longer, 10-ms pump pulses, the wavelength shifted to 2840 nm, 2842 nm and 2846 nm lines after 1 ms of laser emission (this is shown in Fig. 4.19 and Fig. 4.20). This phenomenon can be explained by an increased population of the $^4I_{13/2}$ manifold (with longer lifetime than $I_{11/2}$) during the pumping process that subsequently led to an increased re-absorption. The laser therefore switched to a transition less affected by re-absorption. This behavior was not observed in CW operation due to significantly lower pump intensity.

For CW operation, we switched to the 9-W wavelength-stabilized narrowband pump diode laser, because the spectral thermal drift of the non-stabilized diode did not allow for reaching the optimum wavelength in CW operation without cooling the pump laser below the dew point. 9 W output power was fully sufficient for the Er:Y_2O_3 laser and the pump absorption of narrowband 976-nm pump was similar like with the broadband 974-nm source. The laser performance of

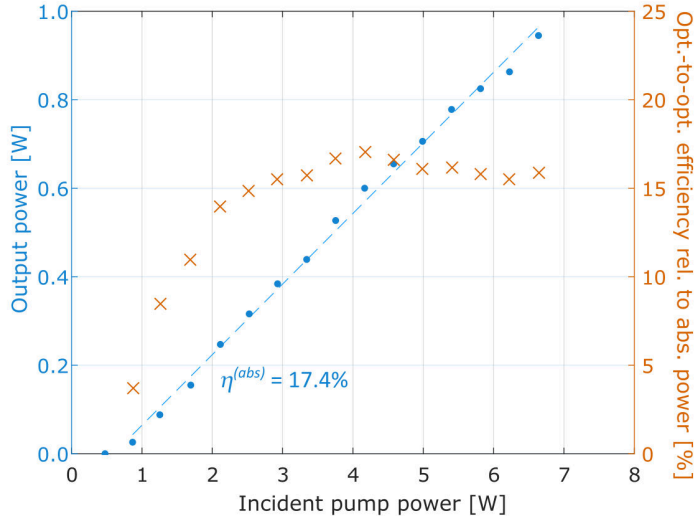

Fig. 4.21: Output power and efficiency (related to absorbed pump power) of the Er:Y_2O_3 laser in continuous-wave operation.

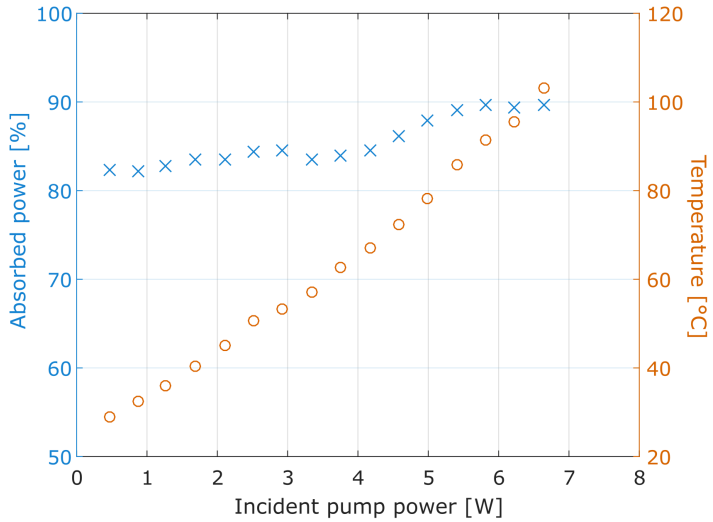

Fig. 4.22: Ratio of absorbed pump power and peak surface temperature of the Er:Y_2O_3 laser in CW regime.

Er:Y_2O_3 under continuous pumping in terms of output power and optical-to-optical efficiency vs. incident pump power is shown in Fig. 4.21. The lasing threshold was reached at incident pump power of 0.72 W and the generated output power was increased to 0.95 W at an incident pump power of 6.64 W (optical-to-optical efficiency of 14.3%) with slope efficiency of 16.0% (17.4% related to absorbed pump power). Further increase in the pump power did not lead to higher output power. Pump absorption under non-lasing conditions increased with pump power from 82% to 90% (see Fig. 4.22) similarly to the case of QCW operation. The maximum temperature of the ceramic increased up to 103 °C at 6.6 W pump power, but no damage of the gain medium was observed in CW regime despite the very high temperature gradient. This shows the exceptional mechanical properties of the Y_2O_3 host material.

The output spectrum of the laser (Fig. 4.23) showed a strong spectral line at 2725 nm and also a substantially weaker line at 2839 nm. Laser oscillations were not observed at any other wavelength in the CW regime.

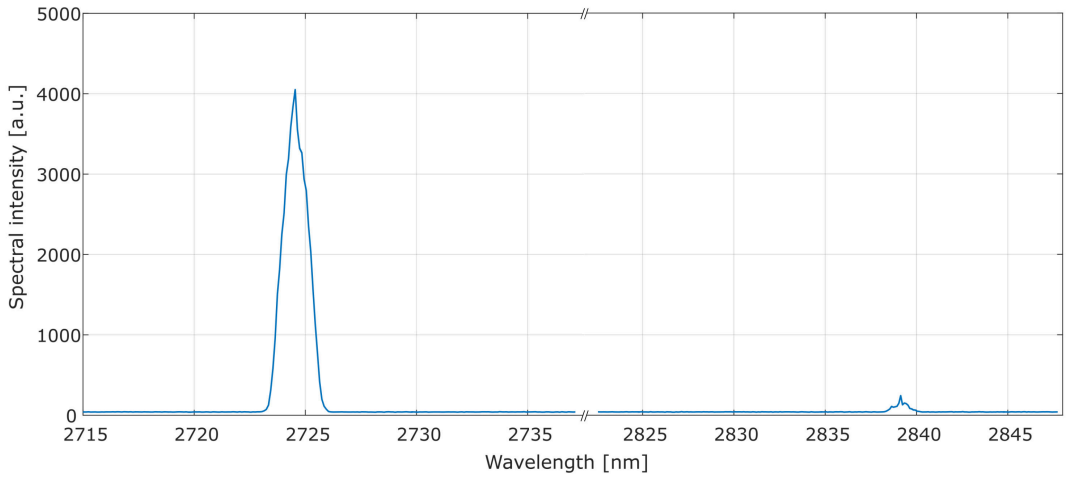

Fig. 4.23: Output spectrum of the Er:Y_2O_3 laser in CW operation with pump power of 4 W. N.B. The horizontal axis is discontinued between 2735 and 2825 nm.

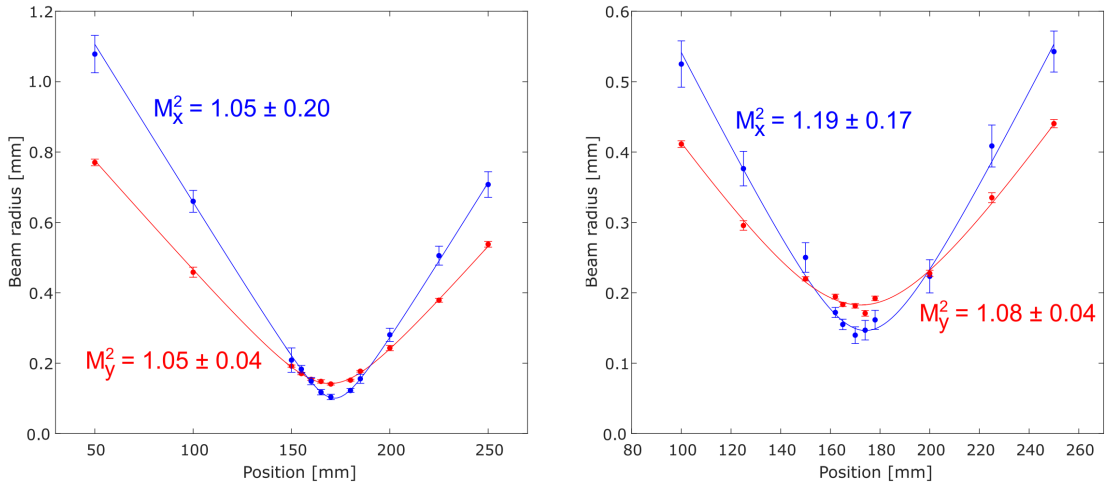

Fig. 4.24: Measurement of the M^2 parameter of the output beam in CW operation at pump power of 1.2 W (left) and 4.5 W (right). The horizontal beam radius is shown in blue, the vertical one is shown in red.

Beam quality was measured using the knife-edge technique, since we lacked a beam profiler for the mid-IR range. Measurement of the beam caustics in horizontal and vertical planes was carried out for two different pump power levels — 1.2 W and 4.5 W of incident pump power. Collimated output beam was focused with a 200-mm plano-convex lens and the M^2 parameter was determined from multiple beam width measurements near the beam waist.

The output beam was found to be almost diffraction-limited thanks to an interplay between the diameter of the pumped area and the power of the thermal lens formed in the gain medium. When calculating the thermal lens from the equation (4.4), one obtains focal length of 22 mm for pump power of 1.2 W and 5.6 mm for 4.5 W. This yields eigenmode diameter in the gain medium of ca. 190 μm at the lower pumping level and around 140 μm for high pump power (overlap factors with the 210 μm pump beam of 90% and 67%). This result indicates that beam quality close to the diffraction limit should be obtainable at 1.2 W pumping with this setup, and

at higher pump level the beam quality should deteriorate, yet the fundamental-mode operation might be maintained.

The measured M^2 parameters were $M_x^2 = 1.05 \pm 0.20$ and $M_y^2 = 1.05 \pm 0.04$ at low pump power and $M_x^2 = 1.19 \pm 0.17$ and $M_y^2 = 1.08 \pm 0.04$ at high pump power (Fig. 4.24). The slight astigmatism and better beam quality in the vertical direction can be explained by the dimensions of the ceramic sample (clear aperture of 1 mm in vertical and 2 mm in horizontal direction) and the fact that the pumped area was positioned near the bottom side of the ceramic, so the temperature profile and thermal lens were also asymmetric. The results were in accordance with our expectations.

The maximum output power of the laser was limited mainly by heat and further power scaling should be possible by choosing ceramic with lower doping concentration to better distribute the heat load along the gain medium. Also, Er:Y_2O_3 ceramic with doping concentration around 7 at.% was shown to lase more efficiently than 15 at.% ceramic [63]. Furthermore, laser efficiency at high pump intensity is decreased and heat load is increased by ESA and upconversion processes (leading e.g. to very intense fluorescence, observed throughout the experiment) and thus the pumped area should be expanded for higher pump power. Therefore, there is a significant potential for further enhancement in performance of the Er:Y_2O_3 ceramic laser.

However, further investigation of erbium-doped laser ceramics done by my collaborators, group of Professor Ryo Yasuhara, showed that a similar 11 at.% Er:Lu_2O_3 ceramic offers somewhat better laser performance [142] and it was later preferred for pulse generation. This led to development of a passively Q-switched Er:Lu_2O_3 laser operating at 2.8-μm [143].

Chapter 5

Development of high-power thin-disk laser system PERLA C

This chapter describes the design, development and performance of the PERLA C thin-disk laser system, which I have led since 2015 and it became my main research interest for the following years. PERLA C was intended as a high-repetition-rate laser system operating at 100 kHz, one of the three multi-100-W Yb:YAG thin-disk beamlines of the HiLASE thin-disk programme – together with the 1-kHz Perla B and 100-Hz Perla A.

The ultimate goal of this 100-kHz laser system was generation of optical pulses with 500 W of average power and 1-2 ps duration in high-quality beam ($M^2 < 1.5$). In 2015, when the work on the main amplifier of PERLA C started, these proposed parameters were unmatched by any reported mJ-level laser system. This held true until 2017 (reported 1-kW, dual-disk RA [101]), when also the target average power was obtained from PERLA C for the first time (although with uncompressed output). It then took a similar amount of time to hone the system's other parameters and move from the first demonstration to a reliable system with full application potential. The development of this state-of-the-art laser system was presented in a book chapter [A12], in several journal papers [A5,A10,A11], and at international conferences [A15,A18,A20,A21,A23]. The laser system was used for various applications (some are listed in Sec. 5.6) resulting in journal publications [A6,A8,A9].

Due to the complexity of the system, many of its parts were developed in collaboration with my colleagues. The 100-W regenerative amplifier and the first iteration of the fiber front end were built by Dr. Martin Smrž and I have been later performing maintenance and partial improvements, mainly for the sake of improved reliability and temporal pulse shape. The next generation of fiber front end was assembled according to my concept jointly with Jitka Černohorská (first two fiber amplifiers) and Vít Bílý (the rest). The bulk Yb:YAG preamplifier was developed by Vít Bílý under my supervision. Finally, most of the work on pulse compression (detailed study of the CVBG compressor, implementation of the grating compressor) was done in close collaboration with Denisa Štěpánková (whom I led as an advisor/supervisor). Their keen assistance and team spirit ensured that the long and sometimes also tedious developmental and honing process remained overall a gratifying experience.

The following sections introduce the overall structure of the laser system and focus further on the individual modules: the laser oscillator, fiber and free-space preamplifiers, the main thin-disk amplifier, the pulse compressor, and additional equipment for manipulation with the output beam. For better coherence of the text, main theoretical and design aspects as well as experimental details connected to specific parts of the system are included together in relevant sections.

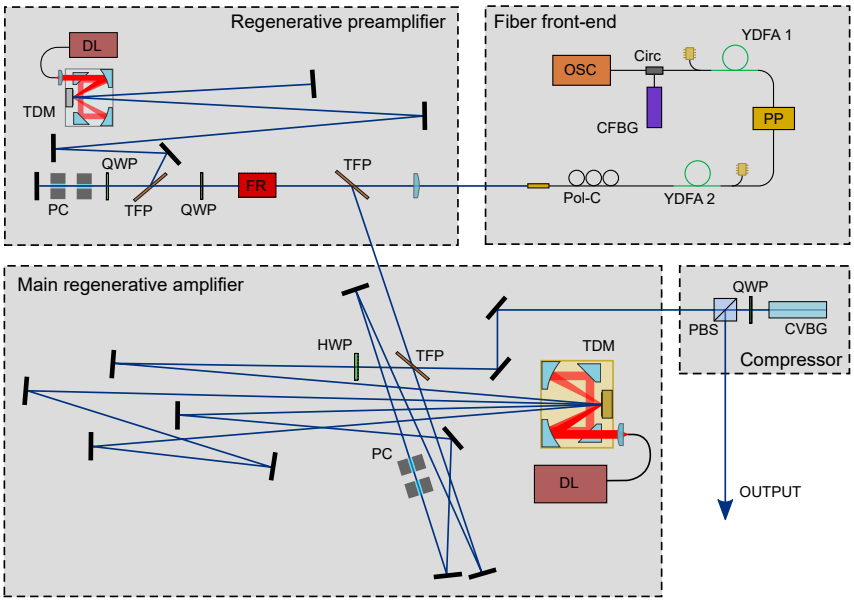

Fig. 5.1: Schematic overview of the PERLA C laser system with a regenerative preamplifier and a CVBG compressor (completion in 2017). OSC – ANDi fiber oscillator, Circ – fiber circulator, CFBG – chirped fiber Bragg grating stretcher, YDFA – ytterbium-doped fiber amplifier, PP – AOM pulse picker, Pol-C – fiber polarization controller, TFP – Thin-film polarizer, QWP/HWP – quarter-/half-wave plate, FR – Faraday rotator, PC – Pockels cell, DL – pump diode laser, PBS – polarization beam splitter.

5.1 Architecture of the laser system

The demanding target parameters required implementation of several different technological approaches. These included a mode-locked ytterbium oscillator for initial formation of picosecond laser pulses, high-peak-power fiber amplifiers, thin-disk regenerative amplification operated in fundamental mode for effective generation of half-kilowatt power with beam quality close to the diffraction limit, and use of the CPA technique (Section 2.2.1) to keep the intensity of light during the amplification process below damage threshold of the optical components.

Fig. 5.1 shows the individual sections of the laser system. It used a multi-stage MOPA (master oscillator power amplifier) scheme. A highly stable train of sub-picosecond pulses was generated in a small-scale mode-locked ytterbium-fiber oscillator. In accordance with the CPA method, duration of the pulses was immediately increased by more than two orders of magnitude in a fiber stretcher. The oscillator and stretcher were followed by a series of fiber amplifiers, forming together the fiber front end (fully described in Sec. 5.2.1). In order to not distort the pulse shape, pulses were amplified gradually in multiple stages and repetition rate was reduced for the same reason by factor of 500. With adequately proportioned main amplifier and free-space preamplifier, the quality of the temporal pulse shape was given mostly by conditions in fiber front end. Its output pulses then seeded the thin-disk regenerative preamplifier (Sec. 5.2.2) amplifying the pulses to $\approx$ 10 W power level. The following main power amplifier (Sec. 5.3) than allowed reaching 550 W of output power and CVBG compressor (5.4.2) was used to compress the laser output up to 220 W to $\approx$ 1.5 ps pulse duration in 2017.

The described system including two regenerative amplifiers was more complex than necessary, leading to lower robustness and more complicated operation and maintenance. A good illustration of its complexity is the scheme of its water-cooling management in Fig. 5.2. This

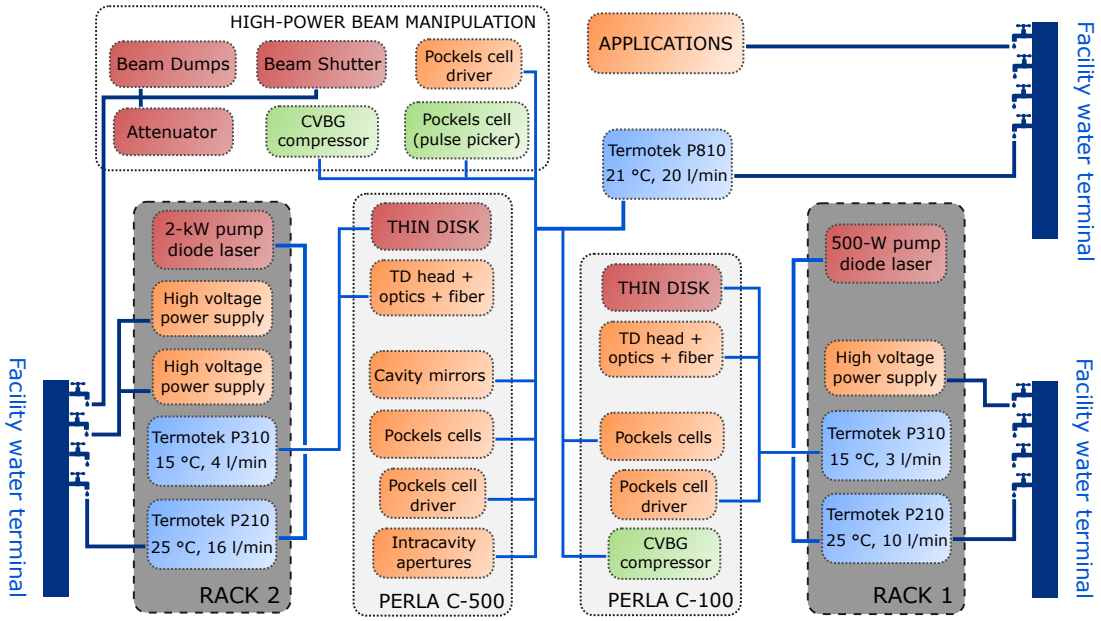

Fig. 5.2: Water-cooling diagram of the PERLA C laser system (setup with two regenerative amplifiers). After the front end upgrade, "Rack 1" and PERLA C-100 was no longer part of the system. Color code: blue – chillers (with water temperature and flow rate), red – devices with high thermal load (stable cooling is critical), orange – medium thermal load, green – low thermal load.

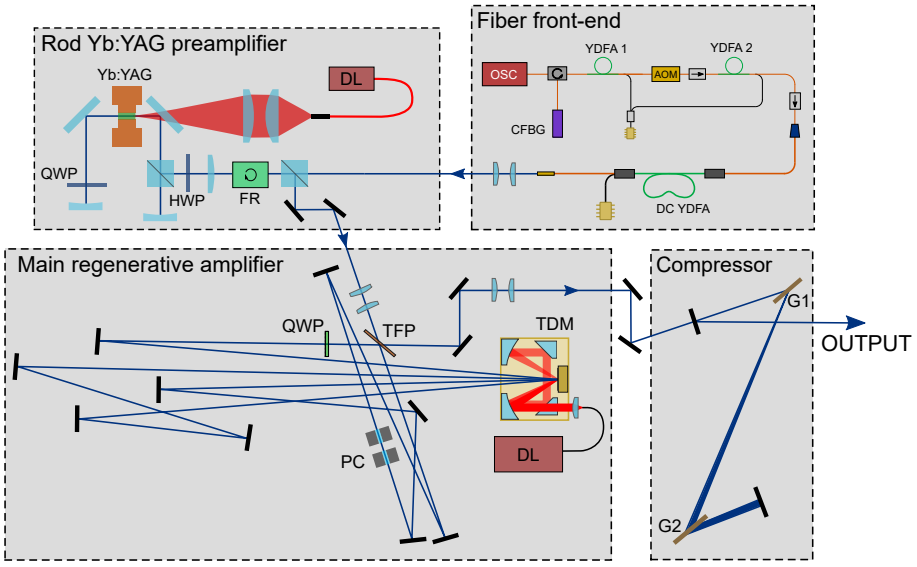

Fig. 5.3: Outline of the upgraded and simplified PERLA C system with PM-fiber front end, rod preamplifier and grating compressor (completed in 2020). OSC – Yb:KGW oscillator, CFBG – chirped fiber Bragg grating stretcher, (DC) YDFA – ytterbium-doped (double-clad) fiber amplifier, FR – Faraday rotator, QWP/HWP – quarter-/half-wave plate, TFP – Thin-film polarizer, PC – Pockels cell, DL – pump diode laser, G1, G2 – dielectric compressor gratings.

motivated a substitution of the regenerative preamplifier by a more powerful fiber front end and overall upgrade of the system (Fig 5.3).

The new fiber front end (Sec. 5.2.3) was seeded by a highly-stable commercial solid-state oscillator and utilized solely polarization-maintaining fibers. Using a double-clad fiber and 4-pass Yb:YAG rod amplifier (Sec. 5.2.4), a more robust watt-level seed was available for the main

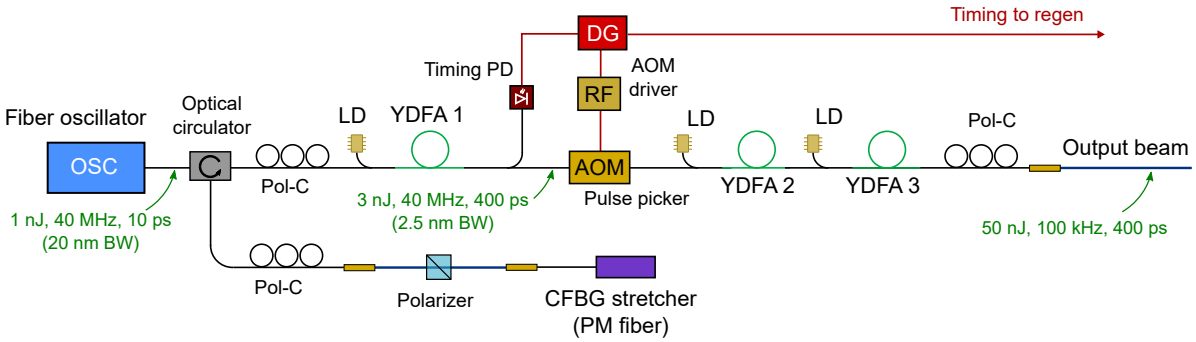

Fig. 5.4: Schematic layout of the first version of the fiber front end. The black lines represent non-PM single-mode fiber with 6-µm core diameter, red lines symbolize coaxial cables and blue lines stand for laser beam in free space. BW – bandwidth, Pol-C – fiber polarization controller, LD – pumping fiber-coupled laser diode (including a pump protector and wavelength combiner), PD – photodiode, YDFA – ytterbium-doped fiber amplifier, DG – delay generator, RF – radio-frequency driver, AOM – acousto-optic modulator, CFBG – chirped fiber Bragg grating.

amplifier. Finally, the output pulses were compressed using a dielectric-grating compressor (Sec. 5.4.3) up to 350 W of average power. This upgrade enhanced the output parameters of the system and simultaneously halved the amount of required maintenance work.

5.2 Seed pulse generation

5.2.1 Single-mode-fiber based front end

The scheme of the fiber front end is shown in Fig. 5.4. It was based on Corning HI-1060 silica optical fiber (and its equivalents), which is a non-polarization-maintaining (non-PM) fiber with 6-µm core and 125-µm cladding diameter, a standard fiber for laser amplifiers pumped around 980 nm (both YDFA and EDFA – ytterbium- and erbium-doped fiber amplifiers). For modifications of this system, communications fusion splicer Fujikura FSM-60S with corresponding accessories was used. The splicer had to be used every time when working on the front end, since fiber connectors, originally used abundantly in the system, turned out to be its bottleneck and were gradually replaced by spliced connections.

Over the time, this fiber system was seeded with various fiber oscillators. Mostly it was the laser oscillator GO pico [144] originally developed by Michał Chyła. It is a compact all-normal dispersion (ANDi) oscillator utilizing nonlinear-polarization-rotation mode-locking technique [145] in single-mode non-PM fiber. It was operated at repetition rate of 37 MHz with average output of about 40 mW (1 nJ pulse energy) with a very broad spectrum (>20 nm) centered at 1030 nm and chirped output pulses with duration around 6 ps. The prototype unit provided a reliable, continuous operation usually over several months and in case of mode-locking interruption, restarting it was a matter of few minutes.

The pulses from the oscillator were routed through a 4-port optical fiber circulator to the chirped fiber Bragg grating (CFBG) pulse stretcher Teraxion TPSR-1030T-4.5F[1841L-260-1(106.51)] with tunable dispersion coefficient of -205 ± 15 ps/nm, based on the Nufern PM980-XP polarization maintaining fiber. Details this component are described in Sec. 5.4.1. This grating worked over bandwidth of 3.3 nm centered at 1030 nm, which means that approximately 85% of the pulse energy from the oscillator was lost on this part alone, since the outer spectral components could not be back-reflected.

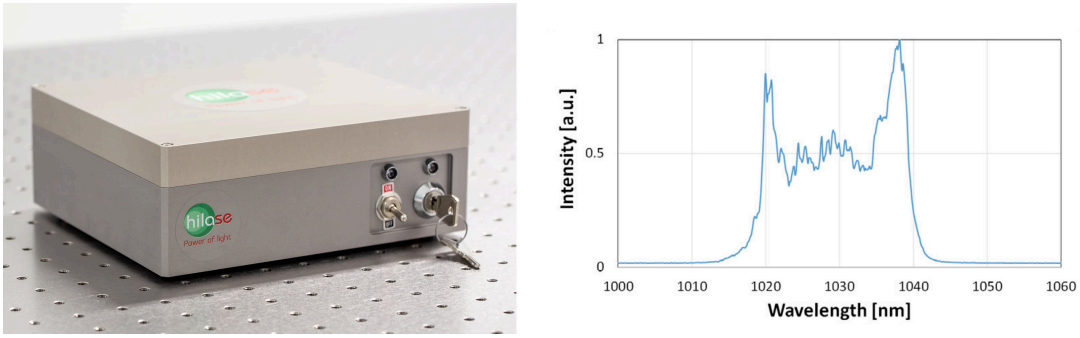

Fig. 5.5: Picosecond fiber laser oscillator GO Pico, developed by Michał Chyła at HiLASE and originally used for seeding the laser system. Typical output spectrum is shown on the right side.

Back-reflected stretched pulses were diverted by the circulator further into the front end (Port 2 $\rightarrow$ 3), while the circulator worked also as an optical isolator, since its Port 4 remained uncoupled. The front end consisted from three YDFA stages using high-concentration Yb-doped fiber (about 10-cm length each), all pumped in forward direction by a 500-mW, 976-nm single-mode laser diodes. In YDFA 1 and YDFA 3, the pump was distributed into two active-fiber segments with division ratio of 40:60. After YDFA 1 (amplifying from 50 pJ to 3 nJ), a small part of the optical pulses was sampled onto a photodiode, whose weak signal was amplified and used for timing of the entire PERLA C laser system (Fig. 5.21). This signal then indirectly controlled the 200-MHz fiber acousto-optic modulator (AOM) Gooch&Housego T-M200-0.1C2G-3-F2S, serving as a pulse picker reducing the repetition rate from 37 MHz to 100 kHz. This enabled reaching higher pulse energy in the following amplifiers, since the average power was greatly reduced. The final two amplifiers then boosted the average power from about 5 pJ to about 50 nJ.

The gain narrowing effect taking place during the amplification process resulted in the bandwidth decreasing from 3.3 nm after the stretcher to 1.5 nm at the output. Polarization of the output radiation was controlled using a 3-paddle fiber polarization controller and outcoupled using a fiber collimator. Precise setting of the polarization was necessary to minimize losses on the following Faraday isolator protecting the front end from back-reflections from the thin-disk regenerative preamplifier. The pump power in all fiber amplifiers was reduced during the optimization process in order to suppress amplified spontaneous emission ASE. The potential occurrence of ASE was identified from shift of the output spectrum to longer wavelengths (mostly in the region of 1030-1045 nm) and presence of a significant unpolarized component in the output – reduction of pump power solved this issue.

After completing the PERLA C system and compressing its output, in autocorrelation trace we later discovered significant satellite pulse of an unknown origin and with delay of $\approx$ 10 ps to the main pulse. After thorough investigation, it turned out it was caused by combination of non-PM fibers of the front end and PM fiber of the pulse stretcher. As a hot fix, the splice between the CFBG and fiber circulator was replaced with a polarization beam splitter inserted in free space between two fiber collimators, launching this way a linearly polarized light into the PM fiber. Together with polarization adjustment of light from the non-PM fiber with another 3-paddle controller, this measure effectively improved the contrast ratio of the main pulse in the AC from approximately 3:1 to more acceptable 20:1. Also, even a small bending of the fiber or a temperature change alters the polarization state of the light guided through it. Since we used polarization-dependent components both in the front end and at its output, this led to some day-to-day fluctuation in seed energy of the regenerative preamplifier and, more importantly, to a variation in output pulse duration of the whole laser system (usually on the order of hundreds of

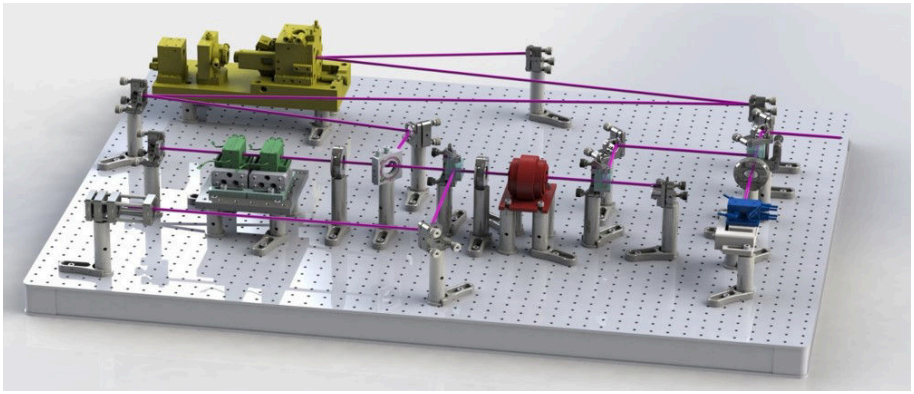

Fig. 5.6: 3D model of the 100-W thin-disk regenerative preamplifier. Main elements: in yellow – thin-disk module, green – Pockels cell, red – Faraday rotator, blue – CVBG pulse compressor.

fs). These findings, together with a need for higher pulse energy, served as a major motivation to develop a PM-fiber front end.

5.2.2 Thin-disk preamplifier PERLA C-100

The pulse energy around 50 nJ (5 mW of average power) from the first generation of the fiber front end was lower by more than three orders of magnitude than what would be the optimum seeding energy for the main amplifier (as shown in Section 5.3.4). In the case of the first generation of the front end, it was natural to use the existing 100-W thin-disk regenerative amplifier PERLA C-100 [146] for which the front end was originally developed. Its 3D model is shown in Fig. 5.6.

This thin-disk regenerative preamplifier used a thin-disk laser module TDM1.0 from Dausinger + Giesen GmbH with permissible pump power of 1 kW and pumped with a fiber-coupled diode laser Dilas M1F10L12 with maximum output power of 500 W at 969 nm wavelength (wavelength was VBG-stabilized) coupled into a 1-mm core fiber. The Yb:YAG thin disk with 7 at.% concentration had 10 mm diameter and 220 μm thickness and the diameter of pumped area on the disk was 2.7 mm.

This amplifier used a 2.7 m long linear optical cavity with 2.2 mm eigenmode diameter on the thin disk. The Pockels cell was comprised of two $8 \times 8 \times 25$ mm^3 BBO crystals (eigenmode diameter here was 1.7 mm) and it was used with a complementary quarter-wave plate and switching quarter-wave voltage of 3.85 kV for locking the seed pulse in the cavity and its final ejection.

50-nJ seed pulses with repetition rate of 100 kHz were stored in the cavity for 90 roundtrips [exponential intracavity pulse build-up measured with a photodiode behind one of the cavity mirrors is shown in Fig. 5.7(a)]. After leaving the cavity, output pulses were separated from the seed using a Faraday rotator. Maximum pulse energy of the output was 1.2 mJ (120 W of average power), which could be obtained at pump power of 430 W, i.e. with O-O efficiency of 28% [Fig. 5.7(b)]. The output could be compressed using a CVBG compressor to pulse width below 2 ps with pulse energy decreasing to 1 mJ. Compressed beam then could be used for experiments, e.g. for nonlinear frequency conversion.

For seeding the main amplifier, it was not necessary to use the full output power of this regen; the portion of output power used for seeding the ring amplifier was 1-20 W. The distance between the amplifiers was over ten meters (given by the historical development in the laboratory), and therefore, beam pointing stability was an issue. This was solved with an active

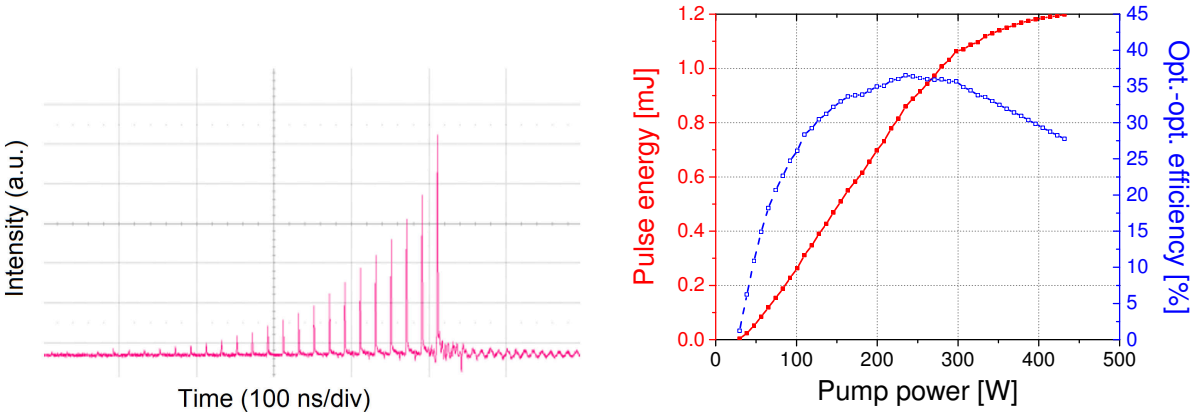

(a) (b)

Fig. 5.7: (a) waveform of the pulse build-up inside the cavity of the preamplifier; (b) output power and O-O efficiency of the regenerative preamplifier.

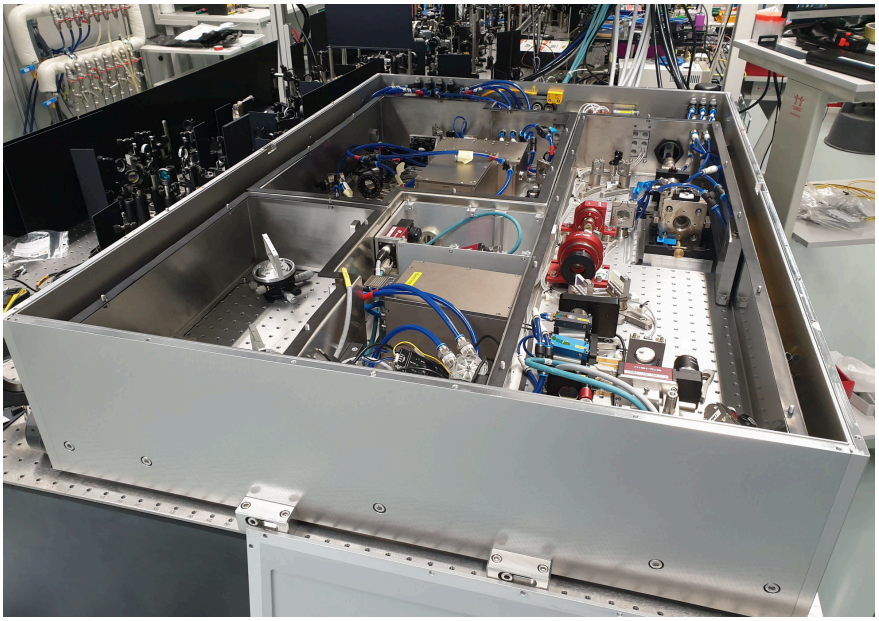

Fig. 5.8: Reconstruction of the 100-W regenerative amplifier according to the industrial standards (completion planned for June 2021).

beam pointing stabilization (Sec. 5.5). Since the regenerative preamplifier was replaced by the new version of fiber front end, it was decided that this thin-disk amplifier is going to be refurbished and upgraded according to HiLASE's experience with industrial lasers. The status of the upgrade from May 2021 is captured in Fig. 5.8.

5.2.3 Front end based on polarization maintaining fibers

Adoption of polarization maintaining fibers, together with use of a solid-state oscillator, allowed us to build a more robust seed source for the laser system, with more reproducible results on day-to-day basis. This came at the cost of increased price of fiber components and need for an advanced fusion splicer, in our case it was Fujikura FSM-100P. This front end (Fig. 5.9) was mostly based on the Nufern PM980-XP telecommunication fiber (and its equivalents) with

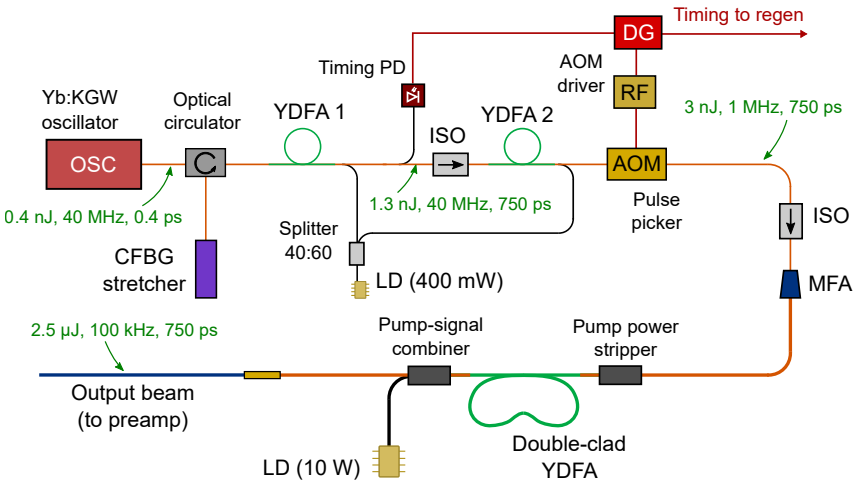

Fig. 5.9: Schematic layout of the upgraded PM-fiber front end, completed in 2019. The black lines represent non-PM fibers whereas the orange lines are PM fibers (thinner ones with 6-µm core diameter and wider ones are 10-µm-core PM double-clad fibers). Red lines symbolize coaxial cables and blue stands for laser beam in free space. CFBG – chirped fiber Bragg grating, YDFA – ytterbium-doped fiber amplifier, LD – pumping fiber-coupled laser diode (including a pump protector and wavelength combiner), PD – photodiode, DG – delay generator, RF – radio-frequency driver, AOM – acousto-optic modulator, ISO – optical isolator, MFA – mode field adapter.

5.5 µm core diameter and 125 µm cladding diameter and on ytterbium active fiber Nufern PM-YSF-LO (low doping concentration fiber). The mode field diameter (MFD) of both fibers was 6.5 um. In order to obtain higher output power, for the last amplifier we used a PM large-mode-area double-clad fiber (LMA DCF) Nufern PLMA-YDF-10/125-VIII with core diameter of 11 µm and cladding diameter of 125 µm. All fibers used the PANDA-type stress structure inducing strong birefringence in the fiber, so that an externally induced mechanical stress would not affect light propagation along the fiber, given its polarization was aligned with fast or slow axis of the fiber.

The oscillator in this case was a commercially available solid-state laser Onefive ORIGAMI-10 [147] based on quasi-soliton mode-locking of Yb:KGW gain medium (currently the manufacturer does not disclose the principle of operation, this is rather a surmise based on information from another owner) and with PM-fiber-coupled output. This compact laser operates at 40 MHz repetition rate with 14 mW of output power, pulse duration of 440 fs, and spectral bandwidth of 9 nm centered around 1028 nm. Thanks to the soliton mode-locking, both pulse shape and spectrum should be ideally of sech^2 shape [measured spectrum is in Fig. 5.10(a)].

Similarly as in the original front end, femtosecond pulses from the oscillator were sent through an optical circulator to a CFBG stretcher Teraxion TPSR-1030T-4.5F with broader bandwidth of 4.5 nm centered at 1030 nm and dispersion parameter of -190 ± 30 ps/nm (GDD of 106.5 ps^2). Thanks to wider wavelength range of the stretcher and narrower bandwidth of the oscillator, the energy loss on the stretcher was not so significant like in the former case, partially compensating lower pulse energy of the oscillator. The circulator here worked also as an optical isolator, since its Port 4 remained unused and thus it isolated the oscillator from the rest of the system (moreover, the Origami oscillator contains an isolator as well). The stretched pulse duration was estimated using Eq. (5.11) from p. 83 from the bandwidth of ≈ 4 nm and dispersion of the CFBG as 750 ps.

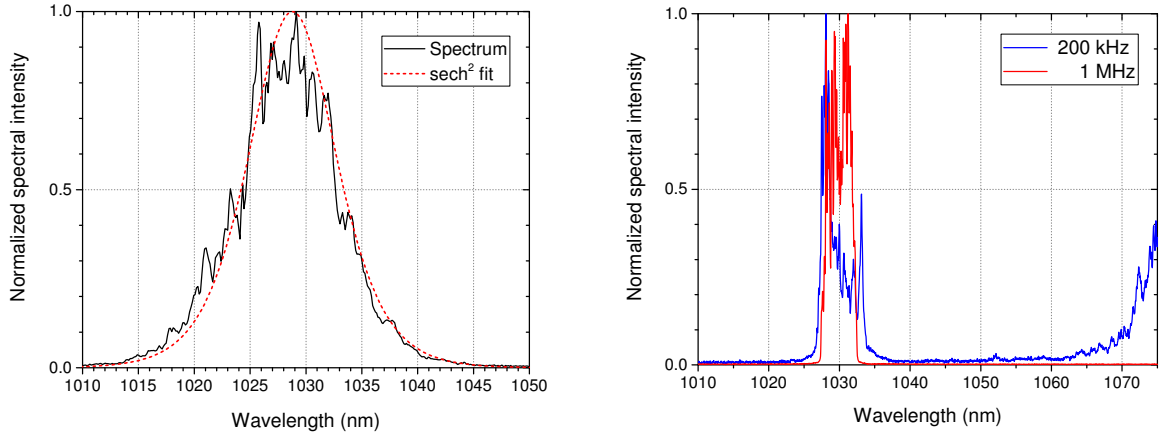

Fig. 5.10: (a) output spectrum of Onefive Origami-10 femtosecond laser oscillator; (b) evidence of occurring SRS in the DCF amplifier for higher pulse energies (4 W of pump power, 700 mW average output, pulse energy 0.7 μJ at repetition rate of 1 MHz vs. 3.5 μJ at 200 kHz). Wavelength range above 1075 nm was not accessible with the spectrometer.

Backward pump configuration (pump radiation travels in direction opposite to signal) was chosen for all fiber amplifiers, since it generally leads to weaker nonlinear effects (pulse is amplified the most at the end of the fiber). The configuration of fiber amplifier was designed using the Fiber Lasers and Amplifiers Design Toolbox for MATLAB [148] which can be used for modeling performance of ytterbium and erbium laser amplifiers and oscillators. The prediction on efficiency and output power of YDFAs were substantially more optimistic (i.e. higher) than what was achieved experimentally; however, it gave us a good notion of the ideal length of active fibers in the system.

The first two YDFAs are pumped by one SM-fiber-coupled 976-nm laser diode with its 400 mW of output power divided in 40:60 ratio between the YDFA 1 and 2. The first amplifier used 4 meters of active fiber and produced power of 50 mW (pulse energy 1.3 nJ). The output was sent through a sampler (2% fiber splitter) and optical isolator. A photodiode was used to sample the pulses and to trigger a delay generator controlling the timing of laser system. The second amplifier consisted of 220 cm of active fiber and increased the average power to 130 mW (3.3 nJ pulse energy). Afterwards, an 300-MHz acousto-optic modulator Gooch&Housego T-M300-0.1C2G decreased the pulse repetition rate to range from 100 kHz to 1 MHz. This part of the front end was again isolated from the rest and a mode field adaptor (MFA) was used for smooth transition between the 5.5 μm core regular fiber and 11 μm core LMA fiber.

The final double-clad fiber (DCF) amplifier was pumped with a 10-W, 976-nm laser diode BWT K976D02RN with 105 μm core diameter. Pump light was launched in the 4 meter long active DCF via a pump-signal combiner and the unabsorbed portion of radiation was attenuated in a power stripper. The permissible pump power was limited by temperature of splices on the active fiber, which were fixed to an aluminum breadboard using heat-conductive pads. Their temperature was maintained below 70 °C in order to preserve long term integrity of the fiber. This limited the pump power to 4.2 W, yielding average output power of 0.8 W regardless of the repetition rate. During the initial short-term testing with all amplifiers at full pump power and an additional YDFA between the AOM and MFA (similar parameters like YDFA 2), it was possible to reach output power over 4 W. The output of the DCF amplifier was spliced to a fiber collimator with 0.5-mm output beam diameter. The output beam was sent through a Faraday isolator into the bulk preamplifier (Sec. 5.2.4).

When examining the output spectrum at lower repetition rates, we detected an emergent spectral component above 1060 nm and subsequent power loss and distortion of the spectral shape in the main component centered at 1030 nm [Fig. 5.10(b)]. This was caused by the stimulated Raman scattering (SRS), which in case of silica fiber and 1030 nm pump wavelength has peak gain around 1080 nm. The threshold peak pulse power for SRS in forward direction can be estimated as [149]

$$P_{th} \approx \frac{16 A_{eff}}{g_R L_{eff}}, \tag{5.1}$$

where A_{eff} denotes the effective core area in the fiber (assumed is the core area, since MFD of the fiber has not been specified), g_R is the Raman gain coefficient (approximately $9.1 \cdot 10^{-14}$ W/m for pump at 1.03 μm [150]), and L_{eff} is effective fiber length. Threshold power for reverse scattering is higher by $\approx 25\%$ and does not need to be taken into account here. Length of passive fiber after the DCF amplifier was about 3.5 m (fiber segments from the pump-signal combiner and collimator) and in the backwards-pumped 4-m active fiber the pulse power rises more steeply than exponentially, so it can be estimated $L_{eff} \approx 4$ m. The threshold peak power is then 4.2 kW; this translates with the estimated 750 ps pulse duration into threshold pulse energy of 3.5 μJ. We detected occurence of SRS with pulse energy as low as 3 μJ and this showed to be roughly the upper pulse energy limit of this front end for seeding the laser system without disrupting the temporal profile of the compressed pulses. Most straightforward ways to raise this limit would be to shorten the passive fiber after the DCF amplifier, to use fibers with even larger mode area, or to further stretch the pulse.

In conclusion, the fiber front end can currently generate seed pulses with energy up to 2.5 μJ, average power up to 800 mW and its repetition rate can be set using the AOM to an arbitrary factor of 40 MHz (tests were performed for range from 100 kHz to 1 MHz). For further use, the DCF was usually operated with at 100-kHz repetition rate with pulse energy of 2 μJ (200 mW of average power).

5.2.4 Yb:YAG rod preamplifier

With the PM-fiber front end (Sec. 5.2.3) superseding the original front end seeding the regenerative preamplifier, the maximum accessible seed pulse energy was 2.5 μJ, i.e. 20-80 times less than what we used before. In order to reduce this energy deficit while keeping the system simple (i.e. not using two regenerative amplifiers), we developed a compact 4-pass bulk Yb:YAG amplifier.

As the gain medium we used a 10 mm long Yb:YAG rod with 3×3 mm^2 aperture, 2 at.% Yb^{3+} doping concentration, and both faces AR-coated for pump and signal wavelength (940-1030 nm). To achieve four passes of the signal through the gain medium, we used scheme with a Faraday rotator and quarter-wave plate, as illustrated in Fig. 5.11. Light from fiber-coupled 60-W, 969-nm diode laser BWT K969AA5RN was imaged through a short-pass dichroic mirror (Thorlabs DMSP1000) onto the crystal with beam waist diameter of 400 μm. The seed beam from the fiber front end was focused on the pump spot using a 300-mm lens and for the three subsequent passes, the beam was relay-imaged on the same spot with 500-mm and 300-mm concave HR mirrors.

With this setup at full pump power, it was possible to amplify the 100-kHz, 2-μJ pulses from the fiber front end to pulse energy of 48 μJ (power of 4.8 W), which was comparable to the seed energy we used with the regenerative preamplifier. The output spectrum [Fig. 5.30(b) on p. 82] had FWHM of 2.3 nm and the beam quality was close to the diffraction limit, with $M^2 \approx 1.1$.

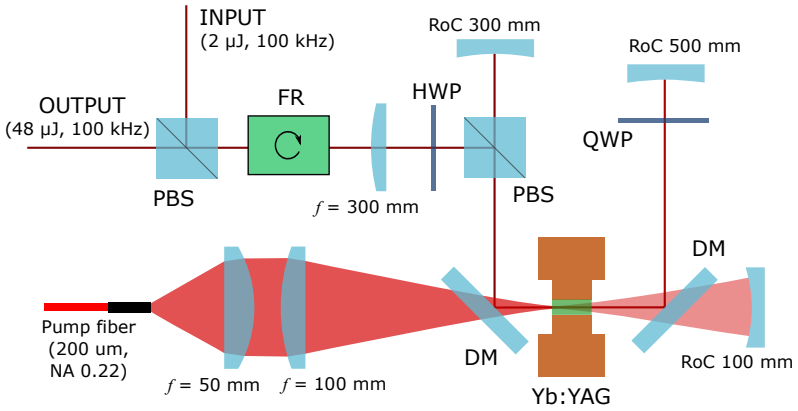

Fig. 5.11: Layout of the bulk Yb:YAG 4-pass preamplifier. PBS – polarizing beam splitter, FR – Faraday rotator, f – focal length of a plano-convex lens, HWP/QWP – half-/quarter-wave plate, RoC – radius of curvature of a concave mirror, DM – dichroic mirror (short-pass wavelength separator), Yb:YAG – gain medium in copper cooling holder.

We were also testing a single-crystal-fiber (SCF) amplifier Taranis from Fibercryst [151], which uses a 30-mm long, 1 at.% Yb:YAG crystal rod with 1 mm radius. Thanks to better heat removal from the SCF fiber (which was soldered in a massive water-cooled heatsink), it could be pumped with more powerful laser diode, in our case we used a 100-W, 940-nm module. In case of SCF, the pump with lower beam quality than the signal beam propagates in the crystal with total internal reflection. With this module, it was possible to obtain about twice higher amplification factor, with output power around 8 W (up to 80 μJ pulse energy). However, this setup was much more sensitive to misalignment due to small clear aperture of the SCF and in the end we chose the more robust solution with a bulk $3 \times 3 \times 10$ mm^3 crystal, which was maintenance-free and allowed us to concentrate more on the main amplifier.

5.3 Main regenerative amplifier

5.3.1 Thin-disk module and pump source

The core part of the main amplifier was the gain element, i.e. the thin disk with the pump chamber (thin-disk module) and pump laser source. Their operation is based on the concept described in Section 2.2.2.

The Yb:YAG thin disk used in the main amplifier [Fig. 5.12(a)] was manufactured at the Institute für Strahlwerkzeuge (IFSW) of the University of Stuttgart. The doping concentration of the disk was 7.2 at.%, its diameter 12 mm and thickness 215 um. Its front side was AR-coated for both pump and emission wavelengths, the back side was HR-coated. The disk was bonded on a synthetic-diamond heatsink of 16 mm diameter and 2 mm thickness. Diamond is the ideal heatsink material, since it has the highest thermal conductivity of all solid-state materials {1200-2250 W/(m·K) for CVD diamond [152]}. The radius of curvature of the disk, given by the concave shape of the substrate, was about 3.7 m. It was wedged by 0.1° in order to prevent the etalon effect and its edges were chamfered to mitigate potential ASE. During operation, the disk was cooled with 14 °C water (safely above the dew point year-round) at flow rate of 3.5 l/min with water pressure of 3 bar.

Sufficient absorption of pump radiation in the thin disk required multiple passes of the pump beam through the disk. To achieve this, we used the pump module G1 from IFSW Stuttgart [Fig. 5.12(c)], which is specified to handle up to 2.5 kW of pump power with wavelength of

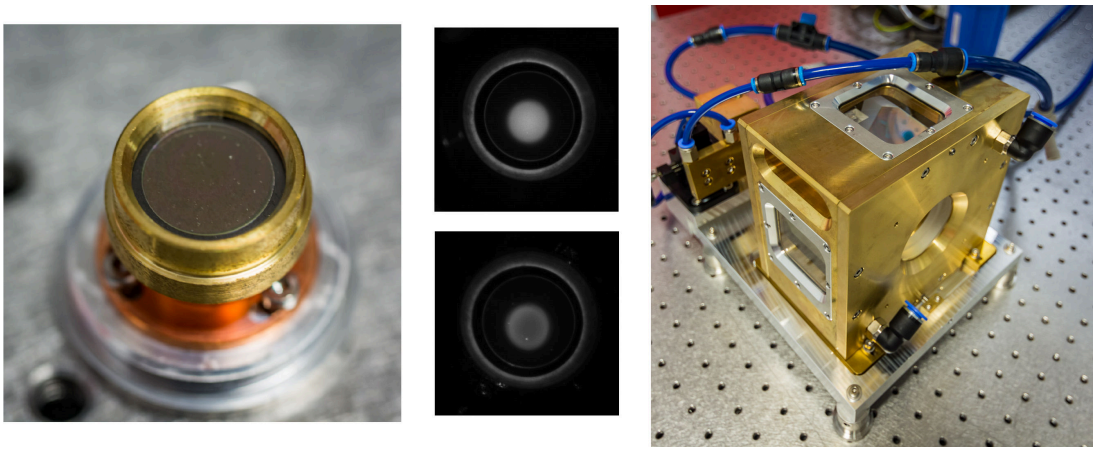

(a) (b) (c)

Fig. 5.12: (a) Yb:YAG thin disk used in the amplifier, (b) camera image of the pump spot on the thin disk at 260 W pump power wihthout (top) and during (bottom) the laser operation, (c) the G1 thin-disk module.

940-980 nm and allows for 24 passes of pump light through the disk (i.e. 12 reflections). It accepts high-power laser fiber cable with the LLK connector, whose core is imaged using a collimation lenses and parabolic mirror (75 mm focal length) onto the disk. In our case of 1-mm fiber core diameter and collimation lens with $\approx$ 15 mm focal distance, the pump spot diameter was 5.2 mm [shown in Fig. 5.12(b)].

Pump light was imaged six times on the pump spot on the disk using a system of a ring parabolic mirror and two pairs of 45° mirrors (as described in Sec. 2.2.2). After these 12 passes through the disk, unabsorbed light exited the pump chamber and was directed back with an end mirror for another 12 passes. Precise overlap of all 12 spots on the disk required careful alignment of the TD module. The most critical parameter was the distance of the disk and the parabolic mirror (its focal point should lie on the disk), which could be adjusted either by moving the disk or the entire pump chamber. Further degrees of freedom were horizontal and vertical tilt of the disk and 3-axis translation of the collimating lens relative to the fiber tip. With a good alignment, the six reflections formed a circular and uniform pump spot of super-Gaussian intensity profile and the beam of unabsorbed pump light could leave the pump chamber without being cut on the optics of the TDM. The alignment then could be finished by adjusting the retroreflecting mirror for the final 6 reflections.

In order to handle the high average power, the pump chamber and its optics, the collimation lens package, and the fiber tip were cooled with 1 l/min water flow rate using a parallel branch of the thin disk's water circuit. The highest permissible pump intensity incident on the thin disk was specified as 6 kW/cm^2, therefore the maximum allowed pump power for 5.2-mm pump spot is 1270 W.

For zero-phonon-line pumping of the disk we used a diode laser DILAS IS57.1 with VBG-stabilized wavelength of 969 nm (FWHM of 0.3 nm) and maximum output power of 2.5 kW (at 70.8 A current and 78.0 V voltage) fiber-coupled into the aforementioned LLK-HP fiber. Measured power curve of the diode laser is in Fig. 5.13(a). Although it was wavelength-stabilized, we detected certain drift in the central wavelength with changing pump current [Fig. 5.13(b)] and water temperature. This was caused by difference in the temperature of the VBG element and the effect was negligible compared to diode lasers without the VBG.

The diode laser was powered with high-power DC supply Agilent N8946A and cooled with 23 °C low-conductivity ($<$ 3 µS/cm) water at flow rate of 16 l/min. We utilized a simple

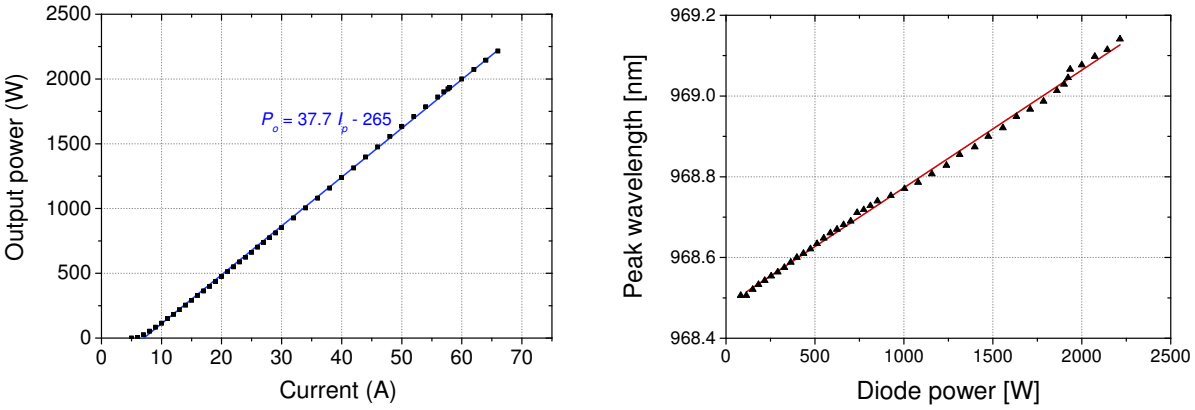

Fig. 5.13: Characteristics of the 2.5-kW, VBG-stabilized pump diode laser: (a) current vs. output power, (b) drift of the central wavelength with increasing power (water temperature 23 °C).

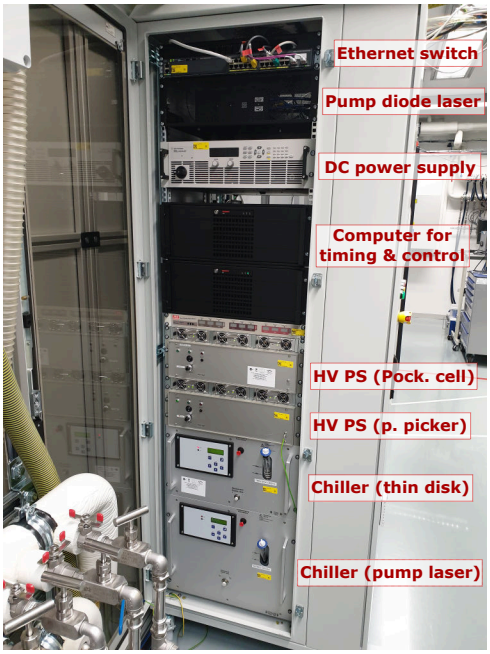

Fig. 5.14: A 19-inch rack with pump, cooling, and power-supply units for the main amplifier. HV PS – high-voltage power supply (for Pockels cell and pulse picker).

analog safety circuit based on relay logic, which continuously watched the function of chillers for the diode laser and thin disk, diode laser status, and laboratory interlock state. In case of malfunction, it immediately turned off the output of the current supply to prevent damage of the diode laser or the disk. The rack containing the auxiliary subsystems (pump, cooling, and power-supply) for the main amplifier is captured in Fig. 5.14.

A sudden failure on the input side of the pump-delivery fiber cable during 1-kW operation in 2020 necessitated a reparation of the module. As a substitute, we used a 1.8-kW diode laser DILAS IS67.4. Beside the reduced maximum output power (which was still higher than what could be used), it had identical output parameters as the original unit, but probably due to slight shift in emission wavelength of 0.4 nm over first months of operation, the pump absorption in the disk was lower and also efficiency of the amplifier decreased. Since then, the maximum

output power of the amplifier was limited to 350-380 W (with the previous module it was 550 W, as stated in Sec. 5.3.4).

5.3.2 Design of the optical resonator

Another key part of a regenerative amplifier is its optical resonator (cavity). Its design determines the spatial characteristics of the output beam and has significant influence on extraction efficiency and stability of the output. The calculations leading to the final design were done in approximation of geometrical optics using the ABCD matrix formalism described in Section 3.5. The results were compared to output of simulations performed in LASCAD software using wave optics without the paraxial approximation. Since the differences in obtained results were insignificant, the use of the approximation of geometrical optics was considered as justified.

After preliminary testing of different configurations and thorough deliberation, we decided to apply a ring cavity scheme instead of a more common standing-wave (SW) cavity. Although the work with ring cavity is somewhat more complicated, it brings several distinctive advantages [153]. Firstly, it does not require a bulky and costly Faraday rotator inserted in the high-power output beam to separate it from the seed beam. Another consequence of geometrically divided seed and output beams is a better isolation of the amplifier from the oscillator or previous amplifying stages. Also contrast of the output (pulse to ASE background) is typically several times smaller than in case of a linear cavity. However, the ring setup has two major drawbacks when used in a regenerative amplifier. Over one roundtrip, the beam passes only once through the gain medium and the electro-optic modulator. This leads to a lower net gain of the amplifier and requires use of twice higher voltage on the Pockels cell then in a SW resonator.

The appropriateness of the ring cavity scheme for multi-hundred-watt picosecond RA was confirmed in following years indirectly by other developers using ring setup in their systems as well – Trumpf Scientific switched between versions of Dira system (installed e.g. at ELI Beamlines) from SW to ring cavity, similarly Dausinger+Giesen converted their VaryDisk installed at HiLASE from linear to ring setup, and finally the dual-TDM kilowatt RA from LMU Munich also employed the ring cavity scheme [101].

It was possible to overcome the two major drawbacks of the ring setup by taking following measures. The half-wave voltage was decreased by using Pockels cell with two long crystals; nevertheless, for high-repetition-rate operation with BBO crystals it was necessary to use a particularly powerful PC driver. The lower gain per roundtrip was compensated by using cavity design with two V-passes through the disk.

Many aspects have to be taken into account to obtain a working design of optical resonator for a regenerative amplifier, and in our case it should adhere to these main constraints:

1. There are two reflections of the beam off the disk per single roundtrip,
2. eigenmode diameter on the thin disk is around 3.9 mm (75% of pump spot diameter) for both bounces and for given working point (pump power/disk temperature) and the laser operates in the fundamental transverse mode,
3. the stability parameter of the cavity lies near the middle of the stability region, so the eigenmode is less sensitive to change in curvature of the disk,
4. it includes a section with a roughly collimated beam, enough room for the Pockels cell, and beam diameter around 3.2 mm (40% of the width of BBO crystals; larger beam would get cropped significantly even when only slightly shifted from the center, smaller beam would unnecessarily increase the B-integral – Sec. 5.3.3),

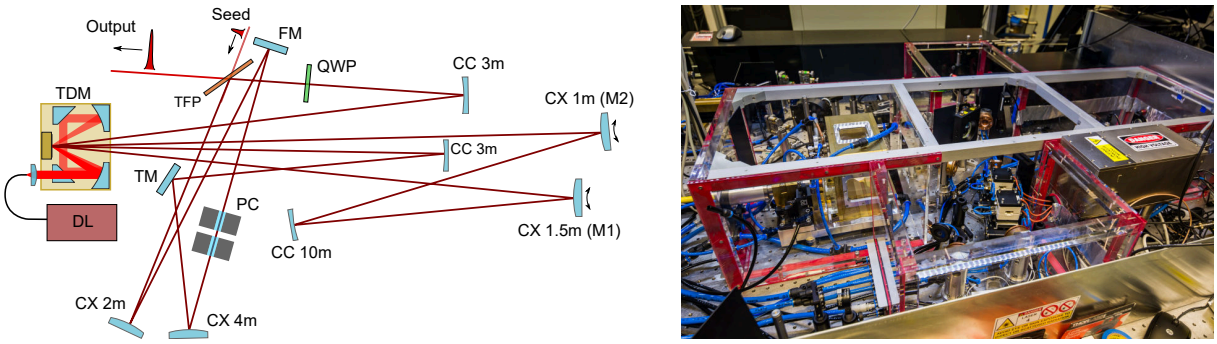

(a) (b)

Fig. 5.15: (a) optical layout of the main amplifier (TDM – thin-disk module, DL – pump diode laser, TFP – thin-film polarizer, FM – flat mirror, QWP – quarter.wave plate, CC – concave mirror, CX – convex mirror, TM – turning 45° mirror, PC – Pockels cell, M1, M2 – motorized mirrors); (b) photo of the main amplifier in its plexiglass housing.

5. the eigenmode size on the optical elements is large enough that fluence on the components is well below the damage threshold of its coatings,
6. it maintains the optimum angle of incidence (AoI) for the optical elements (close to 0° and 45° for mirrors and 55° for the TFP),
7. it is possible, given the dimensions of optomechanical components, to realize the setup on the optical table without beam clipping and the proposed ring cavity has to form a closed curve,
8. length of the cavity should be minimized, but it has to allow the electro-optical modulator to switch its state fully within the roundtrip time.

The resulting cavity addressing these eight aspects is shown in Fig. 5.15(a) and the evolution of diameter of its eigenmode is plotted in Fig. 5.16. The individual items of this list are discussed below.

The *optimum overlap of the pump spot and the eigenmode* for fundamental mode operation of a thin-disk laser is usually considered between 70% [154] and 80% [155]. For our design, we set as target a 75% overlap (3.9 mm at $1/e^2$ level) that should be accomplished for both incidences on the disk during the roundtrip. A crucial parameter for all calculations was the disk radius of curvature (RoC), all the more so that the disk figured in roundtrip matrix of the cavity twice.

During previous experiments done on other laser systems in our laboratory, we found out that the concave disks become flatter with increasing pumping [A13] due to thermal expansion of the disk and its substrate. The method consisted in measuring wavefront (using a Shack-Hartmann sensor) of a probe beam reflected from the disk. For thin disks soldered on CuW heatsinks (a cheaper alternative to diamond), 969-nm pumping with 4.5 kW/cm^2 intensity led to increase in their RoC by about 1.5 m (from 4 m), while for 940-nm pumping the increase was over 3 m. In case of diamond-bonded disk (from different supplier than in this work), this effect was substantially weaker, the RoC rose only by several hundreds of millimeters. However, data for the disks used on PERLA C were not available. The RoC of our disks, measured on an interferometer, was around 3.7 m when not pumped. For calculations I assumed disk RoC of 4 m and considered also configurations with higher disk radius. After all, the most reliable method was to try and find the optimum cavity configuration experimentally under laser operation, since every disk deformed and behaved differently under pumping and we were using the amplifier at

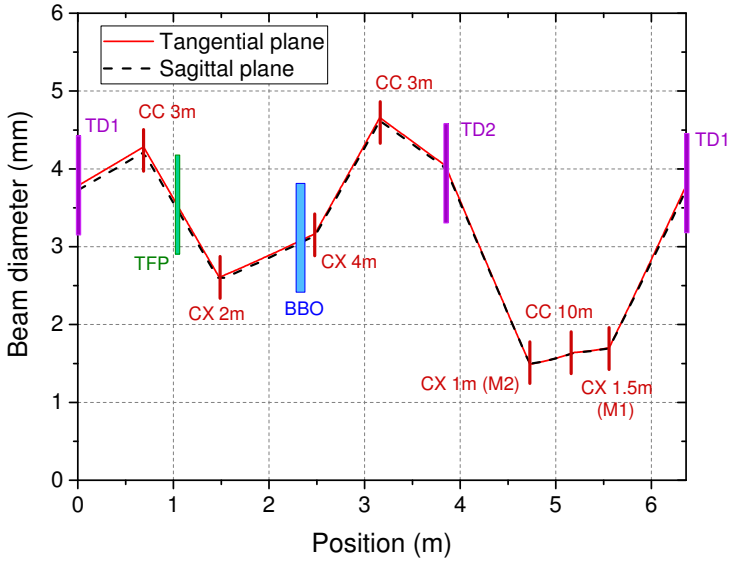

Fig. 5.16: Evolution of the eigenmode diameter along the optical resonator of the main amplifier. The assumed RoC of the thin disk is 4 m (concave shape). TD1,2 – first/second reflection from the thin disk, CC/CX xm – concave/convex mirror with RoC of x m, TFP – thin-film polatizer, BBO – two Pockels cells with BBO crystals, M1, M2 – motorized mirrors.

different working points (i.e. with various pumping power); therefore, there was no single ideal configuration of the cavity.

In order to extend the working range of the cavity in terms of RoC of the disk, the *stability parameter* of the cavity [defined by Eq. (3.1) as $\frac{A+D}{2}$ from the cavity roundtrip matrix] should be far from the stability limits, i.e. -1 and 1. For our configuration, the resonator is stable for TD RoC ranging from 2.9 m to 4.5 m, as shown in Fig. 5.17. As intended, the eigenmode diameter on the thin disk increases with rising RoC almost equally for both reflections on TD. Increasing overlap of cavity mode and pump spot helps to prevent multi-mode operation at higher pumping levels.

The only suitable *place for insertion of the two Pockels cells* was in front of the 4-m convex mirror, where the beam diameter was 3.1 mm and beam divergence about 0.4 mrad, which we considered as negligible in terms of uniformity of the phase shift. The beam size was small enough to keep the losses on crystals' apertures insignificant.

Mode diameter on optical components was kept mostly around 3-4 mm, only on the three mirrors M1, M2 and 10-m concave mirror the beam diameter was 1.5-1.7 mm. This means that at the highest considered energy output of the amplifier of 10 mJ (500 W at 50 kHz repetition rate) the pulse fluence on the mirrors should not exceed 0.6 J/cm^2. The damage threshold fluence of the mirrors used in the cavity was specified by the manufacturer (LAYERTEC) for picosecond pulses as 4-6 J/cm^2 [156], i.e. safely above the maximum fluence in the cavity, although the regime of pulse build-up in RA is more demanding on the optics than that from specifications (1-kHz pulses with 10 ps duration). As could be expected, in case of accidental generation of gigantic pulse in the amplifying chain (e.g. in case of unstable mode-locking of the laser oscillator), potential damage occurred on some of these three mirrors. Substrates of all cavity mirrors were made of ULE glass (Corning 7972, "ultra low expansion") with 25.4 mm diameter. Its low thermal expansion minimizes misalignment of the cavity caused by heat deposition on the mirrors.

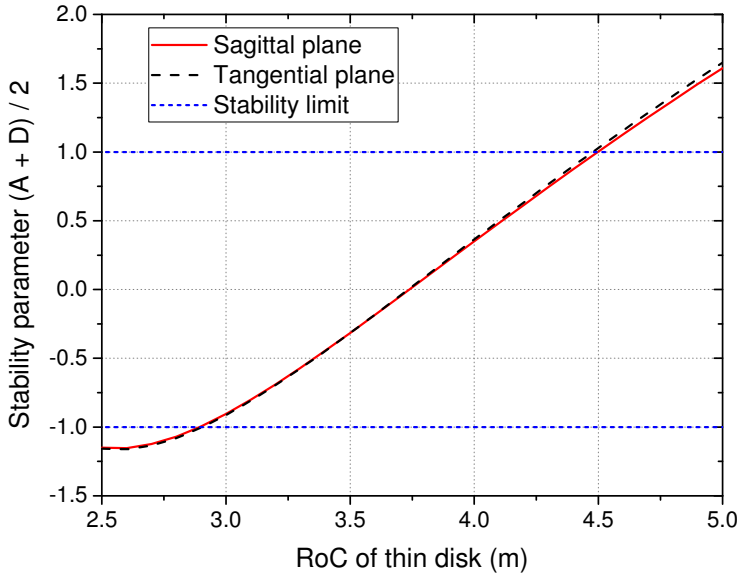

Fig. 5.17: Cavity stability diagram of the main amplifier for various curvature of the thin disk. Values of ± 1 represent limits of the stability region.

Angle of incidence (AoI) of the beam on the reflective elements is important not only for correct functioning of their coatings, but with spherical mirrors, non-normal incidence leads to change of focal distance f of the mirror. While in the normal case a mirror with RoC of R has $f = R/2$, for a mirror tilted by angle α it changes to $f_T = \frac{R}{2}\cos\alpha$ in the tangential plane and $f_S = \frac{R}{2\cos\alpha}$ in the sagittal plane. This behavior may lead to strong astigmatism of the eigenmode and it should be managed by either keeping the AoI on spherical mirrors low or to compensate the effect of convex and concave mirrors. In our case, due to space constraints of the compact setup (the 6.4 m long resonator has footprint of 1000×600 mm^2), it was not possible to fully compensate the astigmatism coming from the convex mirrors – mirror M2 and 4-meter mirror close to the Pockels cell were placed at AoI of 8°. However, the calculated ellipticity of the eigenmode was > 0.98, even though for configurations closer to the stability limit (higher TD RoC than 4 m) the beam would become more elliptical.

The *length of the resonator* was 6.36 m, thus the cavity roundtrip time was about 21 ns. We used a Pockels cell driver with specified rise and fall time of 13 ns and when setting up the timing of the amplification process, there indeed was an allowance of about 7 ns in timing without any noticable effect on laser performance.

To protect the amplifier from influence of the environment, an acrylic (PMMA) box was manufactured for the laser [Fig. 5.15(b)]. In the cavity, four circular water-cooled copper apertures were installed (inner diameter ca. 3 times the beam width) in order to suppress stray beams inside the cavity. In order to improve the long-term alignment stability, we used massive in-house-made flexure mirror mounts designed by Luděk Švandrlík (Fig. 5.19). The mirrors itself were also water-cooled, since without cooling, temperature gradients as high as 50 °C were observed between some cavity mirrors and the environment.

Over the time, we have used in the main amplifier several thin disks. Every disk had slightly different RoC and, more importantly, behaved differently under strong pumping, probably due to a slight inconsistency in the bonding process). Therefore, for each disk it was necessary to find experimentally the ideal cavity configuration. This slight modifications were done within the constraints of the acrylic box by moving the motorized mirrors M1, M2, and by changing the RoC of the mirror between them from convex 5-meter to plane mirror.

Furthermore, with different pump power on the disk, the deformation of the thin disk caused a significant shift of the beam in the cavity, emphasized by the double reflection off the disk per roundtrip. Therefore, the ring cavity had to be realigned for every working point of the laser. In order to make the operation of this laser system accessible to multiple laser operators at different conditions, a definite set of steps for cavity alignment was proposed. It made use of a well-defined alignment of the seed beam, three intracavity iris apertures, and output beam position monitoring with a beam profiler.

5.3.3 Electro-optic modulator for high-power, high-repetition rate amplifier

An electro-optic switch in the optical cavity is a typical feature of regenerative amplifiers. It allows to lock the pulse inside the cavity for amplification and eject it after a well defined number of roundtrips. The switch consists of a Pockels cell (PC), a wave plate and a polarizer. The Pockels cell uses an electro-optic crystal, where birefringence is induced by high voltage applied to its faces, and this way it can act as a voltage-controlled wave plate. In high-power amplifiers, the modulators are based exclusively on the transverse linear electro-optic effect (Pockels effect), in which case the induced phase shift between the two linear polarization states is directly proportional to intensity of electric field applied to the two sides of the crystal parallel with direction of the light beam propagation. In order to induce a quarter-wave phase shift ($\frac{\pi}{2}$ rad) in a crystal with length L and thickness d, the quarter-wave voltage, required for a RA with standing-wave cavity, is equal to

$$V_{\lambda/4} = \frac{\lambda d}{4 r_{22} n_0^3 L}, \tag{5.2}$$

where n_0 is refractive index of the nonlinear material at the laser wavelength λ and r_{22} is its electro-optic coefficient corresponding to the transverse EO effect [23]. Half-wave voltage $V_{\lambda/2}$, used in RAs with ring cavity, is obviously twice higher.

The material of choice for high-power applications is beta barium borate (β-BaB_2O_4, BBO) with high damage threshold, low absorption at 1 μm, and low tendency to piezoelectric ringing compared to other applicable nonlinear crystals such as KTP (KO_5PTi), KD*P (KD_2PO_4), RTP ($RbTiOPO_4$) or $LiNbO_3$. The main disadvantage of the BBO crystal is its low EO coefficient r_{22} of 2.2 pm/V [157, 158]. Therefore, higher voltage and longer crystals are needed than in case of the other materials. In our case of two crystals with length of 25 mm and thickness of 8 mm, the required half-wave voltage is approximately 8.2 kV.

Design and operation of the Pockels cell for the main amplifier had to be adapted to several technical aspects: presence of high optical intensity in the electro-optic crystal, rapidly alternating high voltage on its electrodes, heat generation in the crystals due to high average power, and resonant piezoelectric vibrations in the crystals. The following paragraphs deal with analysis and solutions to these aspects.

Evaluation of B-integral in the main amplifier

The Pockels-cell crystals were the only bulk media in the amplifier. Therefore, with the high optical intensity emerging during the amplification process, they represented the dominant element supporting nonlinear optical effects in the free-space part of the system. These effects often lead to undesired alteration of temporal and spatial characteristics of optical pulses and should be considered and prevented during the design process.

Tab. 5.1: Nonlinear refractive index n_2 of atmosphere and materials used in main amplifier. n_0 – refractive index, λ – reference wavelength.

Material	n_0	n_2 [$\times 10^{-20}$ m^2/W]	λ [μm]	Reference
BBO	1.656	5.6	1.06	[159, 160]
Yb:YAG	1.82	6.5	1.03	[159, 161]
Quartz (α-SiO_2)	1.54	3.1	1.05	[162]
Air	1.0003	0.0042	1.05	[159, 163]

The governing phenomenon is the Kerr effect, which manifests itself by an intensity-dependent change in refractive index due to a nonlinear polarization induced in the medium by optical intensity I. The change in refractive index from the linear (idle) value n_0 is given by formula

$$n = n_0 + n_2 I, \tag{5.3}$$

where n_2 represent the nonlinear refractive index. Reported values of n_2 for materials occurring in the amplifier are listed in Table 5.1.

Response of the medium is practically instantaneous (timescale in the order of femtoseconds) and the n_2 value is proportional to the third-order susceptibility $\chi^{(3)}$ of the medium [164]. This spatio-temporal variation in refractive index leads to distortion of the optical pulse both in time and space.

The temporal aspect leads to self-phase modulation (SPM), altering the phase of the pulse. This results in change in its chirp and spectral broadening, and in CPA systems this is generally an unwanted effect impeding an ideal compression of the amplified pulses. On the other hand, the transverse spatial dependence of refractive index leads to a lensing effect known as self-focusing. With sufficiently high optical power [exceeding the *critical power*, for Gaussian beam $P_{cr} \approx \lambda^2/(6.63 n_0 n_2)$], refractive power of the lens overcomes beam diffraction and may cause formation of local hot spots in the beam or even its collapse into a point or a filament (due to defocusing in plasma generated by enormously increased optical intensity), inevitably damaging the laser. Both these effects are described in more detail in classical textbooks such as [23, 164, 165].

In a regenerative amplifier, the influence of SPM and SF over single pass of the Pockels cell are negligible, but their effect may acummulate over many cavity roundtrips, as the pulse energy grows steadily. A useful quantitative measure of their impact is the maximum nonlinear phase shift of the pulse, referred to as the B-integral,

$$B = \frac{2\pi}{\lambda} \int_0^L n_2(z) I(z)\, \mathrm{d}z. \tag{5.4}$$

Here, λ is the lasing wavelength and L is length of the propagation path of the laser beam along the position z. For a regenerative amplifier, a generally accepted value for safe operation is $B < \pi$ [164], and in order to keep the phase distortion of laser pulses minimal, the ideal value is $B \leq 1$ [34].

In our case, the elements that contribute to the B-integral are the Pockels cell, thin disk, wave plate, and the atmosphere in the cavity. The effect of dielectric coatings on mirrors and other optics was neglected, since it is difficult to evaluate and according to analyses of this

Tab. 5.2: Relative contribution B_{el}/B of different optical elements to the total B-integral. L_{el} – propagation path in the medium per roundtrip, w_{el} – mean mode radius in the element.

Element	L_{el} [mm]	w_{el} [mm]	B_{el}/B [%]
Pockels cell (BBO)	2×25	1.55	87.3
Cavity (air)	6311	1.31*	11.5
Thin disk (Yb:YAG)	4×0.215	1.95	1.1
Quarter-wave plate (quartz)	0.03	1.8	0.02

* Calculated from harmonic mean of eigenmode area (5.6)

matter [166, 167], their contribution is comparable to that of the wave plate, i.e. insignificant. For the calculation, the Eq. (5.4) was simplified as

$$B = B_{PC} + B_{TD} + B_{WP} + B_{atm} \approx \frac{2\pi}{\lambda} \sum_{i=1}^{N} \left[P_{peak}^{(i-1)} \cdot \sum_{el} n_2^{(el)} \frac{L_{el}}{A_{el}} \right], \tag{5.5}$$

where $P_{peak}^{(i-1)}$ denotes the initial peak pulse power on the i-th roundtrip, N is the total number of roundtrips, el is an index summing over the four B-integral contributors, and $n_2^{(el)}, L_{eff}, A_{eff}$ are nonlinear refractive index, propagation path, and mode area for given optical elements. The mode area on the element is given from eigenmode radii in tangential and sagittal plane, $A_{el} = \pi w_T^{(el)} w_S^{(el)}$. The parameters are listed in Tables 5.1 and 5.2 and the eigenmode size was taken from the cavity configuration described in Sec. 5.3.2.

Substituting the integral in (5.4) with the two sums was possible with following simplifications. The beam divergence on the optical elements was neglected and for the beam path in air, a harmonic mean of eigenmode area was calculated as

$$\overline{A}_{mode} = \frac{L}{\int \frac{\mathrm{d}z}{\pi w_T(z) w_S(z)}}. \tag{5.6}$$

From these relations, it was possible to quantify the relative contribution of cavity elements to the B-integral. It shows that Pockels cell accounts for 87% of B, the atmosphere contributes with 12%, and the thin disk only with 1%. Effect of the quartz zero-order quarter-wave plate is insignificant due to its thinness.

The amplification process was then approached in a simpler way, where the pulse energy increased after each roundtrip by two reflections on the thin disk. Since the beam passes through the Pockels cell (the dominant contributor to B) before it bounces off the disk, it is adequate. The change in pulse energy between two consecutive roundtrips ($E_p^{(i)}, E_p^{(i+1)}$) was calculated using the Frantz-Nodvik equation (accounting for gain saturation)

$$E_p^{(i+1)} = E^{(sat)} \ln \left[1 + e^{g_0} \left(e^{E_p^{(i)}/E^{(sat)}} - 1 \right) \right], \tag{5.7}$$

where g_0 represents the net gain coefficient per single roundtrip and $E^{(sat)}$ is saturation energy of the active medium [can be calculated from saturation fluence (4.3) from p. 39 using $E^{sat} = F^{sat} \cdot A$, $m = 4$, and for Yb:YAG $\sigma_{em} + \sigma_{abs} = 2.3 \cdot 10^{-20}$ cm^2]. Net roundtrip gain then

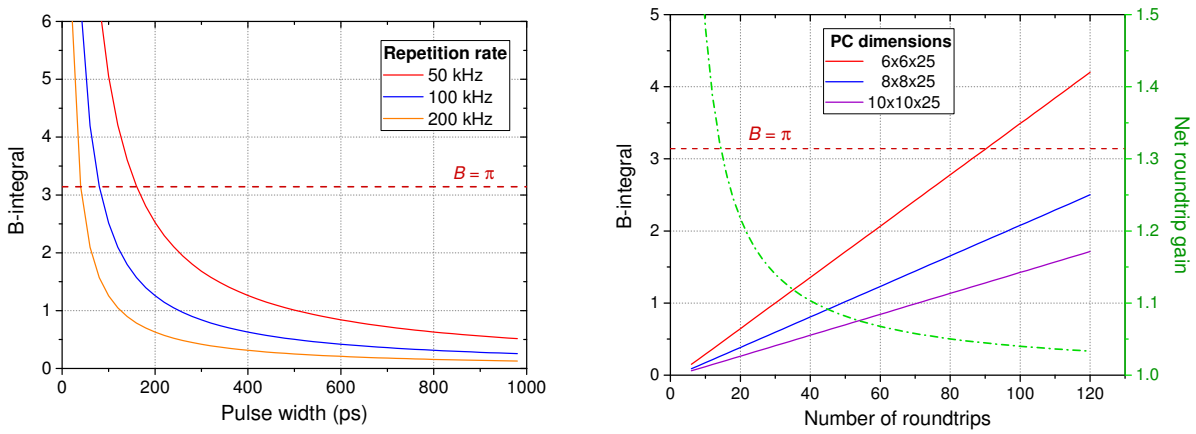

(a) (b)

Fig. 5.18: Computed values of B-integral for (a) different repetition rates and various pulse durations (output power 500 W, 70 roundtrips) and (b) different size of the two BBO crystals in PC (in mm, scaling the mode diameter) and various number of roundtrips in the cavity with pulse duration of 350 ps. The green line represents the corresponding net roundtrip gain necessary for amplifying a 10-W seed pulses to average output power of 500 W.

Tab. 5.3: Typical parameters used for calculating the B-integral.

Parameter	Symbol	Typical value
Seed power	$P^{(0)}$	10 W
Output power	$P^{(N)}$	500 W
Number of roundtrips	N	30-100
Repetition rate	f_{rep}	50 kHz
Pulse duration	τ_p	350 ps
Peak power*	$P^{(i)}_{peak}$	$P^{(i)}/(0.88\tau_p f_{rep})$

* Assuming sech^2 pulse shape

is $G_0 = e^{g_0}$. The net gain is finally computed by an iterative method from two boundary conditions, specifically $P^{(0)}$ is the seed power and $P^{(N)}$ is the target output power.

This calculation was used for validation of various parameters of the amplifier. Typical parameters are listed in Tab. 5.3. The target output power for the amplifier was 500 W and lowest considered repetition rate was 50 kHz. The parameters with the highest potential pulse energy (10 mJ) were set as the default for further analysis.

For instance, duration of the stretched pulse has an immediate effect on B (via the peak power P_{peak}). This dependence is shown in Fig. 5.18(a) and hints that the pulse duration in amplifier should be at least 200 ps. Employing the CPA technique is absolutely necessary, as for unstretched, 1-ps pulses the B-integral reaches values as high as 500. We started building the laser system with stretcher and compressor with dispersion parameter of 220 ps/nm yielding duration of the stretched pulse around 350-400 ps (see Sec. 5.4.1), which yields reasonable values of B-integral below 1.5 rad for every eventuality.

Similarly, a dependence of B on number of roundtrips was investigated [Fig. 5.18(b)]. Exact roundtrip gain was not known and even small change in G_0 leads to significant change in

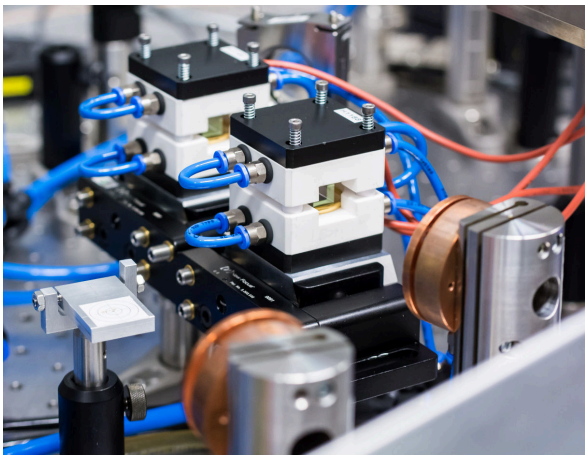

Fig. 5.19: Pockels cell together with flexure mirror mounts in the main amplifier.

predicted output power. Based on previous experience and reports in the literature, the expected roundtrip gain with 4-passes through the disk per each roundtrip was between 1.05 to 1.2 and the resulting expected number of roundtrips to achieve the desired amplification was between 20 and 100. The Fig. 5.18(b) shows also the influence of mode size in the Pockels cell, which was intended as 40% of the PC crystal thickness. All the considered BBO dimensions (6, 8 and 10 mm thickness) maintain B at an acceptable value for most configurations, but a pair of $8 \times 8 \times 25$ mm^3 crystals comes out as a good compromise in nonlinear phase shift, half-wave voltage, and crystal price, which is roughly proportional to their volume.

This method was used also for determining the net gain and real B-integral in the system from the data presented in Sec. 5.3.4 (Fig. 5.28). In summary, thanks to high repetition rate and therefore a moderate pulse energy, the nonlinear effects in the half-kilowatt amplifier can be maintained with the proposed parameters at an acceptable level.

Technical realization of the high-repetition-rate electro-optic switch

The Pockels cell needed a special crystal holder to house the BBO crystals. In the main amplifier we used a second generation of PC holders (Fig. 5.19) designed at HiLASE by Luděk Švandrlík (the first generation was used in PERLA C100 with half the voltage). The housing was made from ceramics with internal cooling water channels and a pair of circular, horizontally oriented copper electrodes with gold plating. The heat transfer through the ceramics and electrodes was sufficient to prevent overheating of the crystals due to light absorption and rapidly alternating electric current. The Pockels cell was fixed using four spring-loaded screws that allowed for tuning of the clamping force applied on the crystal.

The ceramic housing, round electrodes, and absence of any other material other than the crystal between the electrodes increased the resistance of the holder to sparking between electrodes. The holder was tested to withstand voltage up to 13 kV, which is approximately the breakdown voltage of air for 8-mm gap and moderate relative humidity [168]. Still, sparking between the electrodes was observed, when an impurity (pencil mark) was present on a side face of the BBO crystal.

For driving the Pockels cell, we used a high-power switch dpp5c6 from Bergmann Messgeräte Entwickelung KG (BME) with HV power supply PCD12g2. Its maximum operating voltage is 5 kV and maximum repetition rate at full voltage is 550 kHz, while 1-MHz operation is possible at reduced repetition rate of 550 kHz with typical rise and fall time of 13 ns with 6 pF load capacitance. It uses a double push-pull scheme depicted in Fig. 5.20(a). In this case,

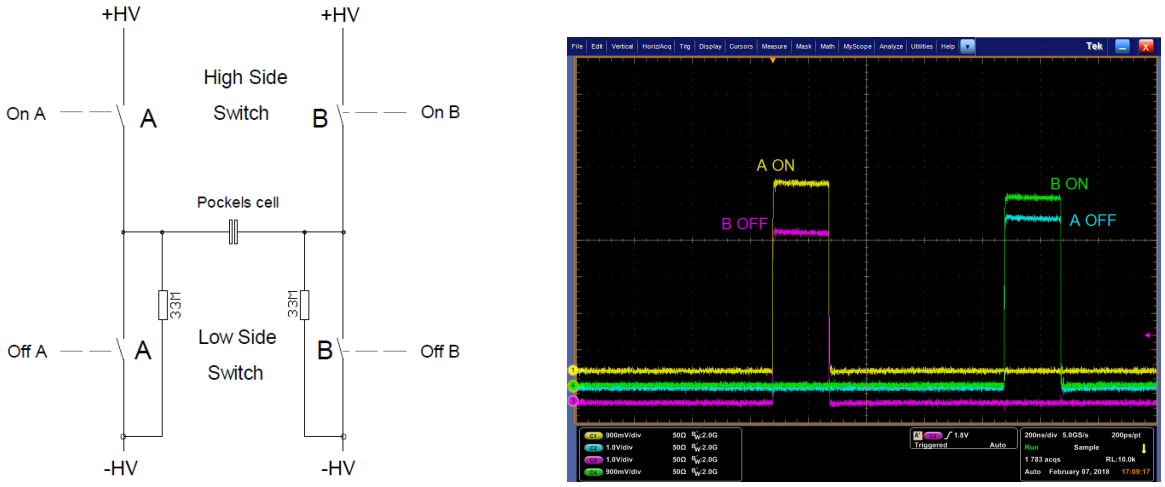

(a) (b)

Fig. 5.20: (a) simplified diagram of the high-voltage switches in the double push-pull Pockels cell driver from and (b) waveform of TTL pulses controlling corresponding switches of the Pockels cell driver (timescale 200 ns/div).

the difference in electric potential on PC electrodes is alternating between ± 5 kV ("bipolar" regime). Therefore, it is possible to reach the quarter-wave voltage of 4.1 V, given by (5.2), and switch its polarity to alternate between the "on" and "off" state of the PC. This is an alternative way of operation of a ring-cavity RA to the classical method of switching between zero and half-wave voltage ("unipolar" regime), and half-wave plate in the cavity is in our case substituted by a quarter-wave plate. Also one has to bear in mind that the polarization state of light between the PC and wave plate is circular. The advantages of this approach are lower risk of electrical discharge between the electrodes and lower heat load on the driver allowing higher repetition rate.

The Pockels cell driver was triggered by four 5-V TTL signals shown in Fig. 5.20(b). The A and B high voltage switches were kept in opposite states by sending them the "on" and "off" signals simultaneously. This was facilitated by a so-called splitter box, which converted two signals from the central delay generator, "ON" and "OFF" (coinciding with the two states of the amplifier), to these four channels according to a programmable logic set to this mode of operation. Its other function was to keep the switches of the driver in a well-defined state, preventing them from short-circuiting in case the trigger was lost for more than several milliseconds.

The entire control scheme of PERLA C laser system is illustrated in Fig. 5.21. The splitter box for the Pockels cell of the main amplifier was controlled with a 6-channel delay generator from BME, which was triggered by an amplified signal from a photodiode in the fiber front-end. The same delay generator and similar Pockels cell driver was controlling the Pockels cell in the regenerative preamplifier (Sec. 5.2.2). The acousto-optic modulator in the fiber front end (Sec. 5.2.1), controlled by a single analog channel, was then controlled by a separate delay generator Highland Technology T560, since the BME delay card did not allow to send pulses as short as 5 ns required by AOM to pick a single oscillator pulse (37 MHz repetition rate). Another delay generator (Stanford DG645) was then required to control Pockels cell in the pulse picker and to send timing signal to potential applications (e.g. to a scanner). In general, the implemented timing system allowed for a reliable control of the laser system with sub-nanosecond temporal resolution.

After introducing the PM-fiber front end and bulk preamplifier (Sec. 5.2.3 and 5.2.4), it was possible to simplify the timing system. The AOM in front end was also controlled with

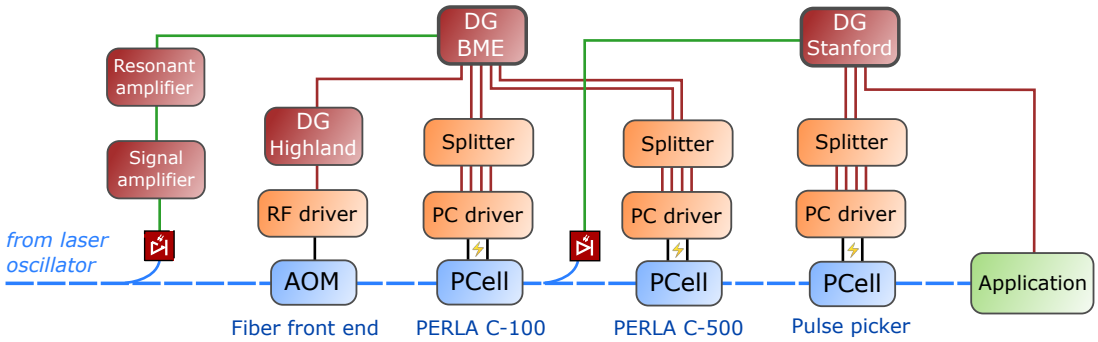

Fig. 5.21: Diagram of the control timing system of acousto- and electro-optic modulators in the PERLA C laser system. Color code of the lines: blue – path of the optical pulses, green – analog electric signal, red – 5-V TTL signals, black – RF (AOM) or high-voltage (PC) driving signal. DG – delay generator, RF – radio-frequency, AOM – acousto-optic modulator, PC(ell) – Pockels cell.

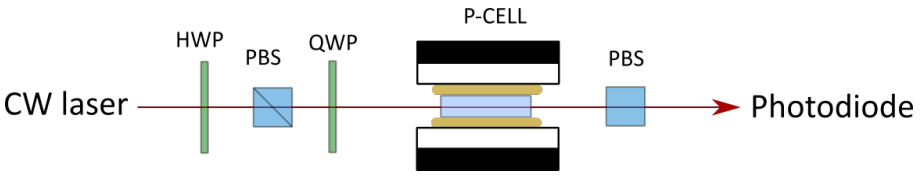

Fig. 5.22: Measurement setup for detection of resonant frequencies of BBO crystals. HWP, QWP – half- and quarter-wave plate, PBS – polarization beam splitter, P-CELL – Pockels cell.

a photodiode-triggered Highland T564 delay generator. This than triggered a Stanford DG645 delay generator managing the BME Pockels cell drivers for the main amplifier and pulse picker.

Mitigation of piezoelectric ringing

When high-voltage pulses are applied on nonlinear crystals like BBO, acoustic waves are generated in the material due to the piezoelectric effect. Birefringence of the crystal induced by the Pockels effect is then altered via elasto-optic effect and for certain driving frequencies, associated with dimensions of the crystal and acoustic wave velocity in the material, a strong resonant acoustic wave can be formed and last long after the driving electric pulse was applied. This *piezoelectric ringing* significantly deteriorates the performance of such Pockels cell and may even break the nonlinear crystal.

While BBO PCs are generally resonance-free for switching rates up to several kilohertz [169], in frequency region of tens and hundreds of kHz we detected a vast amount of resonant frequencies of various magnitude. Although the phenomenon was noticed early after first employments of Pockels cells [170], reports on laser systems with BBO PCs have been usually limited to mentioning its presence at certain repetition rates [171, 172]. Since we planned to use the laser system in a wide range of repetition rates (roughly from 50 to 200 kHz) and encountered piezoelectric ringing on multiple repetition rates, a detailed investigation of this phenomenon was performed. Almost two years (and several crystals in our PCs) later, in 2019, Sinkevicius and Baskys published an analysis using a similar method with affirmative conclusions [173].

Before this investigation of piezoelectric ringing was carried out, several BBO crystals were damaged in the Pockels cell. In some instances, only a decreased contrast of the PC and beam pointing instability of the laser was observed, in some cases this was even accompanied with an audible whistling noise. In another instance, the crystal gradually traveled between electrodes

of the PC holder (Fig. 5.19) and when side of the crystal was hit by the laser beam, the crystal broke (this was later solved by inserting a ceramic adapter holding the crystal horizontally in place). Furthermore, when the repetition rate coincided with a strong resonance of the crystal, it could lead to immediate cracking of the crystal caused solely by the stress and strain induced by the acoustic wave. An additional difficulty was that the resonant frequencies shifted as the crystals were heated during laser operation and onset of the ringing was hard to predict.

The Pockels cell was characterized with $8 \times 8 \times 25$ mm^3 and $10 \times 10 \times 25$ mm^3 z-cut crystals produced by Caston Inc. (Fuzhou, China). The PC driver was of the same model as the one used in the main amplifier (BME Bergmann, 5-kV, bipolar, up to 1 MHz). The crystals were mounted in our inhouse-developed holders – both the type used in the main amplifier (Fig. 5.19) and the one used in regenerative preamplifier (Fig. 5.6). The linearly polarized probe beam for the measuring setup (Fig. 5.22) was obtained using a CW ytterbium fiber laser (1030 nm), a half-wave plate and cube polarization beamsplitter (PBS). A quarter wave plate was then inserted to convert it to a circularly polarized beam, which propagated through the cell. Finally, an analyzing PBS (perpendicularly oriented to the first one) and a photodiode Thorlabs DET10A/M completed the setup. A circularly polarized beam was used for probing in order to maximize sensitivity of the resonance detection.

The Pockels cell was tested in frequency range from 10 kHz to 1.25 MHz with step of 10 Hz (below 100 kHz) and 100 Hz (above 100 kHz). Voltage applied on the crystal alternated between ± 0.25 kV (bipolar operation), which was low enough to prevent damage of the crystal even at the principal resonance (226 kHz for the 8-mm crystal). The "on-time" of the Pockels cell was set to 1.2 µs (similar to the regime of operation of the main amplifier used at that time) and for high repetition rates over 250 kHz it was gradually reduced to 600 and 300 ns. Typical waveforms from a 2-GHz oscilloscope obtained at different resonant frequencies are in Fig. 5.23. While figures (a) and (e) show weaker resonances without a clear relation to the dimensions of crystal, waveforms (b)-(d) show subharmonic frequencies of the dominant resonance (f) at 226 kHz (corresponding to crystal thickness and velocity of longitudinal acoustic wave of about 3500 m/s [174]).

In total, 260 different resonant frequencies were identified for the $8 \times 8 \times 25$ mm^3 crystal [shown in Fig. 5.24, (a) shows the entire range in logarithmic scale, (b) shows the detail of frequency range relevant to our amplifier]. The most important information were the frequency values and due to the sheer number of detected resonances, magnitude of the resonances was classified according to the amplitude of measured signal without a precise manual measurement.

The strongest detected resonant frequencies can be listed in kHz as follows: 75.4, 113, 162, 189, 212, 217, 222, 226, 270, 290, 378, 425, 435, 671, and 870 (values in identical colors represent mutually associated (sub)harmonic frequencies). Origin of resonances other than the "blue" ones is not clear at the moment.

The measurement with larger, 10-mm crystal showed good correspondence between crystals of different thickness, with the frequency scaling inversely proportional to the dimensions. The dominant resonance of the larger crystal was determined as 180.75 kHz (exactly 80% of 226 kHz). This rule also holds when considering the measured data for $3 \times 3 \times 25$ mm^3 and $4 \times 4 \times 25$ mm^3 crystals from the report [173] (which also indicates a modest influence of crystal length). Characterization of the Pockels cell with the older type of holder showed some differences in the weaker resonances and slight overall shift in frequency, caused probably by a different way of crystal mounting.

Further tests also indicated that ringing frequencies slightly shift with increasing driving voltage [Fig. 5.25(a)] and with changing clamping force applied on the crystal by the holder [Fig. 5.25(b)]. Amplitude of modulation of the refractive index is according to the data linearly

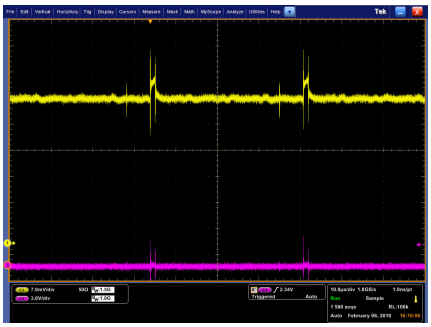

(a) 27.1 kHz

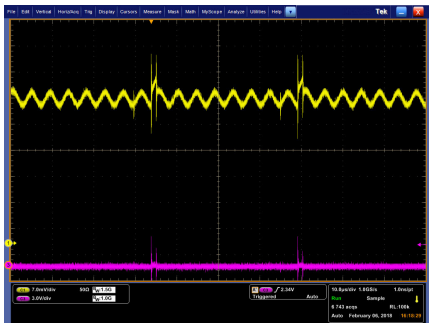

(b) 28.3 kHz

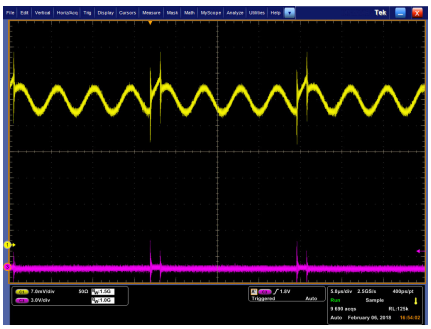

(c) 56.6 kHz

(d) 113 kHz

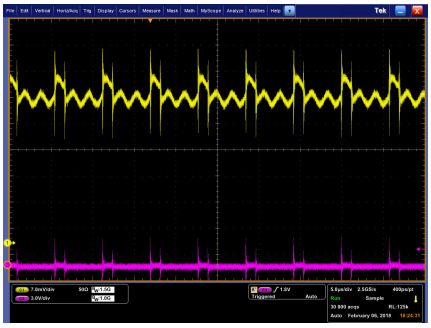

(e) 174 kHz

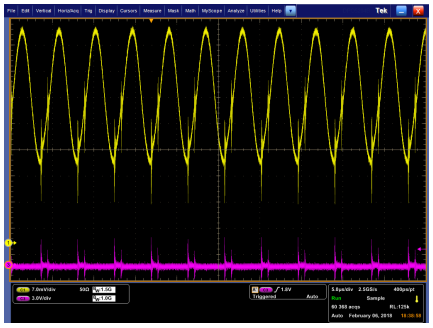

(f) 226 kHz

Fig. 5.23: Oscilloscope waveforms from measurement of piezoelectric resonances at different driving frequency of the Pockels cell with $8 \times 8 \times 25$ mm^3 BBO crystal. Amplitude of voltage applied on the crystal was 0.25 kV. Yellow channel – Signal from photodiode, purple channel – trigger signal from an active probe sensing the switching events.

dependent on the driving voltage and there was not found any significant difference between Pockels cell working in bipolar regime and unipolar regime with double voltage. Finally, firmly tightened crystal holder helps significantly with reduction of the piezoelectric ringing and reduces risk of damaging the crystal (provided it is tightened carefully and uniformly).

The outcome of this study led to solving the issues with operating the Pockels cell at various repetition rates, particularly by avoiding problematic repetition rates and properly mounting the crystals. Also, the gained experience helped the laser operators to identify laser instability caused by weak piezoelectric ringing much sooner than before. Given the long list of resonant frequencies and their dependency on multiple aspects, these could not have been always avoided and weak ringing was often suppressed just by changing the clamping force applied on the crystal.

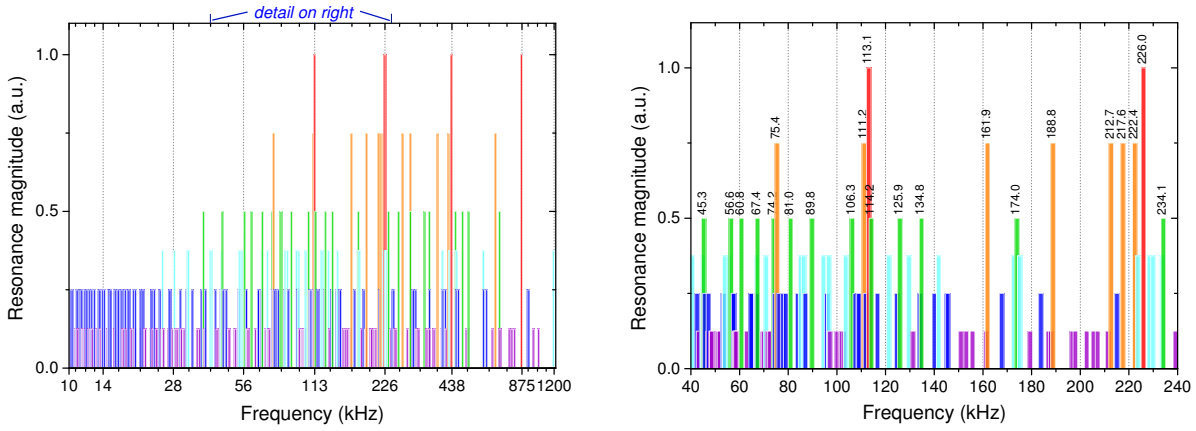

(a) (b)

Fig. 5.24: Detected resonant frequencies in an $8 \times 8 \times 25$ mm^3 BBO crystal (a) in full range from 10 kHz to 1.2 MHz (logarithmic scale) and (b) in range from 40 to 240 kHz (linear scale).

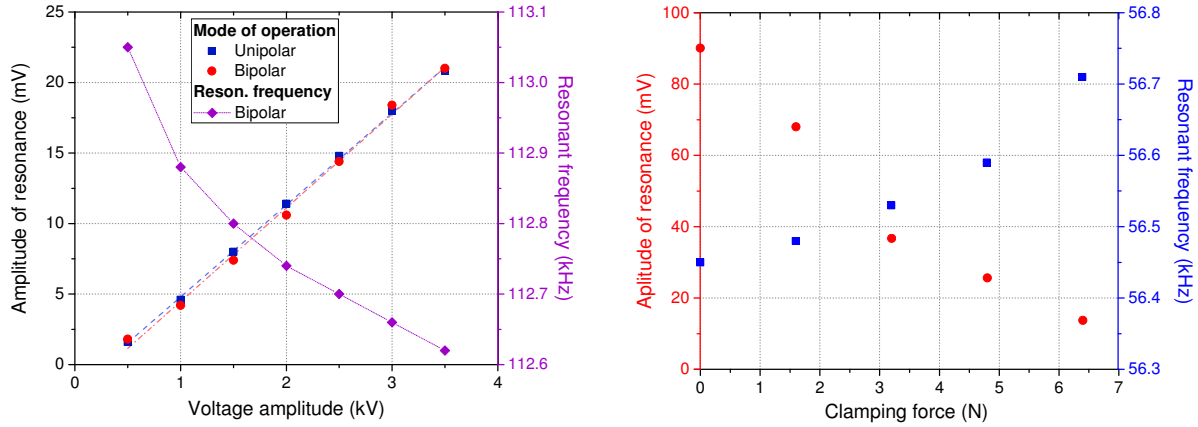

(a) (b)

Fig. 5.25: (a) resonant amplitude and frequency vs. driving voltage difference for unipolar and bipolar mode, (b) dependence of resonant amplitude and frequency on clamping force applied on the crystal (0 N means a loose holder).

5.3.4 Performance of the ring amplifier

The design of the optical resonator was first validated in continuous-wave mode of operation. In that case, the polarizer and a half-wave plate worked as an output coupler with variable transmittance. A ring cavity in CW (unseeded) operation produces two outputs corresponding to beam propagating in a clockwise and a counter-clockwise direction. The total output power was determined as a sum of power in each beam and while this sum remained stable, the power ratio of the beams fluctuated between roughly between 40% and 60%. The maximum obtained output power was 565 W at 1215 W of pump power [Fig. 5.26(a)]. The laser operated in the fundamental transverse mode with optical-to-optical efficiency of 46.6% and slope efficiency of 52.1%.

To make sure we use the thin disk within its safe operational limits, we used a thermal camera FLIR A35 to measure temperature of the disk at different pump power levels [Fig. 5.26(b)]. To adhere to the manufacturer's recommendation on maximum incident pump intensity of 6 kW/cm^2 and to keep the disk temperature below 120 °C, we further limited the applied pump

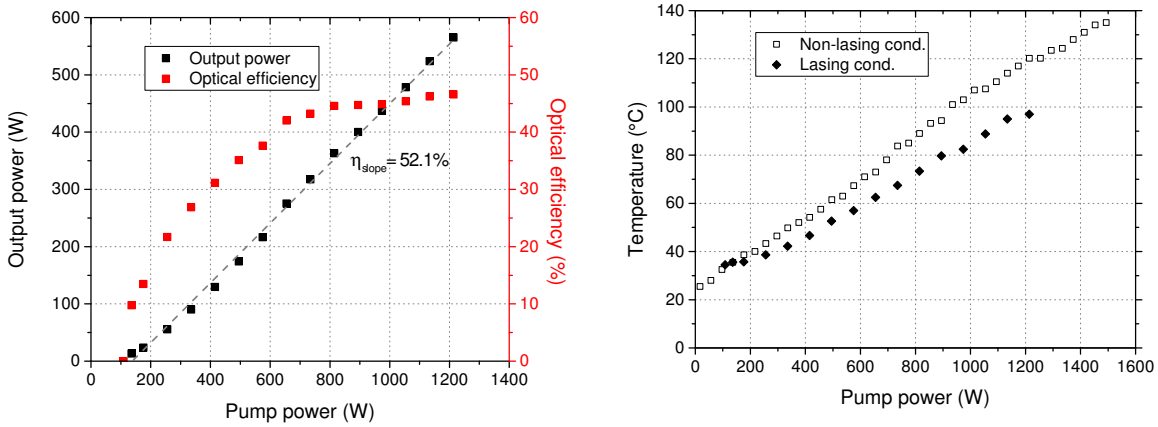

Fig. 5.26: (a) Output power (sum of two output beams) and O-O efficiency of the main amplifier in CW operation(η_{slope} – slope efficiency), (b) temperature in the center of the thin disk (with and without lasing).

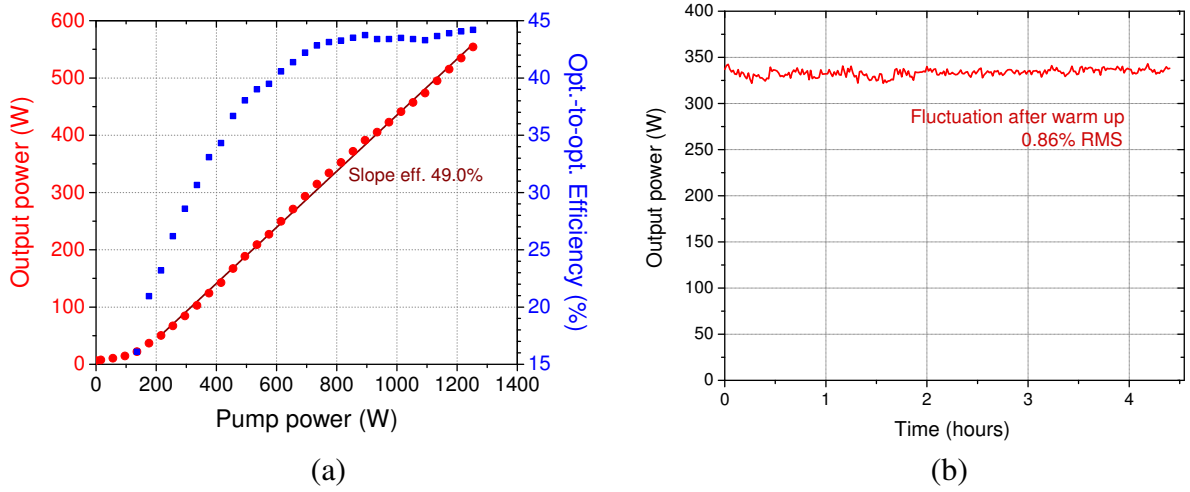

Fig. 5.27: Performance of the main amplifier at repetition rate of 100 kHz. (a) output power and O-O efficiency, (b) output power log over more than 4 hours of operation (RMS power fluctuation of 1.2%), after 2 hours the laser was realigned and used for an experiment with 0.86% RMS power stability.

power to 1250 W. When the laser was operated in CW, the disk temperature at full power decreased to 97 °C due to lower thermal load thanks to the lasing action.

In seeded operation (with regenerative preamplifier as the seeder), the power curve was similar to CW operation. Fig. 5.27(a) shows the output power during maximum power run with 10 W of seed power, repetition rate of 100 kHz, and amplification time of 1.47 us (70 roundtrips) resulting in 49.0% slope efficiency. The output power peaked at 554 W (5.5 mJ pulse energy) at 1253 W of pump power, giving extraction efficiency of 43.4%. Highest pulse energy achieved with the amplifier was 9 mJ at 50-kHz repetition rate (power 450 W). The amplifier operated in fundamental transverse mode with beam quality parameter $M^2 \approx 1.3$ at full power (output beam quality of the laser system is covered in Sec. 5.4).

When starting the amplifier for full-power operation, for the first 30 minutes the laser was pumped with the electro-optic modulator turned off in order to heat up the system. Then the

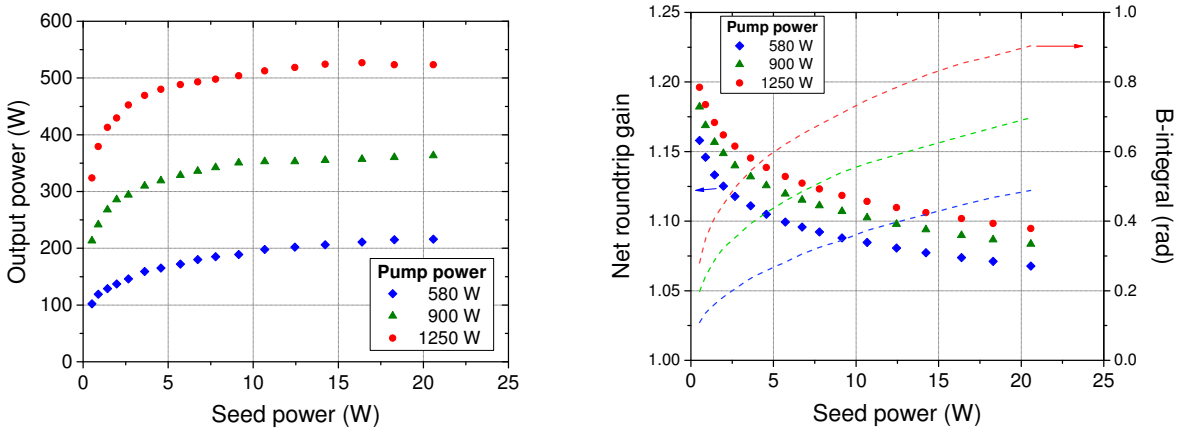

Fig. 5.28: (a) output power of the main amplifier vs. seed power at 100 kHz and 70 roundtrips at different pump levels, (b) computed B-integral and net roundtrip gain for measured data using method from Sec 5.3.3.

optical resonator was aligned (about 2 minutes) and the Pockels cell was switched on by gradually increasing voltage on its electrodes. Full power was then reached virtually immediately, although some fine tuning was necessary until the amplifier reached state of thermal equilibrium (typically 10-120 minutes depending on pump power). The maximum power used for experiments with this amplifier was 350 W; Fig. 5.27(b) shows power log from first four hours of an 11-hour run at 340 W. The power fluctuation after thermalization was 0.86% without need for further realignments.

Fig.5.28(a) shows the dependence of output power on seed power for three different working points. These data were used also used to calculate B-integral and gain according to the method described in Sec. 5.3.3 – the results are shown in Fig.5.28(b). The roundtrip gain at full power is between 1.06 and 1.10 and the B-integral is in every case below 0.9. In case of 50-kHz operation, it would not exceed 1.8 rad, which is still a safe value.

The amplifier was clearly working in saturation, since increasing seed power above 10 W and number or roundtrips above 36 brought only a modest increase in output power; this is evident from Figures 5.28 and 5.29(a). Unlike in e.g. 1-kHz Yb:YAG regenerative amplifiers, gain saturation is not apparent from the shape of intracavity pulse build-up [Fig. 5.29(b)]. While in the low-repetition-rate RAs in saturation the build-up shows a hyperbolic-tangent shape, in our amplifier with period between the amplification cycles much lower than the upper-state lifetime of Yb:YAG (regime similar to CW operation), the change in population inversion between each cycle is almost negligible and pulse build-up remains close to exponential shape, only the overall gain is reduced.

The output spectrum of the amplifier was centered at 1030 nm and the spectral bandwidth FWHM was approximately 1.5 nm for every configuration. The bandwidth of the oscillators and pulse stretchers was significantly broader and gain narrowing took place in the system. Fig. 5.30 shows spectra of individual amplifying stages of the laser system. In the case of the first generation of fiber front end end regenerative amplifier (Sec. 5.2.1 and 5.2.2), the 3.3-nm from the stretcher spectrum narrowed already in the fiber front end and the Yb:YAG RAs maintained its width at 1.5 nm. With the PM-fiber front end and rod Yb:YAG preamplifier (Sec. 5.2.3 and 5.2.4), the 4.5 nm pulses from the stretcher kept bandwidth of 3.9 nm at the output of the fiber system and rod preamplifier reduced it to 2.3 nm. In this case, the output

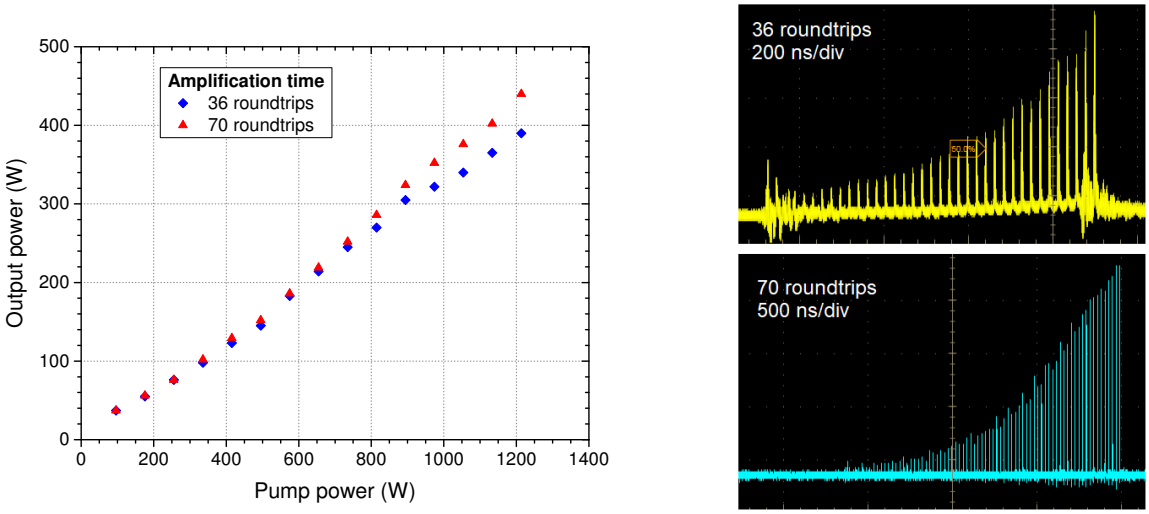

(a) (b)

Fig. 5.29: (a) output power of the main amplifier for 36 and 70 roundtrips, (b) pulse build-up for 36 roundtrips, 5-W seed, and 70-W output power (top) and for 70 roundtrips, 1-W seed, and 60-W output power (bottom), both with pump power of 250 W. Noise signal at the start and end of the amplification process comes from electromagnetic interference from the Pockels cell.

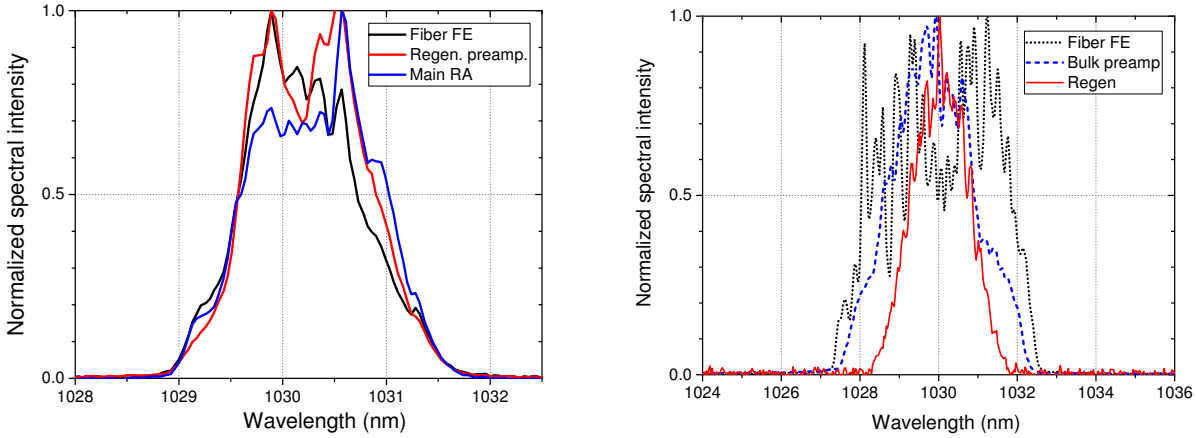

(a) (b)

Fig. 5.30: Output spectrum of the different amplifying stages of the PERLA C laser system, (a) of the non-PM-fiber front end, regenerative preamplifier, and main amplifier, (b) of the PM-fiber front end, Yb:YAG rod preamplifier, and main amplifier.

spectrum bandwidth of the entire laser system was 1.6 nm with transform-limited pulse duration of 0.85 ps.

5.4 Chirped-pulse amplification and pulse compression

Former sections of this chapter demonstrated that in order to reach the target parameters, it is necessary to reduce peak intensity in the amplifiers – mainly to prevent damage in optical components, mitigate SRS in the fiber section, and reduce the impact of nonlinear effects (i.e. the B-integral) in the regenerative amplifier. This was achieved mainly by using the method of chirped-pulse amplification (Sec. 2.2.1), introducing linear chirp to the pulse in a pulse stretcher

with large, controlled amount of chromatic dispersion. The second foundation of this technique is the pulse compressor applying to the output pulses a phase correction opposite to that introduced by the stretcher and amplifiers. This section addresses these aspects of the PERLA C laser system.

To quantify the dispersion, one has to focus on spectral phase of the optical pulse. The temporal shape of laser pulses is fully described by its electric field intensity E, which may be expressed equivalently in both time and frequency domains (connected bijectively via Fourier transform). The electric field of a pulse with central frequency ω_0, intensity shape $I(t)$, and (temporal) phase $\phi(t)$ can be written as

$$E(t) = \sqrt{I(t)}e^{i[\omega_0 t+\phi(t)]}, \ or \quad \widetilde{E}(\omega) = \sqrt{S(\omega)}e^{i\varphi(\omega)} \tag{5.8}$$

in spectral domain, with $S(\omega)$ being its spectral intensity shape and $\varphi(\omega)$ its spectral phase. The description in spectral domain is usually more useful and the spectral intensity is easy to measure. A pulse with constant spectral phase is a "transform-limited" pulse and represents a pulse with highest peak power for given spectral shape. Expanding spectral phase of a general pulse with center frequency ω_0 into a Taylor series, one obtains

$$\varphi(\omega) = \sum_{n=0}^{+\infty} \frac{1}{n!} \left.\frac{d^n\varphi}{d\omega^n}\right|_{\omega_0} (\omega-\omega_0)^n = \varphi_0+\varphi_1(\omega-\omega_0)+\frac{1}{2}\varphi_2(\omega-\omega_0)^2+\frac{1}{6}\varphi_3(\omega-\omega_0)^3+\dots \tag{5.9}$$

The first term φ_0 represents a constant phase and second term φ_1 called group delay results in shift of position of the pulse in time. These terms do not change the pulse shape, unlike the quadratic term φ_2 which is the group delay dispersion (GDD)

$$\mathrm{GDD} = \frac{d^2\varphi(\omega)}{d\omega^2}. \tag{5.10}$$

GDD is responsible for linear chirp (constant rate of change of instantaneous frequency with time) of the pulse and is the main parameter characterizing pulse stretchers and compressors (unit fs^2 or ps^2). A related material property, GDD per unit of length, is called group velocity delay (GVD, unit fs^2/mm). When expressing the quadratic dispersion in terms of wavelength rather than frequency, dispersion parameter D_2 is typically used (usual unit ps/nm). The conversion relation between the two quantities is

$$D_2 = -\frac{2\pi c}{\lambda_0^2}\,\mathrm{GDD}.$$

A positive value of GDD (or GVD) and negative value of D_2 correspond to normal dispersion.

Finally, the cubic term φ_3 is called the third-order dispersion (TOD) and it should be taken into account for optimum pulse compression, although for picosecond pulses with few nanometer bandwidth, its role is much less significant than that of the GDD. Higher-order dispersion terms are not relevant for picosecond pulses, which are the main scope of this work.

Group delay dispersion and dispersion parameter D_2 are also useful when estimating influence of the dispersive element on pulse duration. The pulse elongation in terms of FWHM can be assessed as [175]

$$\Delta\tau_p \approx |\mathrm{GDD}| \cdot \Delta\omega = |D_2| \cdot \Delta\lambda. \tag{5.11}$$

5.4.1 Dispersion management throughout the laser system

In order to reach stretched pulse duration in all amplification stages of the system in the order of hundreds of ps, large amount of dispersion was necessary. The fiber and free-space parts each contributed with its material dispersion to the total GDD of the system with less than 1 ps^2. A much higher amount of dispersion around 200 ps/nm ($\approx$ 110 ps^2) was needed to maintain the pulse duration at the end of the amplification process (bandwidth ≈ 1.5 nm) above 300 ps.

Such stretching factor could be achieved using e.g. material dispersion of a 6-km long silica fiber (at cost of a significant power loss), a CVBG (Sec. 5.4.2), or a Martinez-type grating stretcher [66]. The solution we used was a chirped fiber Bragg grating (CFBG), which combined several advantages. It complied with the all-fiber conception of the fiber front end, it had low insertion loss of over 80%, and – most importantly – it was allowed fine tuning of its dispersion via temperature profiling along the fiber grating.

For this pivotal component we chose a commercial solution from TeraXion because it provided more precise dispersion tuning and higher reliability than our in-house developed solution. In case of the CVBG compressor, we used a correspondingly tailored CFBG with anomalous dispersion and GDD of -115 ± 9 ps^2. However, this stretcher was not suitable for the Treacy-type compressor with anomalous dispersion and we switched to a newer model with GDD of 106.5 ± 17 ps^2. The characteristics of the grating were adjusted for a grating compressor and its TOD was adjustable within -3 ± 6 ps^3.

This CFBG Teraxion TPSR allowed us to tune in real time its central wavelength (temperature offset), second-order dispersion (linear change in temperature over position in fiber), and third-order dispersion (quadratic temperature change). The tuning range wide enough to cover material dispersion in the laser system and pulse shape optimization was usually performed by adjusting the stretcher rather than the compressor. The pulse duration of stretched pulses after the main amplifier (before compression) was verified using 15-GHz photodiode and 16-GHz oscilloscope as 350 ps.

5.4.2 CVBG compressor

The originally intended pulse compressor for the laser system was a chirped volume Bragg grating (CVBG) from OptiGrate Corp. This method was chosen over the standard grating compressor because such monolithic element is in comparison extremely compact and alignment-free. On the other hand, dispersion of a CVBG cannot be tuned once it is manufactured and as a bulk element, it may be susceptible to pulse distortion (spatial and temporal) due to thermal effects and Kerr effect. The highest average output power compressed with a CVBG up-to-date was 107 W from a 1064 nm, 17-MHz Yb-fiber laser [176], operating with lower pulse energy of 6 μJ and M^2 value above 1.5.

The CVBG is a reflection grating holographically recorded in a block of photo-thermo-refractive glass [177]. This process creates a quasi-periodic modulation of refractive index in the material, with period of the resulting grating slowly varying along the axis of the glass block. This leads to a spectral dependence of penetration depth for different spectral components of an incident laser beam, thus modifying the spectral phase of the compressed pulses. In this way, large amount of dispersion can be introduced to the optical pulse, making it suitable for picosecond laser systems.

Different gratings were tested, but for high-power compression we used a 76 mm long CVBG with aperture of 10×10 mm^2. The reflection spectrum of the grating was centered at 1030.3 nm with bandwidth of 3.3 nm, its dispersion parameter was 205 ps/nm (GDD 115 ps^2), and the specified absorption coefficient near 1 μm was only $3 \cdot 10^{-4}$ cm^{-1}. The grating could

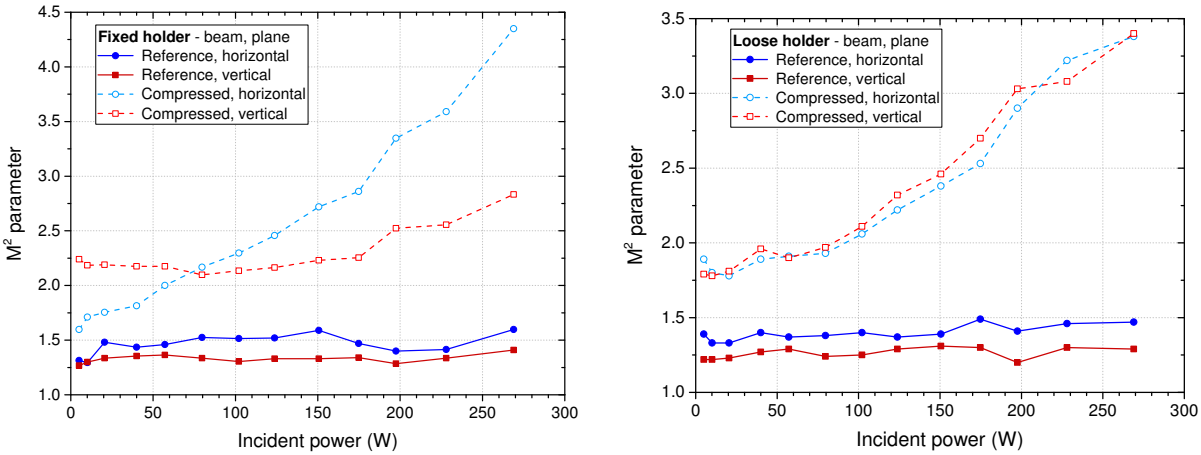

(a) (b)

Fig. 5.31: Measurement of the beam quality parameter M^2 vs. the incident laser power for (a) tightly fixed and (b) loosely mounted CVBG.

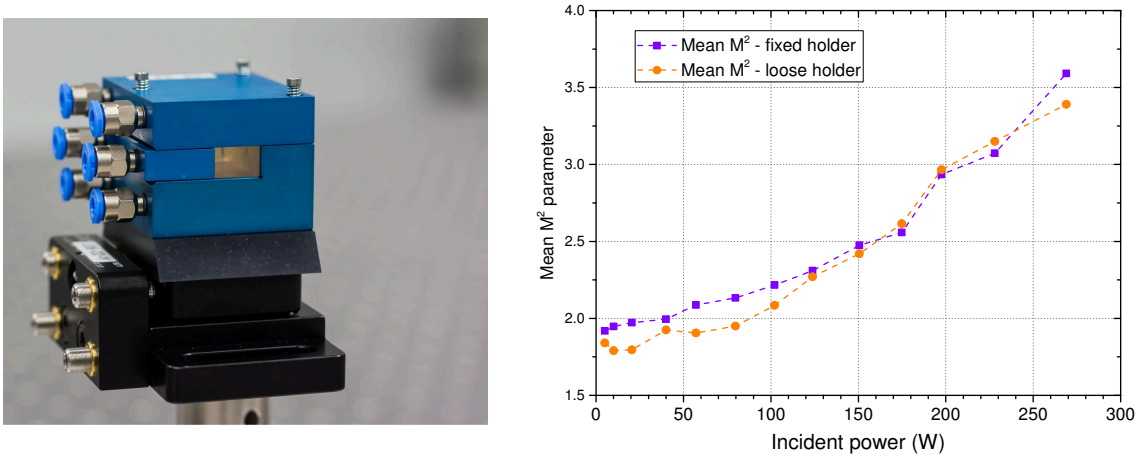

(a) (b)

Fig. 5.32: (a) photo of a CVBG in its holder (aluminum version for 50 mm long gratings), (b) geometric mean of vertical and horizontal $M^2_{x,y}$ parameters for both tightly and loosely mounted CVBG.

introduce both normal and anomalous dispersion depending on its orientation, and so it could be used also as a stretcher – initially we used a matched pair of CVBGs as for stretching and compression, but later we switched to a CFBG stretcher for the advantage of fine dispersion tuning. The beam diameter on the grating was around 4 mm and the incident and reflected beams were separated using a thin-film polarizer and quarter-wave plate. The CVBG was placed in a water-cooled brass holder fixed with spring-loaded screws shown in Fig. 5.32(a).

The CVBG was used successfully for pulse compression already in the 100-W regenerative amplifier (Sec. 5.2.2). With a significantly more powerful laser, we encountered substantial issues with beam quality of the compressed beam. On the other hand, the grating did not affect the spectrum of the pulses and allowed compression below the target pulse width of 2 ps. It was tested with incident power up to 269 W (there we stopped due to strong thermal lensing and deterioration in beam quality beyond any usable extent) and the maximum temperature increase on the front side of the CVBG was about 5 °C. The diffraction efficiency of the CVBG gradually

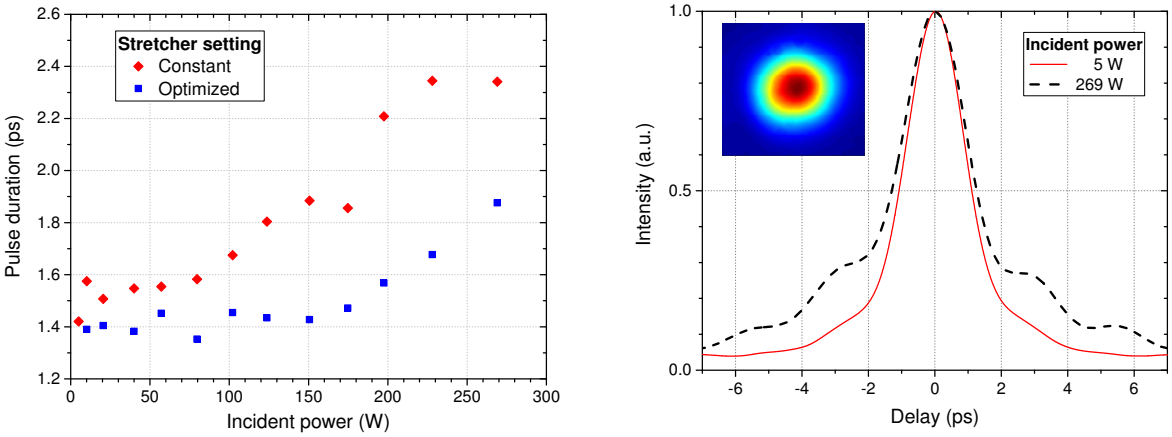

(a) (b)

Fig. 5.33: (a) evolution of pulse width (FWHM) with laser power and (b) autocorrelation trace of pulses compressed in CVBG for low and and maximum incident power and spatial profile of 200-W compressed beam.

decreased from 84% at low power to 80% at full power. Heat deposition on the CVBG led to formation of a thermal lens, whose power we estimated as high as 0.5 m^{-1} at full power.

Originally, we mounted the CVBG in the holder with estimated clamping force of 12 N from the top part. The measured M^2 parameter is shown in Fig. 5.31(a). The reference beam (output of the main amplifier) had M^2 of around 1.3 in vertical and 1.5 in horizontal plane. The M^2 evolution of the compressed beam was strongly asymmetric with the vertical M_y^2 almost static around 2.2 and increasing from 200-W of incident power to 2.8. In contrast, the horizontal M_x^2 increased almost three times from 1.6 to 4.4. This asymmetry led us to an investigation into the effect of mechanic pressure on the beam quality.

With a holder without the top piece (i.e. 0 N clamping force) and the side parts in contact with the CVBG but without any applied force, distinctively different M^2 trend was observed – it is shown [5.31(b)]. The M^2 was symmetric in the two planes and rose gradually from about 1.7 at low power to 3.4 at 269 W. An interesting trend can be seen from Fig. 5.32(b), where a mean M^2 defined as $M^2_{mean} = \sqrt{M_x^2 \cdot M_y^2}$ is plotted for both mounting configurations. It shows that although the mechanic stress on the grating gave rise to an asymmetry in beam quality, the overall beam quality remains roughly the same.

The high power beam caused also some distortion to the pulse shape of the compressed pulses (Fig. 5.33). When optimizing the stretcher setting at each step, it was possible to keep the pulse duration around 1.4 ps for power up to 170 W and at 269 W it peaked at 1.9 ps, while when keeping a constant stretcher setting, pulse duration at full power rose above 2.3 ps. Higher power led also to an emergence of wings in the autocorrelation trace containing significant portion of the pulse energy; this aspect is not clearly evident just from the FWHM pulse width value.

Our explanation of the main mechanism in beam quality deterioration in CVBG is that the thermal lensing is wavelength-dependent due to different optical path in the CVBG for different spectral components. However, this was not proven by measurement (e.g. of spatial chirp at multiple positions after the grating). The deterioration in beam quality with the CVBG compressor meant worse applicability of the laser system for experiments. Furthermore, in another laser system in our laboratory with pulse energy above 10 mJ, intensity dependent

lensing, presumably connected to the Kerr effect, was observed. This led us to development of a more conventional grating compressor.

5.4.3 Pulse compression with dielectric gratings

After previous pulse compression attempts with CVBG and facing issues with beam quality, we switched to the Treacy-type stretcher [67], which is a time-proven and the most straightforward grating compressor scheme. The typical configuration with two parallel gratings was used here (illustrated in Fig. 5.3 in the "compressor" part), although a single-grating scheme (economical but delicate alignment-wise) or a rather lavish four-grating scheme would be also applicable. With sufficient grating separation, this optical system can introduce large amounts of second-order dispersion by means of angular dispersion resulting in optical path difference of the spectral components. The spectral phase of those components over two passes through the compressor with length L can be described as

$$\varphi(\lambda) = \frac{4\pi}{\lambda} \cdot \frac{1 + \cos(\mathrm{AoD}_\lambda)}{\cos(\mathrm{AoI})} \cdot L$$

where AoD_λ stands for angle of diffraction into the -1$^{\mathrm{st}}$ order, connected with the incidence angle AoI via the grating equation $\sin(\mathrm{AoD}_\lambda) = \sin(\mathrm{AoI}) + \lambda/\Lambda$, with Λ being the grating period. The length L of the compressor is connected with the normal separation of gratings as $d = L/\cos(\mathrm{AoD})$.

The GDD produced by the grating compressor can be obtained by differentiating the spectral phase according Eq. (5.10). The GDD of a Treacy compressor then is [178]

$$\mathrm{GDD} = \varphi_2 = \frac{\lambda_0^3}{\pi c^2 \Lambda^2} \cdot \frac{1}{\cos^2(\mathrm{AoD}_{\lambda_0})} \cdot L. \tag{5.12}$$

The collimated, yet spectraly dispersed beam after the second grating is usually returned in the reverse direction in parallel direction at different height using a roof-top mirror (back-reflecting pair of mirrors placed at 90° to each other) and than the output beam is picked by a mirror lying under the input beam. In our case the grating separation was rather large and we could use without any perceptible beam distortion a single, slightly tilted back-reflecting mirror, creating height difference of $\approx$ 15 mm between the input and output beam on the first grating.

For the grating compressor we initially used reflection dielectric gratings from MarTec Photonics with groove density of 1600 mm^{-1} (period 625 nm) designed for angle of incidence of 48°-51°. Due to the rather low groove density, the required compressor length was 2.7 m and the compressor was folded using an HR mirror. These gratings had high diffraction efficiency of $\approx$ 99% with overall compressor transmission around 95%. However, it was not possible to compress the laser pulses below 2-ps pulse duration and minimum achievable beam quality parameter was $M^2 \approx 2$. After consulting the issue with the manufacturer, we were able to explain it by $\approx$ 150 pm variation in grating period over the beam spot on second grating that emerged during interference beam lithography manufacturing process. Corresponding displacement of the spectral components matched well the output beam profile. This rendered the gratings unusable for our laser system.

Transmission dielectric gratings finally used in the laser system were manufactured by JENOPTIK Optical Systems GmbH. They have very high groove density of 1841.6 mm^{-1} (period 543 nm) and are designed for wavelength range 1020-1040 nm and for use in the -1$^{\mathrm{st}}$ diffraction order under Littrow angle (71.5° at 1030 nm, greatly angle-selective). The speci-

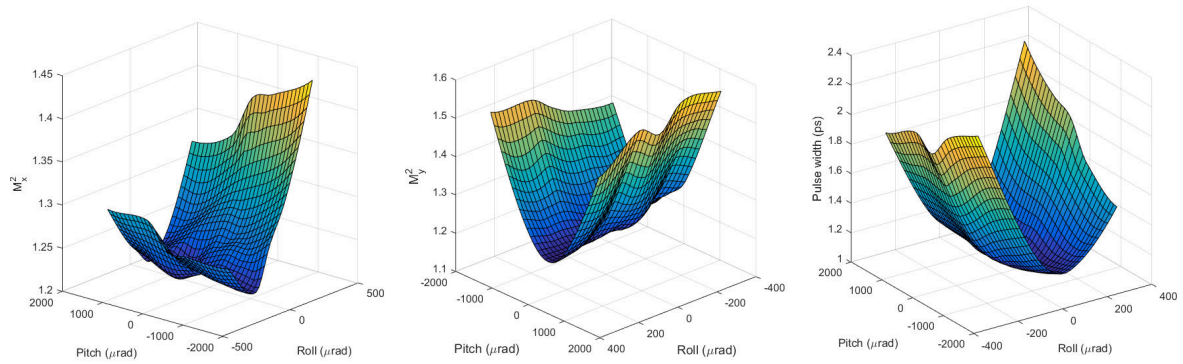

Fig. 5.34: Influence of tilt misalignment of the second compressor grating on $M^2_{x,y}$ and pulse duration (each plotted surface is the best fit to 33 measured points). One can see that M^2_y is most sensitive to pitch (vertical axis) adjustment and almost invariant to tilt in roll axis (perpendicular to the grating), while the situation with pulse duration is exactly opposite. Similar links could be seen in the other combinations of axes: pitch–yaw and roll–yaw (yaw axis is horizontal, perpendicular to roll and pitch axes).

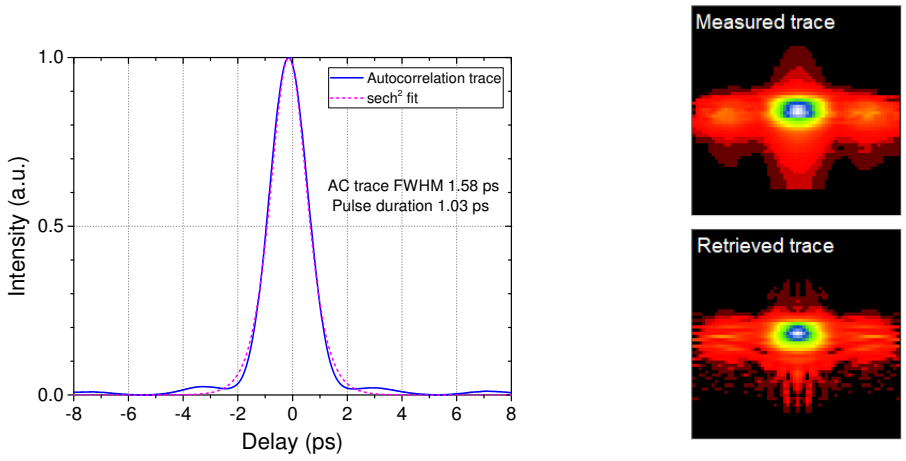

(a) (b)

Fig. 5.35: (a) measured intensity autocorrelation trace after pulse compression with the grating compressor, the FWHM pulse duration acquired from a sech^2 fit is 1.03 ps; (b) measured FROG spectrogram and its reconstruction by an iterative FROG algorithm.

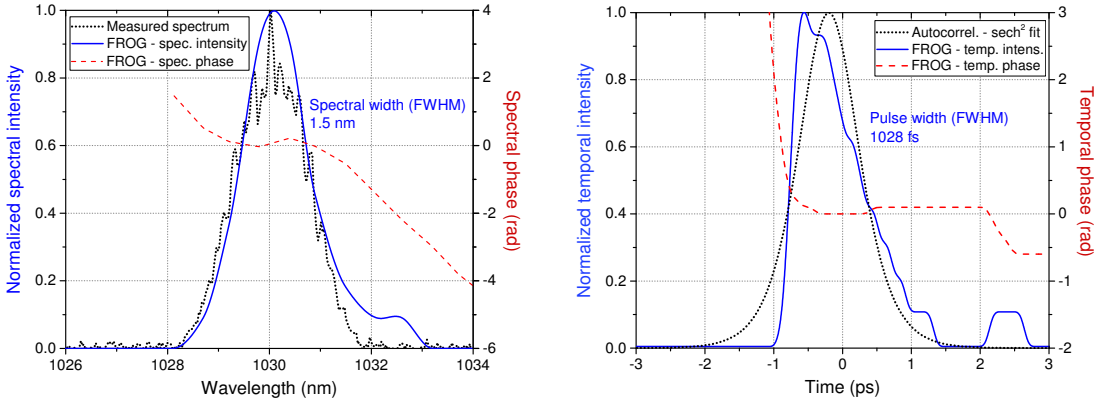

(a) (b)

Fig. 5.36: (a) spectrum and spectral phase reconstructed from the FROG spectrogram in Fig. 5.35(b) and comparison with measured spectrum from Fig. 5.30(a); (b) FROG reconstruction of the temporal shape and phase of output pulses in comparison with the pulse shape estimated from the fit of intensity autocorrelation in Fig. 5.35(a).

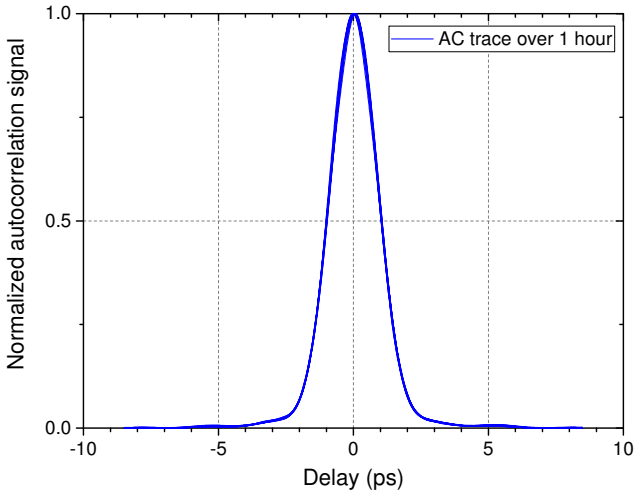

Fig. 5.37: Intensity autocorrelation of the compressed output measured every 2 minutes for one hour (31 measurements). Here, the measured pulse duration was 1.1 ps (assuming sech^2 pulse shape).

fied diffraction efficiency is >98% and damage threshold fluence is over 1 J/cm^2. The grating structure is encapsulated inside the fused silica substrate, meaning both sides of the gratings could be AR-coated and remain cleanable. The dimensions of the gratings are 59×34 mm^2 and 80×34 mm^2. In case of the second grating, the 80-mm width was just enough to comfortably accommodate the spatially dispersed beam without cropping edges of the 1.6-nm broad spectrum.

To compensate dispersion of the pulse stretcher, the required grating separation according to Eq. (5.12) was about 0.88 m (distance along the beam path). To align the compressor (i.e. parallelism of the two gratings) precisely and reliably in all three rotational degrees of freedom, we developed a novel alignment method, which is currently being prepared for publication. It consists of monitoring simultaneously the M^2 parameter of the beam (in horizontal and vertical planes) together with pulse duration and consecutively adjusting the pitch, yaw, and roll of the second grating, while compensating the beam shift by adjusting tilt of the end mirror (the technique is partly illustrated in Fig. 5.34). It emerged that optimizing the beam quality and pulse width by consecutively adjusting the three axes leads within a few iterations (typically two) to finding the setting with minimum M^2 and pulse width that apparently corresponds to perfectly parallel gratings. It was not necessary to adjust the compressor length from the calculated value, since the required minor dispersion adjustment could be done in with the CFBG stretcher.

With this compressor, it was possible to compress the output pulses to 1.0 ps. The result of intensity autocorrelation measurement is showed in Fig. 5.35(a). This result was verified by a FROG measurement (Sec. 3.3) displayed in Fig. 5.35(b), with good agreement between the reconstructed pulse and with direct spectrum and autocorrelation measurements, as may be seen in Fig. 5.36.

Since we experienced a significant instability in pulse shape on output of another laser system in our laboratory, we checked this characteristics on our laser system as well. The logged results are shown in Fig. 5.37. The pulse shape remained constant for entire time period (1 hour). This characteristic depends mostly on stable function of laser oscillator and fiber front end, which were apparently working correctly.

The diffraction efficiency of the dielectric gratings was higher than 99% as the overall power efficiency of the compressor was around 97%. The compressor was tested with output power

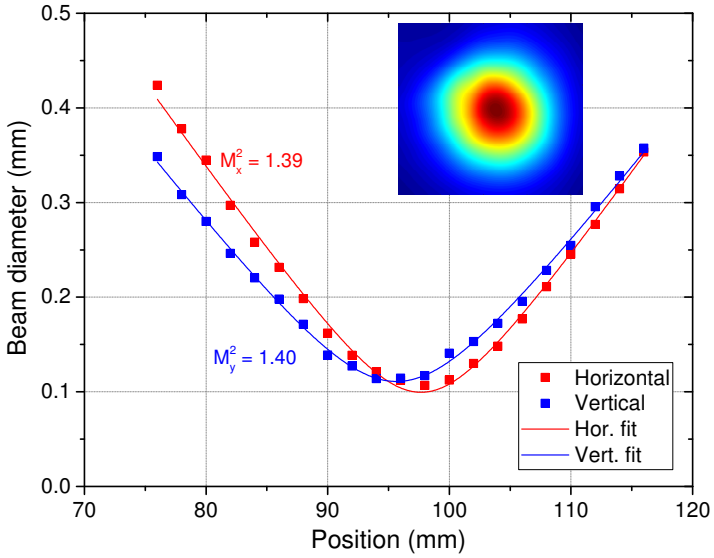

Fig. 5.38: Beam quality measurement of the high-power ($\approx$ 350 W) beam after the grating compressor. Inset: spatial profile of the compressed beam at output power of 300 W.

up to 350 W and there was no observation of influence of the laser power on pulse duration or beam quality. The M^2 parameters of the compressed and reference (uncompressed) beams were also equal within measurement error and at full power (350 W at that time) the M^2 of the laser system was 1.4 (Fig. 5.38).

In conclusion, this configuration of pulse compressor emerged as a virtually perfect optical system for reduction of laser pulse duration with no detrimental effect on beam quality and spectrum, almost 100% transmission, and with good resilience to high average optical power.

5.5 Output beam manipulation

The high-power beam exiting the laser system was handled using multiple elements. Overview of the setup is shown in Fig. 5.39. The output beam from the laser was collimated using a Galilean telescope/beam expander and its diameter was set to approximately 4 mm. For variable attenuation, a half-wave plate and thin-film polarizer were inserted in the beam, with the diverted beam terminated on a power meter, monitoring the output from the amplifier.

The beam was then routed to a pulse picker and compressor. In order to ensure correct beam alignment on these elements, we used a commercially available system for beam pointing stabilization, Aligna from TEM Messtechnik [179]. This system consisted of two motorized mirrors (4 axes) with step and piezoelectric motors, a detection system measuring beam position and beam direction (4 degrees of freedom), and control electronics. The mirror motors and detectors formed a feedback loop, that was defined by a 4×4 matrix for both types of motors. Although the control program featured a self-learning algorithm for determination of the optimum matrices, in practice it was necessary to deduce the approximate matrices for given geometric configuration of mirrors in order to allow the algorithm to converge. Working beam stabilization then provided repeatable pointing of the beam on day-to-day basis and improved beam pointing stability of the laser system from approximately 10 µrad to 5 µrad.

The pulse picker [Fig. 5.40(b)] was basically the same device as the electro-optic switch (with two $8 \times 8 \times 25$ mm^3 BBO crystals) in the regenerative amplifier and was operated in the bipolar regime (4-kV quarter-wave voltage with alternating polarity). It allowed gating of the

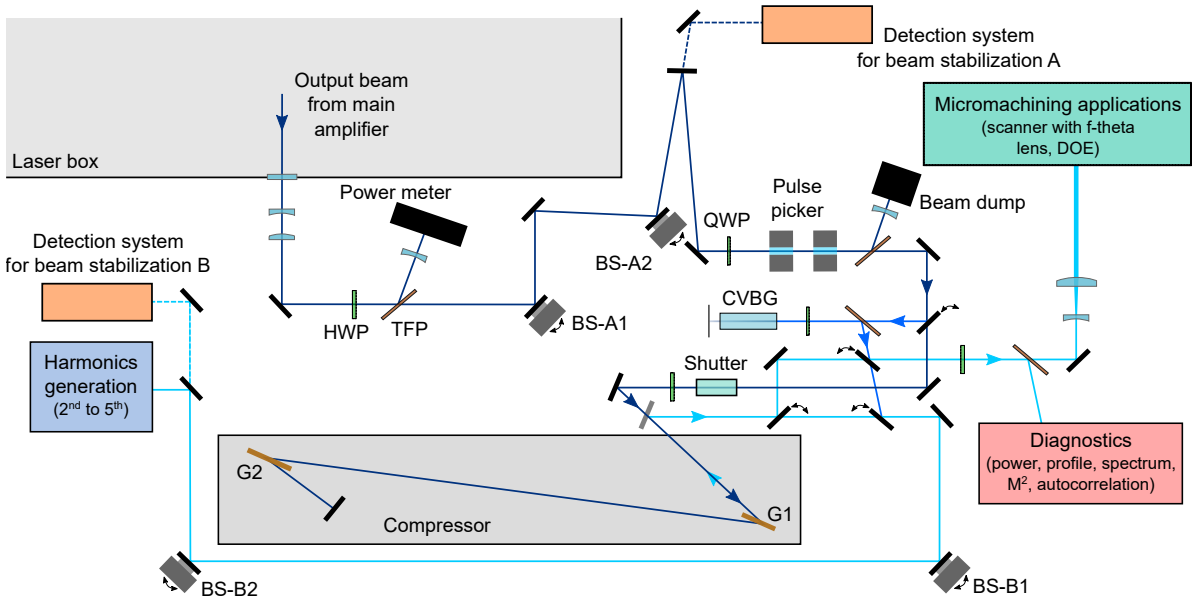

Fig. 5.39: Optical setup for beam compression, characterization, and delivery to applications. QWP/HWP – quarter-/half-wave plates, BS – motorized mirrors for beam-stabilization, CVBG – chirped volume Bragg grating, G1, G2 – diffraction gratings, DOE – diffractive optical element. Dark-blue beam represents uncompressed beam, cyan beam is the compressed beam, and medium-blue beam represents the branch of the CVBG compressor.

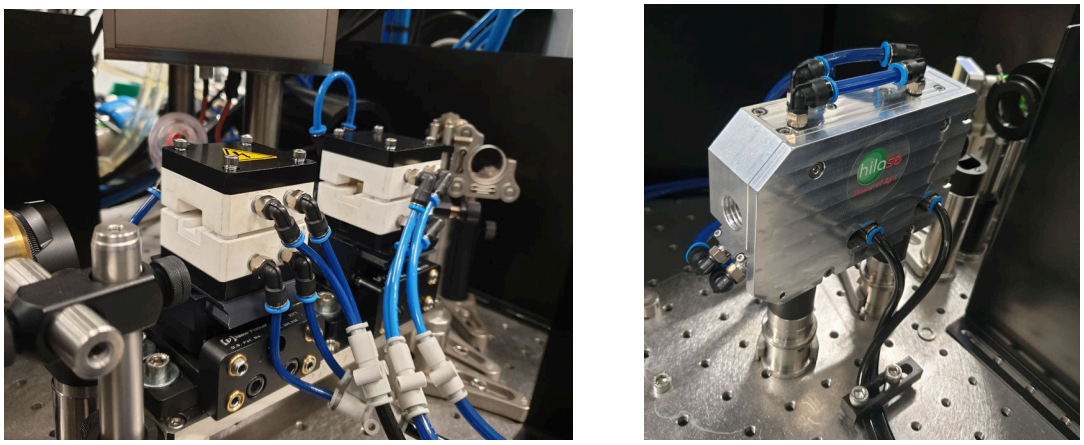

(a) (b)

Fig. 5.40: (a) Pockels cell of pulse picker at the output of the main amplifier (b) pneumatic beam shutter between the pulse picker and beam compressor.

laser pulses in coordination with the scanner for micromachining applications, reduction of the repetition rate, or creating bursts of pulses. The pulse picker used timing from the clock of the main amplifier and had transmission of approximately 99% due to the contrast of the Pockels cell (around 1:200) and insertion loss of the BBO crystals and TFP – when there was no need for pulse picking, the quarter-wave plate was folded and with no applied voltage, loss on the pulse picker was insignificant.

After the pulse picker, the beam could be passed to the grating compressor (Sec. 5.4.3), or diverted to the CVBG compressor (Sec. 5.4.2). Outputs of both compressors were then routed to the application areas along the same paths. In the beam path directed to the grating compressor, there was inserted also a pneumatic shutter [Fig. 5.40(b)]. This shutter was operated by

compressed air and allowed safe attenuation of the beam thanks to an integrated water-cooled beam dump. For some applications (requiring long bursts of pulses), the shutter could substitute the function of the pulse picker, since a timing function was implemented, allowing to open the shutter from ca. 0.1 s to 999 s.

The compressed beam could be directed to the first application area with micromachining station (including a scanner with f-theta lens, optionally a diffractive optical element for multi-beam manufacturing, motorized 3D translation stage for the workpiece, and fume suction system), or could be diverted to a diagnostics area with equipment for temporal, spectral, and spatial characterization of the laser output. The other beam branch led to the harmonics generation setup (generation of second to fifth harmonics and their applications) and due to a long beam path and need for better beam pointing stability and day-to-day repeatability, a second (identical) beam pointing stabilization was placed between the pulse compressor and the harmonics setup.

5.6 Selected applications of the laser system

This section brings a brief overview of some experimental results, obtained from applications of the PERLA C laser system and which led to publication results. In these experiments, I was responsible for the 1-μm laser part.

The most power-demanding experiment until now was performed for a private company and consisted in micromachining of titanium alloy and ceramics composite with 100-kHz picosecond pulses at average power up to 350 W.

5.6.1 Multi-beam micromachining and surface structuring

Picosecond laser pulses can be used for structuring of metallic and other surfaces, giving them strong hydrophobic and self-cleaning or hydrophilic properties. Such surface attributes are of high interest e.g. for automotive and aerospace industries or for biomedical applications. Technique of laser ablation is used to form a microscopic and nanoscopic structures that alter the roughness and wetting properties of the metallic surface, which is usually also further treated in order to pronounce the effect and improve its durability.

An effective way of preparation of superhydrophobic aluminum surface is to treat it after the laser patterning process with a fluorine compound. Other method is a very time-consuming, but environment-friendly aging processes. In our work [A8] led by Radhakrishnan Jagdheesh, $\approx$ 100-kHz picosecond pulses from PERLA C laser system were used to pattern Al7075 aerospace aluminum alloy with nearly superhydrophobic properties, and after an additional 4-hour storage in vacuum chamber, a superhydrophobic to ultrahydrophobic structure was obtained.

Fig. 5.41 shows the lamellar nano-scale structures fabricated on the aluminum alloy with two-directional laser scans with pulse-to-pulse overlap of 99%. The change in "pitch" (spatial shift between the scans) had strong impact on the result, since for pitch higher than 100 μm, micro-scale pillars covered with nanostructures were formed. These formations significantly improved the functional properties of the surface and provided stable and durable superhydrophobic surface.

Further experiments, performed with Petr Hauschwitz and colleagues, were focused on multi-beam laser processing and creating of laser-induced periodic surface structures (LIPSS). Using a prototype diffractive optical element (DOE) and 50-kHz picosecond pulses with more than 150 W of average power, 2601 spots (51×51 matrix) were produced simultaneously and a

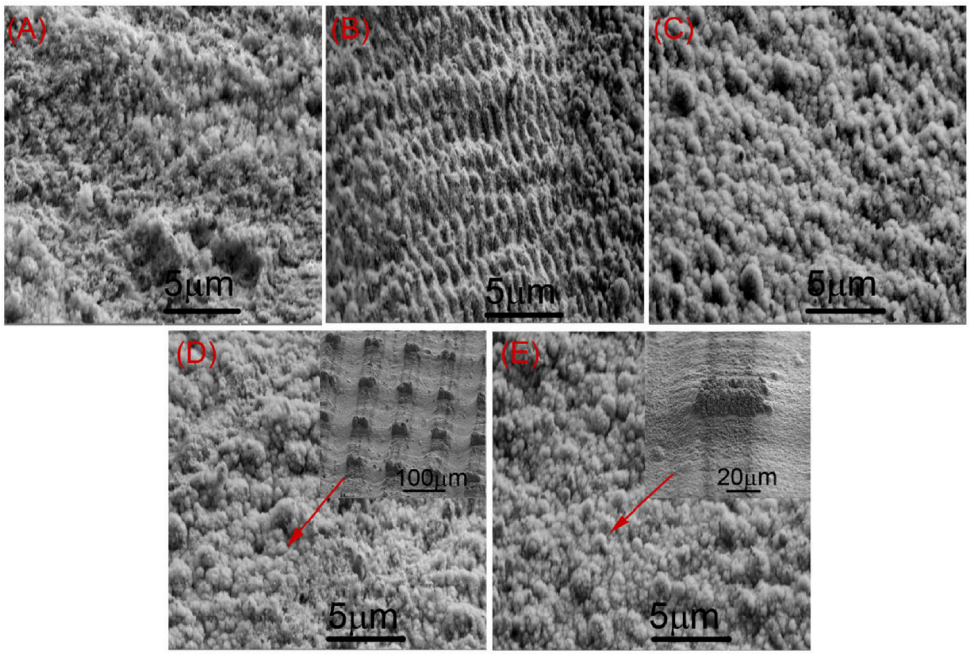

Fig. 5.41: SEM photographs of sub-1μm-scale structures fabricated with 240 picosecond pulses from PERLA C per spot with fluence of 0.86 J/cm^2 and pitch of (A) 20 μm, (B) 40 μm, (C) 60 μm, (D) 100 μm, and (E) 150 μm [A8].

periodic functional surface with area of 1 mm^2 could be formed in less than 10 ms. The encouraging initial results are currently waiting for finalization and publication. These applications are extremely sensitive to beam quality and effort is made to improve the output beam quality of the laser system to $M^2 \approx 1.2$.

5.6.2 High-power harmonics generation

The high-power picosecond pulses from the PERLA C laser system were used for efficient wavelength conversion to visible and deep-UV (DUV) light by Hana Turčičová. The setup for the harmonics generation, as presented in [A6], is shown in Fig. 5.42. To generate second harmonics (515 nm), it used LBO (lithium triborate, LiB_3O_5) with Type I phase matching and maintained at temperature of 47 °C. The fourth harmonics (257.5 nm) was then obtained from a CLBO (Cesium lithium borate, $CsLiB_6O_{10}$) crystal and the fifth harmonics (206 nm) was produced as a sum frequency of precisely synchronized fundamental and fourth harmonics beams. The CLBO crystals were used also in Type I phase matching and were kept at temperature of 150 °C in argon atmosphere in order to protect them from ozone produced from air under hard UV radiation as well as from humidity, since CLBO is highly hygroscopic.

Until now, the harmonics generation was tested thoroughly for input power up to 70 W at the fundamental wavelength, since so far it has been sufficient for applications, but it is planned to start its power scaling in near future. With the current setup, it was possible to obtain nearly 50 W of average power at 515 nm wavelength with typical conversion efficiency (CE) of 65-70%. In case of fourth harmonics, 9 W output at 257.5 nm was obtained with CE from 515 nm around 25%. The power in fifth harmonics, which is the most challenging to produce, has currently peaked at 1.4 W at 206 nm. These values are on par with the current state of the art in ≈ 100-kHz picosecond pulses in DUV spectral region.

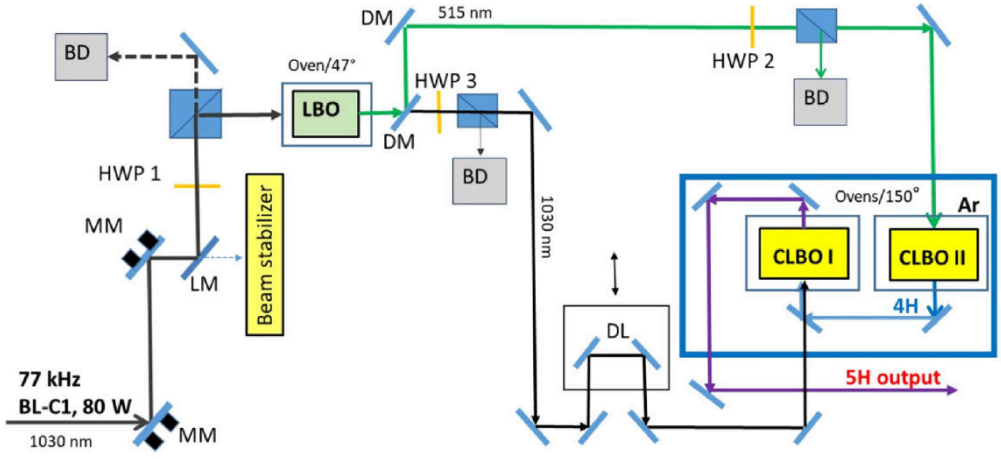

Fig. 5.42: Setup for second, fourth, and fifth harmonics generation at the output of the PERLA C laser system [A6]. MM – motorized mirror, LM – leaking mirror, HWP – half-wave plate, BD – beam dump, DM – dichroic mirror, DL – delay line.

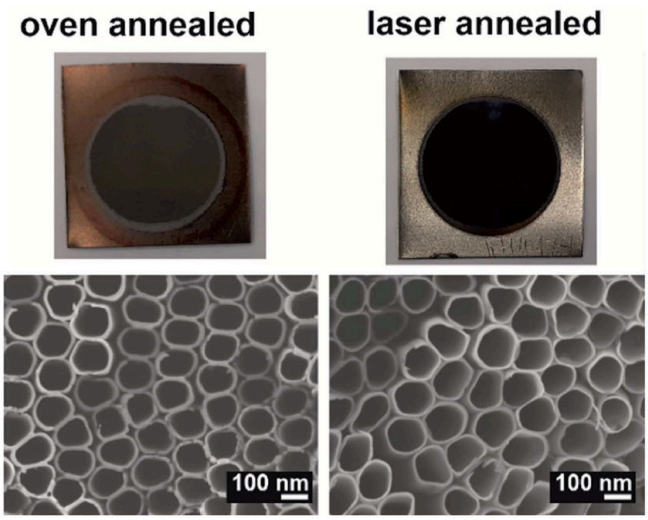

Fig. 5.43: Comparison of photographs and SEM images of oven- and laser- annealed TiO_2 nanotube layers [A9].

The main motivation for generating harmonic wavelength of the Yb:YAG laser was processing of materials transparent or low-absorbing for 1-μm radiation, such as glass or ceramics, more suitable for micromachining using green or DUV light. UV light was also useful for some scientific experiments, such as the process described in the next section.

5.6.3 Laser-induced crystallization of anodic TiO_2 nanotube layers

Fourth harmonics of the PERLA C laser system (wavelength of 257.5 nm) was successfully used for laser annealing of TiO_2 nanotubes (TNT) layers [A9]. Highly ordered, anodic TiO_2 nanotubes have high potential for use in solar cells, various sensors, or water splitting. The standard way of their preparation is annealing in a furnace at temperature around 400 °C, which is a time-consuming process taking several hours.

Laser annealing of TiO_2 nanotubes has potential to significantly shorten this process to several minutes and can be used for selective-area treatment. Using the fourth harmonics of

the PERLA C with average power of 5 W in 90-kHz picosecond pulses and with $\approx$ 2.5-mm diameter of a Gaussian beam, it was possible to effectively induce crystallization of TiO_2 and to treat 1-cm^2 area in 14 minutes.

The laser annealing of TNT layers using this laser was performed for the first time without any melting of the nanotubes. When compared with oven-annealed TNT layers, laser-annealed layers showed higher amount of defects and the TiO_2 was not fully crystallized, but it showed better surface stoichiometry and the same surface structure. This makes this method of TNT annealing very promising for further investigation.

Chapter 6

Conclusion

This dissertation thesis was dealing with research and development of picosecond diode-pumped solid-state lasers with high repetition rate and high average power. After a short introduction, an overview of solid-state materials was given and most important techniques used in high-power lasers were presented. The main focus of this work were ultrafast thin-disk lasers, whose current state of the art was surveyed within the theoretical part of this work as well.

The next section summarizes the experimental results presented in this thesis, while Sec. 6.2 points out the most important achievements, advancing the current state of knowledge in the field of laser physics.

6.1 Summary of achieved results

The first experimental part of the work focused on novel laser materials of promising properties for use within the thin-disk laser concept. The first tested material was ceramic ytterbium-doped mixed garnet YGAG ($Y_3Ga_2Al_3O_{12}$) with composition very similar to the widely used Yb:YAG, but with much wider emission bandwidth at temperature of liquid-nitrogen, which is important for ultrashort pulse generation, while cryogenic cooling is one of possibilities how to further scale output power of lasers activated with rare-earth ions. By direct comparison with crystalline Yb:YAG with identical parameters, it was found out that the laser performance of Yb:YGAG ceramic samples was on par with Yb:YAG. At cryogenic temperature, 10 W of output power was generated in continuous-wave operation with optical-to-optical efficiency of 35% and continuous wavelength tuning in range of 8.1 nm was demonstrated. By employing mode locking with a semiconductor saturable absorber (SESAM) at temperature of 80 K, train of pulses with duration of 2.4 ps at wavelength of 1026 nm was obtained, which is more than four times shorter than what has been reported with Yb:YAG.

Another tested material was erbium-doped yttria (Er:Y_2O_3) ceramics with laser emission wavelength around 2.7 μm. Erbium-doped materials represent the most straightforward access to this spectral region for diode-pumped solid-state lasers, and their adoption to thin-disk technology would significantly extend its capabilities. In the initial experiments, a disk and a rod room-temperature Er:Y_2O_3 laser with very low efficiency were developed, but after optimization of laser parameters, a compact 0.95-W continuous-wave laser emitting at 2.72 μm with slope efficiency of 17.4% was obtained. In pulsed regime with 1-ms, 10-Hz pump pulses, peak power as high as 9 W was generated. Moreover, the laser operated with a beam quality close to the diffraction limit, with M^2 parameter value below 1.2 at all conditions.

The major part of this work described the development of a high-power thin-disk Yb:YAG laser system PERLA C. This included construction of a fiber front end, Yb:YAG rod preampli-

fier, main thin-disk regenerative amplifier, and a pulse compressor. The system of fiber oscillator and multiple preamplifying stages was tuned to produce a highly stable train of pulses with negligible phase distortion and energy sufficient to seed the main amplifier operating at repetition rate of 100 kHz. The thin-disk amplifier used a compact ring optical cavity optimized for stable fundamental-mode operation over a wide range of pump power and two reflections off the disk per roundtrip, which allowed operation with very high efficiency, comparable with continuous-wave thin-disk lasers with much simpler configurations. A technical challenge of implementation of high-voltage, high-repetition-rate electro-optic modulator was solved by studying the resonant frequencies of Pockels cell crystals and influence of their mounting. With 1.25 kW of pump power at 969 nm wavelength, the main amplifier produced 100-kHz, 1030 nm pulses with average output power of 0.55 kW (optical-to-optical efficiency of 43.4%, slope efficiency 49.0%) in a good-quality beam with M^2 of 1.4 and with power fluctuation of 0.86% over several hours. At reduced repetition rate of 50 kHz, maximum pulse energy of 9 mJ was obtained. For pulse compression, initially a chirped volume Bragg grating (CVBG) was used, but with high incident power, significant deterioration in beam quality and pulse shape was observed. After a detailed study of the CVBG compressor with power up to 270 W, we switched to a Treacy-type compressor using transmission dielectric gratings. This compressor with high transmission of approximately 96% allowed pulse compression to 1-ps pulse duration without any influence on beam quality. The compressor was tested for power up to 350 W (full power was not available from the main amplifier at the time of completion due to replacement of the pump diode laser and thin disk), but since there was no deterioration in output parameters with increasing power, it should hold also for full-power beam. The laser system has been successfully used for various experiments, including laser micromachining and surface structuring, high-power harmonics generation, or laser-induced crystallization of TiO_2 nanotube layers. In summary, the requirements on output parameters of this laser system were met and it is available for experiments.

By summarizing these results, it may be concluded that the goals of this thesis were accomplished. I am supposed to confirm here explicitly that all the results mentioned in previous paragraphs were an outcome of my individual work, only the fiber front end, rod preamplifier and pulse compressor of PERLA C were developed in collaboration with undergraduate students under my supervision and according to my design. And of course, the application experiments were carried out by my colleagues – specialists in respective fields, with me providing the laser part.

Regarding the publication activitities, over the PhD course I authored 3 and co-authored 9 articles in peer-reviewed journals, contributed as a co-author to one book chapter, and presented 13 and co-authored 23 international conference contributions. Additionally, I have acted as a supervisor or advisor of three undergraduate students and led their work in the laboratory (besides the already mentioned work, with one of the students, Tomáš Hambálek, we developed two thin-disk Yb:YAG oscillators, a 5-W picosecond SESAM-mode-locked laser and 3-W, 280-fs Kerr-lens-mode-locked laser).

6.2 Contribution to progress of laser science

During the work on the topics presented in this thesis, a large number of new findings was gained, which helped us with further development of laser systems at the HiLASE Centre. From the novelty point-of-view, the main achievements can be summarized as follows:

- A comparative experiment with Yb:YAG in Sec. 4.1 proved that a novel Yb:YGAG transparent ceramic can offer similar laser performance and, more importantly, 2.4-ps pulses were generated at liquid-nitrogen temperature from the first mode-locked laser oscillator based on this material. This showed that this material can offer significant advantage over Yb:YAG for ultrashort laser pulse generation and amplification at low temperature. This ceramics was later studied by my colleagues (including development of a room-temperature femtosecond Yb:YGAG regenerative amplifier) and Yb:YGAG thin disks are currently being prepared for experiments.

- A diode-pumped 0.95-W Er:Y_2O_3 ceramic laser emitting at 2.7 μm was realized. Its distinguishing feature was high optical-to-optical efficiency of 14.3% and excellent beam quality ($M^2 < 1.2$), making it the brightest watt-level $\approx$ 3-μm erbium laser operated at room temperature.

- A half-kilowatt high-repetition-rate picosecond thin-disk laser system operating in fundamental transverse mode was developed. The thin-disk amplifier is the most powerful single-thin-disk regenerative amplifier reported up to date and it operated with an outstanding optical-to-optical efficiency over 43%. This one-of-a-kind laser system then could be used for various experiments yielding new scientific results.

The results in this list were reported in peer-reviewed journals and presented at several scientific conferences. However, the largest volume of the acquired knowledge lay in the technical details and nuances that are hard to find in the literature and still they are indispensable for robustness and proper working of high-power laser devices. Some of this information I tried to capture in this work. The field of high-power laser systems may not be the most accessible and prolific in terms of generating scientific outputs, but once the system containing thousands of optical, electronic, and mechanical components happens to run flawlessly and starts generating ultrashort and extremely bright pulses of pure, concentrated energy virtually just by plugging it into the power grid, one does realize the beauty of this branch of science and technology.

Bibliography

[1] HiLASE Centre. (2021). "Hilase – superlasers for the real world", [Online]. Available: https://www.hilase.cz/en/ (visited on 05/28/2021).

[2] A. Einstein, "Zur Quantentheorie der Strahlung", *Physikalische Zeitschrift*, vol. 18, pp. 121–128, 1917.

[3] M. Planck, "Zur Theorie des Gesetztes der Energieverteilung im Normalspectrum", *Verhandlungen der Deutschen Physikalischen Gesellschaft*, vol. 2, pp. 237–245, 17 1900.

[4] J. P. Gordon, H. J. Zeiger, and C. H. Townes, "The maser—new type of microwave amplifier, frequency standard, and spectrometer", *Phys. Rev.*, vol. 99, pp. 1264–1274, 4 1955. DOI: 10.1103/PhysRev.99.1264.

[5] T. H. Maiman, "Stimulated optical radiation in ruby", en, *Nature*, vol. 187, no. 4736, pp. 493–494, 1960, ISSN: 1476-4687. DOI: 10.1038/187493a0.

[6] LaserFest. (2021). "The first ruby laser", [Online]. Available: http://www.laserfest.org/lasers/how/ruby.cfm (visited on 05/28/2021).

[7] P. P. Sorokin and M. J. Stevenson, "Stimulated infrared emission from trivalent uranium", *Phys. Rev. Lett.*, vol. 5, pp. 557–559, 12 1960. DOI: 10.1103/PhysRevLett.5.557.

[8] A. Javan, W. R. Bennett, and D. R. Herriott, "Population inversion and continuous optical maser oscillation in a gas discharge containing a He-Ne mixture", *Phys. Rev. Lett.*, vol. 6, pp. 106–110, 3 1961. DOI: 10.1103/PhysRevLett.6.106.

[9] E. Snitzer, "Optical maser action of Nd^{3+} in a barium crown glass", *Phys. Rev. Lett.*, vol. 7, pp. 444–446, 12 1961. DOI: 10.1103/PhysRevLett.7.444.

[10] R. N. Hall, G. E. Fenner, J. D. Kingsley, T. J. Soltys, and R. O. Carlson, "Coherent light emission from GaAs junctions", *Phys. Rev. Lett.*, vol. 9, pp. 366–368, 9 1962. DOI: 10.1103/PhysRevLett.9.366.

[11] R. J. Keyes and T. M. Quist, "Injection luminiscent pumping of CaF_2:U^{3+} with GaAs diode lasers", *Applied Physics Letters*, vol. 4, no. 3, pp. 50–52, 1964. DOI: 10.1063/1.1753958.

[12] F. J. McClung and R. W. Hellwarth, "Giant optical pulsations from ruby", *Journal of Applied Physics*, vol. 33, no. 3, pp. 828–829, 1962. DOI: 10.1063/1.1777174.

[13] L. E. Hargrove, R. L. Fork, and M. A. Pollack, "Locking of He–Ne laser modes induced by synchronous intracavity modulation", *Applied Physics Letters*, vol. 5, no. 1, pp. 4–5, 1964. DOI: 10.1063/1.1754025.

[14] J. E. Geusic, H. M. Marcos, and L. G. Van Uitert, "Laser oscillations in Nd-doped yttrium aluminum, yttrium gallium and gadolinium garnets", *Applied Physics Letters*, vol. 4, no. 10, pp. 182–184, 1964. DOI: 10.1063/1.1753928.

[15] C. K. N. Patel, "Continuous-wave laser action on vibrational-rotational transitions of CO_2", *Phys. Rev.*, vol. 136, A1187–A1193, 5A 1964. DOI: 10.1103/PhysRev.136.A1187.

[16] D. Strickland and G. Mourou, "Compression of amplified chirped optical pulses", *Optics Communications*, vol. 56, no. 3, pp. 219–221, 1985, ISSN: 0030-4018.

[17] P. F. Moulton, "Spectroscopic and laser characteristics of Ti:Al_2O_3", *J. Opt. Soc. Am. B*, vol. 3, no. 1, pp. 125–133, 1986. DOI: 10.1364/JOSAB.3.000125.

[18] U. Morgner, F. X. Kärtner, S. H. Cho, Y. Chen, H. A. Haus, J. G. Fujimoto, E. P. Ippen, V. Scheuer, G. Angelow, and T. Tschudi, "Sub-two-cycle pulses from a Kerr-lens mode-locked Ti:sapphire laser", *Opt. Lett.*, vol. 24, no. 6, pp. 411–413, 1999. DOI: 10.1364/OL.24.000411.

[19] Thales Group. (2019). "World's most powerful laser developed by Thales and ELI-NP achieves record power level of 10 PW", [Online]. Available: http://www.thalesgroup.com/en/group/journalist/press-release/worlds-most-powerful-laser-developed-thales-and-eli-np-achieves (visited on 05/28/2021).

[20] P. Lacovara, H. K. Choi, C. A. Wang, R. L. Aggarwal, and T. Y. Fan, "Room-temperature diode-pumped Yb:YAG laser", *Opt. Lett.*, vol. 16, no. 14, pp. 1089–1091, 1991. DOI: 10.1364/OL.16.001089.

[21] A. Giesen, H. Hügel, A. Voss, K. Wittig, U. Brauch, and H. Opower, "Scalable concept for diode-pumped high-power solid-state lasers", en, *Applied Physics B*, vol. 58, no. 5, pp. 365–372, 1994, ISSN: 1432-0649. DOI: 10.1007/BF01081875.

[22] C. H. Townes, *The first laser*, L. Garwin and T. Lincoln, Eds. University of Chicago Press, 2010, ch. 8, pp. 105–114, ISBN: 9780226284163.

[23] W. Koechner, *Solid-State Laser Engineering*, 6th ed. Springer-Verlag New York, 2006, ISBN: 978-0-387-29094-2.

[24] D. Rostohar, M. Böhm, J. Brajer, J. Kaufman, S. Zulić, and T. Mocek, "Development of experimental station for laser shock peening at HiLASE", in *Laser 3D Manufacturing V*, H. Helvajian, B. Gu, and A. Piqué, Eds., International Society for Optics and Photonics, vol. 10523, SPIE, 2018, pp. 81–85. DOI: 10.1117/12.2297092.

[25] B. N. Chichkov, C. Momma, S. Nolte, F. von Alvensleben, and A. Tünnermann, "Femtosecond, picosecond and nanosecond laser ablation of solids", *Applied Physics A*, vol. 63, pp. 109–115, 1996. DOI: 10.1007/BF01567637.

[26] B. M. Walsh, "Review of Tm and Ho materials; spectroscopy and lasers", *Laser Physics*, vol. 19, no. 4, p. 2855, 2009. DOI: 10.1134/S1054660X09040446.

[27] W. S. Graves, J. Bessuille, P. Brown, S. Carbajo, V. Dolgashev, K.-H. Hong, E. Ihloff, B. Khaykovich, H. Lin, K. Murari, E. A. Nanni, G. Resta, S. Tantawi, L. E. Zapata, F. X. Kärtner, and D. E. Moncton, "Compact x-ray source based on burst-mode inverse Compton scattering at 100 kHz", *Phys. Rev. ST Accel. Beams*, vol. 17, p. 120 701, 12 2014. DOI: 10.1103/PhysRevSTAB.17.120701.

[28] T. Nakajyo, J. Yang, F. Sakai, and Y. Aoki, "Quantum efficiencies of Mg photocathode under illumination with 3rd and 4th harmonics Nd:$LiYF_4$ laser light in RF gun", *Japanese Journal of Applied Physics*, vol. 42, no. Part 1, No. 3, pp. 1470–1474, 2003. DOI: 10.1143/jjap.42.1470.

[29] C. Herkommer, P. Krötz, R. Jung, S. Klingebiel, C. Wandt, R. Bessing, P. Walch, T. Produit, K. Michel, D. Bauer, R. Kienberger, and T. Metzger, "Ultrafast thin-disk multipass amplifier with 720 mj operating at kilohertz repetition rate for applications in atmospheric research", *Opt. Express*, vol. 28, no. 20, pp. 30 164–30 173, Jul. 2020. DOI: 10.1364/OE.404185.

[30] M. Weber, *Handbook of Lasers*, ser. Laser & Optical Science & Technology. Taylor & Francis, 2000, ISBN: 9780849335099.

[31] A. A. Kaminskii, *Laser Crystals: Their Physics and Properties*, 2nd ed., ser. Springer Series in Optical Sciences. Springer-Verlag Berlin Heidelberg, 1990, vol. 14, ISBN: 978-3-540-70749-3.

[32] A. Kaminskii, "Laser crystals and ceramics: Recent advances", *Laser & Photonics Reviews*, vol. 1, no. 2, pp. 93–177, 2007. DOI: 10.1002/lpor.200710008.

[33] M. F. Churbanov, B. I. Denker, B. I. Galagan, V. V. Koltashev, V. G. Plotnichenko, M. V. Sukhanov, S. E. Sverchkov, and A. P. Velmuzhov, "First demonstration of ~ 5 μm laser action in terbium-doped selenide glass", *Applied Physics B*, vol. 126, p. 117, 2020. DOI: 10.1007/s00340-020-07473-w.

[34] H. Injeyan and G. D. Goodno, *High Power Laser Handbook*, 1st ed. The McGraw-Hill Companies, Inc., 2011, ISBN: 9780071609012.

[35] S. R. Bowman, M. J. Winings, R. C. Y. Auyeung, J. E. Tucker, S. K. Searles, and B. J. Feldman, "Laser and spectral properties of Cr, Tm, Ho:YAG at 2.1 μm", *IEEE Journal of Quantum Electronics*, vol. 27, no. 9, pp. 2142–2149, 1991. DOI: 10.1109/3.135173.

[36] J.-H. Wolter, M. A. Ahmed, and T. Graf, "Thin-disk laser operation of Ti:sapphire", *Opt. Lett.*, vol. 42, no. 8, pp. 1624–1627, 2017. DOI: 10.1364/OL.42.001624.

[37] S. Vasilyev, I. Moskalev, M. Mirov, S. Mirov, and V. Gapontsev, "Multi-watt mid-IR femtosecond polycrystalline Cr^{2+}:ZnS and Cr^{2+}:ZnSe laser amplifiers with the spectrum spanning 2.0-2.6 μm", *Opt. Express*, vol. 24, no. 2, pp. 1616–1623, 2016. DOI: 10.1364/OE.24.001616.

[38] I. Moskalev, S. Mirov, M. Mirov, S. Vasilyev, V. Smolski, A. Zakrevskiy, and V. Gapontsev, "140 W Cr:ZnSe laser system", *Opt. Express*, vol. 24, no. 18, pp. 21 090–21 104, 2016. DOI: 10.1364/OE.24.021090.

[39] S. Vasilyev, J. Peppers, I. Moskalev, V. Smolski, M. Mirov, E. Slobodchikov, A. Dergachev, S. Mirov, and V. Gapontsev, "1.5-mJ Cr:ZnSe chirped pulse amplifier seeded by a kerr-lens mode-locked Cr:ZnS oscillator", in *Laser Congress 2019 (ASSL, LAC, LS&C)*, Optical Society of America, 2019, ATu4A.4. DOI: 10.1364/ASSL.2019.ATu4A.4.

[40] J. Šulc and H. Jelínková, "5 - Solid-state lasers for medical applications", in *Lasers for Medical Applications*, ser. Woodhead Publishing Series in Electronic and Optical Materials, H. Jelínková, Ed., Woodhead Publishing, 2013, pp. 127–176, ISBN: 978-0-85709-237-3. DOI: 10.1533/9780857097545.2.127.

[41] U. Demibas and F. X. Kärtner, "A comparative study of continuous wave Ti:Sapphire, Cr:LiSAF, Cr:LiCAF and alexandrite lasers in thin-disk geometry", in *2019 Conference on Lasers and Electro-Optics Europe & European Quantum Electronics Conference (CLEO/Europe-EQEC)*, 2019, p. 1. DOI: 10.1109/CLEOE-EQEC.2019.8872864.

[42] D. Martyshkin, V. Fedorov, M. Mirov, I. Moskalev, S. Vasilyev, and S. Mirov, "High average power (35 W) pulsed Fe:ZnSe laser tunable over 3.8-4.2 μm", in *CLEO: 2015*, Optical Society of America, 2015, SF1F.2. DOI: 10.1364/CLEO_SI.2015.SF1F.2.

[43] E. Migal, A. Pushkin, B. Bravy, V. Gordienko, N. Minaev, A. Sirotkin, and F. Potemkin, "3.5-mJ 150-fs Fe:ZnSe hybrid mid-IR femtosecond laser at 4.4 μm for driving extreme nonlinear optics", *Opt. Lett.*, vol. 44, no. 10, pp. 2550–2553, 2019. DOI: 10.1364/OL.44.002550.

[44] A. Mandl and D. E. Klimek, "Textron's J-HPSSL 100 kW ThinZag laser program", in *CLEO/QELS: 2010 Laser Science to Photonic Applications*, 2010, pp. 1–1.

[45] C. N. Danson, C. Haefner, J. Bromage, T. Butcher, J.-C. F. Chanteloup, E. A. Chowdhury, A. Galvanauskas, L. A. Gizzi, J. Hein, D. I. Hillier, and et al., "Petawatt and exawatt class lasers worldwide", *High Power Laser Science and Engineering*, vol. 7, e54, 2019. DOI: 10.1017/hpl.2019.36.

[46] E. V. Zharikov, V. I. Zhekov, L. A. Kulevskii, T. M. Murina, V. V. Osiko, A. M. Prokhorov, A. D. Savel'ev, V. V. Smirnov, B. P. Starikov, and M. I. Timoshechkin, "Stimulated emission from Er^{3+}ions in yttrium aluminum garnet crystals at λ = 2.94 μ", *Soviet Journal of Quantum Electronics*, vol. 4, no. 8, pp. 1039–1040, 1975. DOI: 10.1070/qe1975v004n08abeh011147.

[47] A. Wienke, D. Wandt, U. Morgner, J. Neumann, and D. Kracht, "Comparison between Tm:YAP and Ho:YAG ultrashort pulse regenerative amplification", *Opt. Express*, vol. 24, no. 8, pp. 8632–8640, 2016. DOI: 10.1364/OE.24.008632.

[48] K. Scholle and P. Fuhrberg, "In-band pumping of high-power Ho:YAG lasers by laser diodes at 1.9μm", in *Conference on Lasers and Electro-Optics/Quantum Electronics and Laser Science Conference and Photonic Applications Systems Technologies*, Optical Society of America, 2008, CTuAA1.

[49] M. Hemmer, D. Sánchez, M. Jelínek, V. Smirnov, H. Jelinkova, V. Kubeček, and J. Biegert, "2-μm wavelength, high-energy Ho:YLF chirped-pulse amplifier for mid-infrared OPCPA", *Opt. Lett.*, vol. 40, no. 4, pp. 451–454, 2015. DOI: 10.1364/OL.40.000451.

[50] L. von Grafenstein, M. Bock, D. Ueberschaer, U. Griebner, and T. Elsaesser, "Ho:YLF chirped pulse amplification at kilohertz repetition rates – 4.3 ps pulses at 2 μm with GW peak power", *Opt. Lett.*, vol. 41, no. 20, pp. 4668–4671, 2016. DOI: 10.1364/OL.41.004668.

[51] J. Zhang, F. Schulze, K. F. Mak, V. Pervak, D. Bauer, D. Sutter, and O. Pronin, "High-power, high-efficiency Tm:YAG and Ho:YAG thin-disk lasers", *Laser & Photonics Reviews*, vol. 12, no. 3, p. 1 700 273, 2018. DOI: 10.1002/lpor.201700273.

[52] J. Zhang, K. F. Mak, and O. Pronin, "Kerr-lens mode-locked 2-μm thin-disk lasers", *IEEE Journal of Selected Topics in Quantum Electronics*, vol. 24, no. 5, pp. 1–11, 2018. DOI: 10.1109/JSTQE.2018.2814780.

[53] M. Eichhorn, "Quasi-three-level solid-state lasers in the near and mid infrared based on trivalent rare earth ions", *Applied Physics B*, no. 2, p. 269, 2008. DOI: 10.1007/s00340-008-3214-0.

[54] K. Beil, S. T. Fredrich-Thornton, F. Tellkamp, R. Peters, C. Kränkel, K. Petermann, and G. Huber, "Thermal and laser properties of Yb:LuAG for kW thin disk lasers", *Opt. Express*, vol. 18, no. 20, pp. 20 712–20 722, 2010. DOI: 10.1364/OE.18.020712.

[55] J. Zhang, J. Brons, M. Seidel, V. Pervak, V. Kalashnikov, Z. Wei, A. Apolonski, F. Krausz, and O. Pronin, "49-fs Yb:YAG thin-disk oscillator with distributed Kerr-lens mode-locking", in *2015 European Conference on Lasers and Electro-Optics - European Quantum Electronics Conference*, Optical Society of America, 2015, PD_A_1.

[56] A. Sennaroglu, *Solid-State Lasers and Applications*, 1st ed. CRC Press, 2007, ISBN: 978-0367389871.

[57] R. L. Aggarwal, D. J. Ripin, J. R. Ochoa, and T. Y. Fan, "Measurement of thermo-optic properties of $Y_3Al_5O_{12}$, $Lu_3Al_5O_{12}$, $YAlO_3$, $LiYF_4$, $LiLuF_4$, BaY_2F_8, $KGd(WO_4)_2$, and $KY(WO_4)_2$ laser crystals in the 80–300K temperature range", *Journal of Applied Physics*, vol. 98, no. 10, p. 103 514, 2005. DOI: 10.1063/1.2128696.

[58] S. Chénais, F. Druon, S. Forget, F. Balembois, and P. Georges, "On thermal effects in solid-state lasers: The case of ytterbium-doped materials", *Progress in Quantum Electronics*, vol. 30, no. 4, pp. 89–153, 2006, ISSN: 0079-6727. DOI: 10.1016/j.pquantelec.2006.12.001.

[59] A. Brenier, Y. Guyot, H. Canibano, G. Boulon, A. Ródenas, D. Jaque, A. Eganyan, and A. G. Petrosyan, "Growth, spectroscopic, and laser properties of Yb^{3+}-doped $Lu_3Al_5O_{12}$ garnet crystal", *J. Opt. Soc. Am. B*, vol. 23, no. 4, pp. 676–683, 2006. DOI: 10.1364/JOSAB.23.000676.

[60] P. A. Loiko, V. V. Filippov, K. V. Yumashev, N. V. Kuleshov, and A. A. Pavlyuk, "Thermo-optic coefficients study in $KGd(WO_4)_2$ and $KY(WO_4)_2$ by a modified minimum deviation method", *Appl. Opt.*, vol. 51, no. 15, pp. 2951–2957, 2012. DOI: 10.1364/AO.51.002951.

[61] J. Körner, M. Krüger, J. Reiter, A. Münzer, J. Hein, and M. C. Kaluza, "Temperature dependent spectroscopic study of Yb^{3+}-doped $KG(WO_4)_2$, $KY(WO_4)_2$, $YAlO_3$ and $YLiF_4$ for laser applications", *Opt. Mater. Express*, vol. 10, no. 10, pp. 2425–2438, 2020. DOI: 10.1364/OME.398740.

[62] M. Smrž, T. Miura, M. Chyla, S. Nagisetty, O. Novák, A. Endo, and T. Mocek, "Suppression of nonlinear phonon relaxation in Yb:YAG thin disk via zero phonon line pumping", *Opt. Lett.*, vol. 39, no. 16, pp. 4919–4922, 2014. DOI: 10.1364/OL.39.004919.

[63] L. Wang, H. Huang, D. Shen, J. Zhang, H. Chen, and D. Tang, "Diode-pumped high power 2.7 μm Er:Y_2O_3 ceramic laser at room temperature", *Optical Materials*, vol. 71, pp. 70–73, 2017, 11th Laser Ceramics Symposium: International Symposium on Transparent Ceramics for Photonic Applications (11th LCS), Xuzhou, China, November 30-December 4, 2015, ISSN: 0925-3467. DOI: 10.1016/j.optmat.2016.06.014.

[64] R. Švejkar, J. Šulc, and H. Jelínková, "Er-doped crystalline active media for ~ 3 μm diode-pumped lasers", *Progress in Quantum Electronics*, vol. 74, p. 100 276, 2020, ISSN: 0079–6727. DOI: 10.1016/j.pquantelec.2020.100276.

[65] T. Sanamyan, M. Kanskar, Y. Xiao, D. Kedlaya, and M. Dubinskii, "High power diode-pumped 2.7-μm Er^{3+}:Y_2O_3 laser with nearly quantum defect-limited efficiency", *Opt. Express*, vol. 19, no. S5, A1082–A1087, 2011. DOI: 10.1364/OE.19.0A1082.

[66] O. E. Martinez, J. P. Gordon, and R. L. Fork, "Negative group-velocity dispersion using refraction", *J. Opt. Soc. Am. A*, vol. 1, no. 10, pp. 1003–1006, 1984. DOI: 10.1364/JOSAA.1.001003.

[67] E. Treacy, "Optical pulse compression with diffraction gratings", *IEEE Journal of Quantum Electronics*, vol. 5, no. 9, pp. 454–458, 1969. DOI: 10.1109/JQE.1969.1076303.

[68] A. Klenke, E. Seise, J. Limpert, and A. Tünnermann, "Basic considerations on coherent combining of ultrashort laser pulses", *Opt. Express*, vol. 19, no. 25, pp. 25 379–25 387, 2011. DOI: 10.1364/OE.19.025379.

[69] A. Dubietis, G. Jonušauskas, and A. Piskarskas, "Powerful femtosecond pulse generation by chirped and stretched pulse parametric amplification in BBO crystal", *Optics Communications*, vol. 88, no. 4, pp. 437–440, 1992, ISSN: 0030-4018. DOI: 10.1016/0030-4018(92)90070-8.

[70] F. Lureau, S. Laux, O. Casagrande, O. Chalus, A. Pellegrina, G. Matras, C. Radier, G. Rey, S. Ricaud, S. Herriot, P. Jougla, M. Charbonneau, P. Duvochelle, and C. Simon-Boisson, "Latest results of 10 petawatt laser beamline for ELI nuclear physics infrastructure", in *Solid State Lasers XXV: Technology and Devices*, W. A. Clarkson and R. K. Shori, Eds., International Society for Optics and Photonics, vol. 9726, SPIE, 2016, pp. 200 –207. DOI: 10.1117/12.2213067.

[71] S. Zhou, F. W. Wise, and D. G. Ouzounov, "Divided-pulse amplification of ultrashort pulses", *Opt. Lett.*, vol. 32, no. 7, pp. 871–873, 2007. DOI: 10.1364/OL.32.000871.

[72] L. J. Kong, L. M. Zhao, S. Lefrancois, D. G. Ouzounov, C. X. Yang, and F. W. Wise, "Generation of megawatt peak power picosecond pulses from a divided-pulse fiber amplifier", *Opt. Lett.*, vol. 37, no. 2, pp. 253–255, 2012. DOI: 10.1364/OL.37.000253.

[73] M. Kienel, A. Klenke, T. Eidam, M. Baumgartl, C. Jauregui, J. Limpert, and A. Tünnermann, "Analysis of passively combined divided-pulse amplification as an energy-scaling concept", *Opt. Express*, vol. 21, no. 23, pp. 29 031–29 042, 2013. DOI: 10.1364/OE.21.029031.

[74] P. Russbueldt, T. Mans, J. Weitenberg, H. D. Hoffmann, and R. Poprawe, "Compact diode-pumped 1.1 kW Yb:YAG Innoslab femtosecond amplifier", *Opt. Lett.*, vol. 35, no. 24, pp. 4169–4171, Dec. 2010. DOI: 10.1364/OL.35.004169.

[75] S. Nolte, F. Schrempel, and F. Dausinger, *Ultrashort Pulse Laser Technology: Laser Sources and Applications*, 1st ed., ser. Springer Series in Optical Sciences. Springer International Publishing, 2016, vol. 195, ISBN: 978-3-319-17659-8. DOI: 10.1007/978-3-319-17659-8.

[76] B. E. Schmidt, A. Hage, T. Mans, F. Légaré, and H. J. Wörner, "Highly stable, 54mJ Yb-InnoSlab laser platform at 0.5kW average power", *Opt. Express*, vol. 25, no. 15, pp. 17 549–17 555, 2017. DOI: 10.1364/OE.25.017549.

[77] M. L. Spaeth, K. R. Manes, M. Bowers, P. Celliers, J.-M. D. Nicola, P. D. Nicola, S. Dixit, G. Erbert, J. Heebner, D. Kalantar, O. Landen, B. MacGowan, B. V. Wonterghem, P. Wegner, C. Widmayer, and S. Yang, "National ignition facility laser system performance", *Fusion Science and Technology*, vol. 69, no. 1, pp. 366–394, 2016. DOI: 10.13182/FST15-136.

[78] P. D. Mason, M. Fitton, A. Lintern, S. Banerjee, K. Ertel, T. Davenne, J. Hill, S. P. Blake, P. J. Phillips, T. J. Butcher, J. M. Smith, M. D. Vido, R. J. S. Greenhalgh, C. Hernandez-Gomez, and J. L. Collier, "Scalable design for a high energy cryogenic gas cooled diode pumped laser amplifier", *Appl. Opt.*, vol. 54, no. 13, pp. 4227–4238, May 2015. DOI: 10.1364/AO.54.004227.

[79] HiLASE Centre. (2021). "A new world record for BIVOJ laser", [Online]. Available: https://www.hilase.cz/en/a-new-world-record-for-bivoj-laser/ (visited on 05/28/2021).

[80] M. Eichhorn, *Laser Physics: From Principles to Practical Work in the Lab*, 1st Edition. Springer International Publishing, 2014, ISBN: 978-3-319-05127-7.

[81] R.-A. Lorbeer, B. Ewers, C. Santek, D. Beisecker, J. Speiser, and T. Dekorsy, "Monolithic thin-disk laser and amplifier concept", *Optica*, vol. 7, no. 10, pp. 1409–1414, Aug. 2020. DOI: 10.1364/OPTICA.402164.

[82] S. Erhard, A. Giesen, M. Karszewski, T. Rupp, C. Stewen, I. Johannsen, and K. Contag, "Novel pump design of Yb:YAG thin disc laser for operation at room temperature with improved efficiency", in *Advanced Solid State Lasers*, Optical Society of America, 1999, p. MC3. DOI: 10.1364/ASSL.1999.MC3.

[83] B. Ewers, A. Fischer, and R.-A. Lorbeer, "Compact monolithic pump light geometry for thin disk lasers", in *Laser Congress 2019 (ASSL, LAC, LS&C)*, Optical Society of America, 2019, JTh3A.8. DOI: 10.1364/ASSL.2019.JTh3A.8.

[84] H. Stark, J. Buldt, M. Müller, A. Klenke, and J. Limpert, "1 kW, 10 mJ, 120 fs coherently combined fiber CPA laser system", *Opt. Lett.*, vol. 46, no. 5, pp. 969–972, 2021. DOI: 10.1364/OL.417032.

[85] A. Ullman, M. Curtin, G. Needham, H. Wang, and L. Zeldin, "Development of high-brightness thin disk lasers", *Journal of Directed Energy*, vol. 4, no. 1, pp. 110–118, 2010.

[86] T. Gottwald, C. Stolzenburg, D. Bauer, J. Kleinbauer, V. Kuhn, T. Metzger, S. Schad, D. Sutter, and A. Killi, "Recent disk laser development at Trumpf", in *High-Power Lasers 2012: Technology and Systems*, H. Ackermann and W. L. Bohn, Eds., International Society for Optics and Photonics, vol. 8547, SPIE, 2012, pp. 66–73. DOI: 10.1117/12.978990.

[87] S. Nagel, B. Metzger, D. Bauer, J. Dominik, T. Gottwald, V. Kuhn, A. Killi, T. Dekorsy, and S.-S. Schad, "Thin-disk laser system operating above 10 kW at near fundamental mode beam quality", *Opt. Lett.*, vol. 46, no. 5, pp. 965–968, 2021. DOI: 10.1364/OL.416432.

[88] A. Killi, C. Stolzenburg, I. Zawischa, D. Sutter, J. Kleinbauer, S. Schad, R. Brockmann, S. Weiler, J. Neuhaus, S. Kalfhues, E. Mehner, D. Bauer, H. Schlueter, and C. Schmitz, "The broad applicability of the disk laser principle: from CW to ps", in *Solid State Lasers XVIII: Technology and Devices*, W. A. Clarkson, N. Hodgson, and R. K. Shori, Eds., International Society for Optics and Photonics, vol. 7193, SPIE, 2009, pp. 477–485. DOI: 10.1117/12.808255.

[89] Y. H. Peng, Y. X. Lim, J. Cheng, Y. Guo, Y. Y. Cheah, and K. S. Lai, "Near fundamental mode 1.1 kW Yb:YAG thin-disk laser", *Opt. Lett.*, vol. 38, no. 10, pp. 1709–1711, 2013. DOI: 10.1364/OL.38.001709.

[90] J. A. der Au, G. J. Spühler, T. Südmeyer, R. Paschotta, R. Hövel, M. Moser, S. Erhard, M. Karszewski, A. Giesen, and U. Keller, "16.2-W average power from a diode-pumped femtosecond Yb:YAG thin disk laser", *Opt. Lett.*, vol. 25, no. 11, pp. 859–861, 2000. DOI: 10.1364/OL.25.000859.

[91] C. J. Saraceno, F. Emaury, C. Schriber, M. Hoffmann, M. Golling, T. Südmeyer, and U. Keller, "Ultrafast thin-disk laser with 80 µJ pulse energy and 242 W of average power", *Opt. Lett.*, vol. 39, no. 1, pp. 9–12, 2014. DOI: 10.1364/OL.39.000009.

[92] F. Saltarelli, I. J. Graumann, L. Lang, D. Bauer, C. R. Phillips, and U. Keller, "Power scaling of ultrafast oscillators: 350-W average-power sub-picosecond thin-disk laser", *Opt. Express*, vol. 27, no. 22, pp. 31 465–31 474, 2019. DOI: 10.1364/OE.27.031465.

[93] C. R. E. Baer, C. Kränkel, C. J. Saraceno, O. H. Heckl, M. Golling, R. Peters, K. Petermann, T. Südmeyer, G. Huber, and U. Keller, "Femtosecond thin-disk laser with 141 W of average power", *Opt. Lett.*, vol. 35, no. 13, pp. 2302–2304, 2010. DOI: 10.1364/OL.35.002302.

[94] O. Pronin, J. Brons, C. Grasse, V. Pervak, G. Boehm, M.-C. Amann, V. L. Kalashnikov, A. Apolonski, and F. Krausz, "High-power 200 fs Kerr-lens mode-locked Yb:YAG thin-disk oscillator", *Opt. Lett.*, vol. 36, no. 24, pp. 4746–4748, 2011. DOI: 10.1364/OL.36.004746.

[95] J. Brons, V. Pervak, E. Fedulova, D. Bauer, D. Sutter, V. Kalashnikov, A. Apolonskiy, O. Pronin, and F. Krausz, "Energy scaling of Kerr-lens mode-locked thin-disk oscillators", *Opt. Lett.*, vol. 39, no. 22, pp. 6442–6445, 2014. DOI: 10.1364/OL.39.006442.

[96] A. A. Eilanlou, Y. Nabekawa, M. Kuwata-Gonokami, and K. Midorikawa, "Femtosecond laser pulses in a Kerr lens mode-locked thin-disk ring oscillator with an intra-cavity peak power beyond 100 MW", *Japanese Journal of Applied Physics*, vol. 53, no. 8, p. 082 701, 2014. DOI: 10.7567/jjap.53.082701.

[97] J. Brons, V. Pervak, D. Bauer, D. Sutter, O. Pronin, and F. Krausz, "Powerful 100-fs-scale Kerr-lens mode-locked thin-disk oscillator", *Opt. Lett.*, vol. 41, no. 15, pp. 3567–3570, 2016. DOI: 10.1364/OL.41.003567.

[98] C. J. Saraceno, F. Emaury, O. H. Heckl, C. R. E. Baer, M. Hoffmann, C. Schriber, M. Golling, T. Südmeyer, and U. Keller, "275 W average output power from a femtosecond thin disk oscillator operated in a vacuum environment", *Opt. Express*, vol. 20, no. 21, pp. 23 535–23 541, 2012. DOI: 10.1364/OE.20.023535.

[99] S. Klingebiel, M. Schultze, C. Y. Teisset, R. Bessing, M. Häfner, S. Prinz, M. Gorjan, D. Sutter, K. Michel, H. G. Barros, Z. Major, F. Krausz, and T. Metzger, "220mJ ultrafast thin-disk regenerative amplifier", in *2015 Conference on Lasers and Electro-Optics (CLEO)*, 2015, pp. 1–2. DOI: 10.1364/CLEO_SI.2015.STu4O.2.

[100] C. Y. Teisset, M. Schultze, R. Bessing, M. Häfner, S. Prinz, D. Sutter, and T. Metzger, "300 W picosecond thin-disk regenerative amplifier at 10 kHz repetition rate", in *Advanced Solid-State Lasers Congress Postdeadline*, Optical Society of America, 2013, JTh5A.1.

[101] T. Nubbemeyer, M. Kaumanns, M. Ueffing, M. Gorjan, A. Alismail, H. Fattahi, J. Brons, O. Pronin, H. G. Barros, Z. Major, T. Metzger, D. Sutter, and F. Krausz, "1 kW, 200 mJ picosecond thin-disk laser system", *Opt. Lett.*, vol. 42, no. 7, pp. 1381–1384, Apr. 2017. DOI: 10.1364/OL.42.001381.

[102] C. Röcker, A. Loescher, J.-P. Negel, M. Delaigue, F. Morin, C. Hönninger, E. Mottay, P. Villeval, A. Holvoet, D. Lupinski, T. Graf, and M. Abdou Ahmed, "Direct amplification of sub-300 fs pulses in a versatile thin-disk multipass amplifier", *Optics Communications*, vol. 460, p. 125 159, 2020, ISSN: 0030–4018. DOI: 10.1016/j.optcom.2019.125159.

[103] C. Wandt, C. Herkommer, R. Jung, S. Klingebiel, P. Krötz, S. Prinz, M. Rampp, C. Y. Teisset, K. Michel, and T. Metzger, "Ultrafast thin-disk based CPA system with <.1kW output power and <.500 fs pulse duration", in *OSA High-brightness Sources and Light-driven Interactions Congress 2020 (EUVXRAY, HILAS, MICS)*, Optical Society of America, 2020, HM2B.4. DOI: 10.1364/HILAS.2020.HM2B.4.

[104] J.-P. Negel, A. Loescher, A. Voss, D. Bauer, D. Sutter, A. Killi, M. A. Ahmed, and T. Graf, "Ultrafast thin-disk multipass laser amplifier delivering 1.4 kW (4.7 mJ, 1030 nm) average power converted to 820 W at 515 nm and 234 W at 343 nm", *Opt. Express*, vol. 23, no. 16, pp. 21 064–21 077, 2015. DOI: 10.1364/OE.23.021064.

[105] T. Dietz, M. Jenne, D. Bauer, M. Scharun, D. Sutter, and A. Killi, "Ultrafast thin-disk multi-pass amplifier system providing 1.9 kW of average output power and pulse energies in the 10 mJ range at 1 ps of pulse duration for glass-cleaving applications", *Opt. Express*, vol. 28, no. 8, pp. 11 415–11 423, Apr. 2020. DOI: 10.1364/OE.383926.

[106] C. Hönninger, I. Johannsen, M. Moser, G. Zhang, A. Giesen, and U. Keller, "Diode-pumped thin-disk Yb:YAG regenerative amplifier", *Applied Physics B*, vol. 65, no. 3, pp. 423–426, 1997. DOI: 10.1007/s003400050291.

[107] T. Metzger, A. Schwarz, C. Y. Teisset, D. Sutter, A. Killi, R. Kienberger, and F. Krausz, "High-repetition-rate picosecond pump laser based on a Yb:YAG disk amplifier for optical parametric amplification", *Opt. Lett.*, vol. 34, no. 14, pp. 2123–2125, 2009. DOI: 10.1364/OL.34.002123.

[108] M. Chyla, T. Miura, M. Smrz, H. Jelinkova, A. Endo, and T. Mocek, "Optimization of beam quality and optical-to-optical efficiency of Yb:YAG thin-disk regenerative amplifier by pulsed pumping", *Opt. Lett.*, vol. 39, no. 6, pp. 1441–1444, 2014. DOI: 10.1364/OL.39.001441.

[109] J. Novák, J. T. Green, T. Metzger, T. Mazanec, B. Himmel, M. Horáček, Z. Hubka, R. Boge, R. Antipenkov, F. Batysta, J. A. Naylon, P. Bakule, and B. Rus, "Thin disk amplifier-based 40 mJ, 1 kHz, picosecond laser at 515 nm", *Opt. Express*, vol. 24, no. 6, pp. 5728–5733, 2016. DOI: 10.1364/OE.24.005728.

[110] R. Jung, J. Tümmler, T. Nubbemeyer, and I. Will, "Thin-disk ring amplifier for high pulse energy", *Opt. Express*, vol. 24, no. 5, pp. 4375–4381, 2016. DOI: 10.1364/OE.24.004375.

[111] D. Müller, S. Erhard, O. Ronsin, and A. Giesen, "Thin disk multi-pass amplifier", in *Advanced Solid-State Photonics*, Optical Society of America, 2003, p. 278. DOI: 10.1364/ASSP.2003.278.

[112] Thorlabs Inc. (2021). "Relationship between rise time and bandwidth for a low-pass system", [Online]. Available: https://www.thorlabs.com/newgrouppage9.cfm?objectgroup_id=9817 (visited on 05/28/2021).

[113] M. G. Howard W. Johnson, *High-speed Digital Design: A Handbook of Black Magic*, 2nd ed. Prentice Hall, 1993, ISBN: 9780133957242.

[114] D. J. Kane and R. Trebino, "Single-shot measurement of the intensity and phase of an arbitrary ultrashort pulse by using frequency-resolved optical gating", *Opt. Lett.*, vol. 18, no. 10, pp. 823–825, 1993. DOI: 10.1364/OL.18.000823.

[115] C. Iaconis and I. A. Walmsley, "Spectral phase interferometry for direct electric-field reconstruction of ultrashort optical pulses", *Opt. Lett.*, vol. 23, no. 10, pp. 792–794, 1998. DOI: 10.1364/OL.23.000792.

[116] N. Hodgson and H. Weber, *Laser Resonators and Beam Propagation, Fundamentals, Advanced Concepts, Applications*, 2nd ed., ser. Springer Series in Optical Sciences. Springer-Verlag Berlin Heidelberg, 2005, vol. 108, ISBN: 978-0-387-40078-5. DOI: 10.1007/b106789.

[117] Orion Project. (2021). "reZonator", [Online]. Available: http://www.rezonator.orion-project.org/ (visited on 05/28/2021).

[118] C. Horvath and F. Loesel. (2021). "Winlase laser cavity simulation software", [Online]. Available: http://www.winlase.com/ (visited on 05/28/2021).

[119] Y. SATO, J. SAIKAWA, I. SHOJI, T. TAIRA, and A. IKESUE, "Spectroscopic properties and laser operation of Nd: $Y_3ScAl_4O_{12}$ polycrystalline gain media, solid-solution of Nd: $Y_3Al_5O_{12}$ and Nd: $Y_3Sc_2Al_3O_{12}$ ceramics", *Journal of the Ceramic Society of Japan, Supplement*, vol. 112, S313–S316, 2004. DOI: 10.14852/jcersjsuppl.112.0.S313.0.

[120] Y. Sato, J. Saikawa, T. Taira, and A. Ikesue, "Characteristics of Nd^{3+}-doped $Y_3ScAl_4O_{12}$ ceramic laser", *Optical Materials*, vol. 29, no. 10, pp. 1277–1282, 2007, Proceedings of the 1st International Laser Ceramic Symposium, ISSN: 0925-3467. DOI: 10.1016/j.optmat.2006.01.032.

[121] J. Saikawa, Y. Sato, T. Taira, and A. Ikesue, "Absorption, emission spectrum properties, and efficient laser performances of Yb:$Y_3ScAl_4O_{12}$ ceramics", *Applied Physics Letters*, vol. 85, no. 11, pp. 1898–1900, 2004. DOI: 10.1063/1.1791339.

[122] B. M. Walsh, N. P. Barnes, R. L. Hutcheson, R. W. Equall, and B. D. Bartolo, "Spectroscopy and lasing characteristics of Nd-doped $Y_3Ga_xAl_{(5-x)}O_{12}$ materials: Application toward a compositionally tuned 0.94-μm laser", *J. Opt. Soc. Am. B*, vol. 15, no. 11, pp. 2794–2801, 1998. DOI: 10.1364/JOSAB.15.002794.

[123] B.-T. Zhang, J.-L. He, Z.-T. Jia, Y.-B. Li, S.-D. Liu, Z.-W. Wang, R.-H. Wang, X.-M. Liu, and X. tang Tao, "Spectroscopy and laser properties of Yb-doped $Gd_3Al_xGa_{(5-x)}O_{12}$ crystal", *Applied Physics Express*, vol. 6, no. 8, p. 082 702, Jun. 2013. DOI: 10.7567/apex.6.082702.

[124] *Konoshima Chemical Co. Ltd. – ceramics*, http://www.konoshima.co.jp/eng/ceramics/index.html, Accessed: 2021-05-28.

[125] Y. Oishi, K. Okamura, K. Miyazaki, N. Saito, M. Iwasaki, and S. Wada, "Amplifying high energy pulses at 1062.78 nm with diode pumped Nd:YGAG ceramic", in *Advanced Solid-State Lasers Congress*, Optical Society of America, 2013, ATu3A.40. DOI: 10.1364/ASSL.2013.ATu3A.40.

[126] V. Jambunathan, L. Horackova, T. Miura, J. Sulc, H. Jelínková, A. Endo, A. Lucianetti, and T. Mocek, "Spectroscopic and lasing characteristics of Yb:YGAG ceramic at cryogenic temperatures", *Opt. Mater. Express*, vol. 5, no. 6, pp. 1289–1295, Jun. 2015. DOI: 10.1364/OME.5.001289.

[127] J. Huynh, M. Smrž, T. Miura, O. Slezák, D. Vojna, M. Čech, A. Endo, and T. Mocek, "Femtosecond Yb:YGAG ceramic slab regenerative amplifier", *Opt. Mater. Express*, vol. 8, no. 3, pp. 615–621, 2018. DOI: 10.1364/OME.8.000615.

[128] Y. Sato, J. Akiyama, and T. Taira, "Effects of rare-earth doping on thermal conductivity in $Y_3Al_5O_{12}$ crystals", *Optical Materials*, vol. 31, no. 5, pp. 720–724, 2009, Selected Papers from the 3rd Laser Ceramics Symposium: International Symposium on Transparent Ceramics for Photonic Applications, ISSN: 0925-3467. DOI: 10.1016/j.optmat.2008.10.040.

[129] U. Keller, T. H. Chiu, and J. F. Ferguson, "Self-starting femtosecond mode-locked Nd:glass laser that uses intracavity saturable absorbers", *Opt. Lett.*, vol. 18, no. 13, pp. 1077–1079, 1993. DOI: 10.1364/OL.18.001077.

[130] T. Brabec, C. Spielmann, P. F. Curley, and F. Krausz, "Kerr lens mode locking", *Opt. Lett.*, vol. 17, no. 18, pp. 1292–1294, 1992. DOI: 10.1364/OL.17.001292.

[131] C. Hönninger, R. Paschotta, F. Morier-Genoud, M. Moser, and U. Keller, "Q-switching stability limits of continuous-wave passive mode locking", *J. Opt. Soc. Am. B*, vol. 16, no. 1, pp. 46–56, 1999. DOI: 10.1364/JOSAB.16.000046.

[132] K. F. Wall, D. E. Miller, and T. Y. Fan, "Cryo-Yb:YAG lasers for next-generation photoinjector applications", in *Solid State Lasers XXI: Technology and Devices*, W. A. Clarkson and R. K. Shori, Eds., International Society for Optics and Photonics, vol. 8235, SPIE, 2012, pp. 206 –214. DOI: 10.1117/12.907419.

[133] R. Adair, L. L. Chase, and S. A. Payne, "Nonlinear refractive index of optical crystals", *Phys. Rev. B*, vol. 39, pp. 3337–3350, 5 1989. DOI: 10.1103/PhysRevB.39.3337.

[134] *National Institute for Fusion Science*, http://www.nifs.ac.jp/en/, Accessed: 2021-05-28.

[135] T. Li, K. Beil, C. Kränkel, and G. Huber, "Efficient high-power continuous wave Er:Lu_2O_3 laser at 2.85 µm", *Opt. Lett.*, vol. 37, no. 13, pp. 2568–2570, Jul. 2012. DOI: 10.1364/OL.37.002568.

[136] Y.-F. Chen, "Pump-to-mode size ratio dependence of thermal loading in diode-end-pumped solid-state lasers", *J. Opt. Soc. Am. B*, vol. 17, no. 11, pp. 1835–1840, Nov. 2000. DOI: 10.1364/JOSAB.17.001835.

[137] L.-L. Zhu, Y.-J. Park, L. Gan, S.-I. Go, H.-N. Kim, J.-M. Kim, and J.-W. Ko, "Fabrication and characterization of highly transparent Er:Y_2O_3 ceramics with ZrO_2 and La_2O_3 additives", *Ceramics International*, vol. 43, no. 16, pp. 13 127–13 132, 2017, ISSN: 0272-8842. DOI: 10.1016/j.ceramint.2017.07.004.

[138] H. Kawase, H. Uehara, W. Yao, H. Chen, and R. Yasuhara, "Optical chopper based mechanically Q-switched ~3 µm Er:YAP single-crystal laser", *Japanese Journal of Applied Physics*, vol. 60, p. 012 002, 1 Jan. 2021, ISSN: 0021-4922. DOI: 10.35848/1347-4065/abcd7c.

[139] V. Cardinali, E. Marmois, B. Le Garrec, and G. Bourdet, "Determination of the thermo-optic coefficient dn/dT of ytterbium doped ceramics (Sc_2O_3, Y_2O_3, Lu_2O_3, YAG), crystals (YAG, CaF_2) and neodymium doped phosphate glass at cryogenic temperature", *Optical Materials*, vol. 34, no. 6, pp. 990–994, 2012, 6th Laser Ceramics Symposium, ISSN: 0925-3467. DOI: 10.1016/j.optmat.2011.05.035.

[140] Y. Nigara, "Measurement of the optical constants of yttrium oxide", *Japanese Journal of Applied Physics*, vol. 7, no. 4, pp. 404–408, Apr. 1968. DOI: 10.1143/jjap.7.404.

[141] W. R. Manning, O. Hunter Jr., and B. R. Powell Jr., "Elastic properties of polycrystalline yttrium oxide, dysprosium oxide, holmium oxide, and erbium oxide: Room temperature measurements", *Journal of the American Ceramic Society*, vol. 52, no. 8, pp. 436–442, 1969. DOI: 10.1111/j.1151-2916.1969.tb11974.x.

[142] H. Uehara, S. Tokita, J. Kawanaka, D. Konishi, M. Murakami, S. Shimizu, and R. Yasuhara, "Optimization of laser emission at 2.8 μm by Er:Lu_2O_3 ceramics", *Opt. Express*, vol. 26, no. 3, pp. 3497–3507, 2018. DOI: 10.1364/OE.26.003497.

[143] H. Uehara, S. Tokita, J. Kawanaka, D. Konishi, M. Murakami, and R. Yasuhara, "A passively Q-switched compact Er:Lu_2O_3 ceramics laser at 2.8 μm with a graphene saturable absorber", *Appl. Phys. Express*, vol. 12, no. 2, p. 022 002, 2019. DOI: 10.7567/1882-0786/aaf994.

[144] *HiLASE Centre – GO pico: 1030 nm – picosecond fiber oscillator*, http://www.hilase.cz/en/products/go-pico/, Accessed: 2021-05-28.

[145] J. Fekete, A. Cserteg, and R. Szipöcs, "All-fiber, all-normal dispersion ytterbium ring oscillator", *Laser Physics Letters*, vol. 6, no. 1, pp. 49–53, 2009. DOI: 10.1002/lapl.200810098.

[146] M. Smrž, M. Chyla, O. Novák, T. Miura, A. Endo, and T. Mocek, "Amplification of picosecond pulses to 100 W by an Yb:YAG thin-disk with CVBG compressor", in *High-Power, High-Energy, and High-Intensity Laser Technology II*, J. Hein, Ed., International Society for Optics and Photonics, vol. 9513, SPIE, 2015, pp. 16 –22. DOI: 10.1117/12.2178900.

[147] *NKT Photonics – Onefive ORIGAMI ultra-low noise femtosecond laser*, http://www.nktphotonics.com/lasers-fibers/product/onefive-origami-ultra-low-noise-femtosecond-laser/, Accessed: 2021-05-28.

[148] L. Rumbaugh, *Fiber lasers and amplifiers design toolbox*, MATLAB Central File Exchange, Accessed: 2021-05-28, 2021. [Online]. Available: http://www.mathworks.com/matlabcentral/fileexchange/42122-fiber-lasers-and-amplifiers-design-toolbox.

[149] G. Agrawal, *Nonlinear Fiber Optics*, 5th Edition. Academic Press, 2006, p. 648, ISBN: 9780123970237.

[150] M. Ferreira, "Optical amplifiers | Raman, Brillouin and parametric amplifiers", in *Encyclopedia of Modern Optics*, R. D. Guenther, Ed., Oxford: Elsevier, 2005, pp. 297–308, ISBN: 978-0-12-369395-2. DOI: 10.1016/B0-12-369395-0/00663-1.

[151] Fibercryst. (2021). "Taranis amplifier", [Online]. Available: https://www.fibercryst.com/taranis-amplifier/ (visited on 05/28/2021).

[152] D. Twitchen, C. Pickles, S. Coe, R. Sussmann, and C. Hall, "Thermal conductivity measurements on CVD diamond", *Diamond and Related Materials*, vol. 10, no. 3, pp. 731–735, 2001, 11th European Conference on Diamond, Diamond-like Materials, Carbon Nanotubes, Nitrides and Silicon Carbide, ISSN: 0925-9635. DOI: 10.1016/S0925-9635(00)00515-X.

[153] V. Yanovsky, C. Felix, and G. Mourou, "Why ring regenerative amplification (regen)?", *Appl. Phys. B*, vol. 74, pp. 181–183, 2002. DOI: 10.1007/s00340-002-0887-7.

[154] J. Mende, E. Schmid, J. Speiser, G. Spindler, and A. Giesen, "Thin disk laser: power scaling to the kW regime in fundamental mode operation", in *Solid State Lasers XVIII: Technology and Devices*, W. A. Clarkson, N. Hodgson, and R. K. Shori, Eds., International Society for Optics and Photonics, vol. 7193, SPIE, 2009, pp. 493 –504. DOI: 10.1117/12.809031.

[155] T. Metzger, "High-repetition-rate picosecond pump laser based on an Yb:YAG disk amplifier for optical parametric amplification", Ph.D. dissertation, Technischen Universität Berlin, 2009.

[156] *LAYERTEC catalog – Common laser types*, http://www.layertec.de/files/catalog/2020/LAYERTEC_Optics_And_Coatings_Common_Laser_Types.pdf, Accessed: 2021-05-28.

[157] M. Abarkan, J. Salvestrini, M. Fontana, and M. Aillerie, "Frequency and wavelength dependences of electro-optic coefficients in inorganic crystals", *Applied Physics B*, vol. 76, no. 7, pp. 765–769, 2003. DOI: 10.1007/s00340-003-1196-5.

[158] M. Roth, M. Tseitlin, and N. Angert, "Oxide crystals for electro-optic Q-switching of lasers", *Glass Physics and Chemistry*, vol. 31, no. 1, pp. 86–95, 2005. DOI: 10.1007/s10720-005-0028-6.

[159] M. N. Polyanskiy, *Refractive index database*, http://refractiveindex.info, Accessed on 2021-05-28.

[160] R. Ganeev, I. Kulagin, A. Ryasnyansky, R. Tugushev, and T Usmanov, "Characterization of nonlinear optical parameters of KDP, $LiNbO_3$ and BBO crystals", *Optics Communications*, vol. 229, no. 1, pp. 403–412, 2004, ISSN: 0030-4018. DOI: 10.1016/j.optcom.2003.10.046.

[161] Yasuki Takeuchi, Junji Kawanaka, and Masayuki Fujita, "Nonlinear refractive index of a YAG crystal at low temperature", in *CLEO/Europe - EQEC 2009 - European Conference on Lasers and Electro-Optics and the European Quantum Electronics Conference*, 2009. DOI: 10.1109/CLEOE-EQEC.2009.5192480.

[162] A. N. Azarenkov, G. B. Al'tshuler, N. R. Belashenkov, and S. A. Kozlov, "Fast nonlinearity of the refractive index of solid-state dielectric active media", *Quantum Electronics*, vol. 23, no. 8, pp. 633–655, 1993. DOI: 10.1070/QE1993v023n08ABEH003139.

[163] E. T. J. Nibbering, G. Grillon, M. A. Franco, B. S. Prade, and A. Mysyrowicz, "Determination of the inertial contribution to the nonlinear refractive index of air, N_2, and O_2 by use of unfocused high-intensity femtosecond laser pulses", *J. Opt. Soc. Am. B*, vol. 14, no. 3, pp. 650–660, 1997. DOI: 10.1364/JOSAB.14.000650.

[164] A. E. Siegman, *Lasers*. University Science Books, 1986, ISBN: 9780935702118.

[165] J.-C. Diels and W. Rudolph, *Ultrashort Laser Pulse Phenomena Fundamentals, Techniques, and Applications an a Femtosecond Time Scale Second Edition*, Second Edition. Academic Press, 2006, ISBN: 978-0-12-215493-5.

[166] B. G. Bovard and H. A. Macleod, "Nonlinear behaviour of optical coatings subjected to intense laser irradiation", *Journal of Modern Optics*, vol. 35, no. 7, pp. 1151–1168, 1988. DOI: 10.1080/09500348814551241.

[167] T. Amotchkina, M. Trubetskov, and V. Pervak, "Experimental and numerical study of the nonlinear response of optical multilayers", *Opt. Express*, vol. 25, no. 11, pp. 12 675–12 688, 2017. DOI: 10.1364/OE.25.012675.

[168] D. Rodriguez, R. S. Gorur, and P. M. Hansen, "Effect of humidity on the breakdown characteristics of air in non-uniform fields at 30 kHz", *IEEE Transactions on Dielectrics and Electrical Insulation*, vol. 17, no. 1, pp. 45–52, 2010. DOI: 10.1109/TDEI.2010.5412001.

[169] G. D. Goodno, Z. Guo, R. J. D. Miller, I. J. Miller, J. W. Montgomery, S. R. Adhav, and R. S. Adhav, "Investigation of β-BaB_2O_4 as a Q switch for high power applications", *Applied Physics Letters*, vol. 66, no. 13, pp. 1575–1577, 1995. DOI: 10.1063/1.113675.

[170] A. R. Newbery, "The output characteristics of a slowly Q-switched neodymium in calcium tungstate laser", *Journal of Physics D: Applied Physics*, vol. 1, no. 12, pp. 1849–1851, 1968. DOI: 10.1088/0022-3727/1/12/437.

[171] D. Nickel, C. Stolzenburg, A. Beyertt, A. Giesen, J. Häußermann, F. Butze, and M. Leitner, "200 kHz electro-optic switch for ultrafast laser systems", *Review of Scientific Instruments*, vol. 76, no. 3, p. 033 111, 2005. DOI: 10.1063/1.1867052.

[172] F. Bergmann, M. Siebold, M. Loeser, F. Röser, D. Albach, and U. Schramm, "MHz repetion rate Yb:YAG and Yb:CaF_2 regenerative picosecond laser amplifiers with a BBO pockels cell", *Applied Sciences*, vol. 5, no. 4, pp. 761–769, 2015, ISSN: 2076-3417. DOI: 10.3390/app5040761.

[173] G. Sinkevicius and A. Baskys, "Investigation of piezoelectric ringing frequency response of beta barium borate crystals", *Crystals*, vol. 9, no. 1, 2019, ISSN: 2073-4352. DOI: 10.3390/cryst9010049.

[174] I. Martynyuk-Lototska, T. Dudok, Y. Dyachok, Y. Burak, and R. Vlokh, "Acoustooptic interaction in barium beta-borate crystals", *Ukrainian Journal of Physical Optics*, vol. 5, no. 2, 67—69, 2004, ISSN: 1609-1833. DOI: 10.3116/16091833/5/2/67/2004.

[175] B. E. A. Saleh and M. C. Teich, *Fundamentals of Photonics*, 2nd Edition. John Wiley & Sons, Ltd, 2007, ISBN: 9780471358329.

[176] R. Sun, D. Jin, F. Tan, S. Wei, C. Hong, J. Xu, J. Liu, and P. Wang, "High-power all-fiber femtosecond chirped pulse amplification based on dispersive wave and chirped-volume Bragg grating", *Opt. Express*, vol. 24, no. 20, pp. 22 806–22 812, 2016. DOI: 10.1364/OE.24.022806.

[177] L. B. Glebov, "Volume holographic elements in a photo-thermo-refractive glass", *Journal of Holography and Speckle*, vol. 5, no. 1, pp. 77–84, 2009, ISSN: 1546-9018. DOI: 10.1166/jhs.2009.011.

[178] R. L. Fork, C. H. B. Cruz, P. C. Becker, and C. V. Shank, "Compression of optical pulses to six femtoseconds by using cubic phase compensation", *Opt. Lett.*, vol. 12, no. 7, pp. 483–485, 1987. DOI: 10.1364/OL.12.000483.

[179] TEM Messtechnik. (2021). "Aligna – automated laser beam alignment and stabilization system", [Online]. Available: http://www.tem-messtechnik.de/EN/aligna.htm (visited on 05/28/2021).

Publications of the author related to this work

Articles in peer-reviewed journals

[A1] **J. Mužík**, M. Jelínek, V. Jambunathan, T. Miura, M. Smrž, A. Endo, T. Mocek, and V. Kubeček, "Cryogenically-cooled Yb:YGAG ceramic mode-locked laser," *Opt. Express*, vol. 24, p. 1402, 2016. DOI: 10.1364/OE.24.001402.

[A2] **J. Mužík**, R. Yasuhara, M. Smrž, V. Kubeček, and T. Mocek, "A high-brightness room temperature 2.7 μm Er:Y_2O_3 ceramic laser," *Laser Physics Letters*, vol. 16, no. 3, p. 035801, 2019. DOI: 10.1088/1612-202X/aaff48.

[A3] O. Novák, T. Miura, M. Smrž, M. Chyla, S. Nagisetty, **J. Mužík**, J. Linnemann, H. Turčičová, V. Jambunathan, O. Slezák, M. Sawicka-Chyla, J. Pilař, S. Bonora, M. Divoký, J. Měsíček, A. Pranovich, P. Sikocinski, J. Huynh, P. Severová, P. Navrátil, D. Vojna, L. Horáčková, K. Mann, A. Lucianetti, A. Endo, D. Rostohar, and T. Mocek, "Status of the High Average Power Diode-Pumped Solid State Laser Development at HiLASE," *Applied Sciences*, vol. 5, no. 4, p. 637, 2015. DOI: 10.3390/app5040637.

[A4] M. Smrž, O. Novák, **J. Mužík**, H. Turčičová, M. Chyla, S. S. Nagisetty, M. Vyvlečka, L. Roškot, T. Miura, J. Černohorská, P. Sikocinski, L. Chen, J. Huynh, P. Severová, A. Pranovich, A. Endo, and T. Mocek, "Advances in High-Power, Ultrashort Pulse DPSSL Technologies at HiLASE," *Applied Sciences*, vol. 7, no. 10, p. 1016, 2017. DOI: 10.3390/app7101016.

[A5] A. Endo, M. Smrž, **J. Mužík**, O. Novák, M. Chyla, and T. Mocek, "kW-class picosecond thin-disc prepulse laser Perla for efficient EUV generation," *Journal of Micro/Nanolithography, MEMS, and MOEMS*, vol. 16, no. 4, p. 041011, 2017. DOI: 10.1117/1.JMM.16.4.041011.

[A6] H. Turčičová, O. Novák, L. Roškot, M. Smrž, **J. Mužík**, M. Chyla, A. Endo, and T. Mocek, "New observations on DUV radiation at 257 nm and 206 nm produced by a picosecond diode pumped thin-disk laser," *Optics Express*, vol. 27, no. 17, p. 24286, 2019. DOI: 10.1364/OE.27.024286.

[A7] M. Smrž, M. Chyla, **J. Mužík**, S. Nagisetty, and O. Novák, "Compact, picosecond, kW-class thin-disk laser PERLA for hi-tech industrial applications," *MM Science Journal*, vol. 2019, no. 5, p. 3620-3625, 2019. DOI: 10.17973/MMSJ.2019_12_2019111.

[A8] R. Jagdheesh, P. Hauschwitz, **J. Mužík**, P. Brajer, D. Rostohar, P. Jiříček, J. Kopeček, and T. Mocek, "Non-fluorinated superhydrophobic Al7075 aerospace alloy by ps laser processing," *Applied Surface Science*, vol. 493, p. 287, 2019. DOI: 10.1016/j.apsusc.2019.07.035.

[A9] H. Sopha, I. Mirza, H. Turčičová, D. Pavlinak, J. Michalicka, M. Krbal, J. Rodriguez-Pereira, L. Hromadko, O. Novák, **J. Mužík**, M. Smrž, E. Kolibalova, N. Goodfriend, N. M. Bulgakova, T. Mocek, and J. M. Macak, "Laser-induced crystallization of anodic TiO_2 nanotube layers," *RSC Advances*, vol. 10, p. 22137, 2020. DOI: 10.1039/D0RA02929G.

[A10] D. Štěpánková, **J. Mužík**, O. Novák, L. Roškot, V. Smirnov, L. Glebov, M. Jelínek, M. Smrž, A. Lucianetti, and T. Mocek, "Experimental study on compression of 216-W laser pulses below 2 ps at 1030 nm with chirped volume Bragg grating," *Appl. Opt.*, vol. 59, no. 26, p. 7938, 2020. DOI: 10.1364/AO.400415.

[A11] M. Smrž, **J. Mužík**, D. Štěpánková, H. Turčičová, O. Novák, M. Chyla, P. Hauschwitz, J. Brajer, J. Kubát, F. Todorov, and T. Mocek, "Picosecond thin-disk laser platform PERLA for multi-beam micromachining," *OSA Continuum*, vol. 4, no. 3, p. 940-952, 2021. DOI: 10.1364/OSAC.418293.

Chapter in book

[A12] M. Smrž, **J. Mužík**, and S. S. Nagisetty, "23. Solid-state lasers in EUV lithography and metrology," in *Photon Sources for Lithography and Metrology*, V. Bakshi, Ed., SPIE Press, 2021 (accepted, in production process).

Conference contributions

[A13] **J. Mužík**, M. Chyla, S. S. Nagisetty, T. Miura, K. Mann, A. Endo, and T. Mocek, "Precise curvature measurement of Yb:YAG thin disk," Proc. SPIE **9442**, 94420X (2014). DOI: 10.1117/12.2176185.

[A14] **J. Mužík**, V. Jambunathan, M. Jelínek, V. Kubeček, T. Miura, A. Endo, and T. Mocek, "Laser properties of Yb:YGAG ceramic in comparison with crystalline Yb:YAG," *in CLEO/Europe – EQEC 2015* (2015).

[A15] **J. Mužík**, M. Smrž, T. Miura, A. Endo, V. Kubeček, and T. Mocek, "Development of a kW-level Picosecond Light Source Using Two-Stage Thin-Disk Regenerative Amplifier," *in Advanced Solid State Lasers Congress*, paper AW3A.6 (2015). DOI: 10.1364/ASSL.2015.AW3A.6.

[A16] **J. Mužík**, M. Jelínek, T. Miura, M. Smrž, A. Endo, T. Mocek, and V. Kubeček, "Cryogenically-Cooled Mode-Locked Yb:YGAG Ceramic Laser," *in Advanced Solid State Lasers Congress*, paper AM5A.27 (2015). DOI: 10.1364/ASSL.2015.AM5A.27. *Awarded by 2015 ASSL Conference Outstanding Poster Presentation Award.*

[A17] **J. Mužík**, M. Jelínek, T. Miura, M. Smrž, A. Endo, T. Mocek, and V. Kubeček, "Cryogenically cooled Yb:YGAG ceramic picosecond oscillator," Proc. SPIE **9893**, 98930B (2016). DOI: 10.1117/12.2227437.

[A18] **J. Mužík**, M. Smrž, O. Novák, T. Miura, A. Endo, V. Kubeček, and T. Mocek, "Development of a kW-level picosecond thin-disk regenerative amplifier with a ring cavity," Proc. SPIE **9893**, 989307 (2016). DOI: 10.1117/12.2227714.

[A19] **J. Mužík**, R. Yasuhara, M. Smrž, M. Jelínek, V. Kubeček, A. Endo, and T. Mocek, "Development of 2.7-μm Er:Y_2O_3 ceramic laser operated at room temperature," Proc. SPIE **10238**, 10238164 (2017). DOI: 10.1117/12.2265764.

[A20] **J. Mužík**, M. Smrž, M. Chyla, O. Novák, V. Kubeček, A. Endo, and T. Mocek, "4-mJ, 50-kHz picosecond pulses from PERLA C thin-disk laser platform," Proc. SPIE **WS100**, WS100-9 (2017).

[A21] **J. Mužík**, M. Smrž, M. Chyla, V. Kubeček, A. Endo, and T. Mocek, "Development of a variable repetition rate, kW-level, picosecond ring regenerative amplifier," *in CLEO/Europe – EQEC 2017* (2017).

[A22] **J. Mužík**, M. Smrž, M. Chyla, O. Novák, H. Turčičová, A. Endo, and T. Mocek, "Development of kW-level picosecond thin-disk pre-pulse laser for high-power EUV sources," *in 2017 Source Workshop* (2017).

[A23] **J. Mužík**, M. Chyla, D. Štěpánková, O. Novák, V. Kubeček, M. Smrž, and T. Mocek, "Compact kW-level picosecond Yb:YAG laser system PERLA C," *in SPIE Optics + Optoelectronics 2019* (2019).

[A24] M. Smrž, **J. Mužík**, O. Novák, H. Turčičová, A. Endo, and T. Mocek, "0.5 kW Picosecond Yb:YAG Regenerative Amplifier for Deep UV to Mid-IR Frequency Conversion," *in Stuttgart Laser Technology Forum 2016* (2016).

[A25] M. Smrž, **J. Mužík**, O. Novák, M. Chyla, H. Turčičová, S. S. Nagisetty, J. Huynh, T. Miura, J. Linnemann, P. Severová, P. Sikocinski, A. Endo, and T. Mocek, "Progress in kW-class picosecond thin-disk lasers development at the HiLASE," Proc. SPIE **9726**, 972617 (2016). DOI: 10.1117/12.2212396.

[A26] H. Turčičová, O. Novák, L. Roškot, M. Smrž, **J. Mužík**, A. Endo, and T. Mocek, "Extension of application potential of a picosecond 100 kHz high-average power Yb:YAG thin-disk laser by harmonic generation into VIS, UV, and DUV," Proc. SPIE **WS100**, WS100-11 (2017).

[A27] M. Vyvlečka, J.Černohorská, **J. Mužík**, O. Novák, M. Smrž, A. Endo, and T. Mocek, "Pulse compression optimization of a picosecond high average power thin-disk laser," Proc. SPIE **WS100**, WS100-19 (2017).

[A28] O. Novák, M. Vyvlečka, L. Roškot, **J. Mužík**, M. Smrž, A. Endo, and T. Mocek, "Wavelength Tunable Picosecond Parametric Mid-IR Source Pumped by a High Power Thin-Disk Laser," *in CLEO/Europe – EQEC 2017* (2017). DOI: 10.1364/ASSL.2017.JTh2A.42.

[A29] M. Smrž, M. Divoký, **J. Mužík**, O. Novák, M. Chyla, J. Pilař, M. Hanuš, A. Lucianetti, A. Endo, and T. Mocek, "kW-class picosecond and nanosecond lasers at Hilase for hi-tech industrial applications," *in IEEE Photonics Conference*, pp. 333-334 (2017). DOI: 10.1109/IPCon.2017.8116126.

[A30] M. Chyla, M. Divoký, M. Smrž, **J. Mužík**, A. Reza, P. Sikocinski, L. Chen, P. Severova, O. Novak, H. Turčičová, M. Vyvlečka, L. Roškot, J. Huynh, S. S. Nagisetty, J. Černohorská, H. Zhou, A. Pranovich, J. Pilař, O. Slezák, M. Sawicka-Chyla, V. Jambunathan, A. Endo, A. Lucianetti, D. Rostohar, P. D. Mason, P. J. Phillips, K. Ertel, S. Banerjee, J. M. Smith, T. J. Butcher, M. De Vido, C. Hernandez-Gomez, C. Edwards, J. L. Collier, and T. Mocek, "Status and Development of High Average Power Lasers at HiLASE," *in Conference on Lasers and Electro-Optics*, paper STu4O.6 (2018). DOI: 10.1364/CLEO_SI.2018.STu4O.6.

[A31] H. Turčičová, O. Novák, M. Smrž, **J. Mužík**, L. Roškot, A. Endo, and T. Mocek, "Generation of harmonic frequencies from 2nd up to 5th of a picosecond diode-pumped thin-disk Yb:YAG laser system," *in 8th EPS-QEOD Europhoton Conference* (2018).

[A32] D. Štěpánková, O. Novák, **J. Mužík**, L. Roškot, M. Chyla, M. Smrž, A. Endo, and T. Mocek, "Characterization of a chirped volume Bragg grating compressor in a high-power laser system," *in 8th EPS-QEOD Europhoton Conference* (2018).

[A33] M. Vyvlečka, O. Novák, L. Roškot, M. Smrž, **J. Mužík**, A. Endo, and T. Mocek, "Ten-watt level picosecond parametric mid-IR source broadly tunable in wavelength," Proc. SPIE **10516**, 105161F (2018). DOI: 10.1117/12.2288227.

[A34] O. Novák, B. Csanaková, L. Roškot, M. Vyvlečka, **J. Mužík**, M. Smrž, A. Endo, H. Jelínková, and T. Mocek, "High Power Picosecond Parametric Mid-IR Source Tunable Between 1.5 and 3.2 μm," *in Laser Congress 2018 (ASSL)*, paper ATh2A.15 (2018). DOI: 10.1364/ASSL.2018.ATh2A.15.

[A35] H. Turčičová, O. Novák, L. Roškot, **J. Mužík**, M. Smrž, A. Endo, and T. Mocek "Picosecond deep ultraviolet pulses generated by a 100 kHz thin-disk laser system," Proc. SPIE **11042**, 110420H (2018). DOI: 10.1117/12.2521641.

[A36] D. Štěpánková, **J. Mužík**, O. Novák, L. Roškot, V. Smirnov, L. Glebov, M. Jelínek, M. Smrž, and T. Mocek, „Analysis of chirped volume Bragg gratings for compression of high power 270-W, 2-ps pulses at 1030 nm," *in SPIE Optics + Optoelectronics 2019* (2019).

[A37] H. Turčičová, O. Novák, M. Duda, L. Roškot, M. Smrž, **J. Mužík**, M. Chyla, A. Endo, and T. Mocek "Picosecond pulses of VIS, UV and DUV radiation generated by a 200 W Yb:YAG thin-disk laser," *in SPIE Optics + Optoelectronics 2019* (2019).

[A38] H. Zhou, M. Chyla, P. Crha, J. Horáček, **J. Mužík**, O. Novák, M. Smrž, and T. Mocek, "100 W, TRL 6 thin-disk laser for industrial applications," *in SPIE Optics + Optoelectronics 2019* (2019).

[A39] L. Roškot, O. Novák, **J. Mužík**, M. Smrž, M. Jelínek, T. Mocek, and B. Csanaková, "Supercontinuum-based seed for a tunable parametric picosecond mid-IR source," *in SPIE Optics + Optoelectronics 2019* (2019).

[A40] B. Csanaková, O. Novák, L. Roškot, **J. Mužík**, H. Jelínková, M. Smrž, and T. Mocek, "Characteristics of a high-power picosecond mid-IR parametric generator/amplifier tunable between 1.5 and 3.2 μm," Proc. SPIE **11033**, 110330J (2019). DOI: 10.1117/12.2520215.

[A41] L. Roškot, O. Novák, B. Csanaková, **J. Mužík**, M. Jelínek, M. Smrž, and T. Mocek, "Dependencies of picosecond pulse driven supercontinuum properties on repetition rate," *in CLEO/Europe – EQEC 2019* (2019). DOI: 10.1109/CLEOE-EQEC.2019.8871949.

[A42] H. Turčičová, O. Novák, M. Duda, L. Roškot, **J. Mužík**, M. Smrž, and T. Mocek, "Picosecond Deep Ultraviolet Pulses Generated in Excess of the 1030 nm Fundamental Beam," *in CLEO/Europe – EQEC 2019* (2019). DOI: 10.1109/CLEOE-EQEC.2019.8872770.

[A43] B. Csanaková, L. Roškot, O. Novák, **J. Mužík**, H. Jelínková, M. Smrž, and T. Mocek, "Comparison of seed sources for a high-power, picosecond mid-IR optical parametric amplifier: Optical parametric generation versus supercontinuum," *in CLEO/Europe – EQEC 2019* (2019).

[A44] H. Turčičová, O. Novák, **J. Mužík**, D. Štěpánková, M. Smrž, A. Lucianetti, and T. Mocek, "SHG and SFG processes at a 100 kHz picosecond diode pumped Yb:YAG thin disk laser," *in 9th EPS-QEOD Europhoton Virtual Conference* (2020).

Other publications of the author

Articles in peer-reviewed journals

[B1] **J. Mužík**, M. Jelínek, D. Vyhlídal, and V. Kubeček, "2.6 W diode-pumped actively mode-locked Tm:YLF laser," *Laser Phys. Lett.*, vol. 12, p. 035802, 2015. DOI: 10.1088/1612-2011/12/3/035802.

[B2] D. Vojna, R. Yasuhara, O. Slezák, **J. Mužík**, A. Lucianetti, and T. Mocek, "Verdet constant dispersion of CeF_3 in the visible and near-infrared spectral range," *Optical Engineering*, vol. 56, no. 6, p. 067105, 2017. DOI: 10.1117/1.OE.56.6.067105.

Other work

[B3] **J. Mužík**, "Measurement of femtosecond laser pulses using SPIDER technique," Bachelor thesis, FNSPE of Czech Technical University in Prague, supervised by V. Kubeček (2012, in Czech).

[B4] **J. Mužík**, "Diagnostics of Amplified Pulses of Femtosecond Laser and Their Compression Using Filamentation in Gases," Research project, FNSPE of Czech Technical University in Prague, supervised by V. Kubeček (2013, in Czech).

[B5] **J. Mužík**, "Diode-pumped thulium laser," Diploma thesis, FNSPE of Czech Technical University in Prague, supervised by V. Kubeček (2014, in Czech).

[B6] **J. Mužík**, M. Jelínek, D. Vyhlídal, and V. Kubeček, "Diode-Pumped Actively Mode-Locked Tm:YLF Laser," *in 6th EPS-QEOD Europhoton Conference* (2014).

[B7] **J. Mužík**, V. Kubeček , D. Vyhlídal, and M. Jelínek, "1.2 W actively mode-locked Tm:YLF laser," Proc. SPIE **9441**, 94410E (2014). DOI: 10.1117/12.2087428.

[B8] A. Endo, M. Smrž, O. Novák, H. Turčičová, **J. Mužík**, J. Huynh, T. Mocek, K. Sakaue, and M. Washio, "Picosecond, kW thin disc laser technology for LPP and FEL EUV sources," *in High-Brightness Sources and Light-Driven Interactions*, paper ES4A.2 (2016).

[B9] P. Severová, M. Chyla, **J. Mužík**, M. Smrž, T. Miura, M. Kawasaki, T. Higashiguchi, A. Endo, and T. Mocek, "Investigation and modelling of pump saturation effect on thermal load of Yb:YAG thin disk pumped at various wavelengths," Proc. SPIE **10238**, 102380P (2017). DOI: 10.1117/12.2265822.

List of Figures

List of Tables

Declaration

I hereby declare that I have elaborated the doctoral thesis Development of High-Repetition-Rate Picosecond Thin-Disk Lasers independently under the supervision of Prof. Ing. Václav Kubeček, DrSc. and Ing. Martin Smrž, Ph.D., and that all sources of information used have been cited. This dissertation is my own work and all areas, where the outcome resulted from collaboration with my colleagues, are specified in the text and in Acknowledgements.

In Prague on 31th May 2021

Jiří Mužík

Acknowledgments

Finishing this work would have not been possible without help and support of many colleagues and friends.

First of all I would like to thank my supervisors. To Professor Václav Kubeček I deeply thank for leading me since my undergraduate years, teaching me all the laser laboratory fundamentals I have used on every working day since, and for his continued support. I am also grateful for arranging all the practical aspects of the cryogenic Yb:YGAG laser experiment. To Martin Smrž I thank so much for his friendship, all-embracing assistance, technical insights, and kind, ceaseless support – without this I would never dare to work on a half-million-euro laser system (or at least no longer than until the first mishap).

Next, I want to thank all my colleagues in the thin-disk-laser group of HiLASE for creating such a nice working environment. Especially I wish to thank Michal Chyla for lots of help, his great memory and for sharing the office with me since the beginning; to Denisa Štěpánková for joining me in the quest for a reliable laser system and for sharing all the small routine things that would be too many for one person; to Vítek Bílý for help with the fiber front end, his proficient work with the fiber spools and splicers, succeeding where I would end up tangled-up in optical fiber; to Jitka Černohorská for her support and help with the fiber preamplifiers; to Ondřej Novák for much advice, especially regarding the characterization techniques and instruments; to Luděk Švandrlík for designing 100%-tailored components of great ingenuity and inherent beauty that also often could make us all laugh; and to Jára Huynh, Honza Cvrček, Martin Cimrman and Lukáš Roškot for always sharing a cup of coffee and making the long weeks of 2020/2021 so much more enjoyable.

I would like to thank Dr. Tomáš Mocek for giving me the opportunity to be a part of the excellent HiLASE project. I also thank other colleagues from HiLASE for joining us for successful experiments and for their patience, and to Venki Jambunathan for having and sharing wonderful spectroscopic data for all those crystals and ceramics. I thank the colleagues from the administration and procurement department for shielding us as much as possible from the outer world and to the colleagues from technical team for supporting our experimental endeavors.

I thank Ryo Yasuhara for preparing the experiment with erbium ceramics and his kind assistance during my stays in Japan. I also thank Michal Jelínek for many consultations over the years and his help with measuring the absorption spectra of Er:Y_2O_3 at low temperature.

I also thank Dr. Marwan Abdou-Ahmed from IFSW Stuttgart and Dr. Thorald Bergmann from BME. Without their assistance in unlocking the full potential of the thin disks and Pockels cell drivers, half-kilowatt, 100-kHz regenerative amplifier would remain a dream for us for a few more years.

Last but definitely not least, I thank my parents Věra and Luboš for their support throughout my studies, for encouraging me in my decisions, and for always being there for me.

Finally, I acknowledge the support of following European, Czech, and Japanese grants and research programs:

- Projects co-financed by the European Regional Development Fund, the European Social Fund and the state budget of the Czech Republic (project HiLASE: CZ.1.05/2.1.00/01.0027, project DPSSLasers: CZ.1.07/2.3.00/20.0143, project HiLASE: Superlasers for real world: LO1602, and project HiLASE CoE CZ.02.1.01/0.0/0.0/15_006/0000674)
- European Union's Horizon 2020 research and innovation programme (Grant agreement No. 739573)
- Czech Science Foundation project P102/13/8888
- Student Grant Competition of CTU SGS13/220/OHK4/3T/14, SGS16/247/OHK4/3T/14, and SGS19/191/OHK4/3T/14
- JSPS KAKENHI grant No. 15KK0245 support and support of the National Institute for Fusion Science (KEIN1608)